AD-A125 341 SIMULATION OF DISTRIBUTED-EMISSION AND INJECTED-BEAM CROSSED-FIELD AMPLIF..(U) HARRIS SAI INC ANN ARBOR MI D M MACGREGOR ET AL. APR 80 AFOSR-TR-80-0553 1/3

UNCLASSIFIED F49620-77-C-0091 F/G 9/1 NL

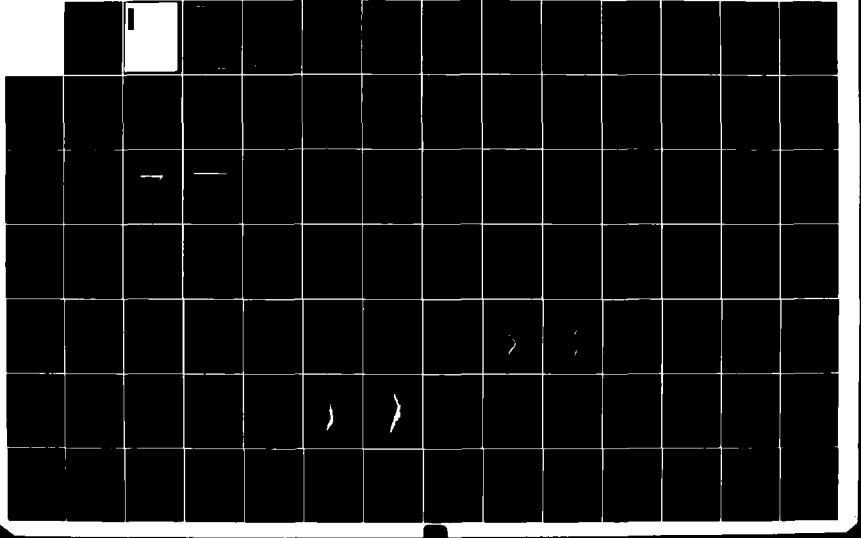

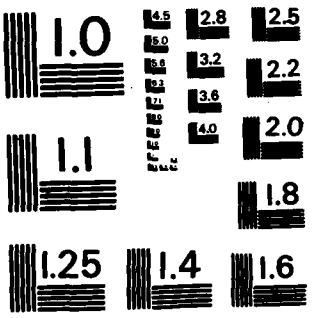

SECURITY CLASSIFICATION OF THIS PAGE (When Data Entered) UNCLASSIFIED

REPORT DOCUMENTATION PAGE

READ INSTRUCTIONS BEFORE COMPLETING FORM

1. REPORT NUMBER: AFOSR-TR-80-0553
2. GOVT ACCESSION NO.: AD-A125341
3. RECIPIENT'S CATALOG NUMBER:

4. TITLE (and Subtitle):
Simulation of Distributed-Emission and Injected-Beam Crossed-Field Amplifiers
Part I: The Distributed-Emission Crossed-Field Amplifier

5. TYPE OF REPORT & PERIOD COVERED:
Final Technical Report
March 1, 1977-Feb. 29, 1980

6. PERFORMING ORG. REPORT NUMBER:

7. AUTHOR(s):
Dr. Donald M. MacGregor
Dr. Thomas P. Fontana and
Dr. Joseph E. Rowe

8. CONTRACT OR GRANT NUMBER(s):
F49620-77-C-0091

9. PERFORMING ORGANIZATION NAME AND ADDRESS:
Harris SAI, Inc.
611 Church Street
Ann Arbor, MI 48104

10. PROGRAM ELEMENT, PROJECT, TASK AREA & WORK UNIT NUMBERS:
61102-F 2305/C1

11. CONTROLLING OFFICE NAME AND ADDRESS:
Air Force Office of Scientific Research
Building 410
Bolling AFB, D.C. 20332

12. REPORT DATE:
April 1980

13. NUMBER OF PAGES:
195

14. MONITORING AGENCY NAME & ADDRESS (if different from Controlling Office):

15. SECURITY CLASS. (of this report):
Unclassified

15a. DECLASSIFICATION/DOWNGRADING SCHEDULE:

16. DISTRIBUTION STATEMENT (of this Report):
Approved for public release; distribution unlimited.

17. DISTRIBUTION STATEMENT (of the abstract entered in Block 20, if different from Report):

18. SUPPLEMENTARY NOTES:

19. KEY WORDS (Continue on reverse side if necessary and identify by block number):
Injected-beam CFA
Crossed-field amplifier
Microwave tubes
Computer simulation
Electron dynamics
Electron gun

20. ABSTRACT (Continue on reverse side if necessary and identify by block number):
Numerical models developed for the crossed-field electron gun predict the current and the beam shape and stability for varied voltages or magnetic field. These programs use a deformable triangular mesh to reproduce the realistic electrode boundaries.

A static iterative analysis predicts beam currents about 5 percent higher than measured for a short Kino gun, but is not

DD FORM 1 JAN 73 1473 EDITION OF 1 NOV 65 IS OBSOLETE

UNCLASSIFIED
SECURITY CLASSIFICATION OF THIS PAGE (When Data Entered)

20.

stable for long cathodes with returning electrons. However, the alternative time-dependent method predicts a stable, well-defined beam in both cases.

Excess shot noise in a long-cathode crossed-field gun is believed to be due to cycloiding electrons which return to the cathode from well beyond the potential minimum. Of three theories compared here, only the Ho and Van Duzer model includes these electrons and predicts an instability. With added shot noise the computer simulation may be capable of reproducing the effect.

Experimental measurements have been obtained by subcontract for a Northrop gridded crossed-field gun. The two-dimensional time-dependent analysis, which ignores the grids, predicts the beam current with good order-of-magnitude agreement. A macroscopic cathode model uses the cathode electric field and the local charge to limit the emission at each time step, with results verified by Child's Law. A three-dimensional charge-free solution demonstrates the field at the grid. This study has established the essential theory and program structures for the planned complete gun simulation in three dimensions.

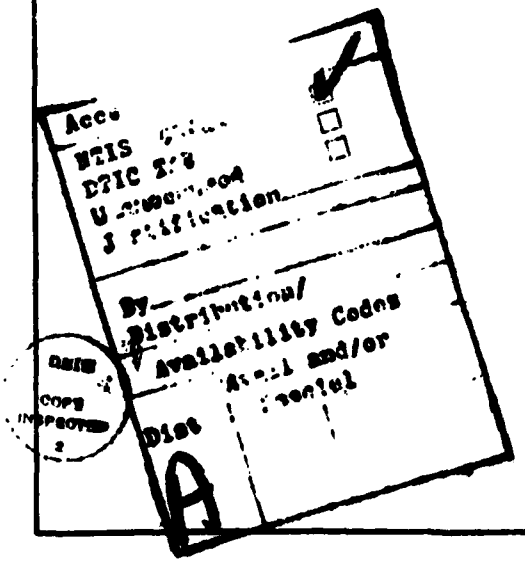

TABLE OF CONTENTS

TABLE OF CONTENTS (cont'd.)

TABLE OF CONTENTS (Concluded)

LIST OF ILLUSTRATIONS

LIST OF ILLUSTRATIONS (cont'd.)

LIST OF ILLUSTRATIONS (cont'd.)

LIST OF ILLUSTRATIONS (Concluded)

LIST OF TABLES

SECTION I

INTRODUCTION

For the past five years, Harris SAI, Inc., Ann Arbor, Michigan, has been developing advanced computer-aided simulations of crossed-field amplifiers. Since March 1, 1977, Harris SAI has been supported in this effort by the Air Force Office of Scientific Research under Contract No. F49620-77-C-0091. This Final Technical Report covers the entire period of the contract: March 1, 1977 through February 29, 1980.

The report is in two parts. Part I describes the work on the distributed-emission crossed-field amplifier. Part II (this volume) describes the parallel effort on the injected-beam crossed-field amplifier.

A. Research Objectives

Crossed-field amplifiers (CFA's) are commonly used to produce microwave power in transportable systems where light weight, compactness, high efficiency, and peak power of kilowatts or megawatts are required. Radar and electronic countermeasure systems are examples. In existing distributed-emission CFA's, it is desirable particularly to raise the gain and efficiency and extend the bandwidth over which the tube will both start and operate in the desired mode. An injected-beam CFA (IBCFA, Figure 1) can be used as the final amplifier in an electronic countermeasure or radar transmitter where relatively high gain of 20 to 30 dB is required at frequencies covering an octave range. Because it can tolerate a wide range of duty cycles at fixed peak power, it is especially

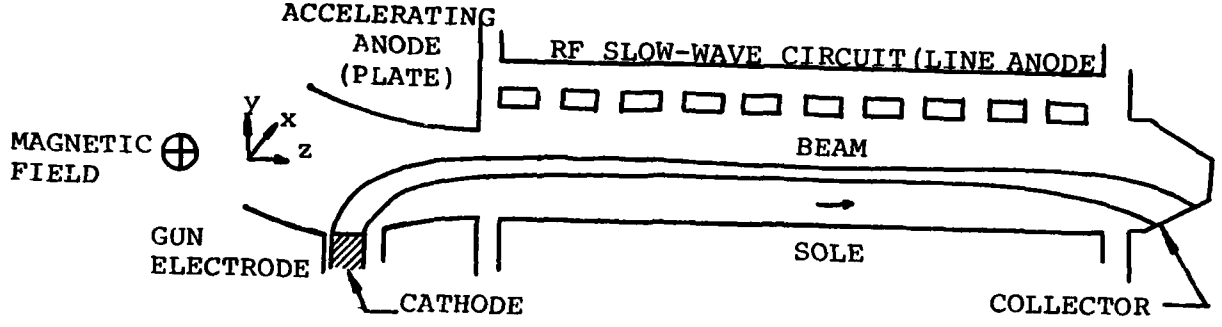

Figure 1. Linear injected-beam crossed-field amplifier (IBCFA).

suitable for multiple functions (e.g. air-to-air or air-to-ground transmission) in a single system. The designer of an IBCFA aims for high efficiency and wide dynamic range with a stable, low-noise beam.

The effort in the IBCFA studies has shifted the emphasis from the RF properties of the tube, included in the original (1977) Statement of Work, to a more detailed study of the electron-gun region. The purpose is to improve the understanding of the beam injection conditions at the RF input, since the gun is recognized to be the source of much of the noise output, including intermodulation, of existing tubes.

The Northrop RW-620 injected-beam CFA was chosen as a production tube suitable for providing measurement data. The gun in this tube has a grid along the cathode in the beam-drift direction, and beam scalloping has been observed in the magnetic-field direction. Therefore, a full three-dimensional model is necessary to accurately predict the beam shape and to simulate design improvements.

The stated objectives of this research are as follows:

(1) Develop an electrostatic model for two-dimensional simulation of a crossed-field gun, using the deformable mesh technique.

(2) Develop a time-dependent two-dimensional crossed-field gun model with a Monte Carlo simulation of noise characteristics.

(3) Apply the model to study the effects of varying the accelerating anode voltage, the magnetic field, the sole voltage, and the cathode temperature on cathode current, beam shape, noise and stability.

(4) Extend the two-dimensional model to a full three-dimensional simulation, including nonuniform magnetic fields and grid wires in the beam-drift direction.

(5) Develop a fast non-iterative solution for the potential distribution on a deformable mesh.

(6) Investigate an existing approximate feedback model for possible extension to three dimensions.

(7) Obtain experimental measurements for the RW-620 crossed-field gun through a subcontract.

(8) Analyze the three-dimensional gridded RW-620 with end hats using a Monte Carlo analysis, and obtain beam noise characteristics at specified positions.

(9) Analyze the RW-620 as a periodically gridded structure so that the effects of end hats can be found by comparison with results of item 8 above.

B. Status of the Research Effort

Harris SAI has completed a significant portion of this work and has established all the basic techniques needed in the full three-dimensional study. The excellent results for the two-dimensional static gun analysis of a Kino short gun serve to validate the deformable-mesh technique. Applying the same static analysis to a longer cathode, such as in the RW-620, shows instability due to returning cycloiding electrons, and it has proved considerably more difficult to obtain a convergent solution. The computed currents are higher than measured. Since April 1979, therefore, work has been concentrated on the time-dependent gun analysis, with emphasis on the correct modeling of the cathode.

Northrop Corporation Defense Systems Division have provided experimental measurements on the RW-620 injected-beam CFA under a subcontract. For this long-cathode gun, the time-dependent two-dimensional analysis gives a clear dynamic steady state

and reasonable quantitative results. A newly developed cathode emission model accounts for returning charge and for the reduced electric field due to grid wires. The three-dimensional solution of Laplace's equation for the RW-620 geometry demonstrates the fields that exist before the beam is introduced.

Because of the large amount of computing time required for the three-dimensional work, it was planned to make use of a Harris 550 computer which was more economical than the alternative University of Michigan machine. This machine became fully operational at Harris Corporate Headquarters, Melbourne, Florida in late 1979. Unavoidable delays in the installation of the machine during 1979 left insufficient time for the three-dimensional IBCFA analysis. Instead, additional work was performed on the concurrent distributed-emission crossed-field amplifier simulation with worthwhile results.

C. Summary

The Harris SAI models of the IBCFA are compared with other recent work in Section II. Details of the deformable-mesh technique are given in Section III. Of the two alternative solution methods developed for the Poisson difference equations, relaxation is more efficient than a direct method. This is because the successive potential solutions are similar and require only about ten iterations each step.

The time-dependent analysis of the anode-sole region (Section IV) has been developed to study the effects of the beam injection on stability in the line-sole interaction region. It uses a fast Poisson solution between rectangular boundaries to reduce the computing time. Noise growth in the gun is neglected.

The two-dimensional static analysis (Section V) gives excellent agreement with published experimental measurements for a short Kino gun in which the cathode is short relative to the cycloid length. However, it has proved difficult to obtain a self-consistent convergent solution for a long cathode with this model (Section VI).

There remains considerable controversy about the existence of an instability due to shot noise at a long cathode. Section VII provides a brief description of the various recent theories. So far, only the Ho and Van Duzer model has predicted this effect.

An accurate model of cathode emission is essential for a correct estimate of the beam current produced in the gun. After a study of possible cathode-emission models of varying complexity, two types of model have been selected as program options. These are (1) a microscopic thermionic emission model in which the local potential creates a minimum to suppress excess charge, and (2) a macroscopic model which estimates the self-consistent solution at each step, assuming a mesh interval larger than the Debye length.

Section VIII describes these models and estimates the required mesh size, time step and effective cathode temperature in a simulation. The macroscopic model now gives space-charge limited currents which are 6 percent above the Child's Law values (only 2 percent in the cylindrical model of the distributed-emission tube), and about 30 percent above the measured values for the Kino short gun. However, improvement of the trajectory calculation should reduce these differences.

Under a subcontract to Harris SAI, Northrop Corporation Defense Systems Division has measured the beam current in several tubes for varied magnetic field, accelerating-anode voltage, and grid voltage. They have also supplied the observed

noise power in the absence of RF drive. Finally, "cold" and "hot" RF measurements are included in Northrop's results.

As an initial application of the three-dimensional model, the potential distribution has been computed in the RW-620 gun using the exact electrode and grid configuration, but without space charge. Graphical results are presented in Section IX.

Simulation results obtained for the RW-620 in two dimensions (Section X) show a stable beam and fair agreement with the measured currents when a grid shielding factor is used. Section XI presents conclusions and plans for continued work.

Details of the RW-620 measurements are given in Appendices A and B. The tube data required and the output information from the time-dependent program are summarized in Appendix C. Appendix D is a program output listing for a typical RW-620 simulation. The computer resources required are listed in Appendix E.

SECTION II

STATE OF THE ART OF INJECTED-BEAM CROSSED-FIELD AMPLIFIER ELECTRON GUN SIMULATION

Most existing crossed-field electron guns have been designed empirically using elementary analyses of simple electrode shapes in nongridded guns.[1] However, the injection conditions of the beam into the anode-sole region of the injected-beam crossed-field amplifier or oscillator are critical in determining noise output and efficiency. Effort is now being directed at improving the understanding of crossed-field beams both experimentally and by computer simulation. The computer models[2-7] known to Harris SAI are summarized in Table 1.

Both the iterative electrostatic and the time-dependent models have been developed by Harris SAI. The time-dependent calculation predicts beam noise and will work for both stable and unstable beams. The time-dependent motion in the anode-sole region was studied previously by Harris SAI using a rectangular interaction region with time-independent initial conditions. Only an ideal Brillouin injected beam was treated.[7] The model now under development combines the gun, transition, and anode-sole regions so as to give realistic injection conditions for the beam between the line anode and the sole.

An accurate calculation of the beam current requires an accurate model of the cathode emission in the local space-charge fields. In the Harris SAI program, a macroscopic model, originally developed by the Naval Research Laboratory for magnetron simulations,[8] ignores the electron velocity distribution and shot noise at the cathode surface. The model is verified by Child's Law, applies to both short and long

TABLE 1

STATE OF THE ART OF CROSSED-FIELD

ELECTRON GUN SIMULATION IN USA

Author	References	Features of Model
Shaw and Kooyers	2 3 4	Two- and three-dimensional time-dependent analysis of short and long guns with rectangular region for solution of Poisson equation, and approximate grid effects. Cannot treat space charge in line-sole region.
True	5	Two-dimensional static (iterative) solution for short and long guns with deformable-mesh Poisson solution.
Lele and Rowe	6	Two-dimensional Monte Carlo (time-dependent) analysis of short Kino gun with rectangular mesh for potential solution.
Chang, Fontana, MacGregor and Rowe (Harris SAI, Inc.)	7 and this report	Two-dimensional static deformable-mesh solution for short gun.
	7	Two-dimensional time-dependent deformable-mesh solution for short and long guns. Rectangular solution for line-sole region with injected Brillouin beam. Model of space-charge-limited cathode emission.
		Three-dimensional model under development.

crossed-field guns, and should treat also the shielding effects of grids.

A gun computer program has been developed by Shaw, et al.,[2-4] for design of dual-mode IBCFA's, but the techniques described for that work appear to be restrictive. Charge motion is computed as a time-dependent solution, but in a rectangular interaction region with simplified boundary conditions in two or three dimensions. The resolution of distance is fixed and determined by the rectangular mesh of points used to solve Poisson's equation. The effects of grid wires can only be approximated. There is only a simple thermionic model of cathode emission.

The deformable-mesh analysis[9,10] is a much more powerful technique. This method involves solving Poisson's equation on an adjustable triangular grid with arbitrary boundary shapes. Computation time can be minimized and accuracy increased by concentrating solution points in critical regions, such as near the cathode. Harris SAI has obtained accurate results for many O-type traveling-wave tube guns and applied this analysis to a short crossed-field gun during the first year of this AFOSR contract. A three-dimensional version of the O-type gun analysis is also giving excellent results for radially gridded guns.[11] The deformable-mesh analysis has been applied to CFA guns also by Litton Industries, but only a two-dimensional electrostatic model has been described in published work.[5]

Harris SAI is developing also a fully three-dimensional calculation. That model includes arbitrary side electrodes (end hats), a spatially variable magnetic field, grids in the principal beam direction, and electronic motion in the magnetic field direction. The grid wires are particularly important for reducing noise and beam interception and raising the efficiency of existing tubes.[12,13] Their physical effects on the beam are not well understood. Also needing an explanation is the

dramatic reduction of noise observed in a long Kino gun when the magnetic field is tilted in the transverse plane by about one degree relative to the cathode.[14]

The RW-620 injected-beam CFA has a narrow, long cathode gun and may exhibit one type of beam instability in which electrons returning to the cathode cause excess noise over the shot noise level. Ho and Van Duzer[15] have demonstrated this using an approximate feedback model and they have summarized experimental results up to 1968. Recent analytic studies of shot noise and potential perturbations,[16,17] and of velocity noise with a fixed potential,[18] however, treat only a parabolic steady-state potential and hence do not include this feedback effect. The diocotron or "slipping-stream" instability[19] is a second major source of noise in crossed-field tubes.

These two instabilities are initiated by shot noise due to random electron emission times and are distinct from the "geometrical amplification" of the initial thermal velocity distribution.[20-22] The latter is a purely steady-state crossed-field phenomenon and is at least partly the cause of the anode current that can be measured in a supposedly "cutoff" crossed-field diode. However, it is doubtful whether a true steady state exists.

SECTION III

POTENTIAL AND TRAJECTORY CALCULATIONS IN THE CROSSED-FIELD GUN

A. Introduction

The aim is to obtain the electron trajectories, the potentials and the beam current with an arbitrary electrode configuration. Two approaches are treated here: a static analysis and a time-dependent analysis.

Both methods trace the motion of representative charges ("super-electrons") through the gun. The static calculation computes all trajectories throughout the gun between successive solutions of Poisson's equation and attempts to find a convergent solution. A solution is defined to have converged when the end points of the trajectories satisfy the criterion that fewer than a specified number of these end points have changed their nearest mesh mode in two consecutive iterative cycles. The time-dependent calculation, on the other hand, does not search for a steady state, but instead solves Poisson's equation at every time step as the trajectories are advanced through the gun. New charge is injected at the cathode at every step. Figures 2 and 3 are outline flow diagrams for the two programs. In both analyses the electrode voltages are independent of time. Thus, the model represents a short-circuited, not open-circuited, diode, and high-frequency effects on the boundary voltages are ignored.

The techniques described here are applied in both static and dynamic analyses. They have been developed initially in two dimensions, but extension to three dimensions is straightforward.

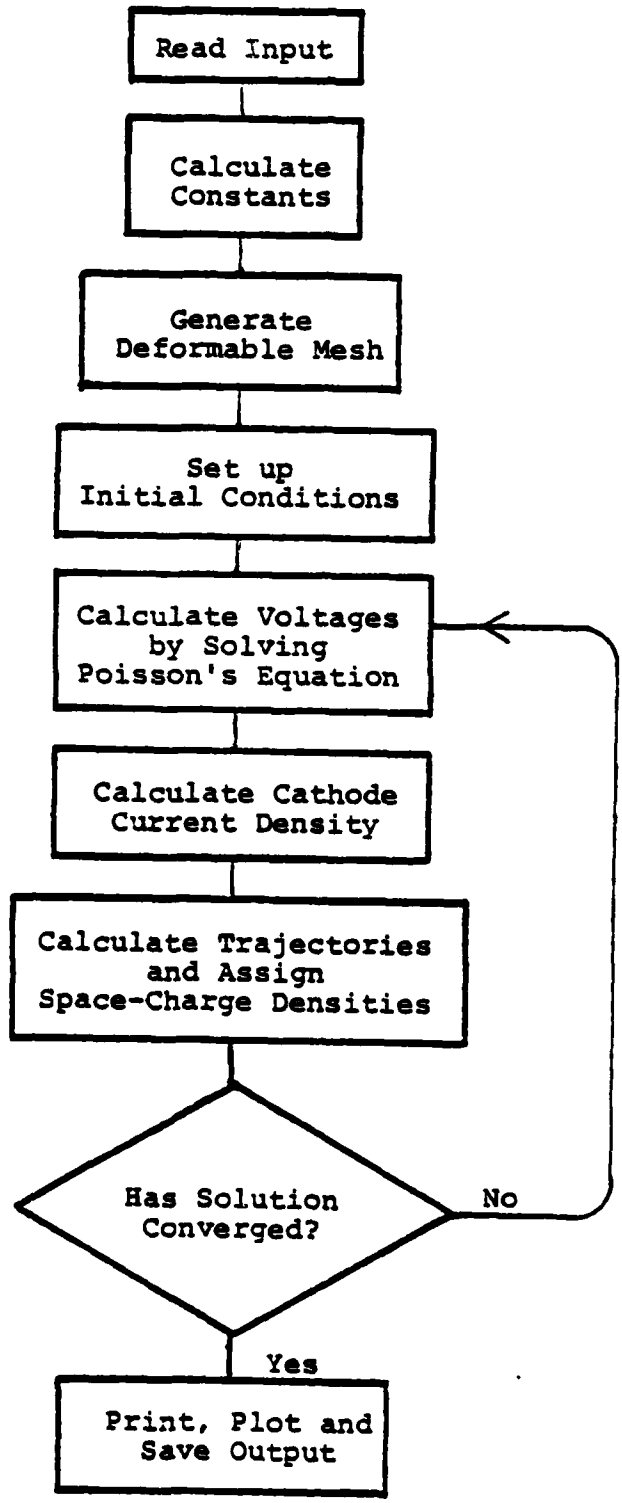

Figure 2. Flow diagram for static electron gun analysis.

x

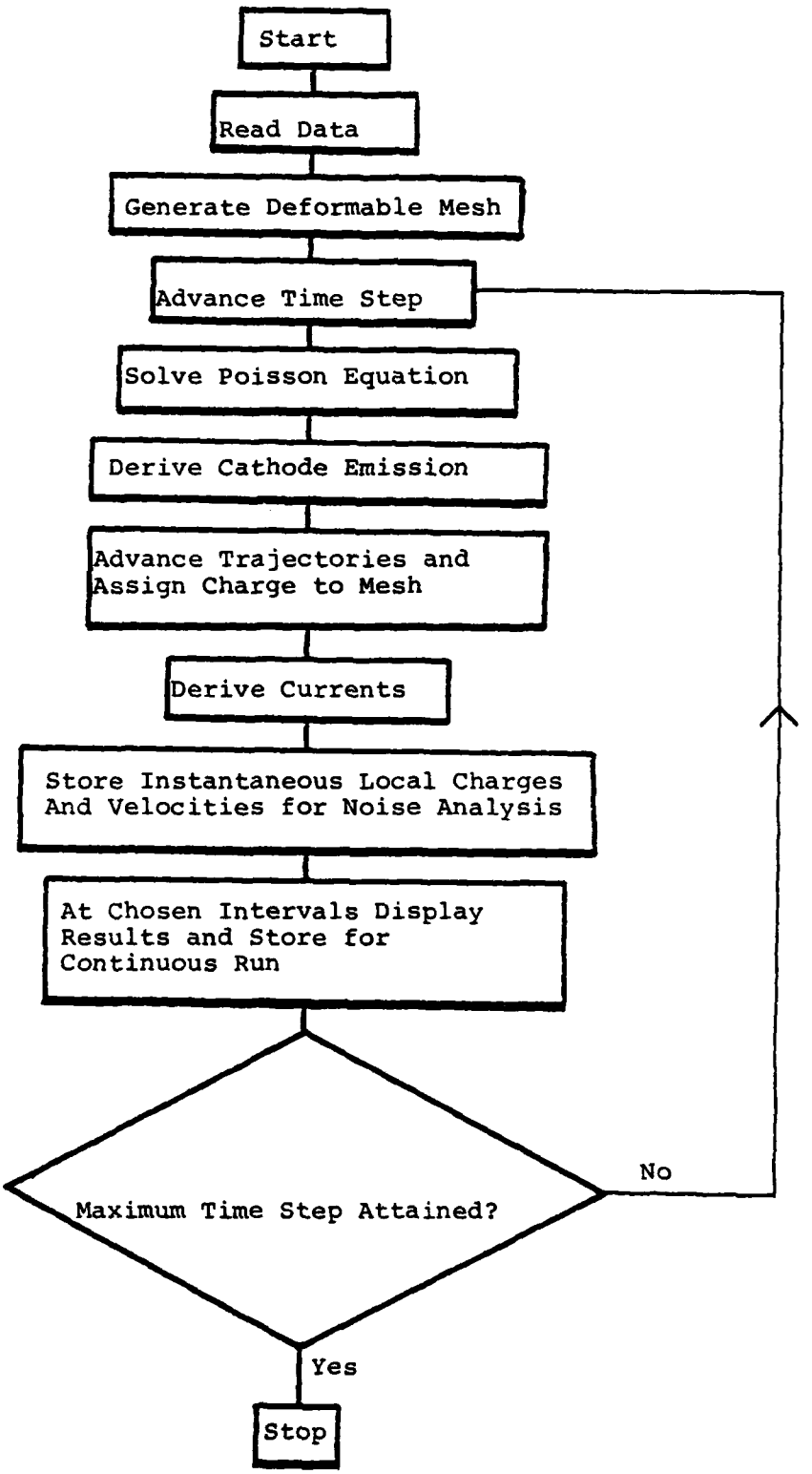

Figure 3. Flow diagram for time-dependent electron gun analysis.

B. The Deformable Triangular Mesh

1. Purpose

The deformable-mesh technique is used in the Harris SAI electron-gun analyses to provide an accurate solution of Poisson's equation with realistic electrode shapes. In the past, many analyses of this type have used a rectangular mesh because of the simplicity of the finite difference equations. However, a deformable triangular mesh has two advantages over a rectangular mesh. First, points of a deformable mesh more closely approximate the boundary of an electrode because the positions of the mesh points are adjustable. Thus, the boundary contains the mesh points instead of being forced to fit the nearest points of a rectangular mesh. Second, more mesh points can be moved into critical regions, ensuring higher accuracy where it is needed. This technique makes it possible to analyze a gridded gun which requires high resolution in the grid region.

2. Generation of the mesh

Before the simulation can be started, a mesh must be generated which outlines the geometry of the gun and defines the position of each node. The first step in generating the mesh is to set up the problem in "logical space," which is a collection of nodes labeled by the coordinate pairs (I,J), where I and J are integers. Each of the nodes in this space has six nearest neighbors, just as each mesh node in real space has six nearest neighbors. The indices (I,J) of a point differ from those of its neighbors by at most one.

The boundaries of the electron gun are supplied to the program by making the boundaries of the structure in logical space coincide with the actual physical boundaries. Three types of boundary points are used for these cases. "B" points are assigned a position and potential, both of which remain fixed

during the simulation. Likewise, the position and potential of "C" points are fixed by the program input data; these points are also capable of emitting electrons and, because they are emission centers, the program generates a fine rectangular mesh in their vicinity. "N" points constitute a Neumann boundary. The position of these points is fixed, but their potential is calculated as the simulation progresses. The program guarantees that the normal component of the electric field at the Neumann boundary is zero.

The particle search routine requires the restriction that at most 2 nodes of any mesh triangle may be defined as boundary points.

In addition to the boundary points discussed, the program recognizes another type of constrained point which is very useful in setting up complicated meshes. This is the "G" point, whose position is fixed by the input data, but whose potential is assigned as the solution of Poisson's equation progresses.

Figure 4 shows a portion of a typical mesh, first in logical space and then after deformation to fit the physical boundary shapes. Figure 5 shows a full mesh for the long-cathode gun analyzed, and Figure 6 is an expanded diagram to show the cathode region.

At the cathode a thin rectangular mesh of "G" points is established. Its size is controlled by two input parameters:

(1) NAC, the number of rectangles normal to the surface, and,

(2) FRT, defined as

$$FRT = 2\,\zeta/(NAC \cdot \xi) \quad , \tag{1}$$

where ζ and ξ are the respective mesh intervals along and perpendicular to the surface. The values in Figure 6 are NAC = 3 and FRT = 3.7.

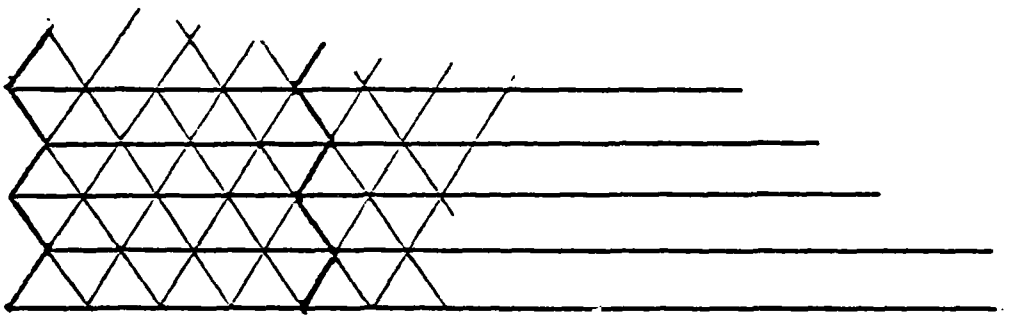

G

Before Deformation

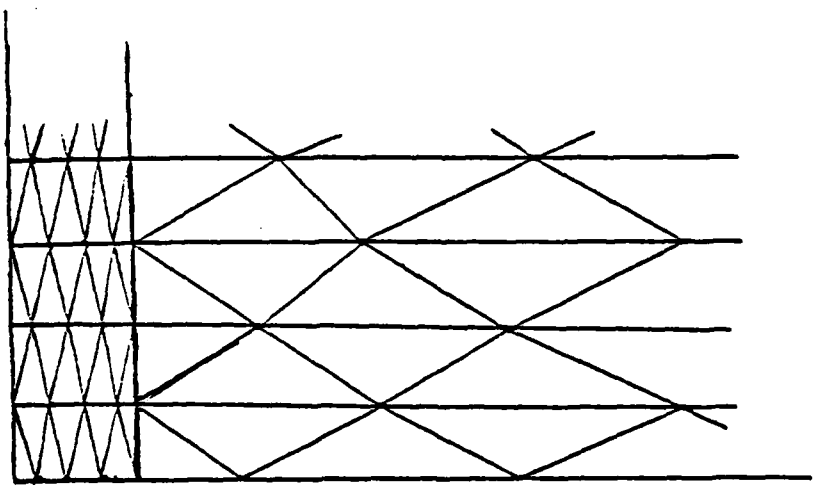

G

After Deformation

Figure 4. Use of the G-type nodes.

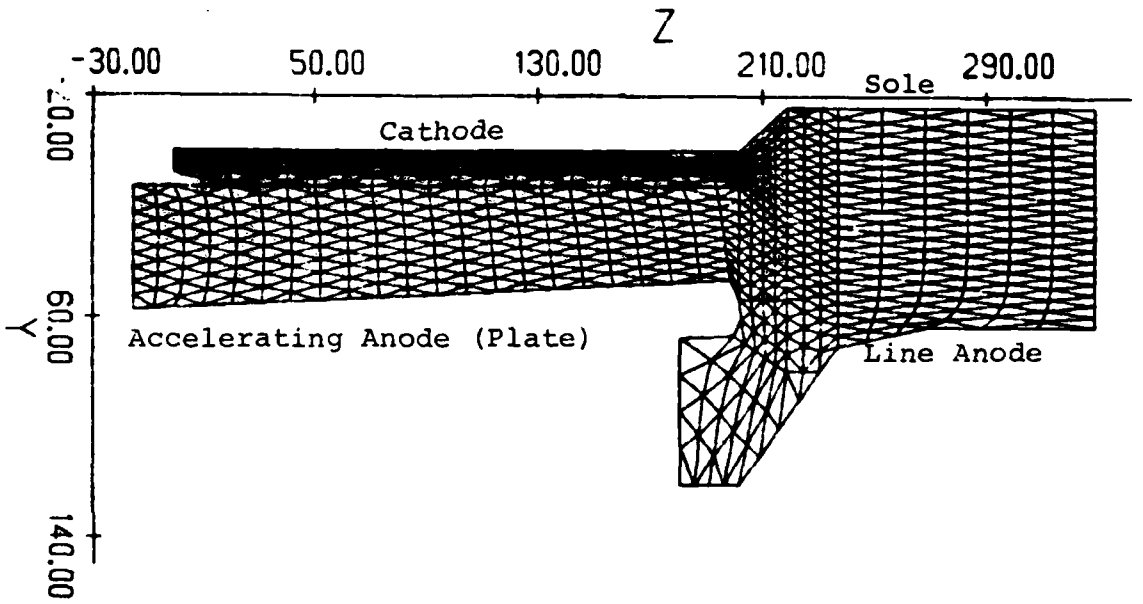

Figure 5. Mesh for simulation of RW-620 IBCFA.

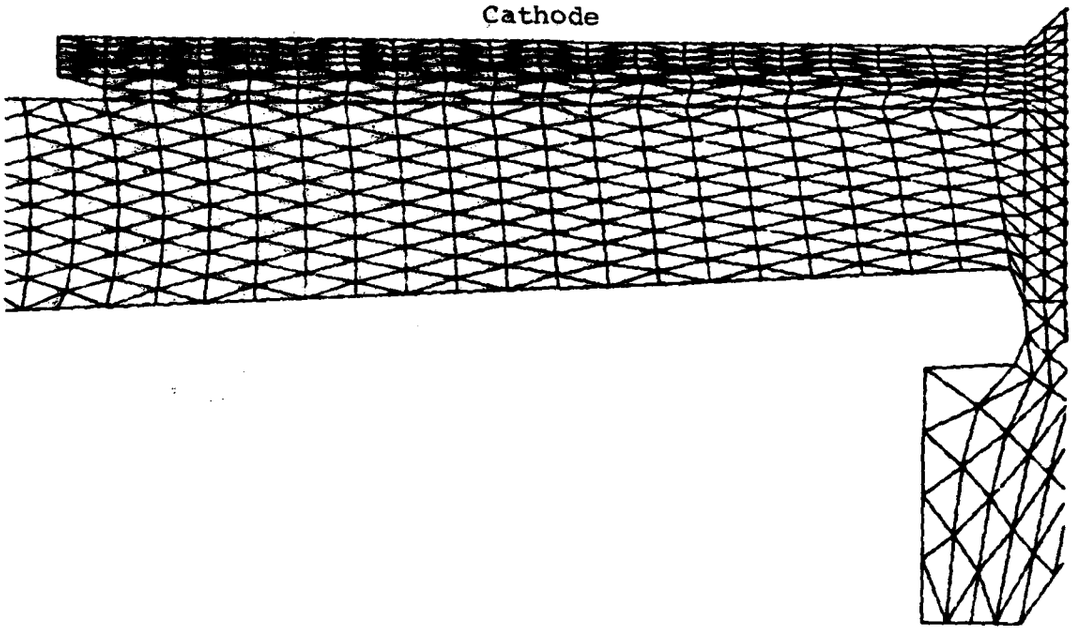

Figure 6. Mesh for RW-620 expanded to show cathode region.

The majority of the mesh points are "R" or interior points, whose positions and potentials are not fixed by the input data. The positions are determined by formulating the zoning problem as a potential problem with the mesh line playing the role of an equipotential line. The program computes the positions of interior points by solving the following Laplace's equations, using the method of successive overrelaxation:

$$\frac{\partial^2 y}{\partial i^2} + \frac{\partial^2 y}{\partial j^2} = 0 \tag{2}$$

and

$$\frac{\partial^2 z}{\partial i^2} + \frac{\partial^2 z}{\partial j^2} = 0 \quad . \tag{3}$$

Here y and z are the actual coordinates of each node and i and j are the indices of the node on the coordinate map. Each mesh point is connected to six neighboring mesh points (Figure 7).

For "R" points, the coordinates y and z are obtained by repeated solution of the relaxation equations

$$y_o^{n+1} = y_o^n + \alpha\left(\sum_{k=1}^{6} y_k^n - 6y_o^n\right)\Big/6 \tag{4}$$

and

$$z_o^{n+1} = z_o^n + \alpha\left(\sum_{k=1}^{6} z_k^n - 6z_o^n\right)\Big/6 \quad , \tag{5}$$

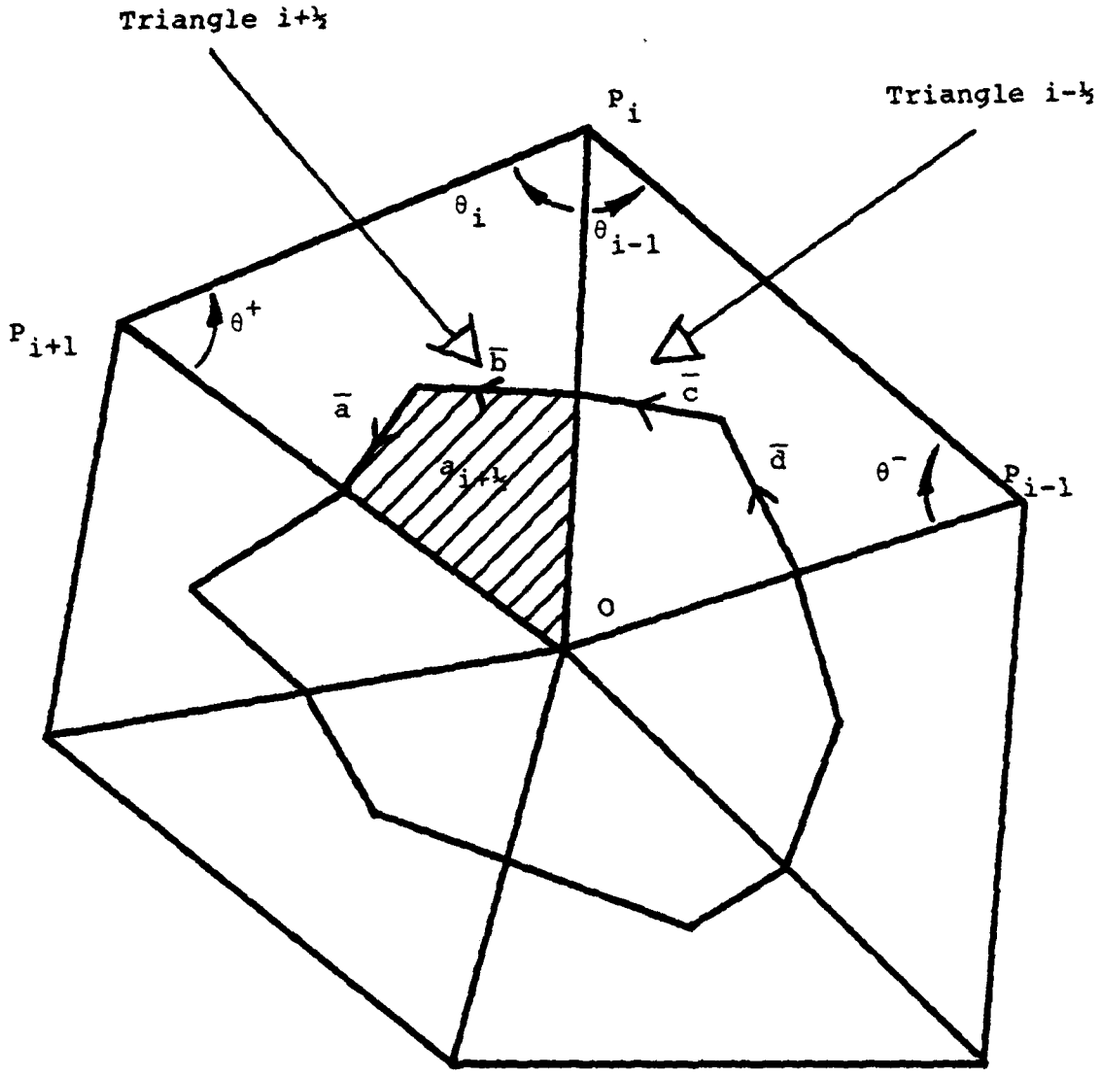

Figure 7. Mesh node, dodecagon, and six neighbors.

where (y_o^n , z_o^n) are the coordinates of the node at the n^{th} iteration, (y_k^n , z_k^n) are the coordinates of the neighboring points for k = 1 to 6, and α (the program variable ALPHA1) is an overrelaxation parameter (usually 1.7). The "G" points and boundary points are not moved. When the difference between the n^{th} and $(n + 1)^{th}$ calculations is less than a chosen tolerance for all nodes (EPS1 percent of the cathode-to-plate distance), the solution procedure is assumed complete. Typically, 31 iterations suffice for a 28 x 36 mesh with a tolerance, EPS1, of 0.01 percent.

C. Poisson's Equation

Poisson's equation is solved for the potential at each point, given the potentials or their derivatives on the boundaries and the space-charge density at each mesh point. Poisson's equation in rectangular coordinates is:

$$\frac{\partial^2 V}{\partial y^2} + \frac{\partial^2 V}{\partial z^2} = -S(y,z) \quad , \tag{6}$$

where V is the potential and S is the source.

At each interior mesh point, the corresponding finite difference equation is of the form:

$$\sum_{i=0}^{6} V_i W_i = S_o \quad , \tag{7}$$

where V_i is the voltage, the W_i are weights and i refers to one of the nodes of a typical hexagon enclosing one node in an irregular triangular mesh (Figure 7).

The weight W_i is computed between neighboring points P_o and P_i as

$$W_i = \frac{1}{2} (\cot \theta^+ + \cot \theta^-) \quad . \tag{8}$$

The term S_o is defined as

$$S_o = \sum_{i=1}^{6} a_{i+(1/2)} \rho_{i+(1/2)} \Big/ \varepsilon_0 \quad , \tag{9}$$

where $a_{i+(1/2)}$ and $\rho_{i+(1/2)}$ are the quadrilaterial area and space-charge density, respectively, for triangle i+(1/2). The quantities θ^+ and θ^- are shown in Figure 7. Although each interior point has six neighbors, only three weights need be stored per point because of symmetry.

D. Boundary Equations

The two types of boundary conditions allowed are

(1) Dirichlet, with specified potential, and

(2) Neumann, with a zero normal electric field.

1. Dirichlet boundaries

On conducting boundaries, where the voltages are specified, the difference equation becomes just

$$V = V_{boundary} \tag{10}$$

at each mesh mode on a Dirichlet boundary.

2. Neumann boundaries

The case of zero electric field normal to a boundary is a simple extension of the general difference equation derived by Winslow.[10]

Suppose that point O (Figure 7) lies on a Neumann boundary. Apply Gauss's theorem to the secondary mesh elements from the triangles in Figure 7 that lie within the region.

Consider a volume of unit height normal to the mesh plane. The normal flux out of the secondary mesh element about point O (part of the dodecagon in Figure 7) is equal to $1/\varepsilon_o$ times the total charge enclosed, and is also equal to the line integral of the normal electric field around the element. For example, if the boundary line is $P_{i-1}OP_{i+1}$ in Figure 7, only the triangles $i+(\frac{1}{2})$ and $i-(\frac{1}{2})$ are used. Here the only non-zero part of the integral of electric field is that normal to the vectors $\bar{a}$, $\bar{b}$, $\bar{c}$ and $\bar{d}$ because of the Neumann condition.

It can be shown that the normal flux $R_{i-(1/2)}+R_{i+(1/2)}$ is given in this case by

$$R_{i+(1/2)} = \frac{V_i - V_o}{2} \cot \theta^+ + \frac{(V_{i+1} - V_o)}{2} \cot \theta_i \qquad (11)$$

and

$$R_{i-(1/2)} = \frac{(V_i - V_o)}{2} \cot \theta^- + \frac{(V_{i-1} - V_o)}{2} \cot \theta_{i-1} \ . \qquad (12)$$

The angles θ^+, θ_i, θ_{i-1} and θ^- are shown in Figure 7. It is assumed that the electric field is uniform within each mesh triangle, i.e. that the potential varies linearly there.

Hence, the difference equations at a Neumann boundary point are the same as for an interior point provided that (a) the weight between a boundary point and an external point is defined as zero, and (b) the weight W between any two boundary points is defined as $\frac{1}{2} \cot \theta_i^+$, where θ_i^+ is the angle

opposite the two points (O and P_{i+1} in Figure 7) from the triangle within the region. If either O or P_i is an interior point, the weights from O to P_i and from P_i to O are both $\frac{1}{2}(\omega t\ \theta^{+} + \cot\ \theta^{-})$.[10]

Two alternative methods have been developed for solving the difference equations: the iterative overrelaxation method and the direct noniterative method.

E. Solution by Overrelaxation

The overrelaxation equation is

$$V_o^{n+1} = V_o^n + \alpha_V G_o \Big/ \sum_{i=1}^{6} W_i \quad , \tag{13}$$

where o represents the point at which the calculation is made and i represents the six neighboring points. The term α_V is an overrelaxation parameter (ALPHAV), normally 1.3, and n is the number of the relaxation cycle.

The residual G_o is defined as

$$G_o = \sum_{i=1}^{6} W_i (V_i - V_o) + S_o \quad . \tag{14}$$

Points outside the boundary are skipped in Equations 13 and 14. The initial values V_o^1 are an arbitrary approximate solution. The solution is defined as convergent when, for every mesh point, the residual G_o is smaller than a chosen value (usually EPSV=0.01 percent of the plate-to-cathode voltage).

F. Direct Noniterative Solution

The alternative non-iterative scheme developed here is demonstrated as more efficient for a solution that requires many relaxation iterations. The approach is that of Halbach and Holsinger,[23] who have determined the electric field distribution at nodes of an irregular mesh covering a closed cavity. Instead of solving finite difference equations for mesh points by overrelaxation for each mesh node, they invert a tridiagonal block matrix representation of the difference equations for the entire structure.

1. Matrix structure

Let there be K (horizontally) by L (vertically) points in the logical mesh space. Then the full matrix for the difference equations has dimensions (K x L) by (K x L). If the mesh points are numbered in successive rows, so that point (I,J) has number K x (J-1) + I, the full matrix is reduced to a tridagonal block form:

$$\begin{bmatrix} a_{11} & a_{12} & & & & & \\ a_{21} & a_{22} & a_{23} & & 0 & & \\ & a_{32} & a_{33} & a_{34} & & & \\ & & \vdots & & & & \\ 0 & & a_{L-1,L-2} & a_{L-1,L-1} & a_{L-1,L} & & \\ & & & a_{L,L-1} & a_{L,L} & & \end{bmatrix} \begin{bmatrix} V_1 \\ V_2 \\ V_3 \\ \vdots \\ V_{L-1} \\ V_L \end{bmatrix} = \begin{bmatrix} S_1 \\ S_2 \\ S3 \\ \vdots \\ S_{L-1} \\ S_L \end{bmatrix} \qquad (15)$$

where: $V_k = \begin{bmatrix} V_{k,1} \\ V_{k,2} \\ \cdot \\ \cdot \\ \cdot \\ V_{k,L-1} \\ V_{k,L} \end{bmatrix}$ $S_k = \begin{bmatrix} S_{k,1} \\ S_{k,2} \\ \cdot \\ \cdot \\ \cdot \\ S_{k,L-1} \\ S_{k,L} \end{bmatrix}$. (16)

Each matrix a_{ij} is sparse and tridiagonal, and of dimension K x K. In the k^{th} row of blocks the diagonal matrix a_{kk} contains the coefficients of potentials in Equation 7 for points in the same row of the logical mesh. The two coefficients from the row above are placed in the right off-diagonal block, $a_{k,\,k+1}$, $K\pm1$ elements to the right of the main diagonal of the full matrix, and the two coefficients from the points in the row below are in the left off-diagonal block, $a_{k,\,k-1}$, $K\pm1$ elements to the right in the full matrix.

If, alternatively, the nodes are ordered along successive columns, the full matrix consists of K x K blocks each of dimension L x L, with only the diagonal and off-diagonal blocks nonzero as before.

Treatment of boundary points is straightforward. When node K is a Dirichlet boundary point ("B" point), the full matrix contains a 1 as the K^{th} diagonal element, zeros elsewhere in the K^{th} row and K^{th} column, and the specified potential $V_{boundary}$ becomes the K^{th} term in the source vector. When a node is a Neumann boundary point ("N" point), the weights to adjacent boundary or interior points are already computed and stored, and the weights to external points are zero.

2. Solution procedure

The inversion of the full matrix is performed by a Gaussian elimination and back-substitution method.[23] The method follows the standard procedure for linear equations, but the elements a_{ij} are matrices instead of single real numbers.

The row or column numbering order is used for greatest efficiency according as $L \leq K$ or $K > L$. For $L < K$ the solution requires inversion of K full L x L matrices.

Additional storage arrays of dimensions (L, L, K-1) and (L,K-1) are needed for the K-1 modified right off-diagonal matrices (L x L), and for the (K-1) source vectors used in the back-substitution. These arrays may, however, be stored on a disk instead of in CPU fast memory.

3. Test results

A simple test problem has been run to compare the direct and iterative (relaxation solutions). The configuration is a rectangular plane-parallel diode with a uniform charge density and a Neumann boundary condition of zero electric field normal to the X-directed boundary sides. The exact solution is known analytically and agrees within 0.5 percent with the numerical solution. The relaxation and direct solutions agree to within 0.1 percent, demonstrating that both methods are accurate.

For an initial solution on a 21 x 21 mesh, the direct method requires about two-thirds as much computing time as the relaxation solution (Table 2). The latter requires as many as 137 iterative cycles to converge. However, for a series of similar solutions as in the electron gun, the relaxation method is the more efficient. As few as 7 iterations will produce convergence when a good approximation has been obtained from the previous time step. Although the two subroutines are

TABLE 2

EFFICIENCY OF DIRECT AND ITERATIVE SOLUTIONS

OF DIFFERENCE EQUATIONS

Mesh Size	Number of Iterations in Relaxation Solution	Computing Time(s) for Iterative Solution	Computing Time(s) for Direct Solution
7 x 8	10	0.042	0.217
21 x 21	137	0.722	0.450

Machine times were obtained on an Amdahl 470V/7 computer.

coded to be interchangeable, the relaxation method is being retained for both static and dynamic calculations.

G. Assignment of Space Charge to Mesh

At a given time step, each charged particle lies within a mesh triangle. The charge is distributed over the three mesh nodes forming that triangle as in Figure 8. Drawing lines from the particle position P to the three nodes subdivides the triangle into three separate triangular areas, A_0, A_1, and A_2, opposite nodes 0, 1, and 2. If q is the charge per particle, the charge assigned to node 0, for example, is $\frac{q A_0}{A_0 + A_1 + A_2}$.

In the two-dimensional model, the calculation refers only to the y-z plane containing the triangular mesh.

In a three-dimensional model, there are several such mesh planes spaced apart in the magnetic-field direction (x-direction). The deformed triangular mesh is the same in all the planes. The charge is assigned to the two nearest planes. If the charge is distant x, and x_2 from planes 1 and 2, then fractions $\frac{x_2}{x_1 + x_2}$ and $\frac{x_1}{x_1 + x_2}$ are assigned, respectively, to planes 1 and 2. The charge assignment over the triangle vertices then proceeds as in the two-dimensional case.

A search algorithm (subroutine NEARST) locates the mesh triangle containing a given point. If the point lies outside the boundary, a switch indicates that no such triangle has been found. A particle at the point is then assumed to be intercepted on a boundary. The specific boundary is determined from the particle coordinates and the electrode dimensions (such as the cathode length or the plate height) that are supplied by the user.

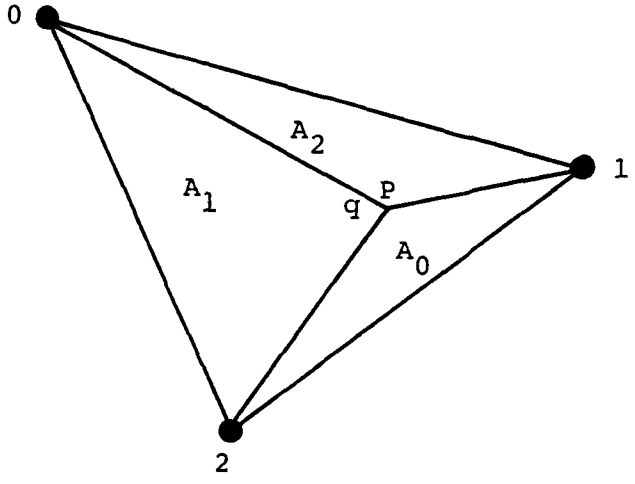

Charge assigned to node: 0 = $\frac{q\ A_0}{A_0 + A_1 + A_2}$

1 = $\frac{q\ A_1}{A_0 + A_1 + A_2}$

2 = $\frac{q\ A_2}{A_0 + A_1 + A_2}$

Figure 8. Charge and its three local mesh points.

In order that the search algorithm can succeed, the mesh must be constructed so that no more than one side of any triangle is a boundary line. In other words, at most two nodes of any triangle may be defined as boundary points. Otherwise, particles in the anomalous triangle will be treated as intercepted. In Figure 7, line OP_{i+1} or line OP_i, but not both, may be defined as boundaries.

Once the charge contributions to the mesh nodes have been summed over all the particles, the charge density ρ associated with each node is computed. Each node is surrounded by a corresponding dodecagonal area (Figure 9), the value ADOD of which is computed when the mesh is generated. For a total charge q_j on mesh node j, the charge per unit area is $q_j/\text{ADOD}(j)$. Only charge within the boundary is included in the charge assigned to point O, and the secondary mesh area (ADOD) at O covers only the portion of the dodecagon contained in the triangles within the boundary at O. No fictitious points need be defined outside the boundary.

For the two-dimensional model, the charge density ρ at node j is then

$$\rho = \frac{q_j}{\text{ADOD}(j) \cdot (\text{beam width in magnetic-field direction})}. \quad (17)$$

For a three-dimensional model, the dodecagon is projected into a volume. There are two planes on each side of a given plane, and the height of the dodecagonal volume equals half the separation distance of these planes. Then the charge density is

$$\rho = \frac{q_j}{\text{ADOD}(j) \cdot (\text{height of dodecagonal volume})}. \quad (18)$$

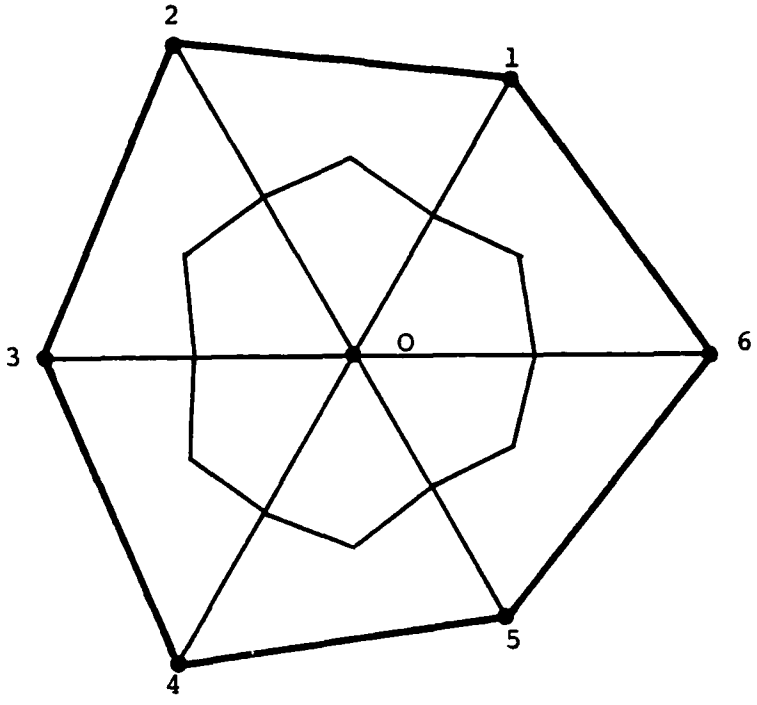

Figure 9. Hexagon and dodecagon associated with six mesh points surrounding a particular mesh point.

H. Electric Field

The electric field components in the plane of the triangular mesh are derived at a given position in the plane using the three nodes of the triangle surrounding the position, and the six neighbors of each node in turn.

Firstly, the two first derivatives at node 0 are calculated from a least-squares-error solution of the six Taylor series equations

$$V_k = V_0 + \frac{\partial V_0}{\partial y}(y_k - y_0) + \frac{\partial V_0}{\partial z}(z_k - z_0); k = 1, \cdots 6 . \quad (19)$$

The solution is the set of derivatives which minimizes the Euclidean norm $||R||$ of the residual vector

$$\xi_k = V_k - V_0 - \frac{\partial V_0}{\partial y}(y_k - y_0) - \frac{\partial V_0}{\partial z}(z_k - z_0); k = 1, \cdots 6 \quad (20)$$

and

$$||R|| = \sqrt{\sum_{k=1}^{6} \xi_k^2} . \quad (21)$$

Next, the above procedure is repeated for each of the remaining two nodes of the triangle enclosing the particle (nodes 1 and 2 in Figure 8).

When the derivatives at the three surrounding nodes have been calculated, the electric field components at the electron position are computed by linear interpolation, following Winslow (Equations 3 and 4 of reference 10).

This procedure differs from that described by True,[9] which derives five first and second derivatives at a single point instead of two first derivatives at three points. The

present method requires less machine storage because only two derivatives at each point need be stored as they are computed. It is also more readily extended from two to three dimensions.

To reduce computing time, the program stores the fields as they are computed at each mesh point and sets a switch to indicate for subsequent particles in the same time step that the local fields there have already been computed.

In the two-dimensional model, the above calculation is performed in the single y-z plane perpendicular to the magnetic field. The calculation is readily extended to three dimensions.

I. Trajectory Equations

Given the electric and magnetic fields, the trajectories of sample electrons are found by solving the Lorentz force equation. Assume the beam to be in the y-z plane direction and the magnetic field in the x-direction. The trajectory equations can be expressed in terms of the field components as

$$\ddot{z} = -\eta(E_z + \dot{y}B_x) \tag{22}$$

and

$$\ddot{y} = -\eta(E_y - \dot{z}B_x) \quad , \tag{23}$$

where E_x, and B_y and B_z are zero and $\eta = e/m$, the charge-to-mass ratio of the electron.

The difference equation solutions are:[24]

$$z_{k+1} = \frac{1}{1+(w^2/4)}\left[2z_k - \left(1-\frac{w^2}{4}\right) z_{k-1} + w\left(y_k - y_{k-1}\right) - \eta\left(E_z + \frac{w}{2} E_y\right)\left(\Delta t\right)^2\right] \quad (24)$$

and

$$y_{k+1} = \frac{1}{1+(w^2/4)}\left[2y_k - \left(1 - \frac{w^2}{4}\right) y_{k-1} - w\left(z_k - z_{k-1}\right) - \eta\left(E_y - \frac{w}{2} E_z\right)\left(\Delta t\right)^2\right] \quad , \quad (25)$$

where

$$w = \eta B_x \Delta t \quad .$$

The trajectories are started by specifying the initial and final coordinates corresponding to a fictitious previous time step. For an initial velocity (v_y, v_z) at coordinates (y,z), the preceding coordinates are ($y-v_y\Delta t$, $z-v_z\Delta t$). At present only a single normal velocity

$$v_y = \sqrt{\frac{\pi}{2}\frac{kT}{m}} \quad (26)$$

is set, corresponding to a cathode temperature T(°K), and where k is Boltzmann's constant and m is the electron mass.

In the static calculation (Section V) the particle is initially placed above the cathode. The time-dependent model places the initial coordinate y on the surface, and the "previous" position $y-v_y\Delta t$ is then behind the surface.

An alternative, time-centered, trajectory calculation[7] was implemented for the time-dependent analysis of the anode-sole region (Section IV). There the electron velocity is determined one half time step behind the position and the electric field. This "leapfrog" method will be incorporated in the three-dimensional model.

SECTION IV

LONGITUDINAL TWO-DIMENSIONAL IBCFA ANODE-SOLE REGION PROGRAM

This computer program simulates the behavior of the injected beam between the anode and the sole, with the assumption that the beam velocity and charge distributions at the start of the region are in a steady, time-independent state. Here the beam may either be given as the analytic Brillouin solution[19,25] or be derived from the electrostatic crossed-field gun calculation. In the latter case, the gun program and interaction-region program are run in sequence with automatic transfer of data via a disk file.

A time-dependent calculation follows electron trajectories through the region, taking into account space-charge forces in the anode-sole and drift directions. It assumes a periodic boundary condition in the drift direction for solution of Poisson's equation in a reference frame moving with the mean drift speed. In this longitudinal two-dimensional program, the charge motion and electric fields are confined to the plane perpendicular to the magnetic field. A more detailed description of the program is given in a separate report.[7]

If a Brillouin beam is used to initialize the calculation, the beam may be subdivided into layers, each with a different initial velocity. If the electron gun results are used, each trajectory is treated as a separate beam layer. Only the final positions of the gun trajectories are stored. At the interface, the shape of these trajectories over the reference frame is approximated by extrapolating backwards parallel to the sole, as in Figure 10, so as to determine the particle positions.

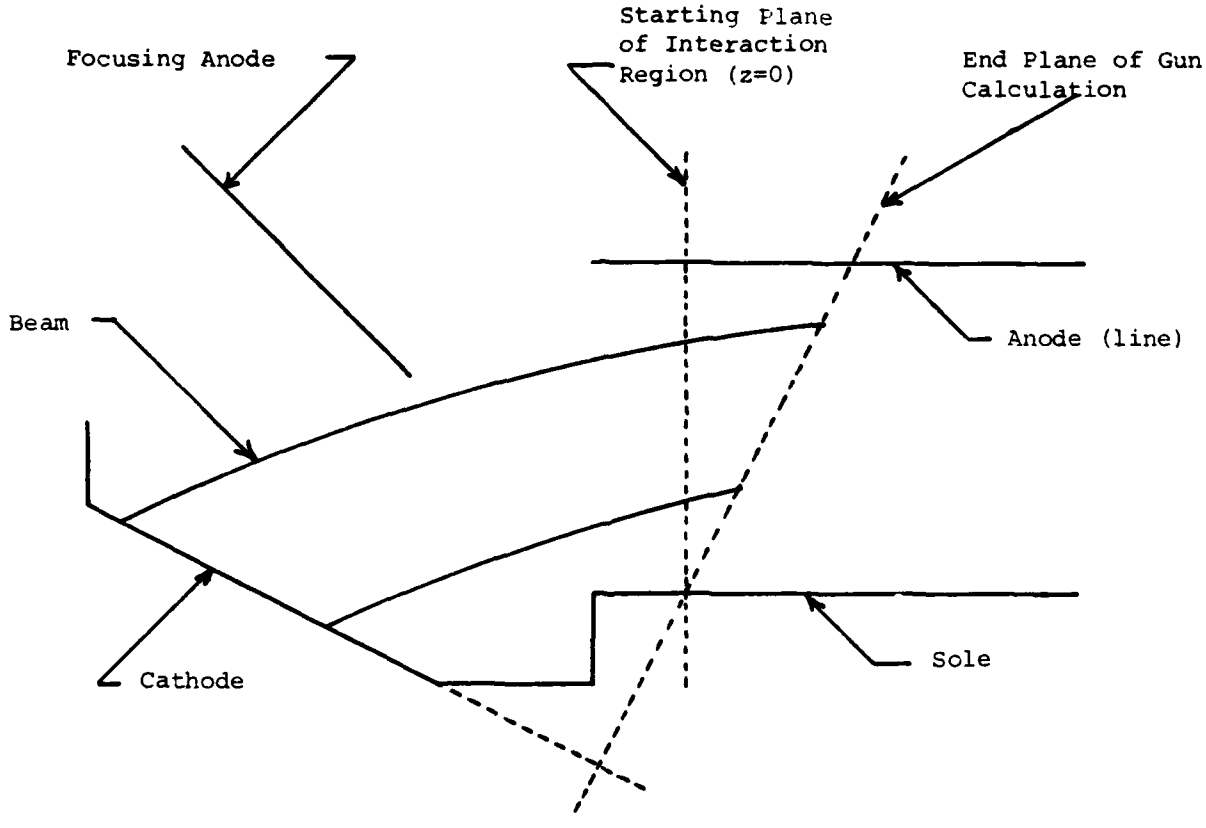

Figure 10. Interface of gun and anode-sole regions.

Then each particle is advanced parallel to the sole with uniform speed in every time step until it passes the plane z = 0. All the particles contribute to the space-charge field, but the actual beam shape behind the starting plane is replaced by the extrapolated shape shown in Figure 11.

In this study the program is used to demonstrate the cycloiding in the anode-sole region of a Kino short gun (Section V). The theoretical beam shape agrees well with the results of published beam-analyzer measurements. The program also demonstrates the growth of the diocotron instability in the RW-620 CFA assuming an ideal Brillouin injected beam (Section X).

The interface is computationally efficient and is realistic provided that the static solution is valid in the gun region. However, for a fully time-dependent analysis of a long gun, it is more accurate to use a single deformable-mesh simulation for both the gun and part of the anode-sole region, since the interface approximations are then eliminated.

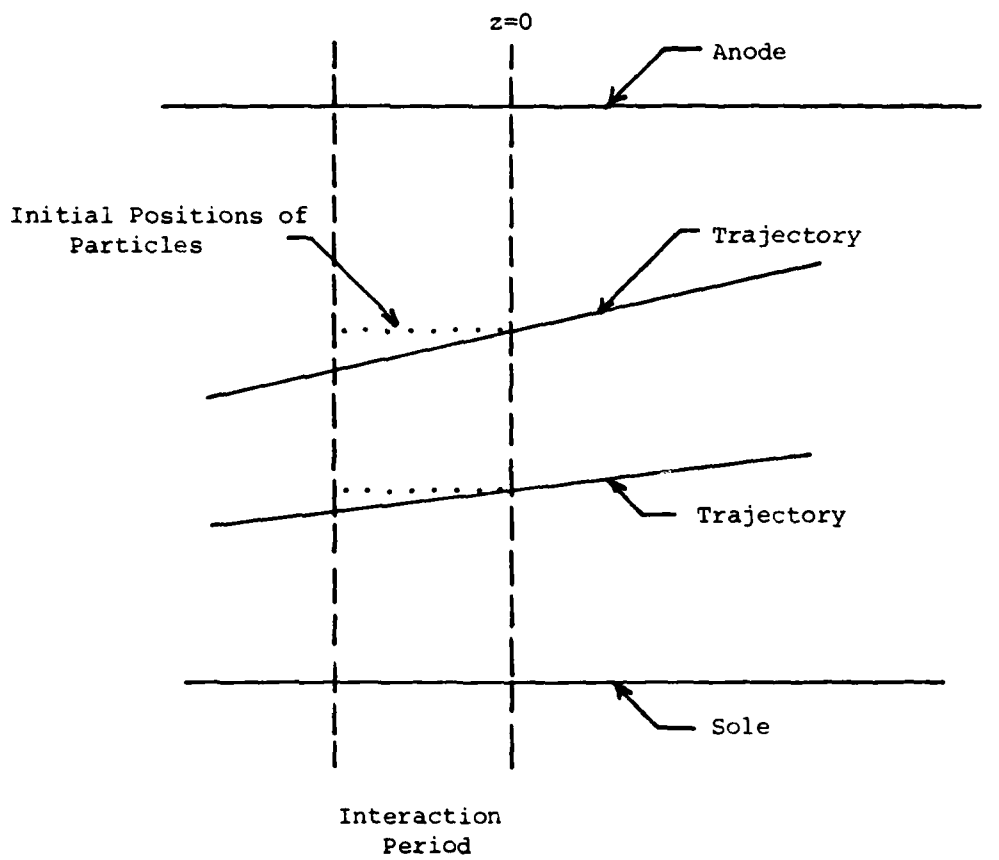

Figure 11. Initial positions of simulation particles for anode-sole-region program.

SECTION V

STATIC SOLUTION FOR THE KINO GUN

A. Gun Configuration

Results for an experimental Kino gun[26,27] (Table 3) are used here to verify the two-dimensional static gun analysis. Figures 12 and 13 show the full mesh and the local rectangular mesh at the cathode. The computed trajectories in Figure 14 show that the cathode is short compared with the electron cycloid length.

B. Steady-State Cathode Emission

The electrostatic method used here aims to find a self-consistent solution for the trajectories, the potentials, and the space-charge-limited cathode current. Figure 2 is an outline flow diagram for the program.

For computing the space-charge-limited cathode emission current, the Child's Law method is used. This method, originally developed for the linear-beam electron gun simulation, works successfully also in the static crossed-field calculation provided that the cathode is short relative to the cycloid length for the emitted electrons. Near the cathode surface, a thin rectangular mesh layer is established by the program, as shown in Figure 15. The rectangles are assumed to be essentially parallel-plate diodes. Thus, the cathode current density can be found by using Child's law:

$$J = k\frac{V^{3/2}}{\xi^2} = kC^{3/2} \quad , \qquad (1)$$

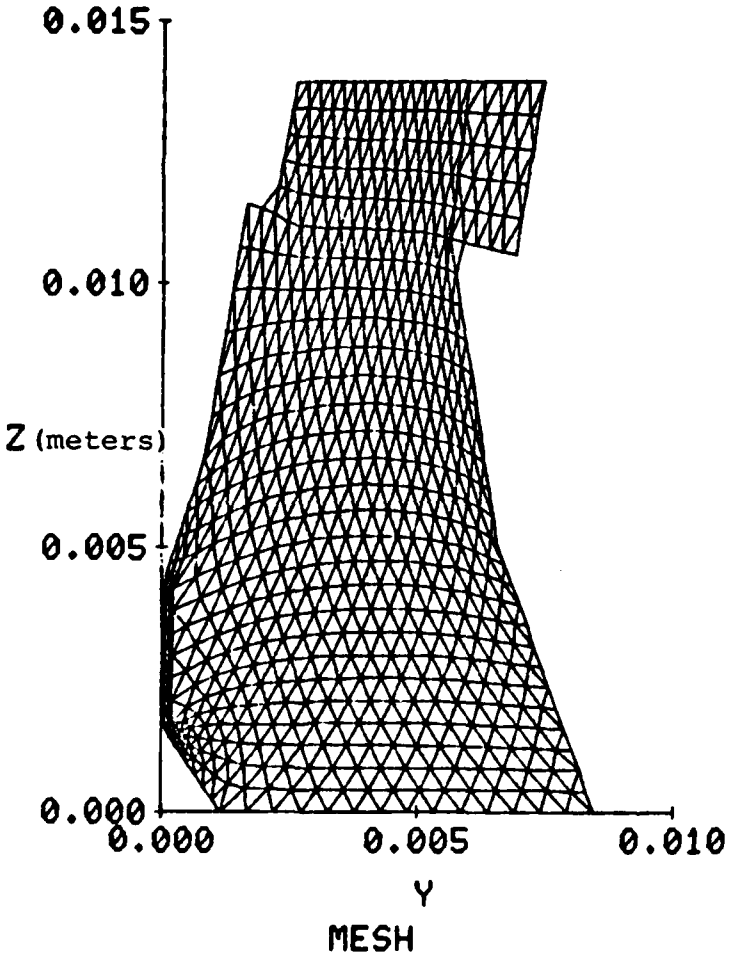

Figure 12. Mesh for simulation of Kino short gun.

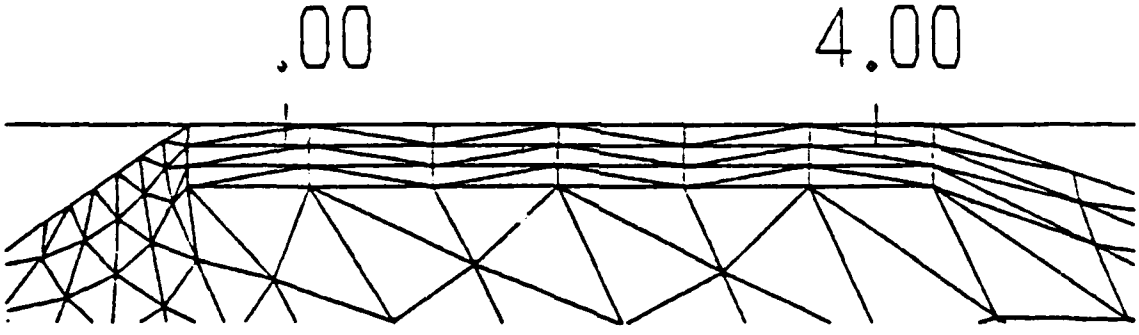

Figure 13. Rectangular mesh at cathode in simulation of K.no short gun.

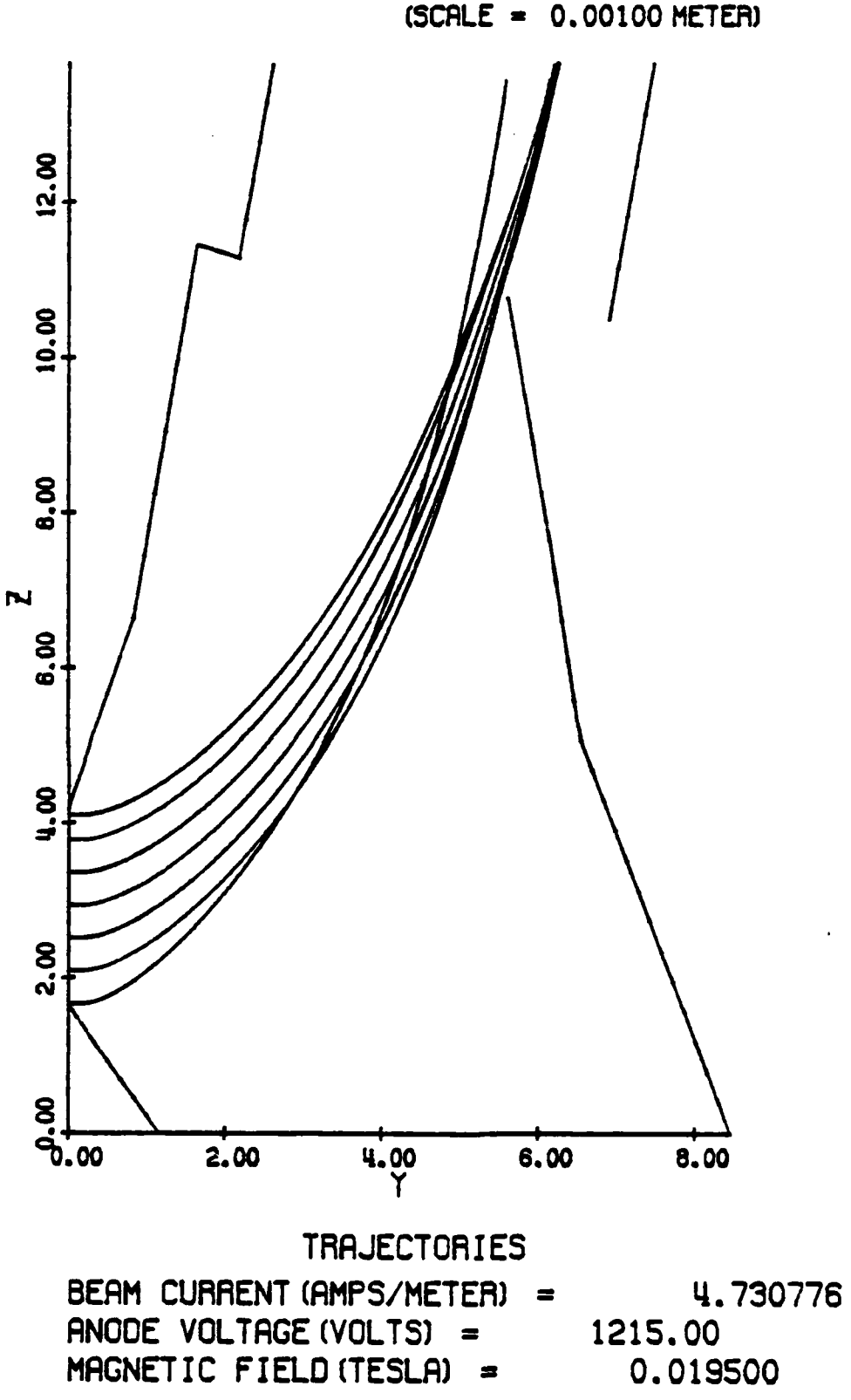

Figure 14. Computed electron trajectories in Kino short gun using experimental electrode shapes and magnetic field of 0.0195 T.

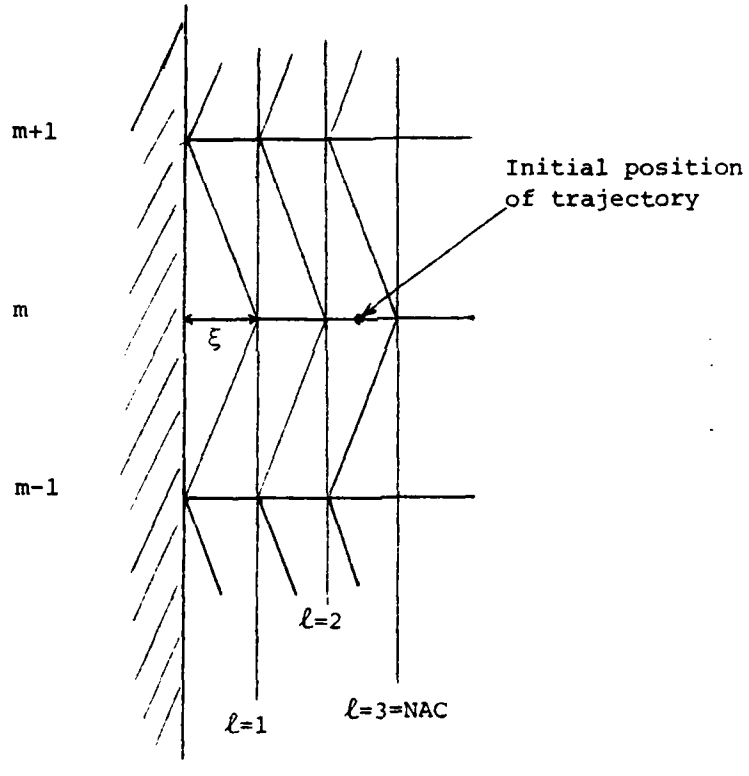

Figure 15. Mesh near the cathode surface.

TABLE 3

DATA FOR SIMULATION OF EXPERIMENTAL KINO SHORT GUN

Quantity	Value
Magnetic field	0.0195 T 0.0219 T 0.0230 T
Anode voltage minus cathode voltage	1600 V
Sole voltage minus cathode voltage	0 V
Focusing anode voltage minus cathode voltage	1215 V
Height of anode above cathode at interface plane	7.45 mm
Height of sole above cathode at interface plane	2.6 mm
Angle between cathode and sole planes	9.74° (0.17 radian)
Length of cathode	2.54 mm
Width of cathode in magnetic field direction	10 mm*
Front ramp electrode angle (relative to cathode)	18.78° (= 0.3279 radian)
Rear ramp electrode angle (relative to cathode)	34.94° (= 0.6098 radian)
Anode-sole distance (measured normal to sole)	4.78 mm
Length of sole included in gun computation	2.6 mm

*Estimated from published values of pulsed current and cathode current density.

where

$$k = \frac{4}{9} \varepsilon_0 \sqrt{2\eta} \tag{2}$$

and

$$C = \frac{V(\xi)}{\xi^{4/3}} \quad , \tag{3}$$

where η is the ratio of electron charge to mass.

If the trajectories bend significantly near the cathode, Equation 12 is not accurate. However, with the aid of deformable mesh techniques, the width ξ of the parallel plate diodes can be made arbitrarily small. Then the trajectories inside the diodes are almost perpendicular to the planes of the diodes and Equation 1 can give fairly good results for the cathode current density calculation in most cases.

At each node on the cathode, a C is determined from Equation 3 for each of the NAC-1 nodes in front of the cathode. Following the method of True,[9] the average C of these NAC-1 nodes is then taken as the C for that cathode node. Letting m denote the nodes along the cathode, the quantity C for this node is

$$C_m = \left[\sum_{\ell=1}^{NAC-1} V(\ell \cdot \xi)/(\ell \cdot \xi)^{4/3} \right] \Big/ (NAC-1) \quad . \tag{4}$$

Next, C_m is laterally averaged with its neighbors by the formula[9]

$$C_m = \frac{R_{m-1} \cdot C_{m-1} + 2C_m + R_{m+1} \cdot C_{m+1}}{R_{m-1} + 2 + R_{m+1}} \quad , \tag{5}$$

where

$$R_{m-1} = \begin{cases} C_m/C_{m-1} , & \text{if } C_m < C_{m-1} \\ C_{m-1}/C_m , & \text{if } C_m \geq C_{m-1} \end{cases} \quad (6)$$

and

$$R_{m+1} = \begin{cases} C_m/C_{m+1} , & \text{if } C_m < C_{m+1} \\ C_{m+1}/C_m , & \text{if } C_m \geq C_{m+1} \end{cases} . \quad (7)$$

This lateral averaging will suppress the oscillation in the current density due to the alternating nature of the mesh at the cathode.

C. Comparison With Measurements

Three computer simulations have been made with fixed voltages and magnetic fields of 0.0195 T, 0.0219 T and 0.0230 T. The results in Table 4 show good agreement with the measurements.

The computed electron trajectories for the gun region are displayed in Figures 14, 16 and 17. The results from the anode-sole region, interfaced to the gun as in Section IV, are shown in Figures 18, 19 and 20 (on a different scale).

For the first run, the analytical value of 0.0195 T is used. The pronounced undulation of the trajectories in Figure 18 shows that the beam is injected too far above the sole. For comparison, the injection positions of the ideal Brillouin beam are marked on Figures 18, 19 and 20.

The periodic distance of the trajectory oscillations approximately equals the ratio of the inital z-velocity and the cyclotron frequency. Increasing the magnetic field to 0.0219 T and 0.023 T lowers the beam and reduces the vertical

TABLE 4

EXPERIMENTAL AND THEORETICAL CURRENTS IN ABBREVIATED KINO SHORT GUN

Magnetic Field (T)	Cathode Current Density (A/m^2)		Computed Total Beam Current (A) From Static Analysis
	Experimental	Computed (mean)	
0.0195	About 1790	1862	0.0473
0.0219	About 1790	1881	0.0478
0.0230	About 1790	1870	0.0475

Analytical value of current density = 1720 A/m^2 at 0.0195 T magnetic field.

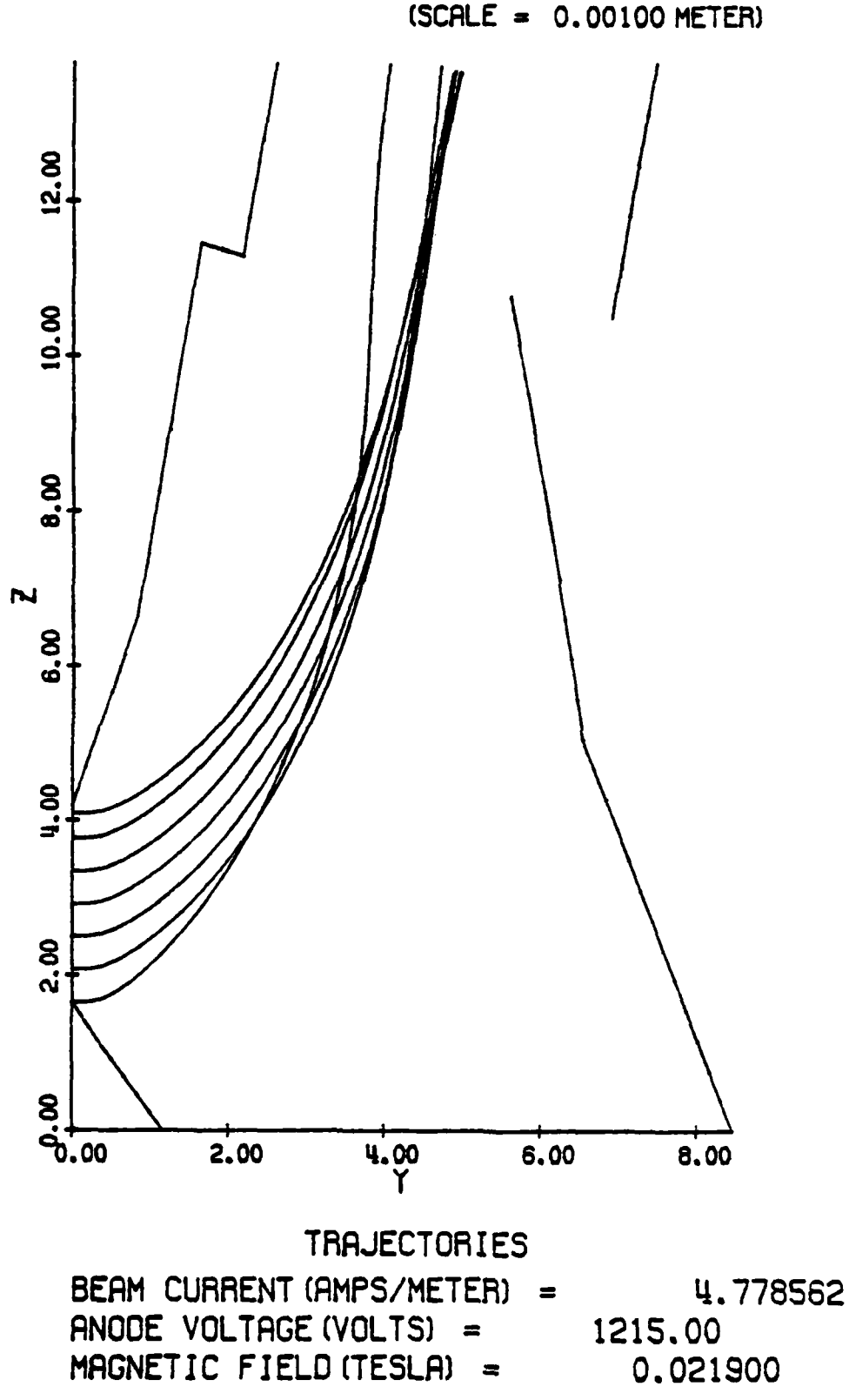

Figure 16. Computed trajectories in experimental Kino short gun with 0.0219 T magnetic field.

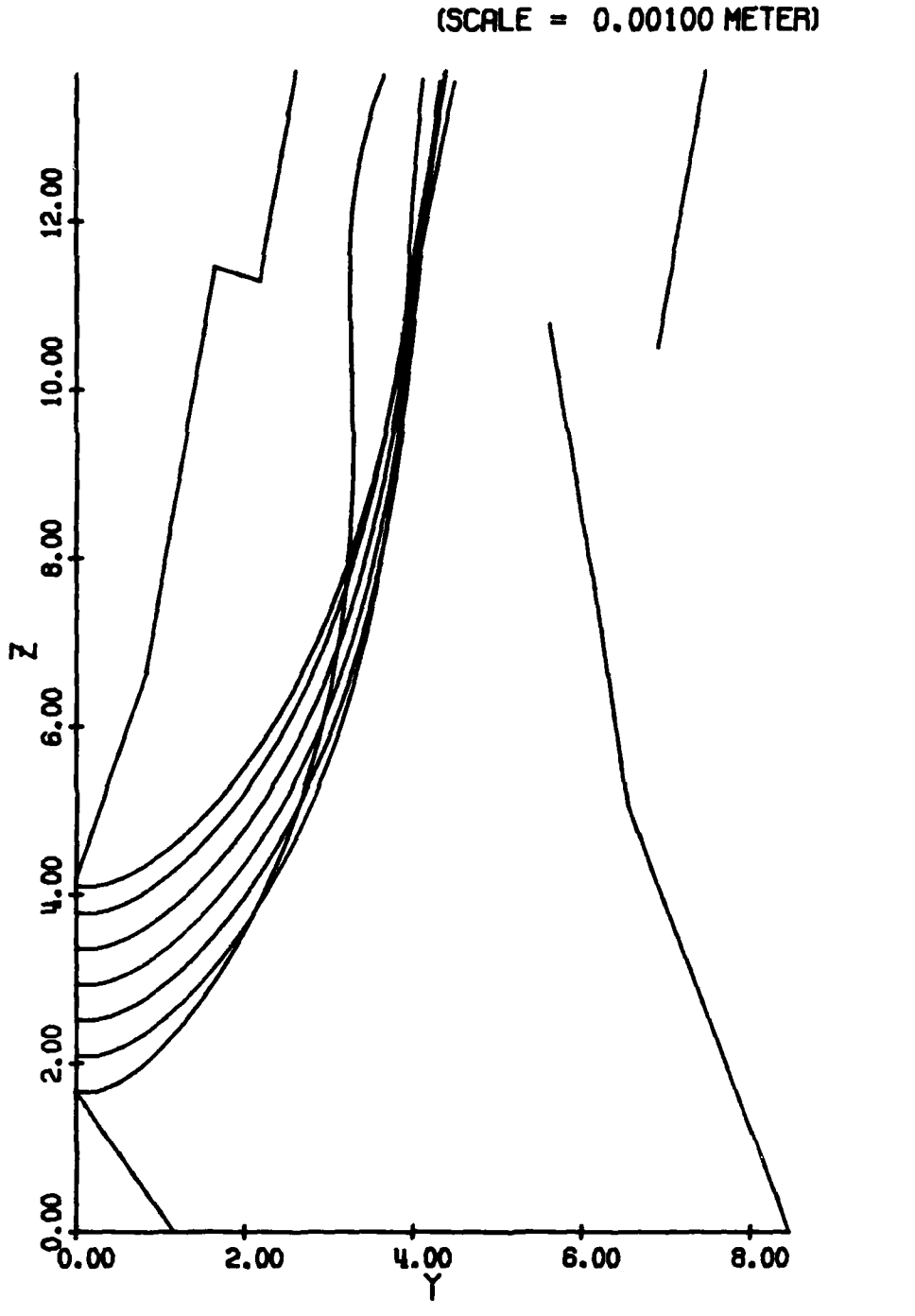

Figure 17. Computed trajectories in experimental Kino short gun with 0.023 T magnetic field.

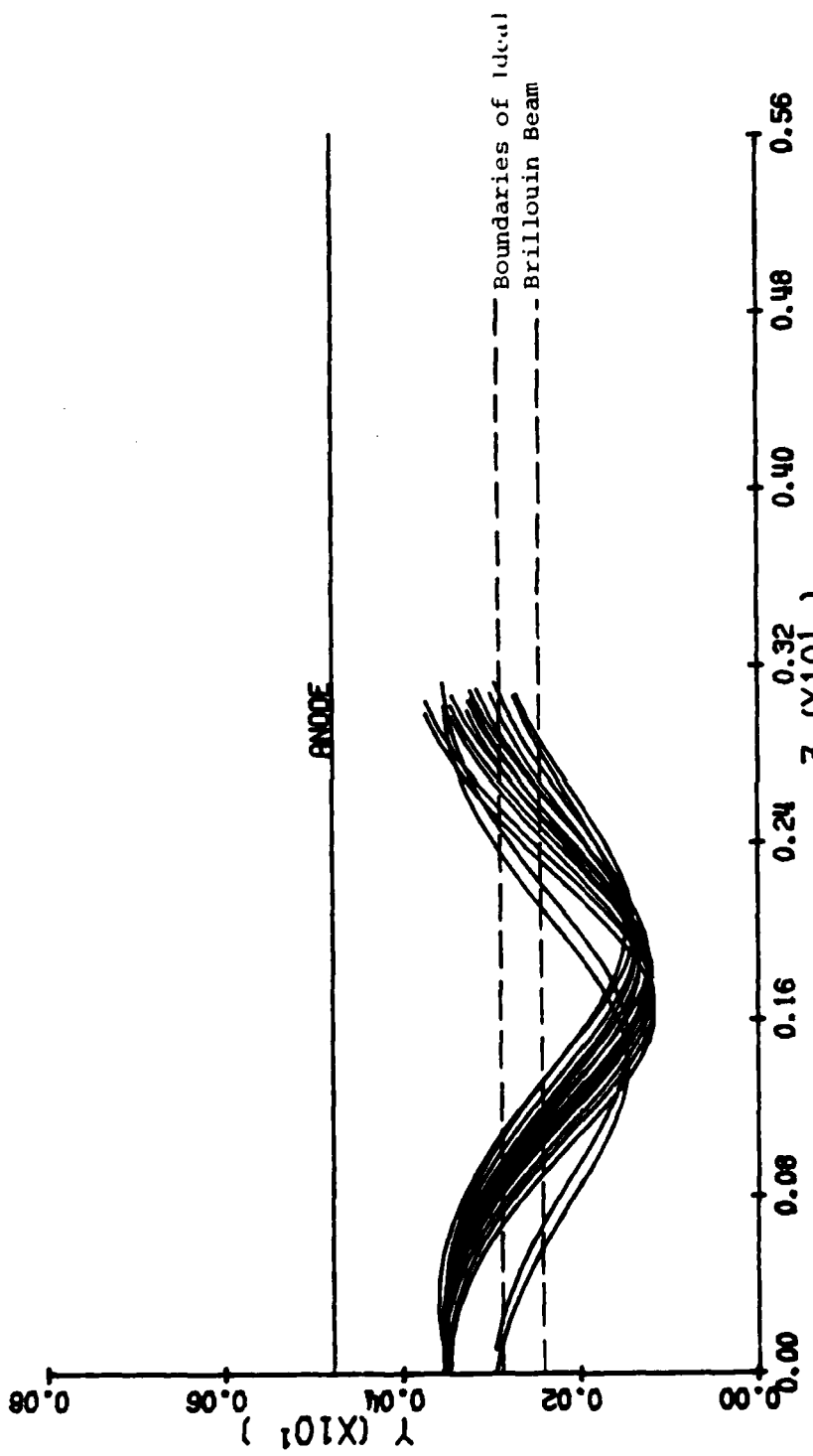

Figure 18. Computed trajectories in anode-sole region with 0.0195 T magnetic field.

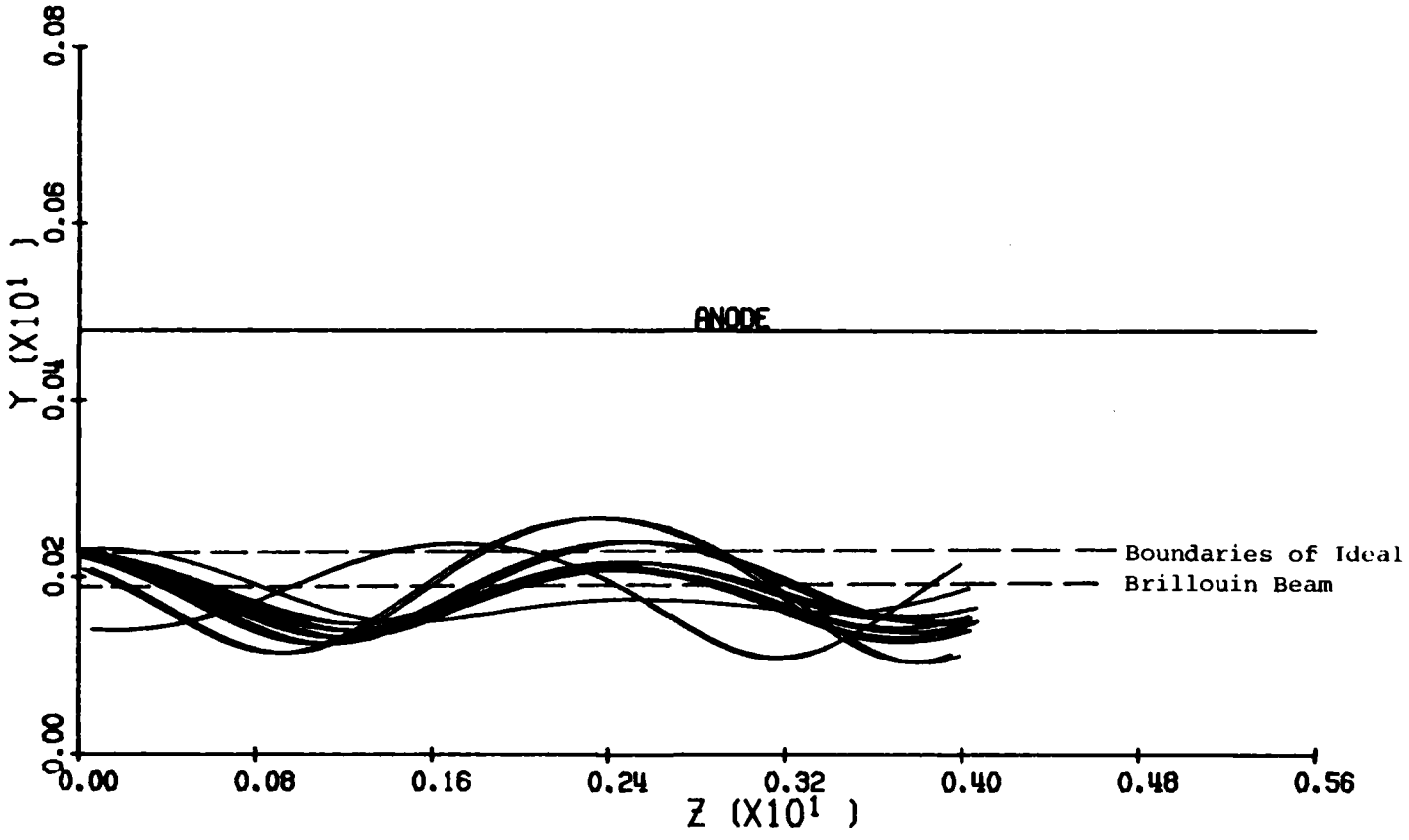

Figure 19. Computed trajectories in anode-sole region with 0.0219 T magnetic field.

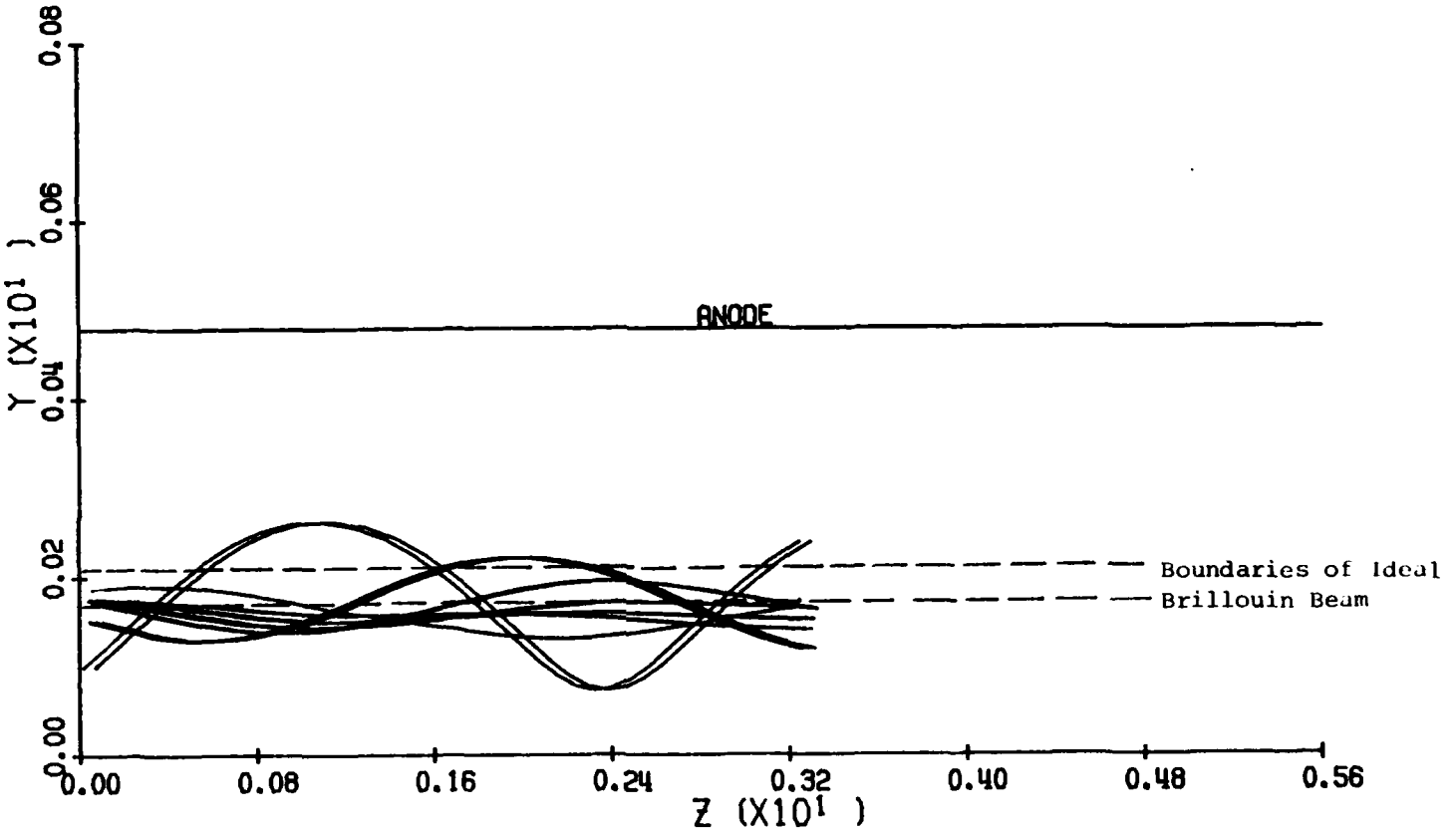

Figure 20. Computed trajectories in anode-sole region with 0.023 T magnetic field.

motion in the anode-sole region (Figures 19 and 20). At the same time, the total currents and the cathode current density shown in Table 4 are almost constant. The computed gun trajectories show that the injection position is sensitive to the magnetic field, while the trajectory shapes close to the cathode are less so. The experimental current densities are about 4 percent less than the computed values, and are also almost constant.

The experimental currents are reproduced in Figure 21, which shows the nearly constant cathode current I_k and also the current I_f intercepted on the focusing anode. This intercepted current falls to zero at about 0.0195 T. The computed trajectories, also, show no interception on the focusing anode as the magnetic field is raised from 0.0195 T. With the lowest field of 0.0195 T, the beam just misses the focusing anode (Figure 14), in agreement with the experimental cutoff result. The experimental results show that maximum beam transmission and minimum beam cycloiding both occur with a magnetic field of between 0.02 T and 0.024 T, well above the Kino value of 0.0195 T. Although Masnari and Rowe ascribed this discrepancy to experimental error,[27] the present computed results support the experiments. The trajectories are sensitive to the electrode angles adjacent to the cathode, which are not included in the analytical theory. In fact, an improved design has been obtained both by Masnari and Rowe and with the present program (see Figure 22).

The trajectories computed with the two programs agree well, although the precise dimensions used by Masnari and Rowe are not available and must be estimated from the published drawing. The trajectories computed in the anode-sole region (Figures 18, 19 and 20) show the least undulation and are closest to the ideal Brillouin beam for the magnetic field of 0.0230 T. This

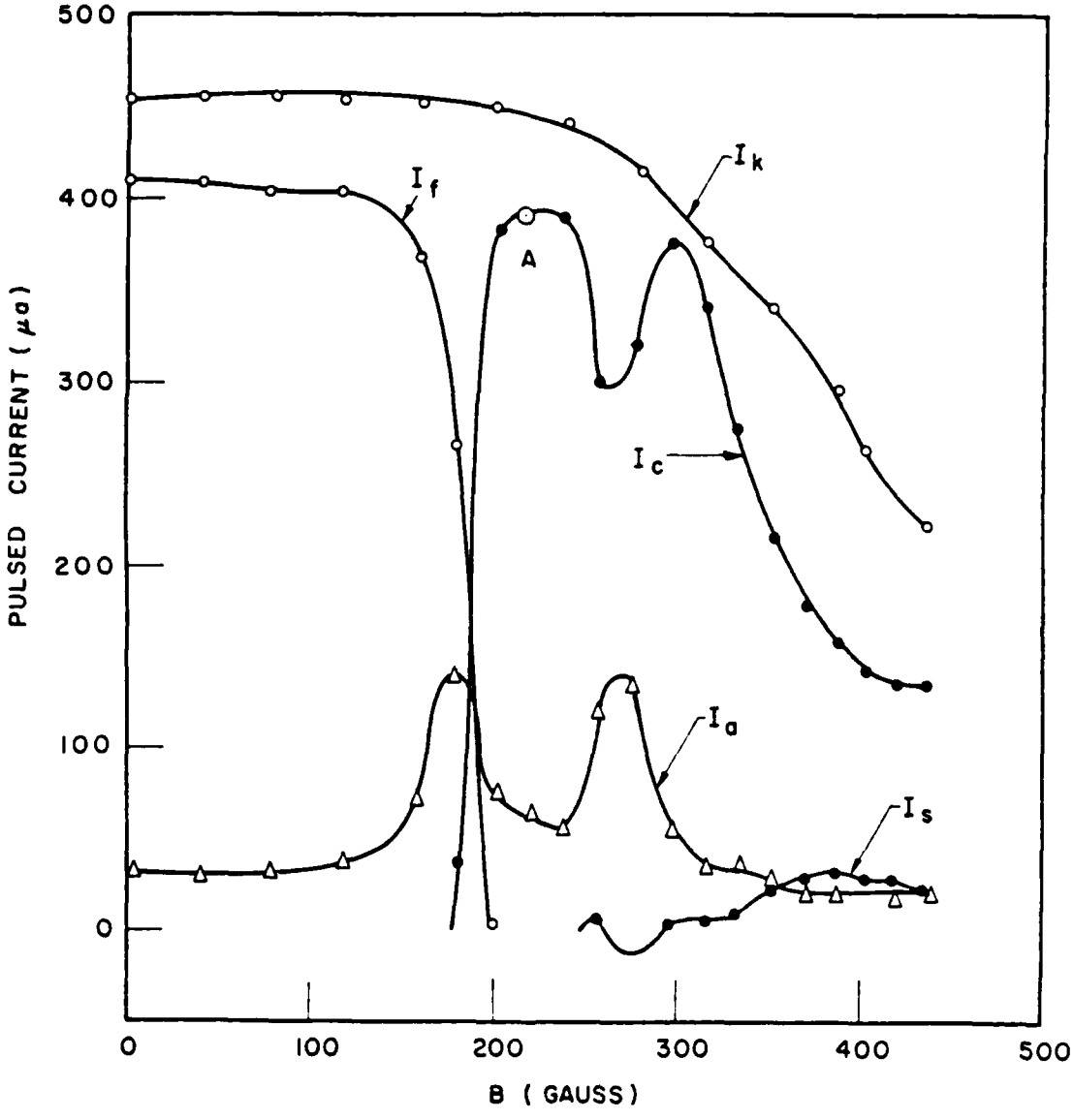

Figure 21. Experimental variation of currents with magnetic field. (ϕ_a = 1600 volts, ϕ_f = 1215 volts) (After Masnari and Rowe)

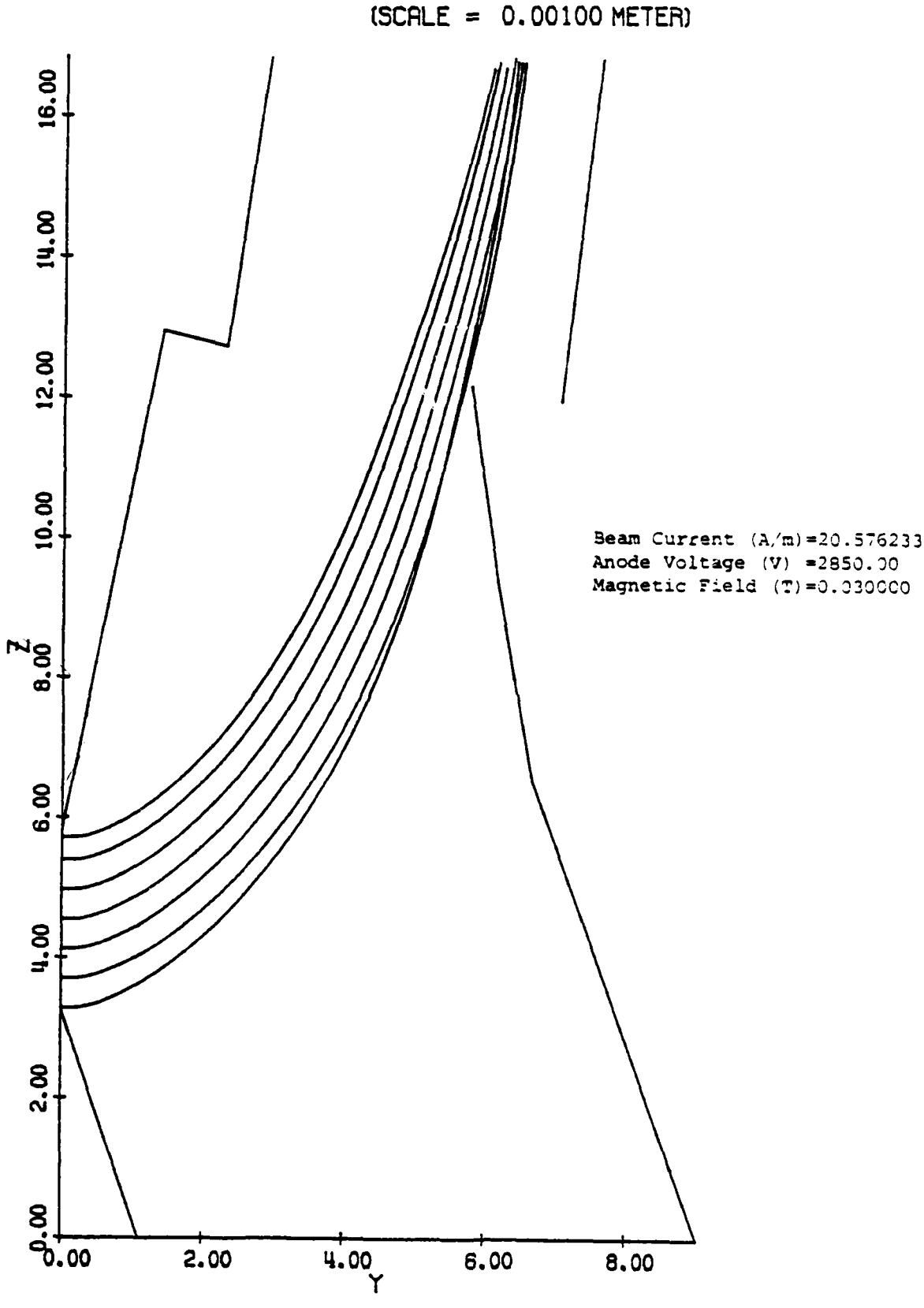

Figure 22. Trajectories computed for the Kino short gun with modified ramp electrodes.

result is supported well by the experimental beam profiles of Figure 23.[26] These cover a distance up to about 25 mm along the z-axis of Figures 18, 19 and 20. The interface plane for the programs is 2.6 mm from the end of the sole nearer to the gun.

For the optimum (0.023 T) magnetic field, the cyclotron wavelength corresponding to the average injection velocity is 27 mm, while the theoretical diocotron gain for a Brillouin beam is computed as 3.7 dB over this distance. However, the diocotron effect does not appear in the present calculations because the periodic length is made a small fraction (0.035) of the cyclotron wavelength, in order to demonstrate the behavior of the ideal static beam. Since the gun is only 12 mm in length, the electrostatic analysis is probably sufficient there also. This is a low-power tube with an available beam power of 76.5 W for the anode-sole voltage of 1600 V and peak pulsed current of 0.0478 A.

The detailed beam profiles in the anode-sole region show some minor discrepancies. Some electrons originating at the rear end of the cathode (about 6 percent of the total current) cross over in the gun and form a distinct bunch below the majority of the beam. The beam tester did not resolve this, possibly because of secondary emission on the grid wires which reduced the resolution of variations in local beam current density. The experimental beam showed less undulation at 0.0219 T than at 0.023 T and the experimentally observed initial upward motion at 0.02 T (Figure 23) is not reproduced on the plot for 0.0195 T (Figure 18). However, in this case the beam was observed then to descend to a minimum height of about 0.085 inch (2.16 mm) on the scale of Figure 20, or 1.86 mm above the sole. This minimum occurred at a distance of 0.875 inch (22.23 mm) from the exit plane of Figure 20, or 19.7 mm from the start of the anode-sole-region computation.

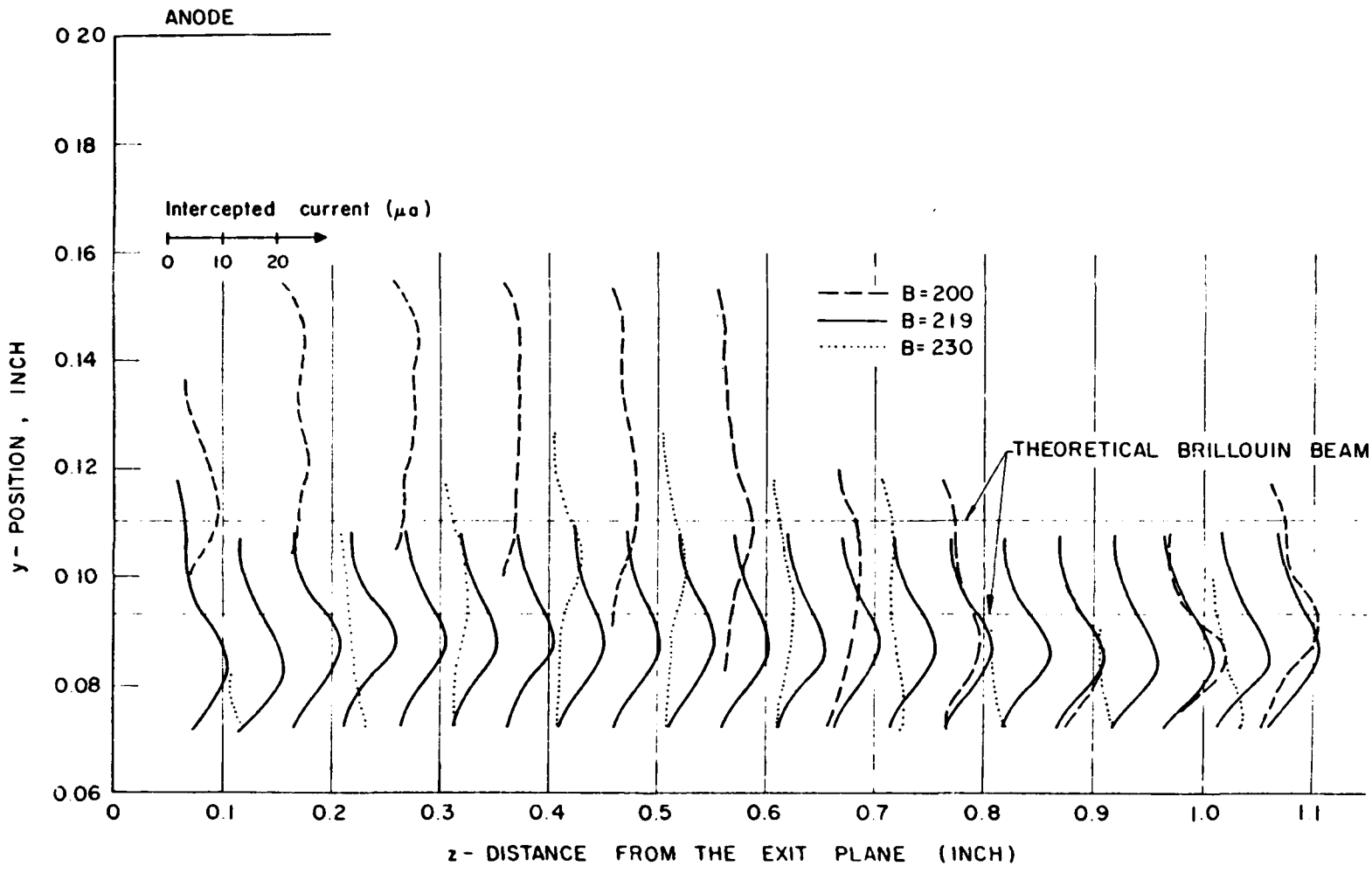

Figure 23. Beam profiles in the anode-sole region for various magnetic field values. (ϕ_a = 1600 volts, ϕ_f = 1215 volts). (After Masnari and Rowe)

This result agrees well with the minimum height attained in the trajectories of Figure 18.

D. Conclusions

The deformable-mesh potential solution and the trajectory equations are shown to reproduce well the behavior of the beam away from the cathode. A more accurate calculation of the beam current may be possible either with an improved static model or with the time-dependent model. For example, more cathode emission points would give more details of the local electric field.

SECTION VI

STATIC SIMULATION OF THE LONG CROSSED-FIELD GUN

Several attempts are described here to obtain a self-consistent solution for the RW-620 gun. In this two-dimensional model the grid is ignored. The design differs significantly from the Kino short gun already described in that the magnetic field is high enough and the cathode long enough for emitted electrons to return to the surface.

A. Cathode Emission in the Static Model

Three different models of cathode emission were used, of which the last yielded a convergent solution under conditions described below. These are:

(1) emission according to Child-Langmuir Law,

(2) emission according to Kino flow,

(3) emission according to the power series of Radley and Birtles.

The mesh structure for the RW-620 gun is shown in Figures 3 and 4. It is the same for all three emission models. Notice that there are two regions. A closely spaced rectangular region along the cathode contains "NAC" intervals in the y-direction perpendicular to the surface, and trajectories are launched from the top of this region. In the remainder of the gun, the triangular mesh is constrained only by the electrode boundaries. The rectangular mesh region along the cathode is treated as a series of rectangular diodes, each extending for one mesh interval along the surface and for NAC mesh intervals normal to the surface. This example uses NAC=3.

1. Emission according to Child-Langmuir Law

In the computer simulation of the electron gun, the cathode region is represented by a series of rectangular diode regions. In the O-type gun and Kino short gun, Harris SAI has successfully used Child's Law to represent emission-limited operation at the cathode. Within each diode region, voltage and charge emitted are given as a function of distance. This feature enables the charge ejected from the cathode to be consistent with the potential obtained from Poisson's solution over the entire tube.

In the RW-620 electron gun, the trajectories of the charge bend back toward the cathode. An electron at the far end of the cathode may cycloid back to the cathode as many as five times.

The static analysis did not converge. This can be attributed to two main difficulties.

(1) Charge returning to the cathode violated assumptions made in applying Child's Law.

(2) The trajectories must be allowed to bend even in the diode region.

Making a fine mesh did not improve convergence. As many as 5,000 nodes have been used to cover the tube. Figure 24 shows a typical cycle in a 3,000-node mesh. Notice the large accumulation of charge at the front of the cathode. This region is expanded in Figure 25. Some current will be intercepted by the cathode in this region.

2. Emission according to Kino flow

This model differs from the Child's Law model in that Kino short gun theory is assumed to hold in each diode region about the cathode. The cathode current density is derived

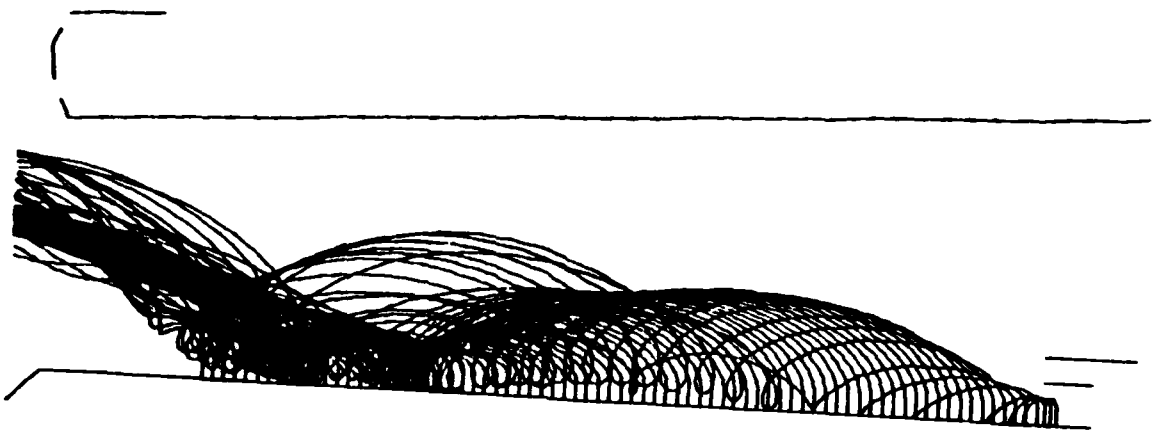

Figure 24. Trajectories about cathode using Child-Langmuir model.

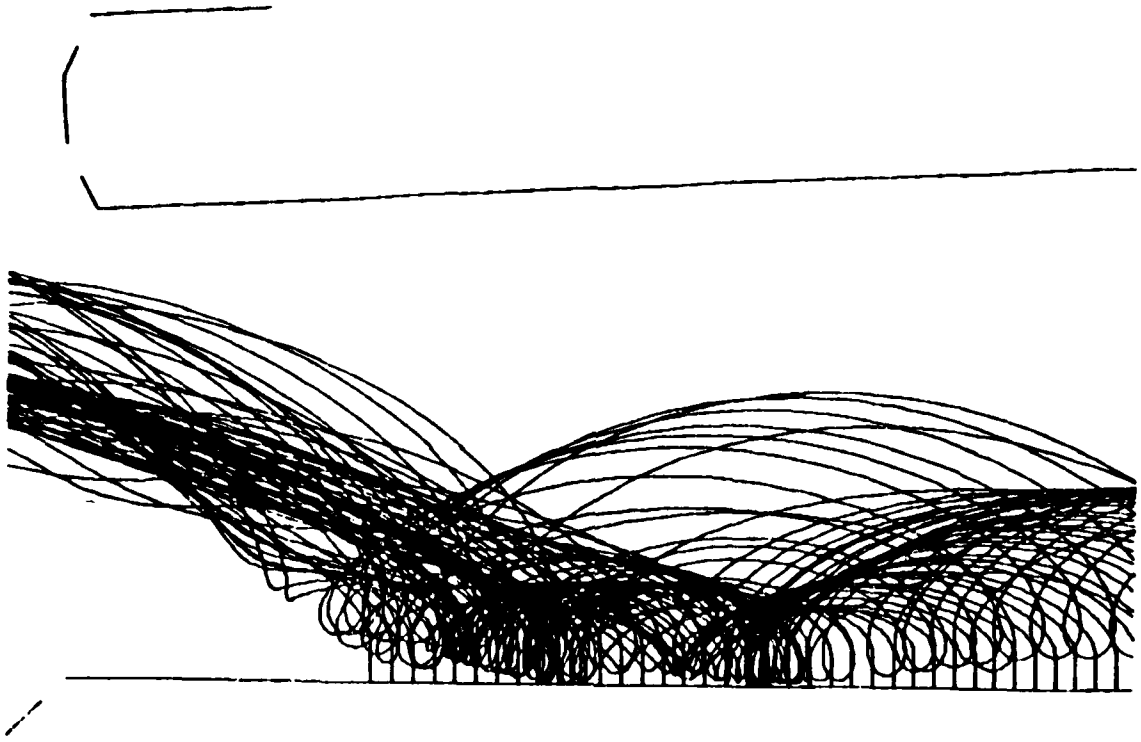

Figure 25. Top of cathode using Child-Langmuir model.

from the potential at the end of the diode region by solving iteratively the Kino flow equations[1] with a zero initial velocity at the cathode surface. The trajectories are then started at the end of the diode region with initial velocities taken from the Kino equations. In the iterative procedure, it is necessary to allow for transit times of more than one cyclotron period.

The current launched from a rectangular region of one cycle is averaged with that of the previous cycle by the following formula;

$$C_{new} = C_{old} + R(C_{calc} - C_{old}) \quad , \qquad (1)$$

where C_{calc} is the calculated current density.

Implicit in this model is the assumption that charge flows through the diode region without returning to the cathode. Consequently, the model will not handle cases of extreme cycloiding. The trajectories, however, are allowed to bend in the diode region. They should allow a more accurate representation of the initial conditions of each trajectory.

Litton Industries have used a similar model with some success on an MBWO gun. This gun is about one cycloid length long.[5] True also reported successful results for a long Kino gun with about three cycloids over the cathode. However, there are no reported comparisons with measurements on an actual gun.

The Kino flow model initially did not yield convergent results for the RW-620 gun. A possible reason for the difficulty is the same large amount of charge which cycloids back toward the cathode. The charge tends to depress the potential in a cathode region to a negative value, which tends to turn the trajectories of the next iteration away from the cathode, and which then raises the potential. Even with a low relaxation

constant R=0.25, the process produced instabilities in which the amount of charge varied greatly in successive iterative cycles. A convergent solution was subsequently obtained by applying the relaxation equation (1) to the charge density at every mesh point.

However, the Kino flow model remains unsatisfactory because of its basic assumption that no charge returns to the cathode. For this reason, the Radley-Birtles model[28,29] was adopted instead.

E. Emission according to the power series of Radley and Birtles

Near the cathode, the potential is used to calculate electron flow equations using the power series solution of Radley, et al.[28]

For each rectangular diode region, the potential power series has the form:

$$V = Ay^{4/3} \left(1 + \frac{\alpha}{A} y^{2/3} - \gamma y^{4/3}\right) \quad . \qquad (2)$$

Charge is assigned to each node in the cathode region and initial conditions for the charge trajectory out of the cathode region are obtained. The nodes on the cathode surface are numbered 1,.., j,.. in the direction from the rear toward the sole. These nodes are taken successively. There is one trajectory emitted for each node j. The program computes the emission current density and the entire trajectory from a given node j before proceeding to the next node (j + 1) along the surface. If a trajectory returns to the cathode, it does so nearer to the sole than the emission point, and its effect can thus be included in the same iterative cycle.

The following steps are performed.

(1) The potential at each mesh node is obtained from the solution of Poisson's equation over the entire mesh.

(2) At the j^{th} node along the cathode, coefficients α_j and γ_j in Equation 2 are obtained from the value of the magnetic field and the cathode current density for the j^{th} node in the previous cycle.[28] In the first cycle, an estimate of current density starts the calculation.

(3) The coefficient A_j is found from a least-square-error fit of Equation 1 to the potentials at the first NAC nodes in the direction perpendicular to the cathode at the j^{th} node along the surface.

(4) A_j is smoothed using values of A from adjacent diode regions along the cathode.

(5) Underrelaxation is applied to A_j. Using the value of A_j in the last cycle ($A_{j\ old}$), A_j is assigned the value:

$$A_{j\ old} + (A_j - A_{j\ old})\ R \quad , \tag{3}$$

where the coefficient R is typically 0.2.

(6) Using A_j, the cathode current density at the j^{th} node is calculated.[28]

(7) At the j^{th} node, the finite-difference derivative $\frac{\partial A_j}{\partial z}$ is calculated.

(8) Using coefficients A_j, α_j, γ_j, and the derivative of A_j, the electron velocities v_y^j, v_z^j, are calculated at a node, denoted N_j, which is NAC mesh intervals in the y-direction from the cathode at the j^{th} node.[28,29] The node N_j is at the interface between the cathode rectangular diodes and the deformable mesh. The velocities are needed for the initial velocity of the ray of charge.

(9) At each of the NAC points in front of the j^{th} cathode node, charge is assigned via the power-series electron flow solution of Radley and Birtles.[29] The charge q_j at the point N_j, NAC intervals above the cathode, is to be used in assigning the charge to the j^{th} ray.

(10) (Optional) If charge from a trajectory k (k is less than j) has been deposited at node N_j because of cycloiding, this charge is subtracted from q_j. The resulting value is proportional to the amount of charge launched on the j^{th} ray. In this manner, charge launched on a ray is consistent with both the power series solution and the presence of a returning charge.

(11) The charge Q_j actually launched on the trajectory ray from node N_j is given by:

$$Q_j = \frac{q_j \, v_y^j \, \Delta t \, \Delta z_j}{A_j} \quad , \tag{4}$$

where Δz_j is the width parallel to the cathode of the j^{th} elemental diode, A_j is the area of the rectangular mesh region associated with node N_j, and Δt is the time step. See reference 9, Equations 5.6 and 6.41.

(12) The ray at node N_j is launched with charge Q_j and initial velocity components v_y^j and v_z^j.

(13) A space-charge weight is added to charge at each of the NAC nodes in front of the j^{th} cathode node. This weight is described by Radley, et al.[28] It provides corrections to the finite-difference residuals near the cathode for a crossed-field gun so that the finite-difference potential solution is consistent with the potential series.

(14) The position on the cathode is incremented to the $(j + 1)^{th}$ node and the calculation repeated from step 2.

B. Comparison of Theory and Measurement

The results of the two-dimensional static analysis of the RW-620 are shown in Table 5 for a magnetic field of 0.25 T and accelerating-anode voltages of 2.5 kV, 3.5 kV, and 4.5 kV. The two-dimensional model gives only the current emitted per unit width in the magnetic-field direction. To compare the calculated and measured currents, it is assumed that the grids shield one half of the cathode in the actual tube.

The two cases - (a) and (b) - correspond, respectively, to including or excluding returning charge in the net charge launched per ray in a given iterative cycle (see step 10 of Seciton VI.A). Case (b) gives the lower beam currents.

For the ideal Brillouin crossed-field beam grazing the cathode in a uniform plane-parallel diode, the anode voltage (below cutoff), the magnetic field, and the anode-cathode spacing together give a unique beam current per unit width and a corresponding beam thickness in the plate-cathode direction. The Brillouin current I per meter width in the magnetic-field direction is given by:[22]

$$I/I_{max} = (1 - (1 - V_a/V_c)^{1/2})^2 \quad , \tag{5}$$

with

$$I_{max} = \frac{\varepsilon_0 \omega_c^3 d^2}{2\eta} \quad , \tag{6}$$

the current per meter width that fills the diode,

$$\omega_c = \eta B \quad , \tag{7}$$

the angular cyclotron frequency, and

TABLE 5

MEASURED BEAM CURRENTS IN RW-620 GUN AND VALUES FROM TWO-DIMENSIONAL STATIC MODEL

Accelerating Anode Voltage (V)	Computed Current Per Unit Width (A/m)		Brillouin Current Per Unit Width (A/m)		Measured Beam Current (A)	Measured Current Per Unit Width (A/m) Assuming an Effective Cathode Width of 4.5 mm
	Case (a)	Case (b)	Rear of Cathode	Front of Cathode		
2,500	395	152	120	247	0.15	33
3,500	750	538	266	722	0.5	111
4,500	832	341	515	1,503 (above cutoff)	1.5	333

Case (a) Launched charge is taken directly from Radley-Birtles solution.

Case (b) Returning charge is subtracted from Radley-Birtles solution to give net launched charge.

The measured values were taken on tube S/N 59242 on December 21, 1977.

$$V_c = \frac{\omega_c^2 d^2}{2\eta} \quad , \tag{8}$$

the cutoff voltage. Here, V_a is the accelerating-anode (plate) voltage, d is the anode-cathode spacing (treated as uniform), B is the magnetic field, and η is the ratio of electron charge to mass. The beam thickness y_{top} is given by:

$$y_{top} = \sqrt{\frac{2I}{\varepsilon_o \eta^2 B^3}} \tag{9}$$

for $V_a < V_c$ (below cutoff) or

$$y_{top} = d \tag{10}$$

for $V_a \geq V_c$ (above cutoff).

The Brillouin currents per meter of cathode width are also shown in Table 2. They are sensitive to the plate-to-cathode spacing, which is tapered from 1.067 mm at the rear to 0.838 mm at the front in the RW-620 (tube S/N 59242). The values for both the front and the rear are tabulated. Since the measured currents fall more rapidly with plate voltage than the Brillouin currents, the effective cathode width appears to be less at the lower plate voltages.

At 4.5 kV, the Brillouin current densities may exceed the density available from the temperature-limited cathode, which supplies between 1×10^5 and 2×10^5 A/m^2 over a length of 4.34×10^{-3} m in the beam-drift direction. The corresponding temperature-limited current attainable per unit width is then between 434 and 868 A/m, sufficient to supply the measured 1.5 A, but not with a Brillouin stream in the gun.

Looking next at the computed currents shows the following.

(1) The computed current densities are of the correct order of magnitude, but are in all cases higher than measured.

(2) Closer agreement is obtained when the charge returned to the cathode from points nearer to the rear is included in deriving the potential distribution and the emission current density at a given point than when the returning charge is ignored.

(3) The values of 538 A/m and 341 A/m at 3,500 V and 4,500 V are anomalous since a higher voltage should produce a higher current. The limitation of the model is its sensitivity to whether or not cycloiding trajectories graze or intersect the cathode. With more simulation trajectories, this sensitivity would be reduced.

Corresponding trajectory plots are shown in Figures 26 through 31, and Figure 32 shows typical equipotentials.

At 2,500 kV, the cathode covers about five cycloid lengths; at 4,500 kV, there are about three cycloids per trajectory over the cathode.

In the anode-sole region (on the left of the figures), a nonlaminar (non-Brillouin) beam appears to be launched with some cycloiding and crossover, but no electrode interception.

C. Conclusion

While the electrostatic solution is useful for the linear-beam tube and the short Kino crossed-field gun, convergence difficulties make it less suitable for the long crossed-field gun. The time-dependent method is more promising for treating electrons that return to the cathode; in fact a time-independent state may not exist in this case.

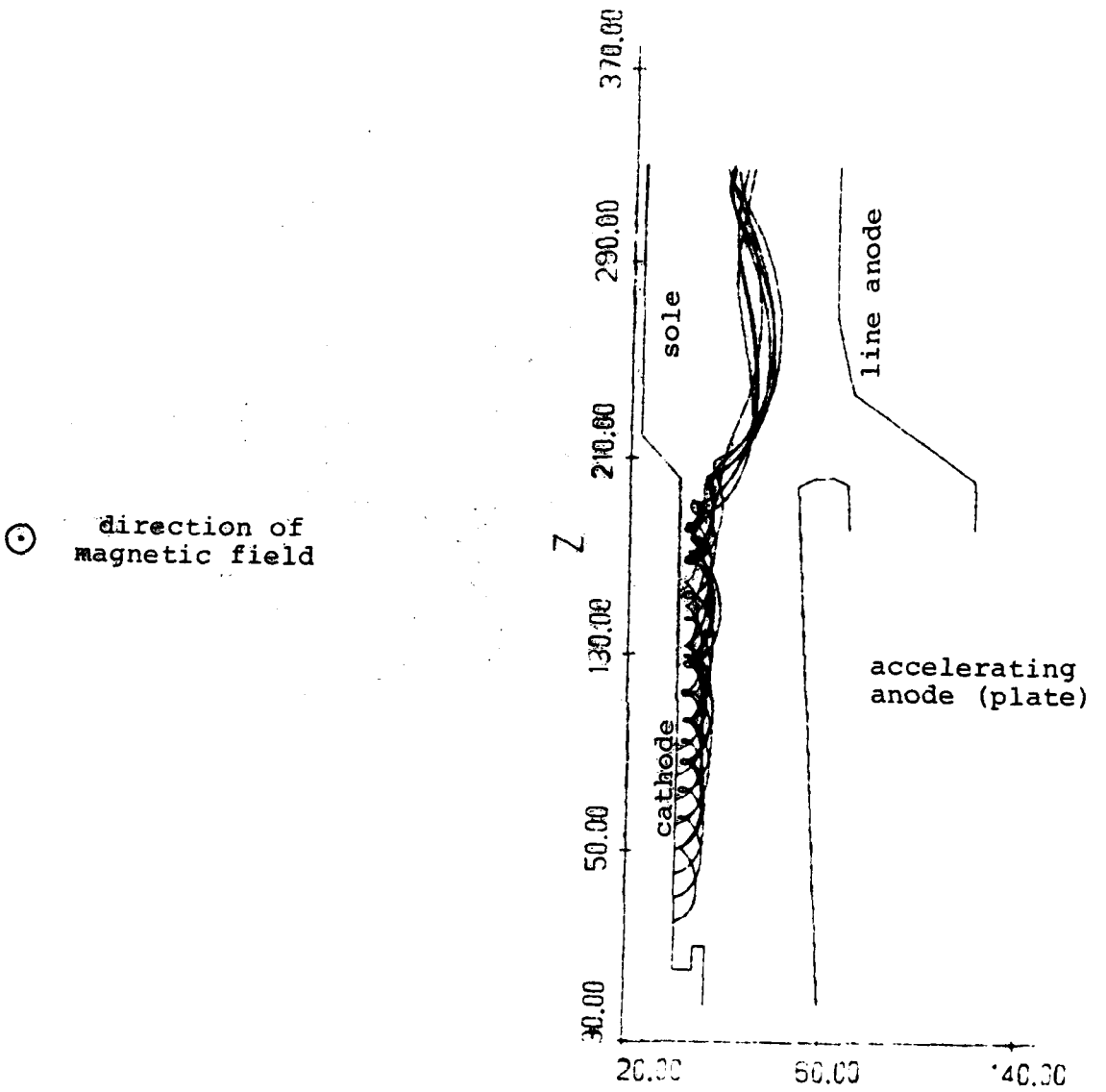

Figure 26. RW-620 trajectories from two-dimensional static model with plate at 2,500 V; returning charge ignored for computing emission.

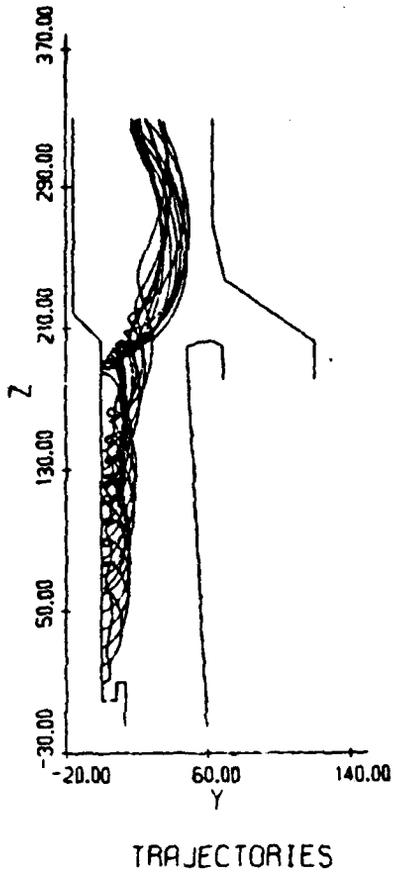

Figure 27. RW-620 trajectories from two-dimensional static model with plate at 3,500 V; returning charge ignored for computing emission.

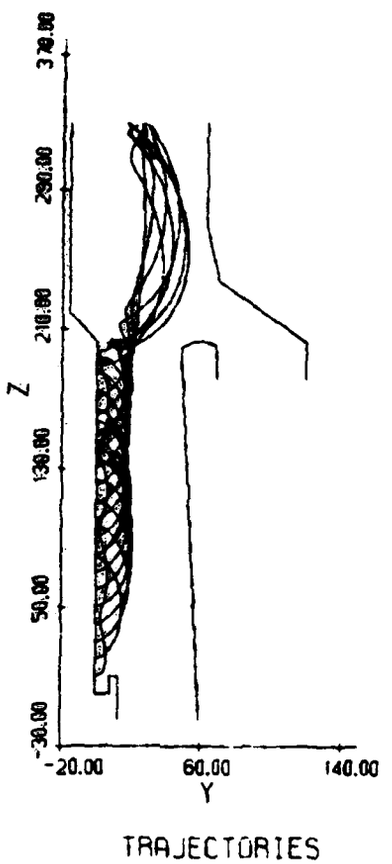

Figure 28. RW-620 trajectories from two-dimensional static model with plate at 4,500 V; returning charge ignored for computing emission.

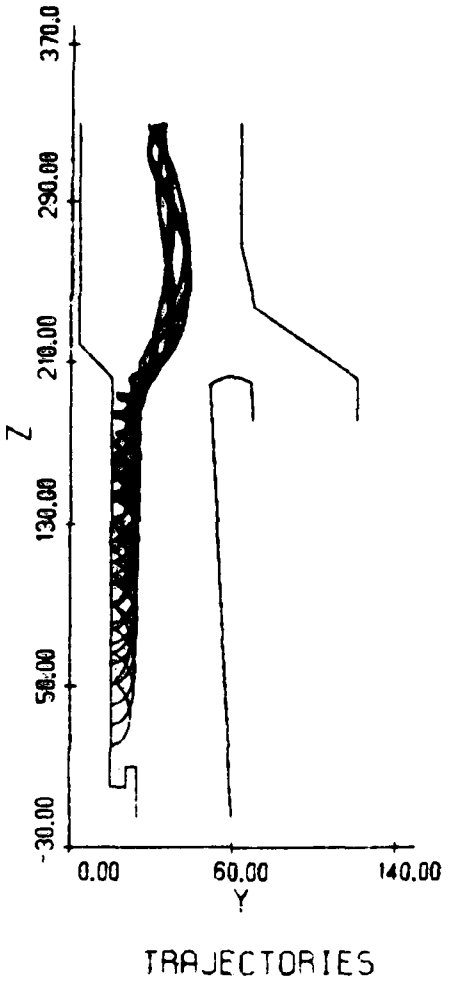

Figure 29. RW-620 trajectories from two-dimensional static model with plate at 2,500 V; returning charge included for computing emission.

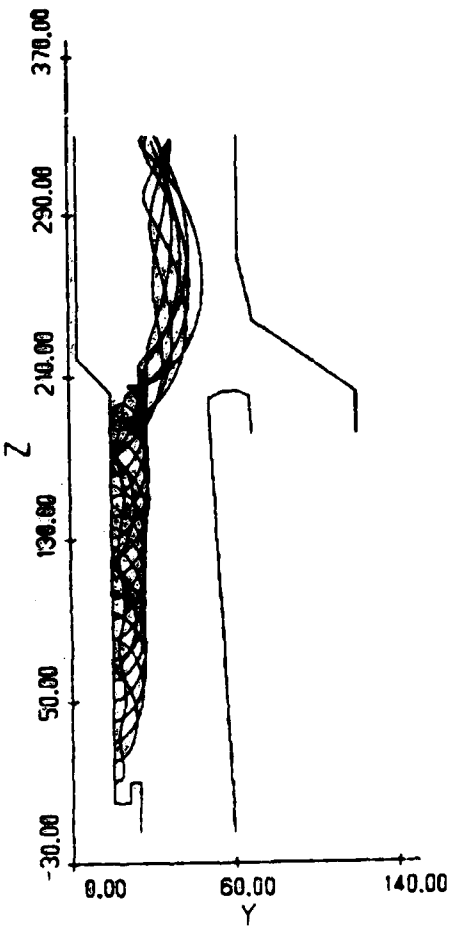

Figure 30. RW-620 trajectories from two-dimensional static model with plate at 3,500 V; returning charge included for computing emission.

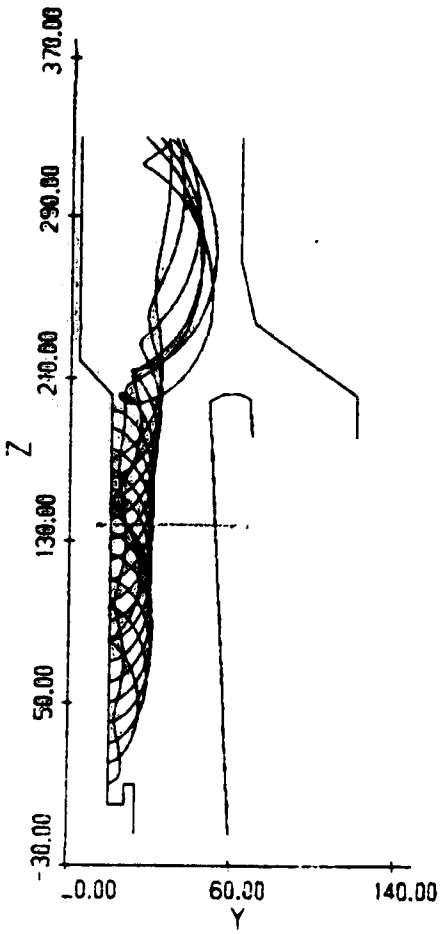

Figure 31. RW-620 trajectories from two-dimensional static model with plate at 4,500 V; returning charge included for computing emission.

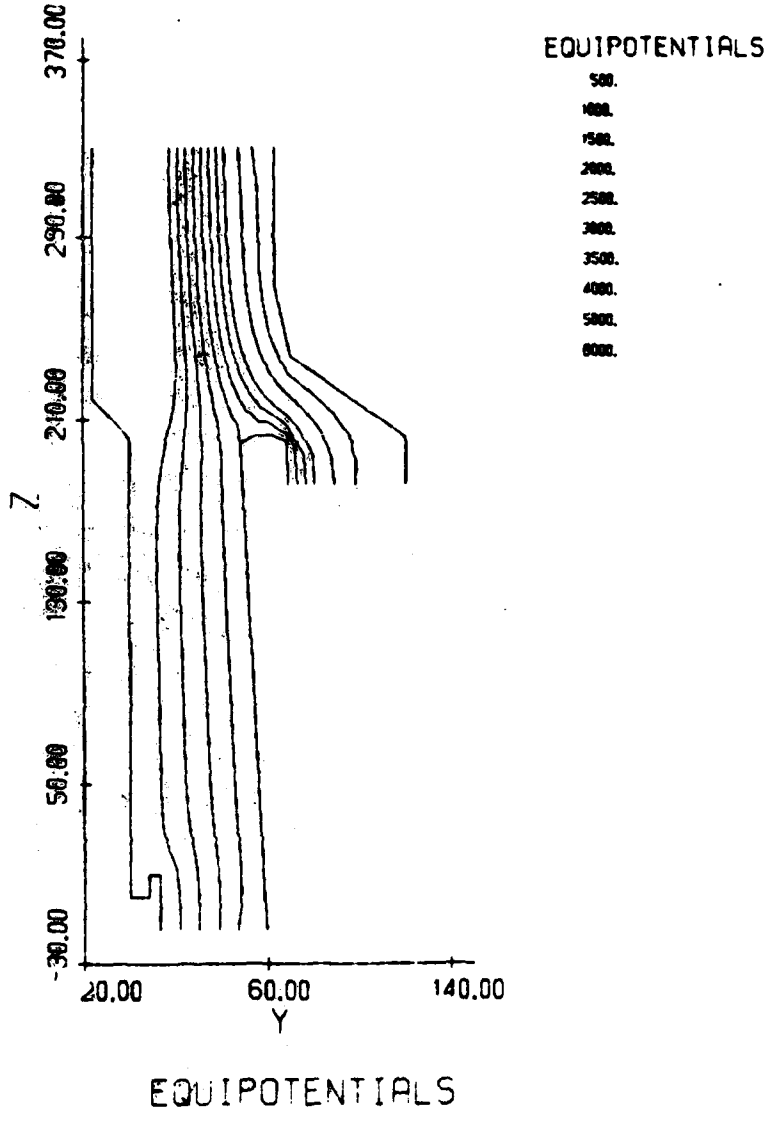

Figure 32. RW-620 equipotentials from two-dimensional static model with plate at 2,500 V; returning charge included for computing emission.

SECTION VII

SHOT NOISE AT THE CATHODE

A. Introduction

There is continuing controversy whether noise due to random emission of electrons at the cathode of a crossed-field gun is smoothed or amplified by returning charge.

Experimental results summarized by Ho and Van Duzer[15] show that excess noise is observed for long cathodes that cover more than 0.55 cycloid lengths. In the physical model, returning electrons cause a feedback of perturbations and a resultant instability. More recently Harker and Crawford[16,17] have concluded that if electron transit times are ignored, the potential minimum always smooths shot noise originating with random perturbations of the emission current at the cathode, just as when the magnetic field is absent. In a parallel study,[18] Shkarofsky has analyzed the effects of shot noise on the thermal velocity distribution for a fixed, unperturbed, parabolic potential, also in an infinite plane-parallel diode. Here "shot noise" is defined as the random fluctuations in the number of electrons emitted in a given time over a region of the cathode and the random fluctuations in their emission times.

In this section, the Ho theory is compared with these alternative models.

B. Diode Model

The diode is made infinitely broad in the magnetic-field direction so that all motion may be confined to the plane perpendicular to the magnetic field. The diode is specified by the anode voltage, the magnetic field, the anode-cathode

spacing, the cathode length in the beam-drift direction, and the maximum current density available at the given cathode temperature. Ho assumes that the potential distribution between the potential minimum and the anode approximates that of a Kino long gun,[1,22] in the region where the equipotentials are roughly parallel to the cathode surface.

A "space-charge-limited" condition is assumed with a parabolic potential distribution between the cathode and potential minimum that is uniform along the unperturbed diode. The space-charge-limited condition is characterized by the existence of a critical plane parallel to the cathode for each value of the initial velocity component parallel to the surface. At the critical plane, the electron will either turn back to the cathode or escape entirely into the electron stream, depending on its initial normal component of velocity. Van Duzer and Whinnery[30] have provided a clear explanation of this effect. If there are no critical planes, the diode is "magnetic-field-limited" and all electrons either intercept the anode or return to the cathode plane.

Ho and Van Duzer use the Kino short gun flow equations to estimate the density J_a of the current component escaping normal to the cathode, and hence to derive the position and depth of the potential minimum and distinguish the space-charge-limited regime. The feedback theory then derives the effects of perturbations of the emitted current.

With the parabolic potential distribution, the space-charge-limited condition is

$$\frac{2|V_m|}{x_m^2} > \omega_c^2 \quad , \tag{1}$$

with $|V_m|$ and x_m the magnitude and position of the potential minimum and ω_c the radian electron cyclotron frequency, ηB. This condition is, equivalently, written as

$$\omega_p > \omega_c \quad , \tag{2}$$

where ω_p is the radian plasma frequency of the electron stream up to the potential minimum and is uniform on the parabolic potential assumption. The term ω_p may be estimated from the value in the nonmagnetic diode,[31]

$$\omega_p^2 = \frac{\eta J_a}{\varepsilon_0} \left(\frac{\pi}{2} \frac{m}{kT}\right)^{1/2} \quad , \tag{3}$$

where m is the electron mass, k is Boltzmann's constant, T is the cathode temperature, and J_a is the density of escaping current normal to the cathode at the potential minimum.

In an actual gun, however, the space-charge-limited and magnetic-field-limited regions are not straightforward to find. The emission current density must be averaged over the width of the cathode and the effects of the end hats on the electric field neglected. Extending the theory to three dimensions appears to be difficult because of the complex electron trajectories produced by the nonuniform electric field and the nonparabolic potential distribution at the sides. The time-dependent numerical simulation is preferable for study of an actual gun, since the realistic electrode boundary conditions can then be applied to solve Poisson's equation.

C. Mechanism of Instability

In the nonmagnetic diode, there is only one "critical plane," located at the potential minimum. An excess emission

current (a shot-noise perturbation) depresses the potential minimum, producing a compensating fluctuation that smooths the shot noise from the temperature-limited value.[30,31] According to Ho and Van Duzer,[32] the instability in the crossed-field diode arises from a cumulative effect of electrons cycloiding and returning to the cathode. Van Duzer's and Whinnery's 1961 model of the crossed-field diode[30] used only a one-dimensional calculation of the time-dependent emission-perturbation current, and did not predict instability. That model treated the effect of an increased emission current on the trajectories of the critical electrons and showed that the thermal velocity distribution is not directly responsible for excess noise. If a deepening of the potential minimum causes an extra near-critical electron to return to the cathode without crossing the critical plane, a corresponding "hole" is formed in the stream. These hole trajectories, assumed to be collected on the anode in the 1961 model, can, in fact, return to the cathode if the cathode is sufficiently long relative to the cycloid length, making the potential minimum less deep and increasing the perturbation current emitted.

At this point Ho and Van Duzer's model differs significantly from that analyzed by Harker and Crawford.[16,17] According to the latter, at a given plane between the anode and the cathode, there are just three classes of electrons:

(1) Electrons with insufficient initial normal velocity to reach the critical plane and which return to the cathode,

(2) Electrons for which the given plane is a critical plane, so that they are moving parallel to the cathode, and

(3) Electrons whose initial normal velocity is sufficient that they can pass their critical plane.

Class (1) contains equal numbers of electrons moving towards the anode and returning towards the cathode. All electrons in class (3) are moving away from the cathode and will eventually reach the anode.

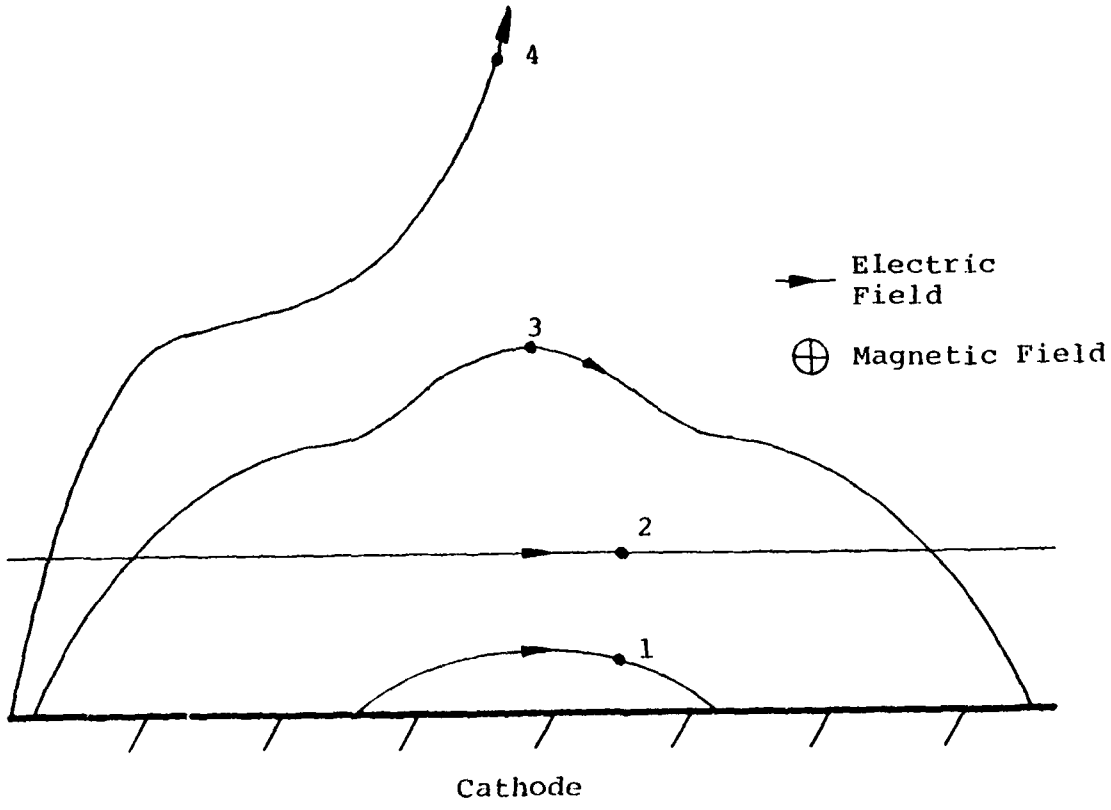

1. Electron returned to cathode before reaching its critical plane.
2. Electron on critical plane.
3. Electron past critical plane but returning to cathode.
4. Electron past critical plane and escaping to anode.

Figure 33. Typical trajectories in crossed-field diode.

This classification is complete when the potential varies parabolically throughout the diode. However, the potential distribution used beyond the potential minimum by Ho and Van Duzer allows some of the electrons from class (3) to return to the cathode. It is these electrons that perturb the potential minimum in that model and produce instability. In Figure 33,electrons 1 and 2 are in classes (1) and (2) respectively, and electrons 3 and 4 of class (3) have passed their critical planes. However, only electron 4 escaped to the anode. A further explanation of the electron trajectories is given by Lindsay (see reference 33, Figure 4).

According to Ho and Van Duzer, a perturbation that deepens the potential minimum creates "holes" in the electron stream. These "holes" follow the same trajectories as the electrons they replace. Ho attributes the instability to the difference between these hole trajectories and the trajectories of emission perturbation electrons. The holes originate at critical planes with normal velocities near zero; emission perturbation electrons that pass their critical plane have larger normal velocity there. The Ho and Van Duzer model uses an iterative, rather than a time-dependent, theory, and uses the lack of convergence to demonstrate instability in a long gun. Their cathode length criterion shows good qualitative agreement with experimental observations on crossed-field guns, both short and long compared with the Kino cycloid length $2\pi^2 \eta J_a/(\varepsilon_0 \omega_c^3)$, where η is the electron charge-to-mass ratio and $\omega_c = \eta B$ is the electron cyclotron frequency for the magnetic field B.

In the RW-620 gun, the ratio of cathode length to Kino cycloid length varies from about 9 to 18 as the beam current density varies from 10 to 5 A/m^2 at 0.25 T magnetic field. This ratio clearly fulfills the criterion for excess noise due to cycloiding. However, the grids in the actual gun may suppress the effect; the full computer simulation is necessary.

AD-A125 341 SIMULATION OF DISTRIBUTED-EMISSION AND INJECTED-BEAM CROSSED-FIELD AMPLIF..(U) HARRIS SAI INC ANN ARBOR MI D M MACGREGOR ET AL. APR 80 AFOSR-TR-80-0553 213

UNCLASSIFIED F49620-77-C-0091 F/G 9/1 NL

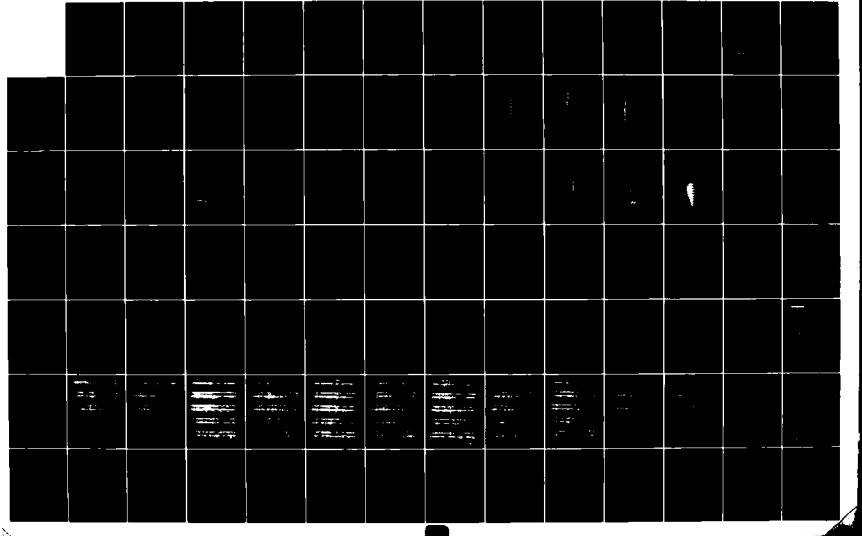

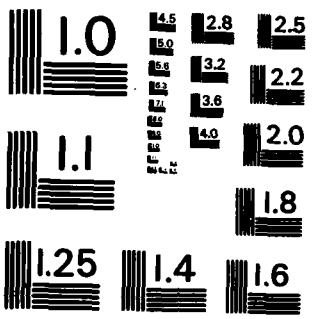

MICROCOPY RESOLUTION TEST CHART
NATIONAL BUREAU OF STANDARDS-1963-A

D. Conclusion

There is no contradiction between the theories mentioned here: all three make different assumptions. Ho and Van Duzer[15,32] have the most general model although their calculations are not analytically rigorous. It appears that an instability may be caused by cycloiding electrons that escape into the electron stream and then return to the cathode. There are no such electrons when the potential is parabolic throughout the diode, as in the analytic models.

The Harris SAI time-dependent computer model may predict instability if a noise current is added to the average local cathode emission, since a fluctuation at one point will affect the subsequent emission along the surface. However, the present RW-620 calculations, with no applied noise current, are stable over 120 cyclotron periods. It would be interesting, also, to perform a detailed computer simulation of a long rectangular crossed-field diode on a scale sufficiently fine to distinguish the critical planes and the potential minimum.

SECTION VIII

TIME-DEPENDENT CATHODE EMISSION

A. Introduction

There are two alternative methods of beam simulation at the cathode. A microscopic approach models the emission at the cathode surface and then uses the derived potentials to give the space-charge-limited current. A small mesh interval and time step are needed; their values are estimated below. Alternatively, a macroscopic model can be used in which the Debye length (defined below) is short-relative to the mesh interval in the model, and the net emitted current is estimated from the electric field. The Child's Law calculation of the static analysis is an example of the latter method.

For economy in computation, it is advantageous to use the largest potential mesh and the smallest number of particles consistent with a realistic simulation. It is also useful to determine which effects are important and which will be resolved by a given model, since the cathode phenomena are critical in determining the beam current and its stability.

B. Debye Length

The Debye length (λ_D) is significant in two ways. First, it is a good estimate of the distance from the cathode to the potential minimum. In the classical non-magnetic space-charge-limited diode,[31] this distance equals $1.225\lambda_D$.

Secondly, the average energy of a cloud of electrons in thermal equilibrium through individual collisions is of the order of kT. If the density of the cloud is perturbed from a uniform state, the resulting space-charge field acting over a sufficient distance can produce energy changes of the same order, kT. The Debye length is a measure of this distance.

The number of particles in a Debye sphere is approximately equal to the ratio of the mean collision time to the period of plasma oscillations. When the Debye length is much less than the device dimensions the beam may be treated as a collisionless plasma.

The Debye length for an electron beam is defined as

$$\lambda_D = \frac{v}{\sqrt{2}\,\omega_p} \quad , \tag{1}$$

where v is a characteristic speed of the particles and ω_p is the angular plasma frequency corresponding to the local charge density. An estimate of ω_p in the crossed-field gun is given by the Brillouin flow condition[19]

$$\omega_p = \omega_c = \eta B \quad , \tag{2}$$

where ω_c is the angular cyclotron frequency in the magnetic field B, and η is the ratio of electron charge to mass.

A more precise definition of λ_D is[31]

$$\lambda_D^2 = \overline{v_y^2}/\omega_p^2 \quad . \tag{3}$$

Here $\overline{v_y^2}$ is the mean square normal component of the thermal emission velocity given by

$$\overline{v_y^2} = 2kT/m \tag{4}$$

for a cathode of temperature T, where k is Boltzmann's constant and m the electron mass. For the term ω_p Birdsall and Bridges[31] use the radian plasma frequency at the potential minimum, given in a non-magnetic diode by Equation 3(VII)

$$\omega_p^2 = \frac{\eta J_y}{\epsilon_0} \left(\frac{\pi}{2} \frac{m}{kT}\right)^{1/2} \quad . \tag{5}$$

The term J_y is the current density escaping normal to the cathode at the potential minimum. An upper limit to J_y is the maximum thermionic current density, J_s, which is attained where the cathode is locally or instantaneously emission limited.

C. Microscopic Emission Model

Here the model requires only the thermionic current density J_s A/m^2 and the number, NEPM, of charge rods to be emitted per mesh interval ζ along the cathode surface. Then the total charge emitted in a time interval Δt is given as

$$Q = - J_s \Delta t \times (\text{cathode area}) \quad . \tag{6}$$

This charge is distributed evenly over the cathode surface at every time step independently of the local eletric field or charge already emitted. The charge per rod per meter width in the magnetic-field direction is

$$q = \text{DQROD} = - J_s \zeta \Delta t / \text{NEPM} \tag{7}$$

Let the mesh intervals along and normal to the cathode equal ζ and ξ, let Δt be the time step of the simulation, and let q be the charge per meter width for a single rod in a two-dimensional model. Estimates of the mesh size and time step required to compute the potential minimum and the effects of thermal velocities there are

$$\xi < \lambda_D \quad , \tag{8}$$

$$\zeta < \lambda_D \quad , \tag{9}$$

$$\Delta t < \lambda_D / \bar{v}_y \quad . \tag{10}$$

The maximum charge per unit length per rod is then

$$|q| = \frac{\varepsilon_0 \, \omega_p^2 \lambda_D^2}{\eta} \tag{11}$$

or

$$|q| = \frac{\varepsilon_0 \, 2kT}{\eta} \ \text{C/m} \tag{12}$$

to give at least one rod per Debye square.

For a three-dimensional model each rod must then be divided lengthwise into at least as many particles as the number of Debye lengths across the device.

Table 6 shows the Debye length at the cathode in the two guns studied here (cathode temperature 1500 K), the maximum mesh size allowed compared with the distance from the cathode to the accelerating anode (plate), and the largest time step and charge per particle that will permit a resolution of the potential minimum. Table 7 summarizes the model parameters actually used for the two crossed-field guns simulated in the present study. It shows also the values used in earlier calculations by Wadhwa and Rowe[34] for a plane-parallel diode and by Lele and Rowe[6] for a short Kino gun. The latter two models were fine enough to distinguish the potential minimum. The same detailed calculation for the RW-620 gun appears impractical.

One way to remove this difficulty is to raise the cathode temperature, T. The Debye length is proportional to $T^{3/4}$, and can thus be made to exceed the practical mesh interval. Of course the noise computed will increase also. For example, the

TABLE 6

DEBYE LENGTHS IN CROSSED-FIELD GUNS, WITH ESTIMATES OF TIME STEPS AND PARTICLE NUMBERS NEEDED FOR DETAILED CATHODE SIMULATION

Gun	Max. Current Density (A/m^2)	Debye Length λ_D(m)	Debye Length / Plate Height	Time Step / Cyclotron Period	Charge Per Rod (C/m)	Minimum Total Rods Needed
Kino short gun	10,000	4.96×10^{-6}	1/1210	1/14	-2.12×10^{-12}	3,600
RW-620 (long gun)	200,000	1.109×10^{-6}	1/1053	1/41	-2.12×10^{-12}	87,800

TABLE 7

MODELING PARAMETERS FOR FOUR CROSSED-FIELD GUNS

Gun	Mesh Interval at Cathode / Debye Length	Mesh Interval / Plate Height	Time Step / Cyclotron Period	Charge Per Rod(C/m)	Total Rods In Simulation
Kino Short Gun	14	1/85	1/10	-7.44×10^{-12}	1207
RW-620 Long Gun	41	1/25	1/10	-7.15×10^{-11}	2723
Wadhwas & Rowe(1963)	1/7.8	1/3010	1/132	-3.22×10^{-11}	about 700
Lele & Rowe(1969)	1/5.5	1/3300	1/212	-2.12×10^{-12}	not known

simulation of the RW-620 gun with its present mesh size requires a temperature of 2.12×10^5 K instead of the actual 1500 K. The noise study of Kooyers and Shaw[4] for a long Kino gun uses a mesh interval of about 20 times the Debye length for an actual cathode temperature of 1323 K. The corresponding effective cathode temperature for generating noise effects in the beam is 71,800 K. In that case ten time steps per cyclotron period and a density of two or more rods per mesh rectangle for a Brillouin stream are sufficient. With space-charge limitation, the minimum beam temperature actually computed by Kooyers and Shaw[4] is about 62,000°K, and their beam current is about 3 percent above the theoretical value.

This microscopic model is retained as an option in the present Harris SAI program. It has not been extensively tested, but initial trials give an excess beam current in the short Kino gun. It is found that all the thermionic current escapes into the beam and no potential minimum is formed to return excess charge. Thus, this method is not generally applicable to guns of varying cathode lengths.

D. Macroscopic Emission Model

Accurate and efficient prediction of the beam current is the primary purpose of this model. It implicitly assumes that the mesh interval exceeds the Debye length at the cathode.

At each time step and at each mesh mode on the cathode, the total charge is counted within one mesh rectangle above the surface. At the node sufficient charge is emitted, then, to reduce the local electric field to zero. If the charge required exceeds the available charge derived from the thermionic current density, only the available charge is emitted. The same algorithm is used with excellent results, in the distributed-emission CFA model. Part I of this report gives a detailed description. It is expected that it will be more

accurate than the microscopic model for the full 3D simulation of the RW-620 gun which has a grid 0.2 mm (4 mesh intervals) above the cathode. To determine the charge per rod the user supplies the parameter FBRILL which is the number of charge rods required to cover one mesh rectangle at the cathode with the density of a Brillouin stream. Thus, the charge per rod per meter width in the magnetic-field direction is

$$DQROD = -\varepsilon_0 \eta B^2 \cdot RDIS \cdot ZDIS/FBRILL \quad , \qquad (13)$$

where RDIS and ZDIS are the mesh intervals along and perpendicular to the cathode. Present runs use the values FBRILL = 3.0 in the KINO short gun and FBRILL = 16.0 in the RW-620 long gun.

To simulate noise effects beyond the potential minimum, random perturbations of the emission current and an initial thermal velocity distribution may be added after the mean emission current has been determined.

E. Tests of the Macroscopic Model

1. Child's Law

The model has been tested using the analytic Child's Law solution in a plane-parallel diode with no magnetic field. The computed currents are at present 6 percent above the analytic values, although the 3/2 power law is obeyed as the voltage is raised. The reason for this error is that the trajectory equations now used for the IBCFA are not time-centered. The initial velocity and positions are specified at the same instant instead of one-half step apart. As a result, an emitted electron sees the full electric field from the previous step during its first trajectory step and its self-field is not included. Future versions of this program will advance the emitted electrons only for one half a time step initially.

In the cylindrical distributed-emission CFA model (Part I of this report), the trajectories are corrected after the solution of Poisson's equation, and the error in the Child's Law simulation is only two percent.

The Child's Law test reveals a second limitation which is due to the triangular mesh structure (Figure 34). The electric fields computed at 'odd-J' mesh points differ from those at 'even-J' points in the presence of space charge even for a uniform electron stream because of the manner in which charge is assigned to the mesh. The effect on the emitted charge is reduced by using the mean of the normal electric fields above two adjacent cathode points to control the emission at each point. The same smoothing is used in the crossed-field gun simulations. A "ripple" on the computed trajectories remains, however (Figure 35).

2. Dynamic simulation of the Kino short gun

Since the Kino short gun has a short cathode relative to the cycloid length, it can be treated either by the static or the time-varying model. The results from the two models (Table 8) show that the cathode currents from the dynamic model now converge to values about 33 percent too high. These currents are, however, less than the available thermionic current supplied to the model, whereas the time-dependent microscopic model failed to show a space-charge-limited condition. The tests should be repeated with the improved calculation of the trajectories at the cathode.

F. Summary

The two cathode modeling options are compared in Table 9. The macroscopic model shows less detail but is computationally more efficient than an accurate microscopic model. It should be incorporated also in the three-dimensional gun simulation.

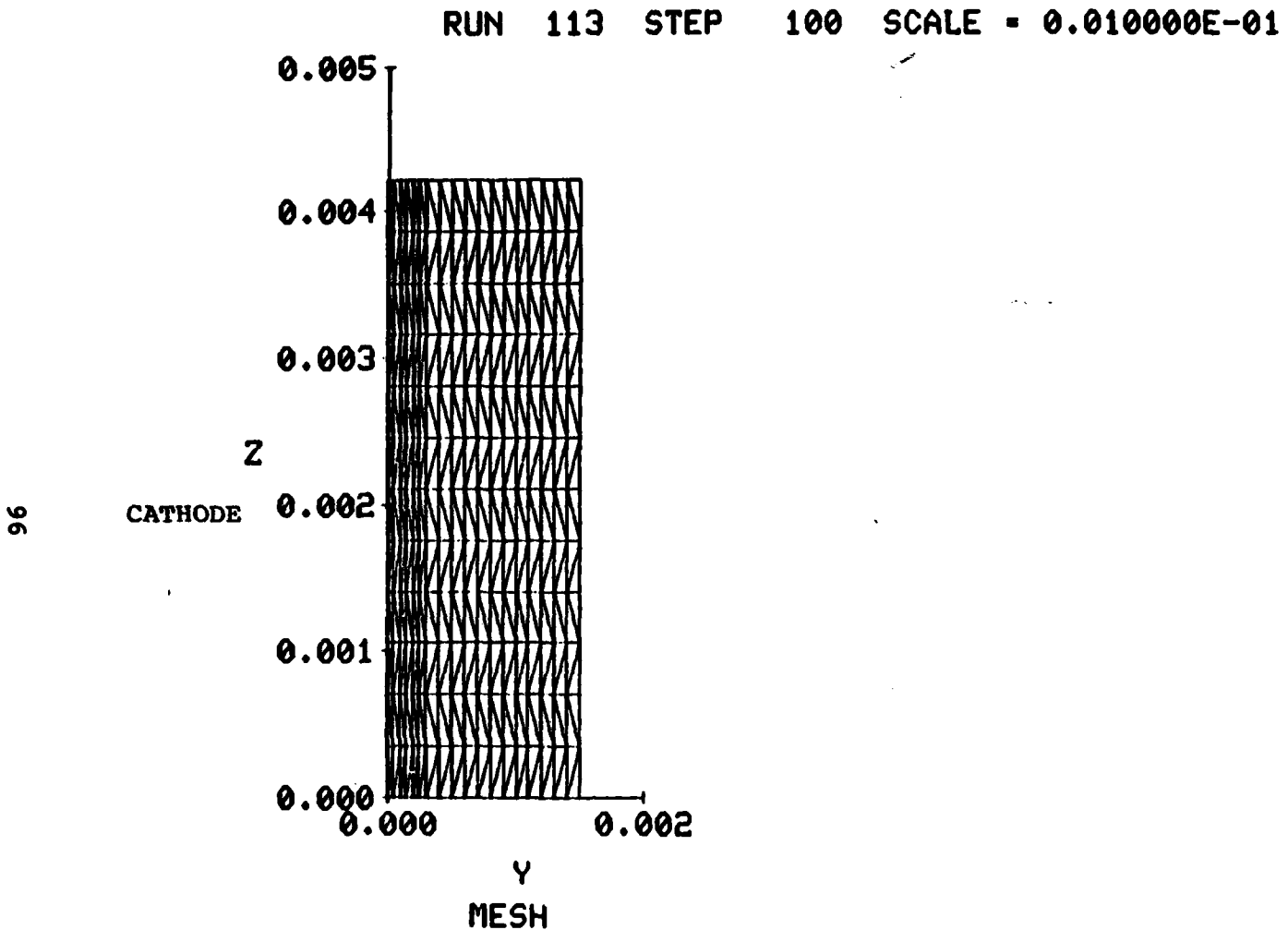

Figure 34. Mesh for test of Child's Law in plane-parallel diode.

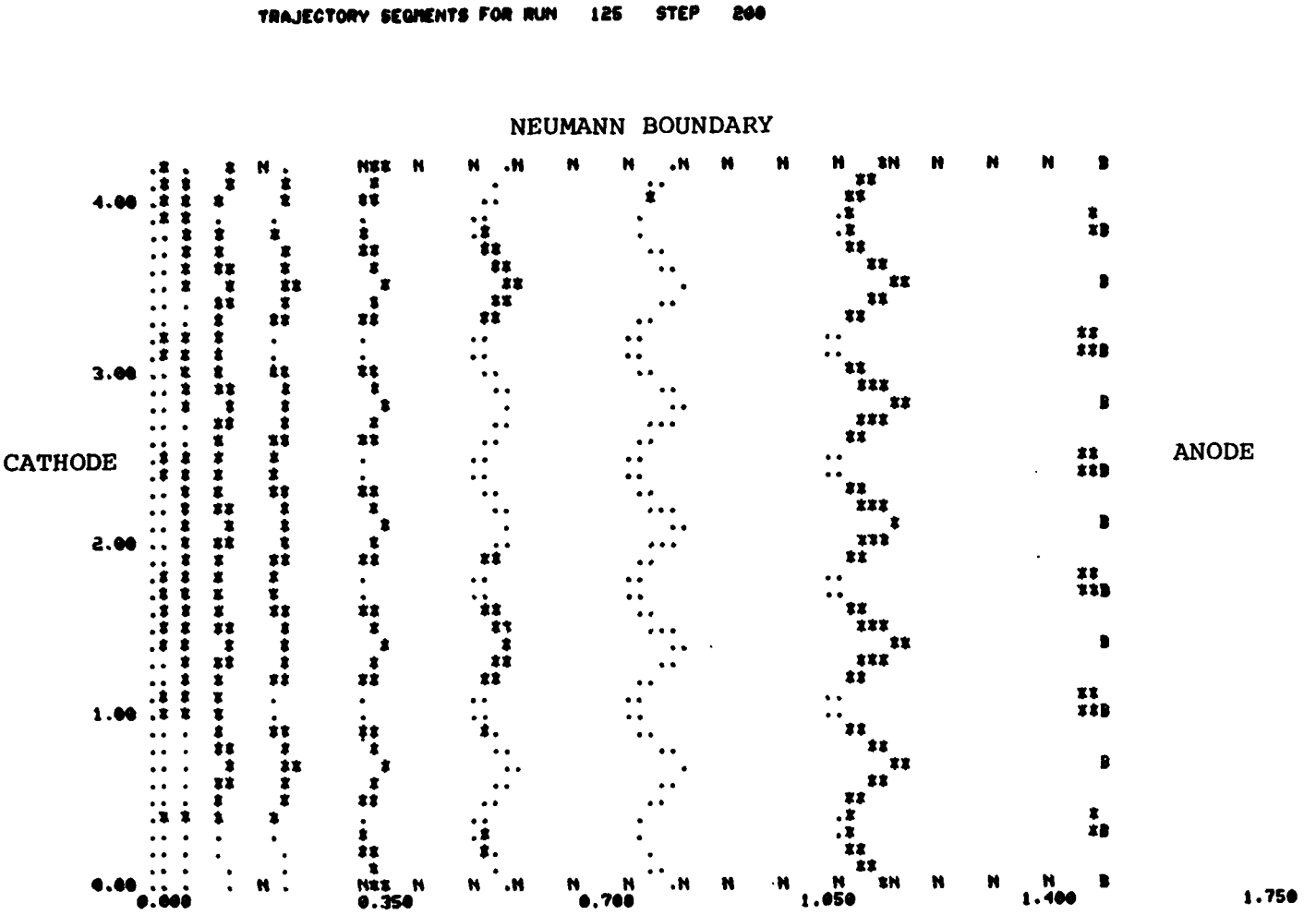

Figure 35. Particle positions in deformable-mesh model of nonmagnetic diode.

TABLE 8

COMPUTED AND MEASURED CATHODE CURRENTS

IN KINO SHORT CROSSED-FIELD GUN

Magnetic Field (T)	Cathode Currents (A)			
	Static Particle Model	Time-Varying Particle Model	Analytic	Measured
0.0195	0.0473	0.0624	0.0437	0.0455
0.0219	0.0478	0.0604		0.0453
0.0230	0.0475	0.0592		0.0450
0.0300		0.0545		0.039

TABLE 9

COMPARISON OF TIME DEPENDENT MODELS

OF CATHODE EMISSION

Beam Property	Microscopic Model	Macroscopic Model
General Features	Cathode emits full thermionic current; net current limited only by returning trajectories.	Emitted charge controlled to cancel electric field on cathode.
Accuracy of Net Current	In short gun, all injected charge escapes into beam. In long gun, (Shaw) 3% accuracy; accuracy with gridded gun not known.	2 % above Child's Law values.
Effective Cathode Temperature	Proportional to $\left(\frac{\text{Mesh Size}}{\text{Debye length}}\right)^{4/3}$	Not known.
Potential Minimum at Cathode	Accurate only with short time step and fine mesh.	Neglected.
Thermal Velocities	Included, but unimportant in practical models.	Included, but probably unimportant.
Shot Noise at Cathode	Included but magnified by discrete particle size.	Imposed on emission current and magnified by particle size.
Smoothing of Shot Noise by Space Charge	Included.	Not included.

TABLE 9 (CONT.)

Beam Property	Microscopic Model	Macroscopic Model
Excess Shot Noise at Long Cathode	Included in principle, but not computed so far.	To be investigated.
Diocotron Growth of Noise Away from Cathode	Included.	Included.

SECTION IX

THREE-DIMENSIONAL POTENTIAL CALCULATION IN THE RW-620 GUN

As the initial stage of the three-dimensional analysis of the RW-620 gun, the charge-free solution shows the shielding effect of the grid wires along the cathode.

A. Mesh Generation

A three-dimensional mesh is set up to fit the electrode and grid boundaries of the RW-620 gun in the following manner.

First, the two-dimensional triangular mesh is generated as Section III describes (see Figure 5). Next, this mesh is projected on each of several planes perpendicular to the magnetic field, with the mesh triangles constrained to match the grid wires and projected from one plane to the next. There is one such plane on each face of a grid wire and two in the space between the grid wires. The boundary potentials over the gaps between the plate and end hats, and between the end hats and the cathode, are linearly interpolated. Since the gun is symmetric about its midplane perpendicular to the magnetic field, the solution need only be computed for one half of the gun.

B. Potential Solution

In three dimensions, Poisson's equation is given by

$$\nabla^2 V = -S(x,y,z) \quad . \qquad (1)$$

A mesh point o has six neighbors, (i=1,···, 6) in the y-z plane (Figure 7) and two neighbors (j+1, j-1) in the x-y plane (Figure 36). The difference equations, derived below, are solved by successive overrelaxation. Taking the volume integral of both sides of Equation 1 and applying the divergence theorem, gives

$$\int_A \nabla V \cdot \hat{n} \; da = -\int_\tau S \; dv \quad , \tag{2}$$

here dv = dx dy dz and da = dx dy or dy dz. The term τ is the volume enclosed by A, which consists of the dodecagon shown in Figure 7 between the two planes P_1 and P_2 shown in Figure 36.

An equation relating V_o to V_i can be derived by evaluating the integrals in Equation 2. The result is

$$\sum_{i=1}^{6} W_i (V_i - V_o) + 2 \left[\frac{V_{j+1} - V_o}{(x_{j+1} - x_{j-1})(x_{j+1} - x_o)} - \frac{V_o - V_{j-1}}{(x_{j+1} - x_{j-1})(x_o - x_{j-1})} \right] \sum_{i=1}^{6} a_{i+(1/2)}$$

$$= - \sum_{i=1}^{6} S_{i+1(1/2)} a_{i+(1/2)} \quad , \tag{3}$$

where W_i and $a_{i+(1/2)}$ are defined in Section III. The potential at point o can be found as

$$V_o = \frac{\sum_{i=1}^{6} (W_i V_i + B_i)}{A_o} \quad , \tag{4}$$

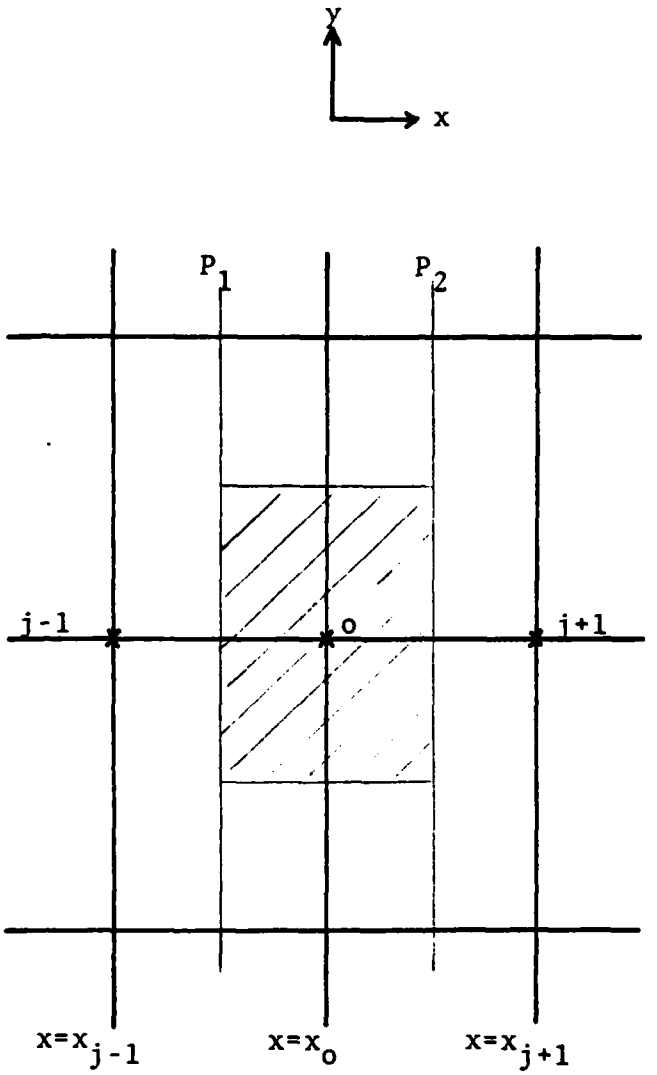

Figure 36. Mesh point o and its two neighbors in x-y plane.

where

$$A_o = \sum_{i=1}^{6}\left[W_i + \frac{2a_{i+(1/2)}}{(x_o - x_{j-1})(x_{j+1} - x_o)} \right] \qquad (5)$$

and

$$B_i = 2a_{i+(1/2)} \frac{V_{j+1}(x_o - x_{j-1}) + V_{j-1}(x_{j+1} - x_o)}{(x_{j+1} - x_{j-1})(x_{j+1} - x_o)(x_o - x_{j-1})}$$

$$+ S_{i+1(1/2)}\, a_{i+(1/2)} \quad . \qquad (6)$$

Numerically, V_o of the (n+1)th iteration can be computed from V_i and V_o of the nth iteration. Therefore, we have

$$V_o^{n+1} = V_o^n + \alpha\left(V_o^{n+1} - V_o^n\right)$$

$$= V_o^n + \alpha\left[\frac{\sum_{i=1}^{6}\left(W_i V_i^{n,n+1} + B_i\right)}{A_o} - V_o^n\right] \quad , \qquad (7)$$

where α is the overrelaxation parameter and n is the number of relaxation steps. $V_o^{n,n+1}$ represents V_i^n, or V_i^{n+1} if it already has been calculated.

The residual is defined as

$$G = \frac{\sum_{i=1}^{6}\left(W_i V_i^{n,n+1} + B_i\right)}{A_o} - V_o^n \quad . \qquad (8)$$

C. Results

The computed equipotentials are shown in Figures 37, 38, and 39. Figures 37 and 38 are views in the magnetic-field direction in planes containing a grid wire (Figure 37) and between two grid wires (Figure 38). Figure 39 is a cross section perpendicular to the grid wires, 0.1" from the rear end of the emitting cathode surface, showing the right end hat and looking in the beam-drift direction. Note that the first five equipotentials above the cathode are at 100 V intervals and the remainder are at 500 V intervals up to 3,000 V. The plate voltage is 4,000 V. The grid is at the cathode potential (0.0 V).

These results show the following.

(1) The mesh interval normal to the cathode is 0.046 mm, small enough relative to the grid height of 0.203 mm for good resolution of the electric field. This result demonstrates the power of the deformable-mesh analysis for a complex electrode shapes.

(2) The nonuniform field due to the end hats is mainly to the right of the grid box and is expected to have a negligible effect on the beam. This result implies that the three-dimensional beam motion in a uniform magnetic field can be computed with a reflecting boundary condition for the motion in the magnetic-field direction and Neumann boundary conditions for the potential. Treating only a single grid wire will provide a considerable saving of computer time.

(3) The grid wires mask a portion of the cathode greater than their area parallel to the cathode by making the electric field zero between the wires and the cathode surface. There are 14 wires each 7.87×10^{-2} mm broad, and the total emitter width of 10.19 mm is halved if the wires mask 4.6 times their area.

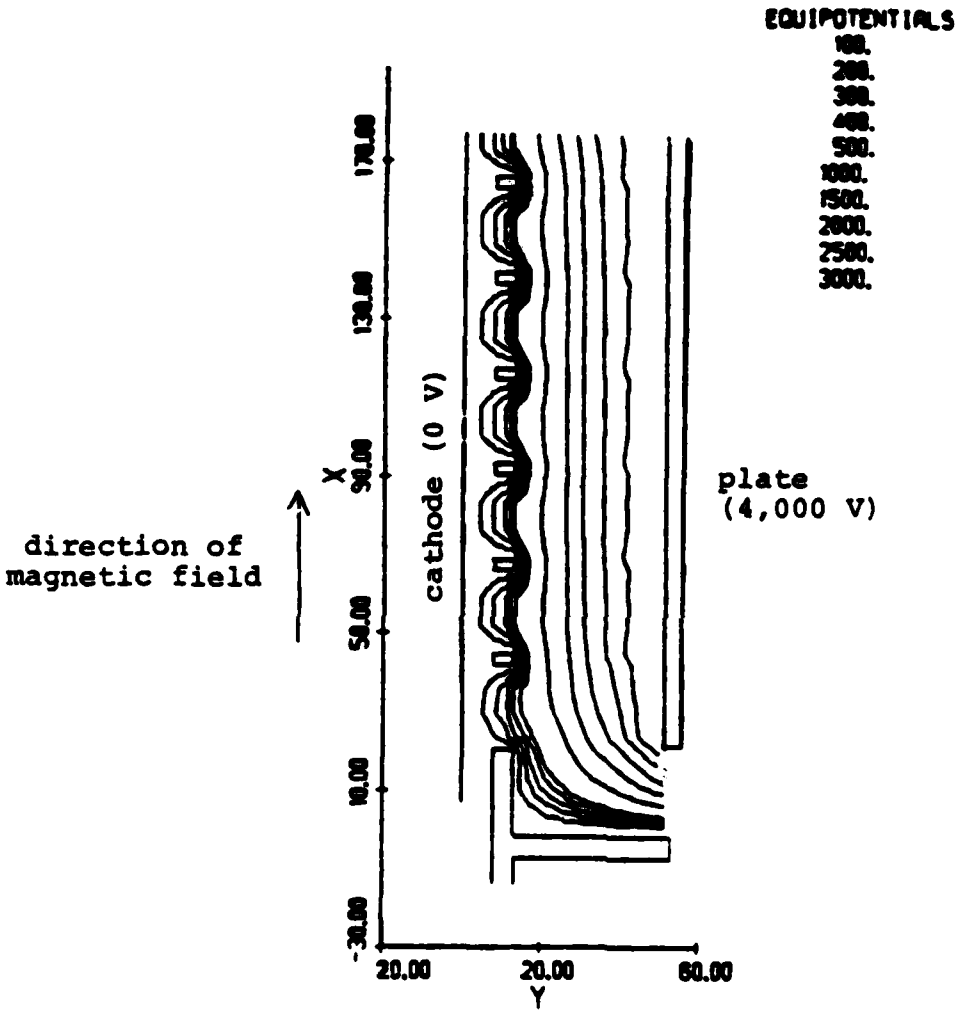

Figure 37. Equipotentials in RW-620 without space charge viewed in beam-drift direction .1 inch from end of emitting surface.

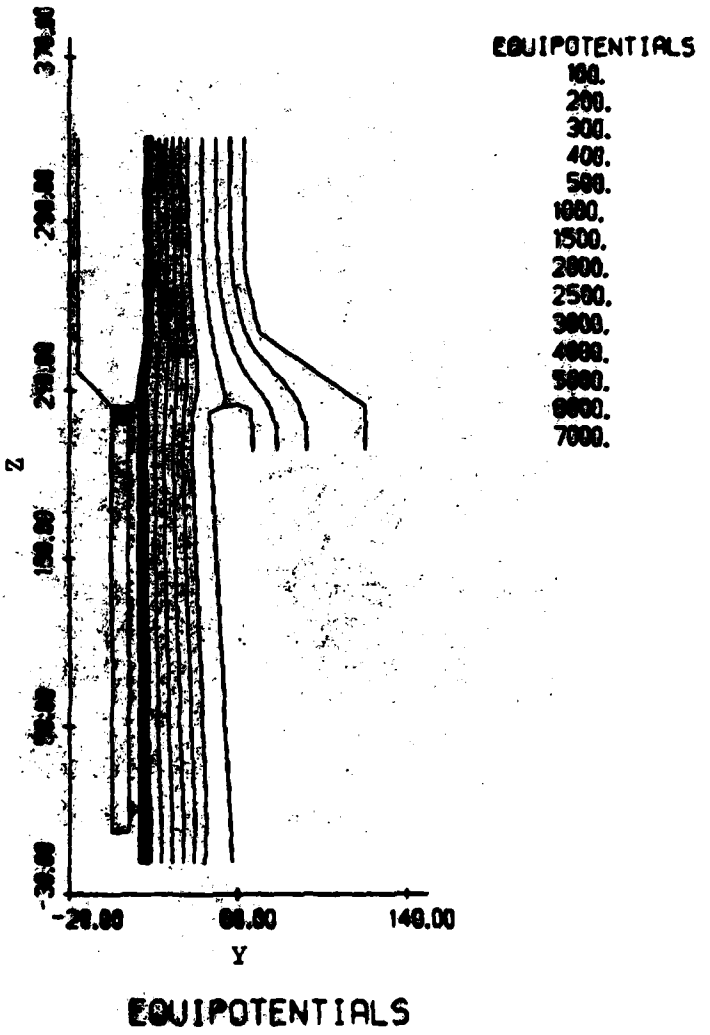

Figure 38. Laplace equipotentials in RW-620 gun viewed in magnetic-field direction in a plane containing a grid wire.

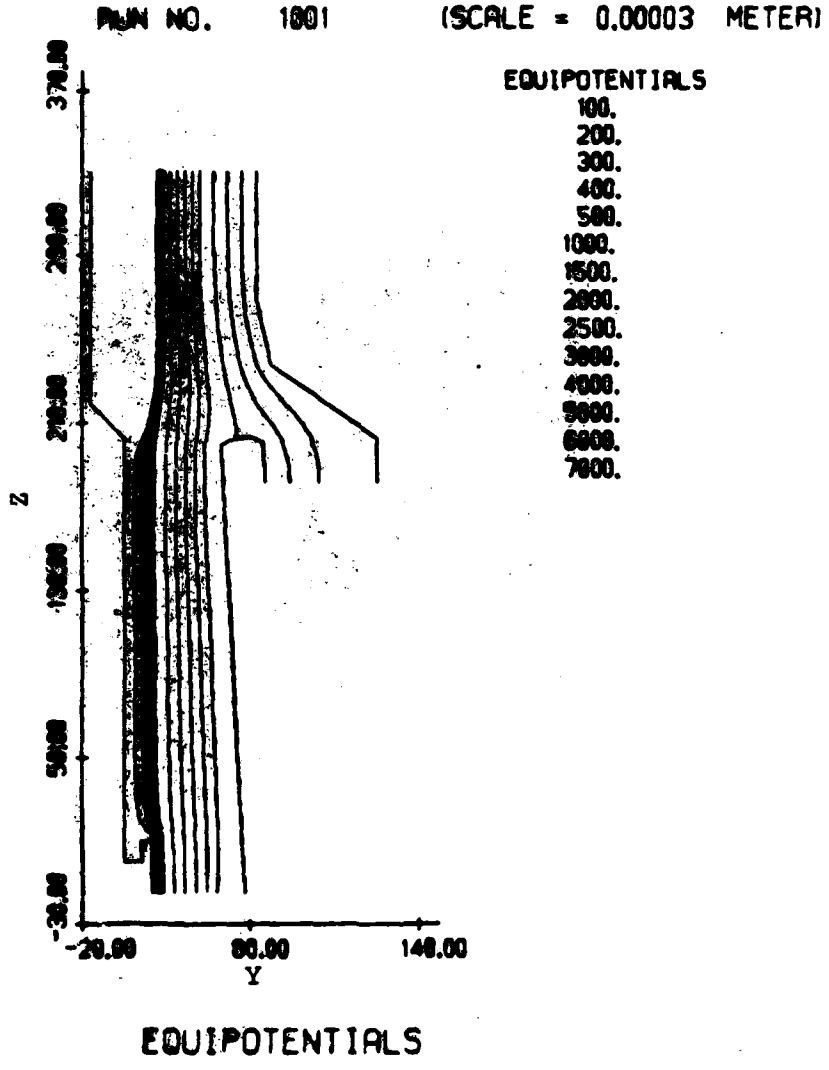

Figure 39. Laplace equipotentials in RW-620 gun viewed in magnetic-field direction between two grid wires.

(4) Between the grid wires, the electric field decreases toward the surface and is less than it would be in the absence of a grid.

(5) The width of the uniform field region above the grids and away from the end hats is about 7.8 mm, two grid wire pitches less than the cathode emitter width. In the anode-sole region, the width of the positive potential region confining the beam was previously estimated at 7.3 mm.[7] Hence, some inward focusing in the magnetic-field direction is expected between the gun and the anode-sole region.

SECTION X

DYNAMIC SIMULATION RESULTS FOR THE RW-620 LONG-CATHODE GUN

This section describes the results of two dimensional dynamic simulations of the RW-620 electron gun. One objective was to test the cathode emission model by determining the RW-620 beam current in the two-dimensional case. Appendix A gives the details of the gun and lists the measured results which should be reproduced in these and future simulations. Here, the gun dimensions are taken for tube model 59242. The magnetic field is 0.25 T throughout the present calculations.

A. Currents and Beam Profiles

The measured and computed currents from three models are compared in Table 10. The time-varying model gives the closest agreement. However, all three currents from these two-dimensional computer models appear to be high. It is expected that the grid will shield less of the cathode surface at the higher plate voltages. Therefore the effective cathode width is probably greater than the assumed 4.5 mm at the higher voltages, and the estimates of 111 A/m and 333 A/m for the current per meter width are then too high for the actual measured currents of 0.5 and 1.5 A. Straightforward modifications to the trajectory calculation will reduce the computed current.

The beam profiles obtained from the instantaneous trajectory segments (Figures 40-43) show how increasing the plate voltage from 2,500 V to 4,500 V controls the cathode current. If the currents per unit width emitted from the cathode are less than computed here, the beams will appear proportionately thinner, in the line-sole direction (at the top of each plot).

TABLE 10

CATHODE CURRENTS FROM TWO-DIMENSIONAL MODELS OF

RW-620 CROSSED-FIELD GUN

Plate Voltage (V)	Computed Current (A/m) Per Meter Width in Magnetic-field Direction				Measured Beam Current (A)	Measured Current Per Meter Width Assuming an Effective Cathode Width of 4.5 mm
	Brillouin (Rear of cathode)	Brillouin (Front of cathode)	Static Particle Model	Time-Varying Particle Model		
2,500	120	247	152	92	0.15	33
3,500	266	722	538	166	0.5	111
4,500	515	1,503 (above cutoff)	341	309	1.5	333

Magnetic Field 0.25T
Cathode width 10.19 mm
Cathode width minus grid width 9.0 mm
Actual beam width not known.

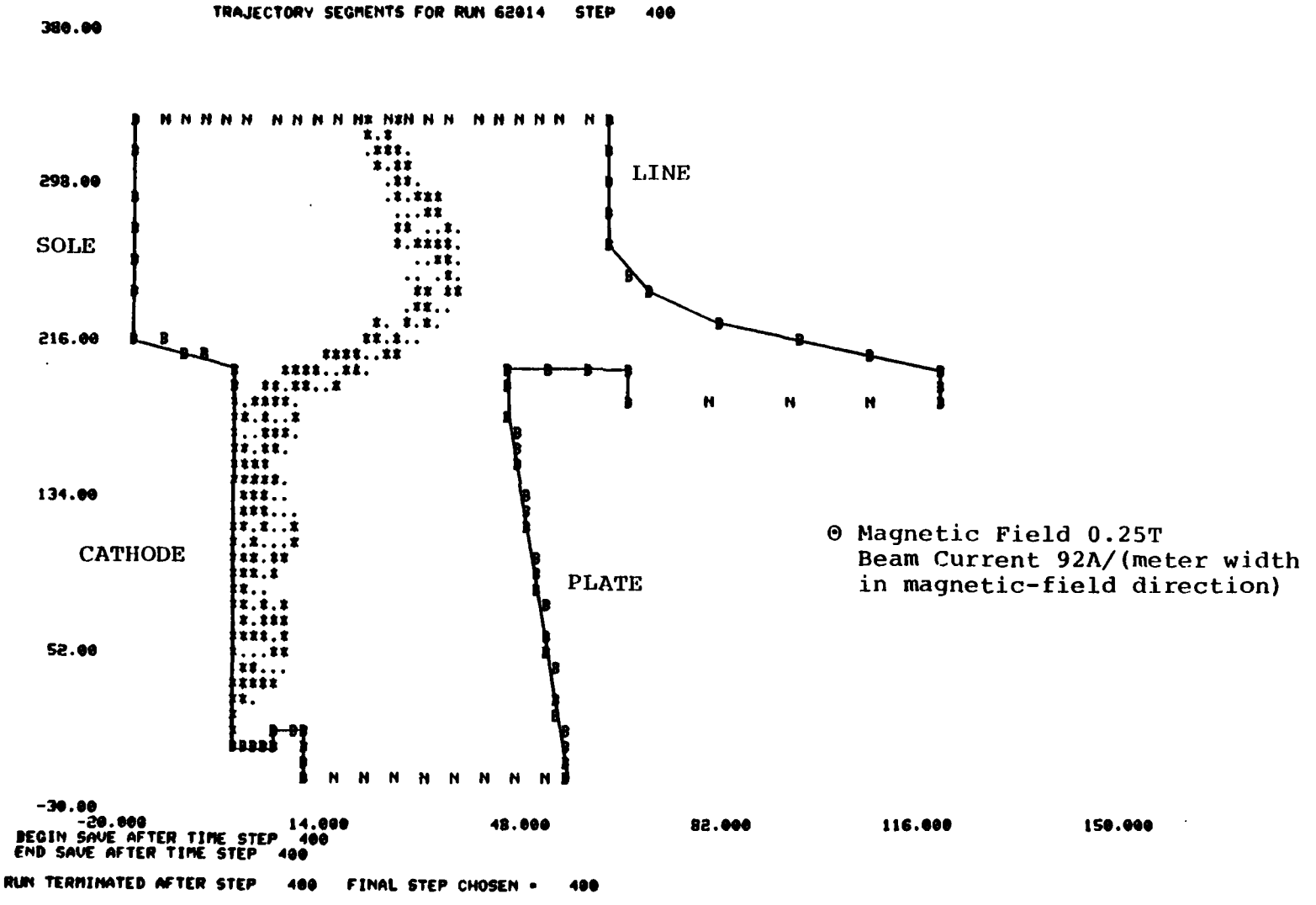

Figure 40. Dynamic 2D simulation of RW-620 crossed-field gun; at 2500 V plate voltage.

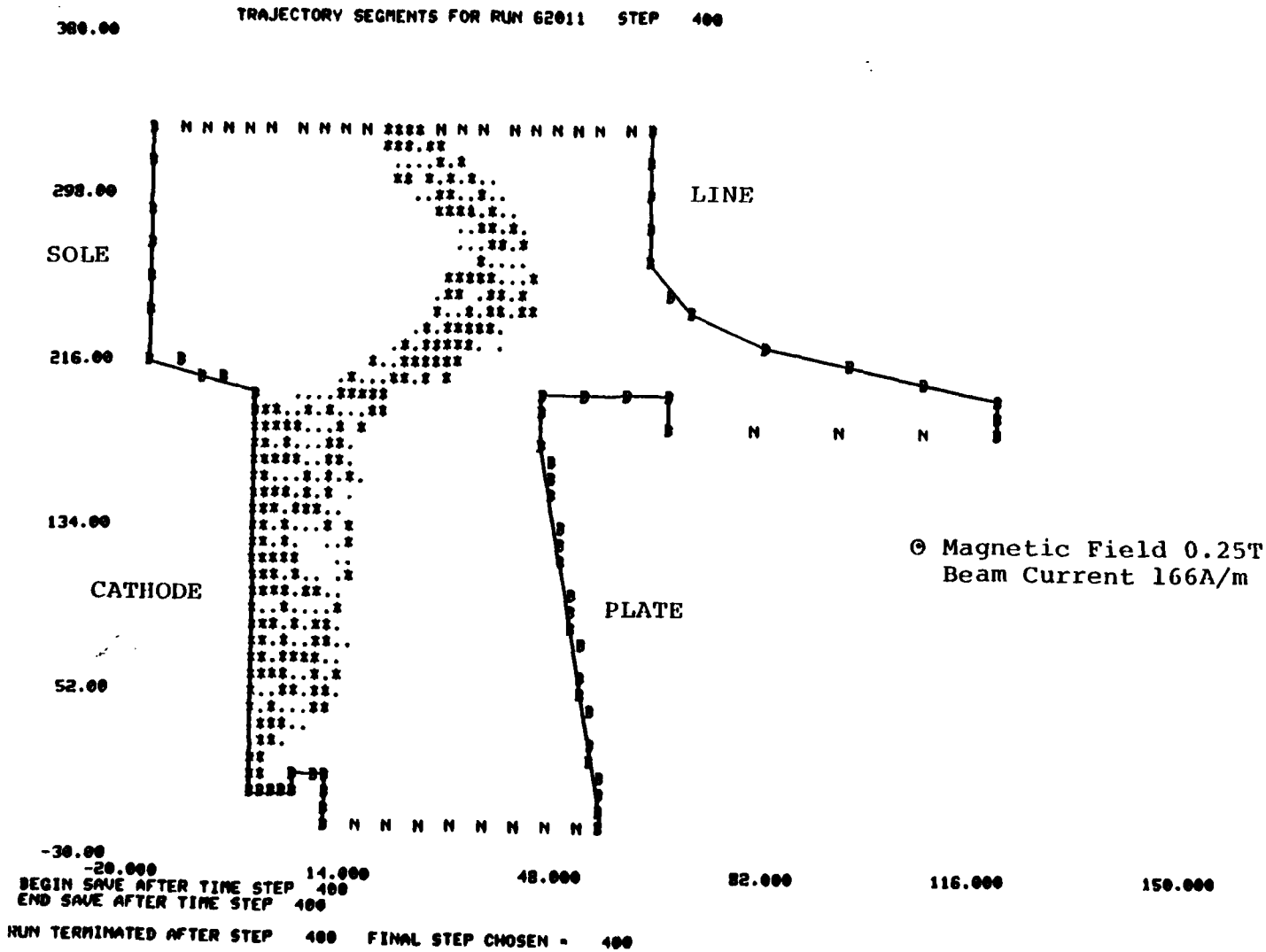

Figure 41. Dynamic 2D simulation of RW-620 crossed-field gun; at 3500 V plate voltage.

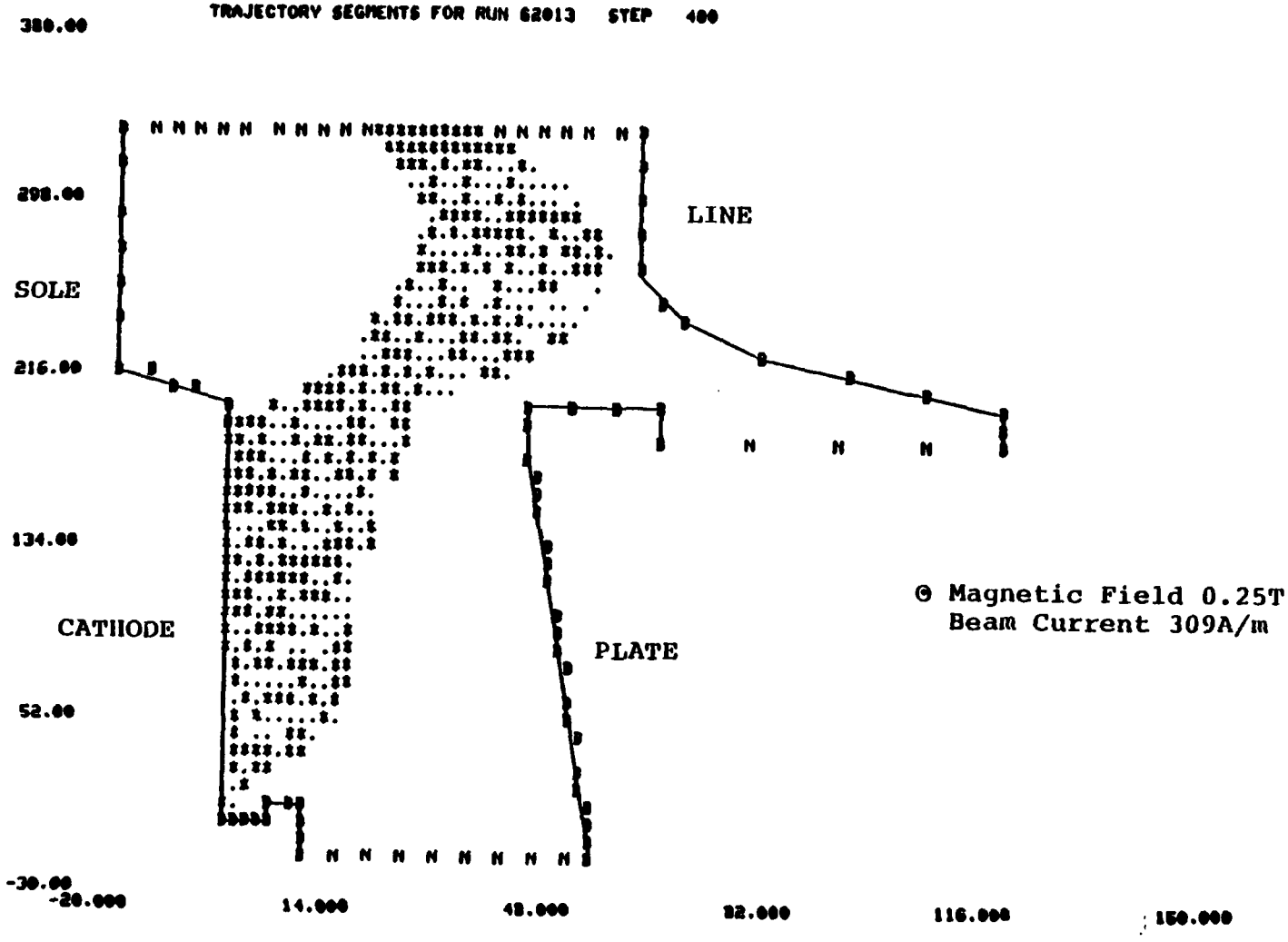

Figure 42. Dynamic 2D simulation of RW-620 crossed-field gun; 4500 V plate voltage.

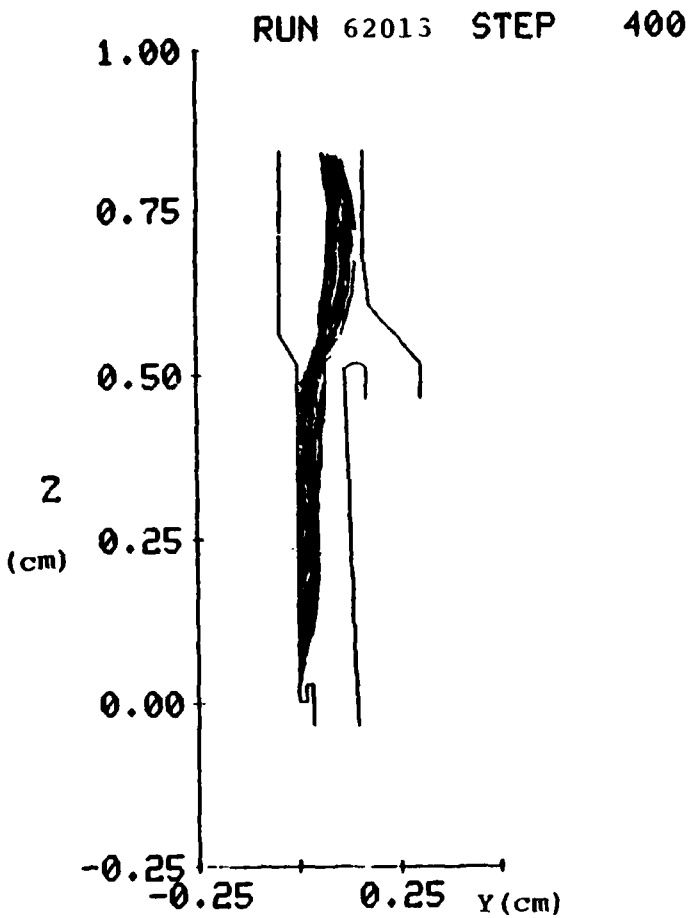

Plate Voltage 4,500V
Magnetic Field 0.25T
Beam Current 309A/(meter width
in magnetic-field direction)

Figure 43. Trajectories plotted from dynamic 2D simulation of RW-620 crossed-field gun.

The numerical results of Table 11 include tests with a varied particle charge and a varied time step. The particle charge of -0.72×10^{-10} C/m corresponds to a density FBRILL=16 particles per mesh rectangle adjacent to the cathode under the Brillouin flow condition, $\omega_p = \omega_c$. Here the number of simulation particles required varies between 1442 (at 2,500 V) and 2723 (at 4,500 V). Ten time steps per cyclotron period give sufficient accuracy.

Three test results are generally consistent. The one anomaly at 2,500 V is removed when the electric field is averaged over two adjacent cathode points to control the cathode emission.

B. Cathode Current Density

The cathode current density (the total emission-limited or space-charge-limited density without subtraction of returning charge) is displayed for the three plate voltages in Figure 44. Seventeen emission points are treated. The minima occur where backbombarding charge increases the local electric field and hence reduces the emission allowed. At 2,500 V there are three peaks and two such minima. At 4,500 V the rear of the cathode (the lower end in Figures 40-43) emits the full thermionic current density of 20 A/Cm^2.

C. Beam Stability

Extending a run from the usual 40 cyclotron periods to 120 cyclotron periods demonstrates (Table 12) that the dynamic equilibrium is reached. In contrast to the static model, this time-dependent model with the macroscopic cathode emission calculation predicts a steady beam current despite the returning charge. In the anode-sole region, the diocotron effect should cause noise to grow by up to 9 dB (at 4,500 V plate voltage) over the 2.9 mm treated here,[7] but this distance is apparently too short to show an instability. There is also no evidence of a feedback instability at the cathode of the type predicted by Ho and Van Duzer.[15]

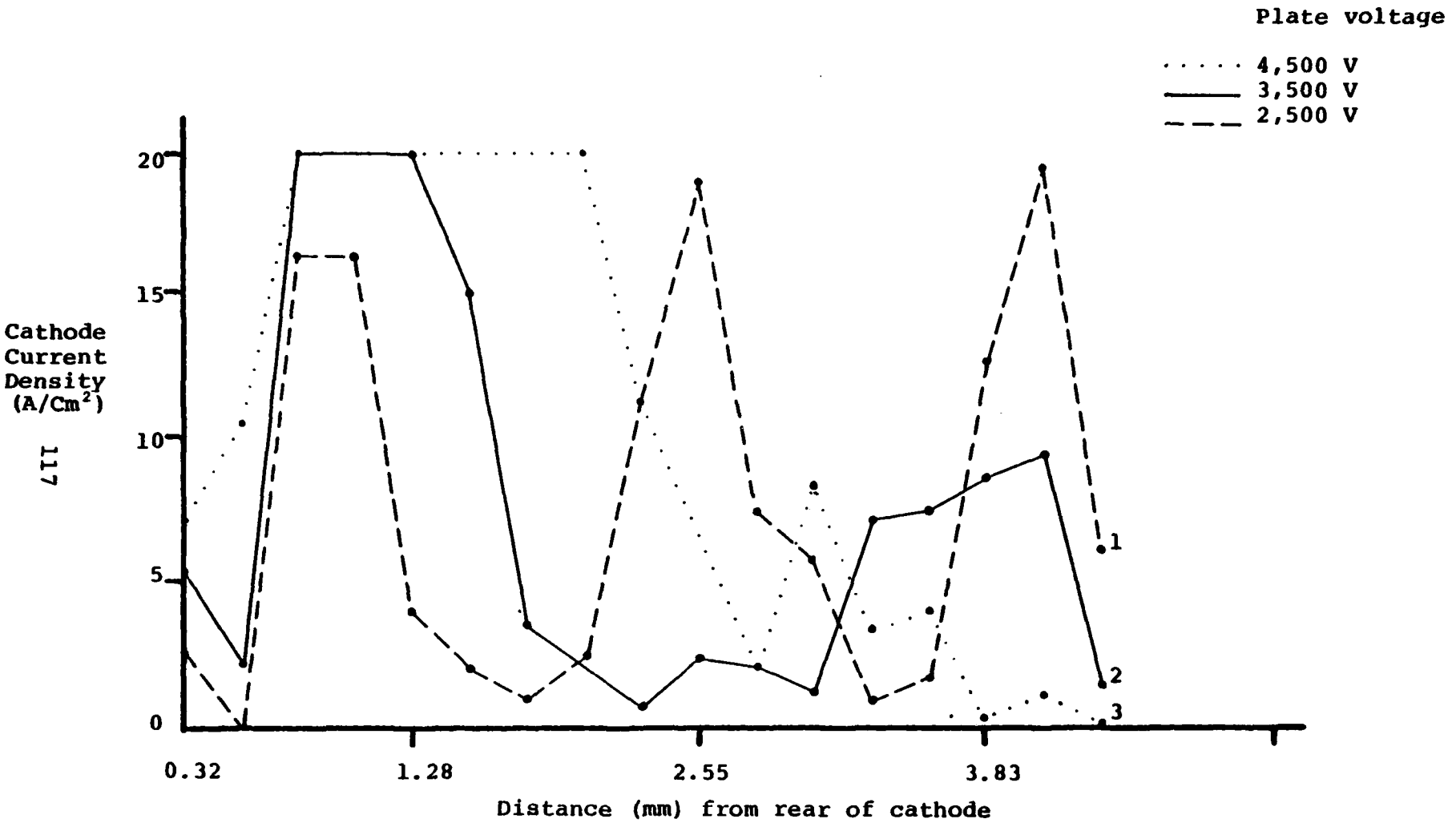

Figure 44. Computed cathode current density in 2D simulation of the RW-620 electron gun.

TABLE 11

DYNAMIC 2D SIMULATION RESULTS FOR RW-620 GUN

Plate Voltage (v)	Charge/rod (C/m)x10^{10}	Time Steps per Cyclotron Period	Emitted Current (A/m)	Returning Current (A/m)	Beam Current (A/m)	Note
2500	-1.43	10	311	240	71	
2500	-0.72	10	240	192	47	Anomalous charge bunch at front of cathode
2500	-0.36	10	298	218	80	
3500	-1.43	10	338	154	183	
3500	-0.72	10	348	167	182	
3500	-0.72	20	352	163	190	
4500	-1.43	10	453	149	305	
2500	-0.72	10	319	225	92	Smoothed field controls emission
3500	-0.72	10	318	151	166	
4500	-0.72	10	439	131	309	

TABLE 12

STEADY-STATE CURRENTS COMPUTED IN RW-620 GUN

Number of Cyclotron Periods	Total Emitted Current (A/m)	Returning Cathode Current (A/m)	Beam Current (A/m)
10	414	182	129
20	347	166	183
30	352	169	182
40	348	167	182
50	350	169	180
60	348	169	179
70	349	169	181
80	348	168	180
90	350	169	183
100	348	168	180
110	349	168	182
120	346	167	179

However, to properly test this hypothesis, a perturbation should be superimposed on the emitted charge.

To quantify an instability with the present gun program, current fluctuations and beam temperature should be computed at three planes: parallel to and above the cathode, at the start of the line-sole region, and at least 3 mm into the line-sole region. The present program includes the code for storing the instantaneous current and particle velocities at these planes, but the noise calculation is not yet implemented. Simple calculations of the average values and mean square fluctuations of current and electron velocity (for a beam temperature) will suffice for the present purpose.

D. Line-Sole Region

In the actual tube, beam currents above about 0.6 A show instability and oscillation. The diocotron effect does not appear in the present deformable-mesh calculations, probably because only 2.8 mm of the sole in included. However, the simulation with the rectangular model of the anode-sole region alone shows beam breakup after about 20 mm. See Figure 45. The beam current per unit width here is only 167 A/m because the 1.5 A current is assumed to cover a 9 mm width. Here an ideal Brillouin beam is injected. The theoretical growth rate for noise is about 1.4 dB/mm. Previous three-dimensional calculations[7], shown in Figures 46 and 47, predicted greater instability because of scalloping between the end hats.

Clearly the beam stability and the observed output noise are affected by the shape of the injected beam at the start of the sole as well as by noise effects produced at the cathode.

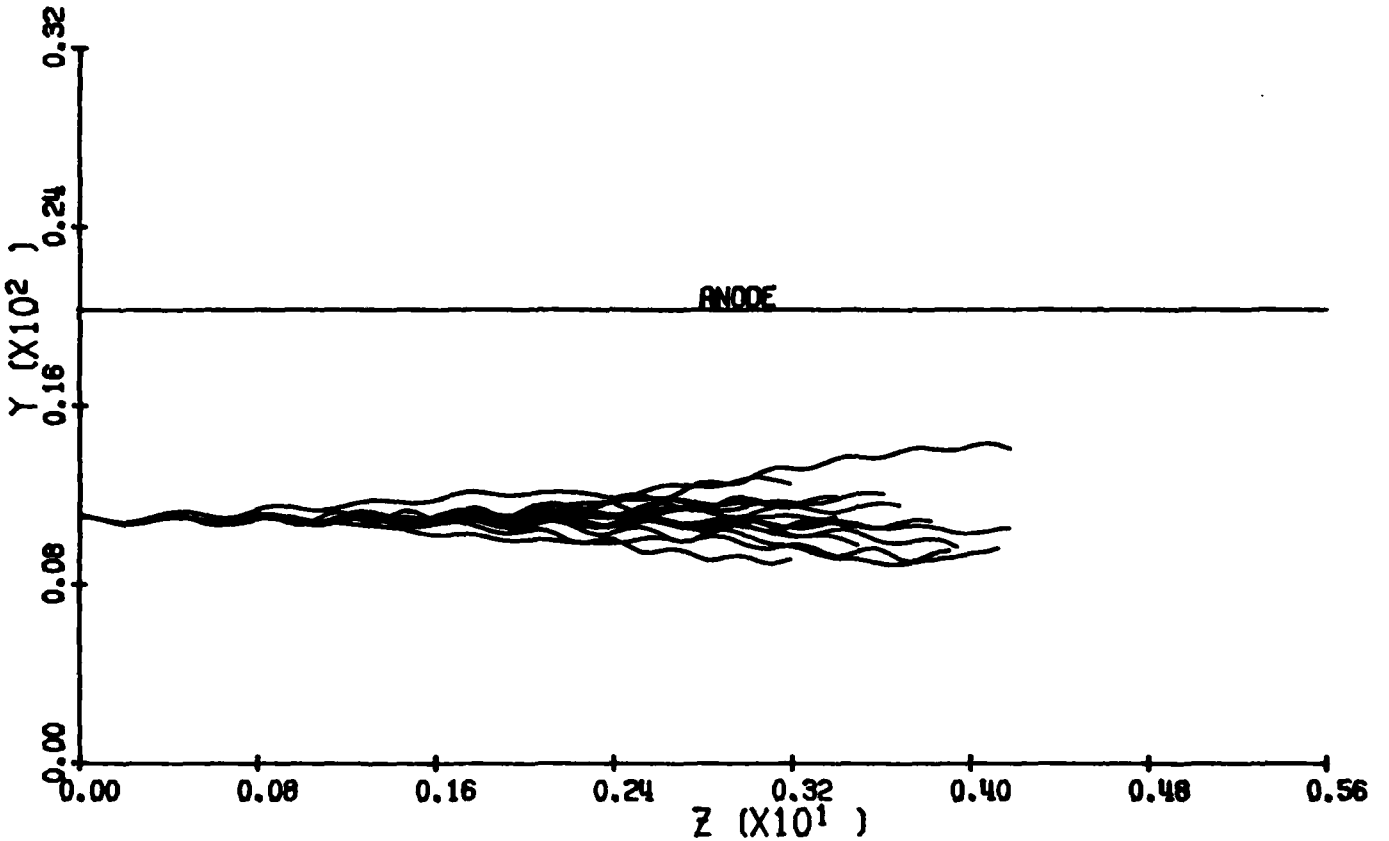

Figure 45. Computed beam profile in the anode-sole direction showing diocotron instability in an IBCFA.

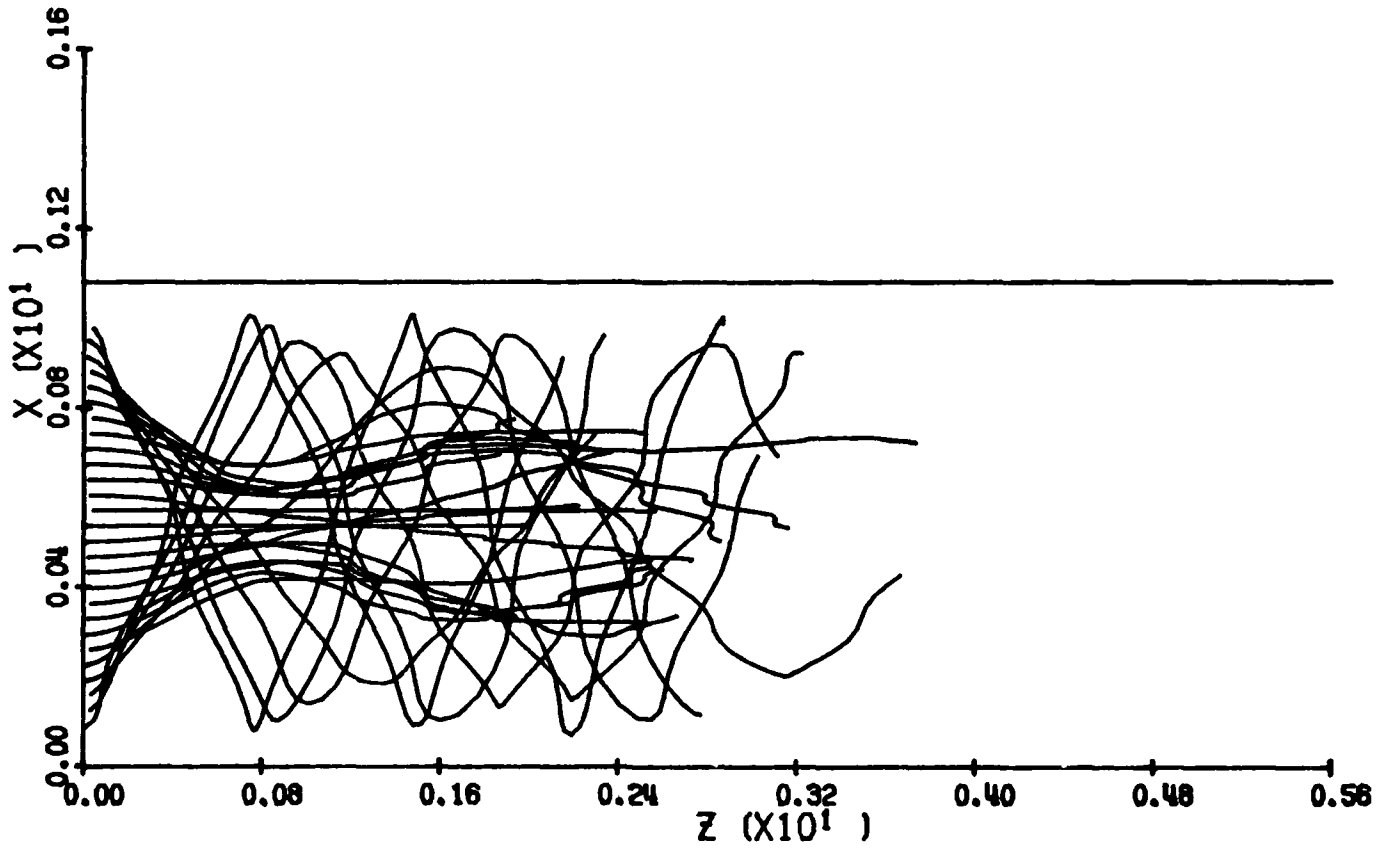

Figure 46. Trajectories viewed from anode in broad unsegmented injected beam (three-dimensional model).

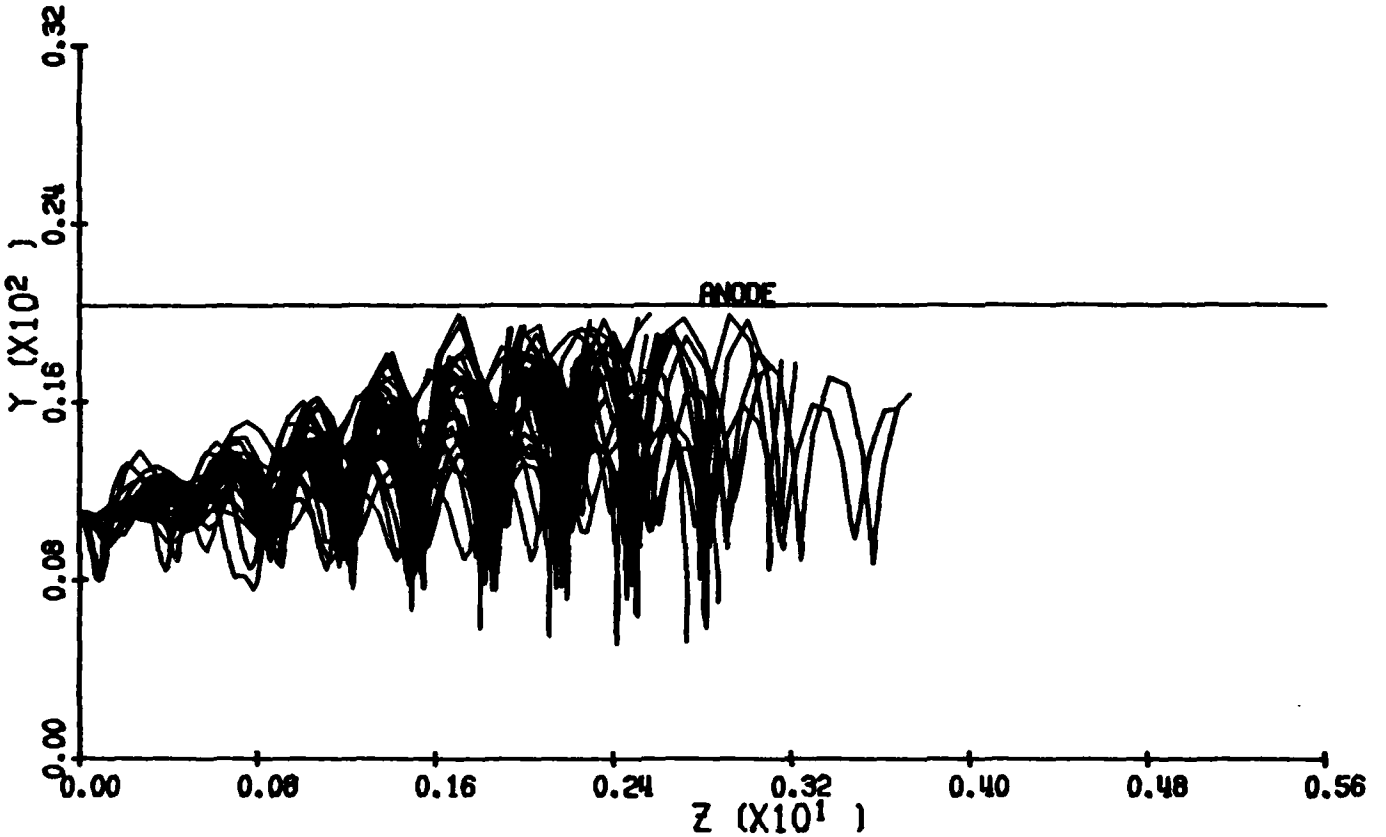

Figure 47. Side view of trajectories in broad unsegmented beam (three-dimensional model).

E. Conclusions From the RW-620 Simulation

These two-dimensional results have confirmed the feasibility of the deformable-mesh model and the macroscopic cathode emission model. Results are consistent as the time step and particle charge are varied. A clear steady state beam develops, both at the cathode with returning charge and in the beam at the exit plane.

Now the full three-dimensional calculation must be developed, since transverse motion and grid shielding effects cannot be neglected in a design study. The following effects in the actual tube should be investigated by computer simulation:

(1) The mechanism by which the focusing anode voltage affects the beam current at a fixed magnetic field;

(2) The degree of cycloiding in the anode-sole region for various sole voltages;

(3) The amount of scalloping in the transverse (magnetic-field) direction;

(4) The effect of the grid in reducing beam cycloiding and anode interception (simulations should be made also without the grid);

(5) The mixing distance for the separate beam filaments created by the grid;

(6) The threshold beam current at which noise output increases as the focusing anode voltage is raised (about 0.3 A measured, compared with an operating 1.5 A);

(7) The effect of the sole voltage on the noise output for a given beam current;

(8) The effect of the grid in improving beam stability;

(9) The effect of the non-uniform magnetic field. (The field at the end hats is about four percent higher than at the center plane.)

In the absence of imposed noise signals, no instability appears at the cathode in present calculations. Next, however, noise currents should be added at the cathode, initially in the 2D model, and then in the 3D model, to determine the effects of fluctuations in the returning charge at points along the surface from the emission. If excess noise is obtained, the 3D calculations should be repeated with a component of magnetic field normal to the cathode surface.

The 8.4 mm length of the gun covered by the present mesh includes 2.9 mm of the line-sole region. This is sufficient for an efficient computation of the beam current and noise growth in the gun region. However, selected 2D and 3D calculations should then be extended to about 20 mm along the sole to determine the beam stability and reproduce the transverse scalloping in that region. This would require about nine times as much computing time as at present.

SECTION XI

GENERAL CONCLUSIONS AND RECOMMENDATIONS FOR FURTHER WORK

The time-dependent analysis of the injected-beam crossed-field amplifier gun with the deformable-mesh potential calculation and realistic boundary shapes has been established as feasible for use in future design studies. The newly implemented macroscopic model of cathode emission produces a stable beam and is particularly well suited to a gridded-gun configuration.

Inclusion of shot noise in this model may help to resolve the continuing controversy about the causes of beam instability at a long cathode. The existing analytical theories are apparently not sufficiently general to include all the charge that returns to the cathode.

Extension to a three-dimensional model now requires only techniques already established in this study. The three-dimensional model can be verified using the detailed experimental results obtained for the RW-620 gun. The program will then be a practical design tool for improving existing injected-beam crossed-field guns.

REFERENCES

1. E. Okress (Ed.), Crossed-Field Microwave Devices, vol. 1, Academic Press, New York; 1961.

2. E. K. Shaw and G. P. Kooyers, "Computer-Aided Design of Electron Guns for Injected-Beam Crossed-Field Amplifiers," IEEE Trans. Electron Devices, vol. ED-26, No. 7, pp. 1100-1102; July 1979.

3. G. P. Kooyers and E. K. Shaw, "The Study of Noise Phenomena in Crossed-Field Electron Beams," Interim Scientific Report, Feb. 15, 1977-Feb. 15, 1978, Contract F49620-77-C-0061, prepared for Air Force Office of Scientific Research by UCA Systems Inc., Palo Alto, CA; April 10, 1978.

4. G. P. Kooyers and E. K. Shaw, "Noise Phenomena in Crossed-Field Electron Beams," Annual Technical Report, Feb. 15 1978-Feb. 15, 1979, Contract F49620-77-C-0061, prepared for Air Force Office of Scientific Research by UCA Systems Inc., Palo Alto, CA; April 1, 1979.

5. R. B. True, "Crossed-Field Guns Analyzed on a Deformable Mesh," Tech. Digest, IEEE International Electron Devices Meeting, Washington, D.C.; 1978.

6. S. G. Lele and J. E. Rowe, "Transport of Noise Fluctuations in Convergent Flow Crossed-Field Electron Guns," IEEE Trans. Electron Devices, vol. ED-16, No. 3, pp. 261-277; March 1969.

7. D. M. MacGregor and J. E. Rowe, "Computer Simulation of Transverse Effects in the Injected-Beam Crossed-Field Amplifier," Final Report, Purchase Order 63908, Prepared for Northrop Corporation Defense Systems Department, Des Plaines, IL by Shared Applications, Inc., Ann Arbor, MI; September 1977.

8. A. T. Drobot, "Simulation Techniques for Self-Consistent Treatment of Electron Dynamics in High Power Microwave Tubes," Technical Digest, IEEE International Electron Devices Meeting, Washington D. C., pp. 633-665; December 1979.

9. R. B. True, "Space-Charge-Limited Beam Forming Systems Analyzed by the Method of Self-Consistent Fields With Solution of Poisson's Equation on a Deformable Mesh," Dissertation, University of Connecticut; 1968. (Available through University Microfilms, Ann Arbor, MI.)

10. A. M. Winslow, "Numerical Solution of the Quasilinear Poisson Equation in a Nonuniform Triangle Mesh," J. Computational Physics, vol. 1, No. 2, pp. 149-152; Nov. 1966.

11. K. Chang, P. F. McGuire, F. Rose, J. E. Rowe and J. E. Stevens, "Three-Dimensional Analysis of TWT Guns," Final Report AFAL-TR-79-1201 for Air Force Avionics Laboratory Contract No. F33615-77-C-1117, Harris SAI, Inc., Ann Arbor, MI; December 1979.

12. G. Dohler, "Beam Injection Control in Broad-Band Crossed-Field Amplifiers," Tech. Digest, IEEE International Electron Devices Meeting, Washington, D. C.; 1974.

13. R. J. Espinosa and R. R. Moats, "Broad-Band Injected-Beam Crossed-Field Amplifiers," IEEE Trans. Electron Devices, vol. ED-24, No. 1, pp. 13-21; January 1977.

14. N. S. Nicholls, L. Damon, and B. P. Scoffield, "Reduction of Noise in High-Power Crossed-Field Amplifiers," Electronics Letters, vol. 9, No. 17, pp. 398-399; August 23, 1973.

15. R. Y. C. Ho and T. Van Duzer, "The Effects of Space Charge on Shot Noise in Crossed-Field Electron Guns," IEEE Trans. Electron Devices, vol. ED-15, No. 2, pp. 75-84; February 1968.

16. K. J. Harker and F. W. Crawford, "Noise in Planar Crossed-Field Guns - I: Theory," IEEE Trans. Electron Devices, vol. ED-26, No. 10, pp. 1623-1633; October 1979.

17. K. J. Harker and F. W. Crawford, "Noise in Planar Crossed-Field Guns - II; Numerical Solution," IEEE Trans. Electron Devices, vol. ED-26, No. 10, pp. 1634-1641; October 1979.

18. I. P. Shkarofsky, "Velocity Noise in a Crossed-Field Planar Diode," Int. J. Electronics, vol. 47, No. 1, pp. 17-40; July 1979.

19. M. Chodorow and C. Susskind, Fundamentals of Microwave Electronics, McGraw-Hill, New York; 1964.

20. M. A. Pollack and J. R. Whinnery, "Noise Transport in the Crossed-Field Diode," IEEE Trans. Electron Devices, vol. ED-11, No. 3, pp. 81-89; March 1964.

21. P. A. Lindsay and G. D. Sims, "Electron 'Temperature' in Crossed-Fields," J. Electronics and Control, vol. 14, No. 3. pp. 273-288; March 1963.

22. G. Smol, "A Study of Electron Flow in Crossed-Field Diodes with Plane Cathodes," Ph.D. Thesis, University of London; March 1971. (Available Through University Microfilms, Ann Arbor, MI.)

23. K. Halbach and R. F. Holsinger, "SUPERFISH - A Computer Program for Evaluation of RF Cavities with Cylindrical Symmetry," Particle Accelerators, vol. 7, pp. 213-222; 1976.

24. J. E. Boers, "Digital Computer Simulation of Crossed-Field Electron Guns," IEEE Trans. Electron Devices, vol. ED-17, No. 4, pp. 373-377; April 1970.

25. J. C. Slater, Microwave Electronics, Van Nostrand, New York; 1950.

26. N. A. Masnari, "Investigation of Convergent Laminar Flow in Crossed-Field Guns," Technical Report No. 80, Electron Physics Laboratory, The University of Michigan, Ann Arbor, MI; November 1964.

27. N. A. Masnari and J. E. Rowe, "Investigation of a Convergent Flow Crossed-Field Gun," International Journal of Electronics, vol. 19, No. 14, pp. 343-359; October 1965.

28. D. E. Radley, D. Dirmikis, and A. B. Birtles, "High-Accuracy Cathode-Current Calculations in Computer Simulation of Electron Guns," Proc. IEE (London), vol. 122, No. 6, pp. 620-624; June 1975.

29. D. E. Radley and A. B. Birtles, "Approximate Solutions to the Electron-Flow Equations," Int. J. Electronics, vol. 21, No. 5, pp. 465-477; 1966.

30. T. Van Duzer and J. R. Whinnery, "High-Frequency Behavior of the Crossed-Field Potential Minimum," IRE Trans. Electron Devices, vol. ED-8, pp. 331-341; July 1961.

31. C. K. Birdsall and W. B. Bridges, Electron Dynamics of Diode Regions, Academic Press, New York; 1966.

32. R. Y. C. Ho and T. Van Duzer, "Approximate Formulas for Crossed-Field Potential-Minimum Parameters," IEEE Trans. Electron Devices, vol. ED-15, No. 2, pp. 70-74; February 1968.

33. P. A. Lindsay, "General Steady State Theory of Linear Magnetrons II," J. Electronics and Control, vol. 17, No. 1, pp. 67-79; July 1964.

34. R. P. Wadhawa and J. E. Rowe, "Monte Carlo Calculation of Noise Transport in Electric and Magnetic Fields," IEEE Trans. Electron Devices, vol. ED-10, No. 6, pp. 378-388; November 1963.

APPENDIX A

THE RW-620 INJECTED-BEAM CFA

A. Introduction

The RW-620 is a grid-controlled high power (3 to 5 kW) octave bandwidth (4 to 8 GHz) IBCFA manufactured by Northrop Corporation. It can be operated in either continuous-wave (CW) or pulse modes with RF output programmable over a 10 dB range by varying the grid-to-cathode voltage. The high efficiency (20 to 30 percent), high gain (20 to 22 dB), and the high power-to-weight ratio and compact construction of the RW-620 make it suitable for airborne systems.

The RW-620 was chosen as suitable for testing of the computer simulations being developed by Harris SAI. Under a subcontract (No. 009482) from Harris SAI, Northrop has provided the tube dimensions and performance characteristics (beam current, noise, and RF output for varied electrode voltages and magnetic field). A copy of Northrop's report is provided in Appendix B.

B. Tube Dimensions

The important dimensions of the RW-620 gun, transition, and anode-sole regions are shown in Figures A1, A2 and A3. Figure A1 shows a cross section containing a grid wire. Figure A2 is a cross section of the gun in which the magnetic field is directed from left to right. Figure A3 shows the end hats that confine the beam in the magnetic-field direction. Each grid wire is made in two sections to prevent buckling. The gap in the wire is, however, ignored in the computer simulation.

The RF circuit consists of 97 bars, each of width 0.016" (along the beam-drift direction) and spacing 0.0118". They are

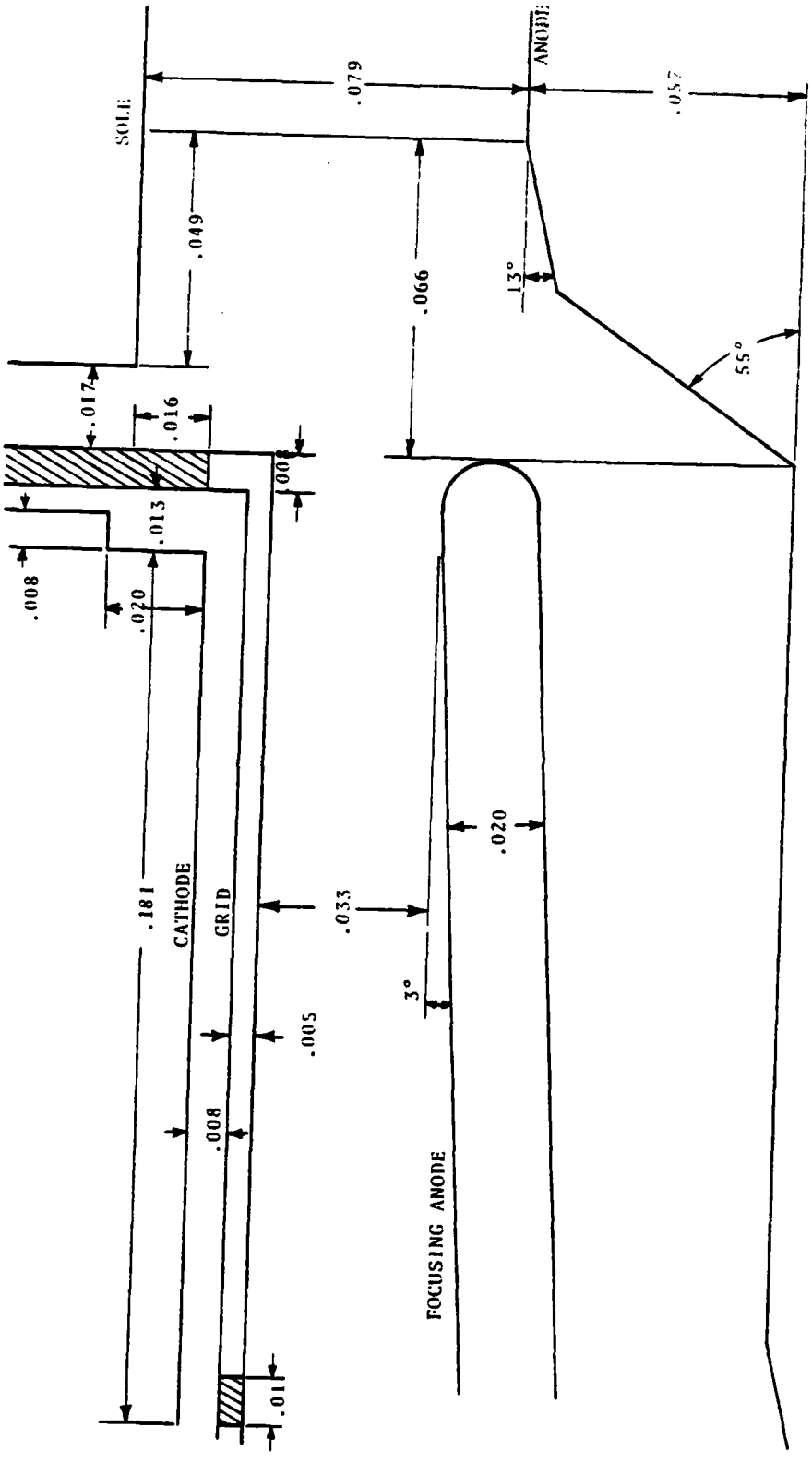

Figure A1. Electron gun for RW-620 IBCFA, viewed in magnetic-field direction. (all dimensions in inches)

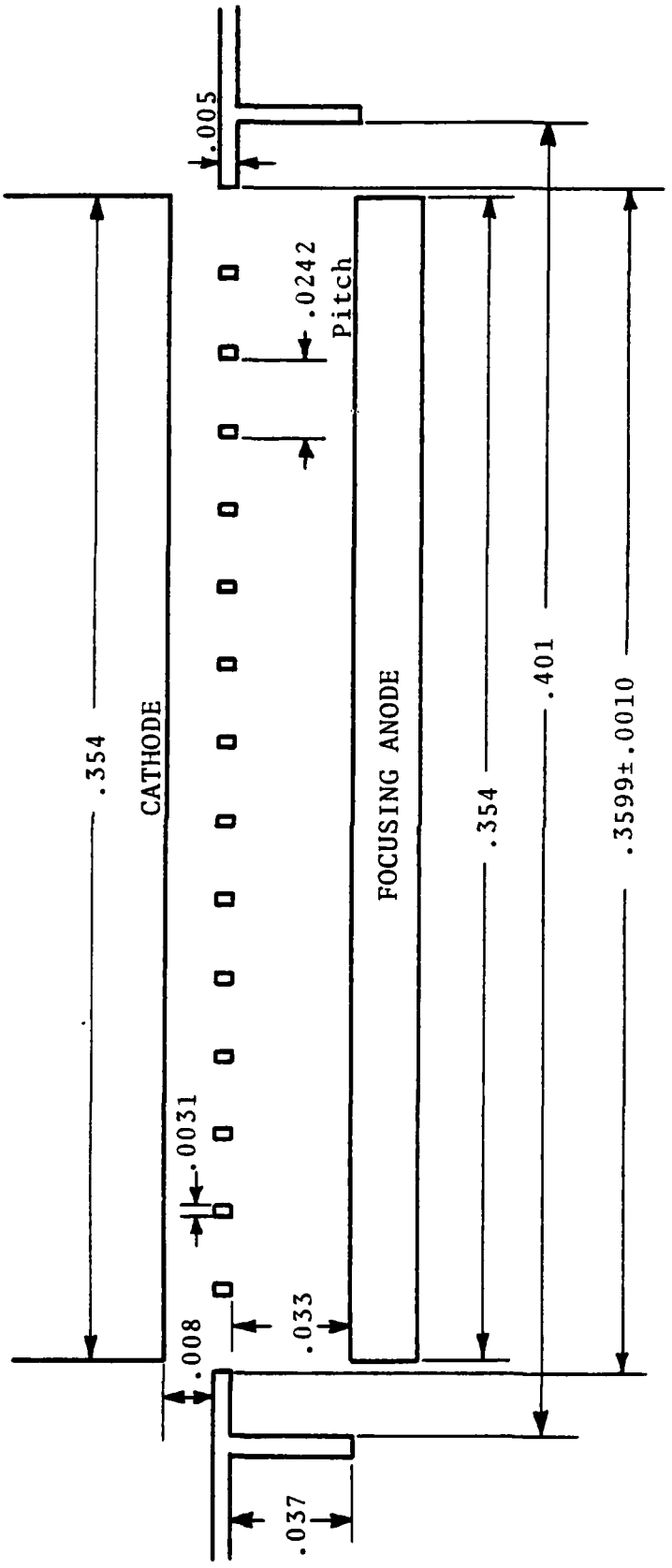

Figure A2. Electron gun for RW-620 IBCFA, viewed in beam-drift direction (all dimensions in inches)

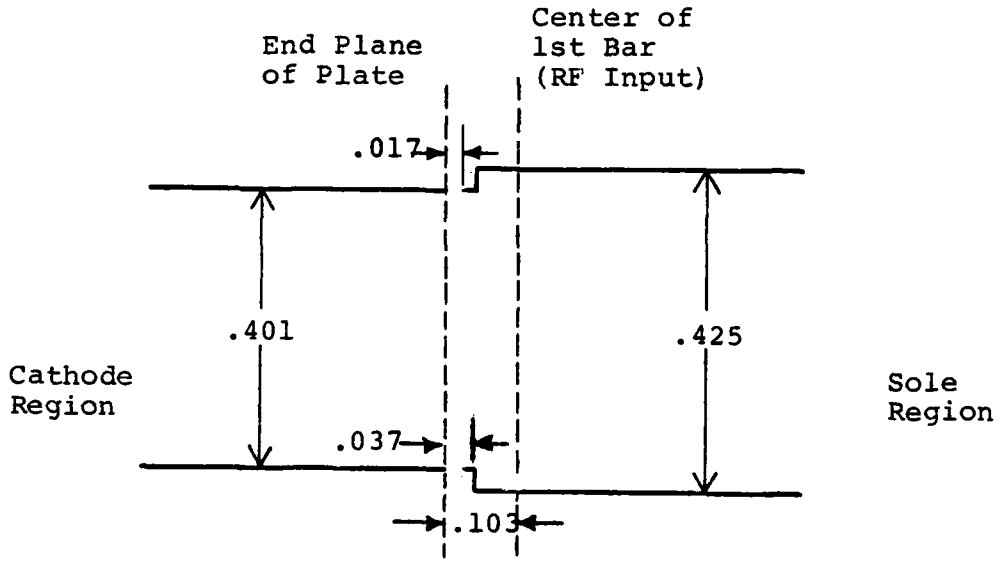

Figure A3. End hats for RW-620 IBCFA at front of gun, as viewed from anode. (All dimensions in inches.)

joined at alternate ends to form a meander line of pitch 0.0556" and total length 2.685" (68.2 mm).

Because of the limits of accuracy in tube production, the precise dimensions of the tube vary with the actual model used. The spacing of the focusing anode and the grid has the most significant effect on the beam current. The variations in this distance are given for four tubes in Table A1.

C. Additional Information

The following additional details of the RW-620 were supplied by Northrop.

(1) In all tube models, the cathode, grid, accelerating anode (plate), sole, and line anode (RF circuit) are electrically isolated and may be at different potentials.

(2) In addition, tube 59242 had an isolated collector when the measurements were made.

(3) The end hats are at the grid potential in the cathode region and at the sole potential in the anode-sole region.

(4) The cathode is an 80 percent dense tungsten matrix impregnated with barium and calcium carbonates and aluminum oxide. It operates at about 1,200° C to produce a thermionic current density of between 10^4 A/m^2 and 2 x 10^4 A/m^2.

(5) As a result of the differences in the grid-plate spacing, the measured current-voltage characteristics differ in different tubes. For example, the beam currents in tubes 59242, 59505, and 59506 are 0.35 A, 0.30 A, and 0.4 A, respectively, at a plate voltage of 2.9 kV and a magnetic field of 0.26 T.

(6) In the absence of RF drive, the maximum beam current without oscillation was observed as about 400 mA in tube 59242 (with isolated line and collector) and 600 mA in the other tubes (with the line and collector connected).

TABLE A1

SPACINGS OF GRID AND FOCUSING ANODE AT

FRONT OF IBCFA GUN IN FOUR PRODUCTION TUBES

Tube Number	Spacing of Grid and Focusing Anode
59242	Between .0328" and .0330"
59505	Between .0331" and .0332"
59506	Between .0316" and .0317"
59508	Between .0325" and .0334"

(7) The noise output in the absence of RF drive is very sensitive to the sole voltage. For example, the noise power measured at the RF input position varies from 1.4 mW to 0.05 mW as the sole voltage is varied between -4.65 kV and -4.8 kV with a fixed beam current of 0.35 A.

D. Operating Points for Computer Simulation

Table A2 shows operating points selected from Northrop's report as suitable for testing the computer model.

TABLE A2

SELECTED OPERATING POINTS FOR THE RW-620 GUN

Tube Number	Magnetic Field (T)	Plate Voltage (V)	Line Voltage (V)	Sole Voltage (V)	Grid Voltage (V)	Measured Beam Current (A)	Purpose of Simulation	Figure numbers in Northrop report (Appendix B)
59242	0.25	2,500	7,000	-4,800	0.0	0.15	Vary plate voltage; compare static and dynamic models	Earlier measurements (December 21, 1977)
59242	0.25	3,500	7,000	-4,800	0.0	0.50		
59242	0.25	4,500	7,000	-4,800	0.0	1.50		
59242	0.286	3,500	7,000	-5,100	0.0	0.46	Vary magnetic field	3
59242	0.286	3,300	7,000	-5,100	0.0	0.35	Vary sole voltage to study noise	3,11
59242	0.286	3,300	7,000	-4,900	0.0	0.35		11
59242	0.286	3,300	7,000	-4,650	0.0	0.35		11
59242	0.286	4,500	7,000	-5,100	-250	0.40	Vary grid voltage	2,8
59242	0.286	4,500	7,000	-5,100	-375	0.10		2,8
59505	0.235	3,280	7,000	-3,420	0.0	0.8	Vary tube dimensions. Currents above measured oscillation thresholds	4,12
59505	0.235	3,000	7,000	-3,420	0.0	0.6		4,12,13

APPENDIX B

NORTHROP CORPORATION REPORT

The results presented here were measured by Northrop Corporation Defense Systems Division, Electron Tube Section, Des Plaines, Illinois under Subcontract No. 009482 from Harris SAI.

The report provided by Northrop follows.

FINAL TECHNICAL REPORT

INJECTED BEAM CFA DATA

FOR

COMPUTER MODELING

Prepared for: Harris SAI, Inc.
Ann Arbor, Michigan
Sub-Contract 009482/3-17-78

Prepared by: R. R. Moats

Northrop Corporation
Defense Systems Division
Electron Tube Section
175 West Oakton Street
Des Plaines, Illinois 60018

Northrop Reference
EP 8540

9 April 1979
094-008950
Issue A

1. INTRODUCTION

It is the purpose of the work reported here to provide data for verification of mathematical models of injected-beam crossed field amplifiers (IBCFA's). Harris SAI inc. is developing such mathematical models for computer simulation of IBCFA performance under Contract No. F49620-77-C-0091, issued by the Air Force Office of Scientific Research. The work reported here has been performed for Harris SAI, inc. by Northrop under Sub-contract No. 009482/3-17-78.

The IBCFA selected for these measurements is Northrop's type RW-620, for which there is a substantial history of operating data, and for which there are numerous tube models available for measurement.

2. DATA ON IBCFA

2.1 Dimensioned Drawings

A set of dimensioned drawings of the gun and interaction space, and the transition between these two regions, has been supplied to Harris SAI, and has been reviewed jointly by Harris SAI and Northrop personnel. This requirement is considered complete.

2.2 Electrode Current

It is a requrement of the sub-contract to measure currents to cathode, collector, accelerating anode, grid, delay line anode, and sole under practical stable beam conditions without RF drive. The IBCFA is stable, i.e., there are no free-running oscillations, only for beam currents well under 1 A peak. Under these conditions, it was found that all of the cathode current reaches the collector, and the sole and delay line currents were zero. Under these conditions, and under all normal operating conditions, grid and accelerating anode currents were zero.

Data are presented here showing grid and accelerator control of beam current. Figure 1 and 2 are representative sets of curves showing grid control for three values of magnetic field (Tube S/N 59508, S/N 59242). Figures 3, 4 and 5 show control of beam current by accelerating anode (S/N 59242, S/N 59505, S/N 59506).

Magnetic field values are derived from the value of electromagnet current, based on calibration made with a set of dummy pole pieces. Although calibration readings are repeatable to within about ±30 Gauss, experience with operating tubes indicates that error is in the range of ± 60 Gauss.

2.3 Noise and Stability

Data are presented here for noise and stability for four different tubes, each with three different values of magnetic field. Measurements are given as a function of beam current, with sole voltage fixed for maximum gain at 6 GHz. There are also some measurements of noise power, as a function of sole voltage with beam current set just below the start-oscillation current. Measurements were made at 10% duty factor.

Tube Serial No. 59542 was connected with coaxial bolometer loads on both input and output. In both the input and the output arm immediately adjacent to the tube there were connected "monitor-T" elements. These transmit RF signals in the straight-through direction and block direct currents, which are transmitted to the side arms. Thus it is possible to measure current intercepted by the delay line. Appropriate coaxial

attenuators, 10 dB at the input and 20 dB at the output, were connected between the monitor-T's and the bolometer loads. A directional coupler connected to a spectrum analyzer was injected in the output arm, to observe oscillations. Noise power was measured at both the input and the output as a function of both grid control and accelerator control of beam current (Figures 6, 7, and 8). Under all circumstances, oscillation began at approximately 0.4 A, a value much lower than normally observed in RW-620's. When the beam current was varied by accelerator control (grid at cathode potential), a minimum of noise power output between 0.2 and 0.3 A peak was observed and noise power increased with decreasing current, at least down to 0.05 A peak. With grid control (accelerating anode set at the value which would give 1.5 A peak with grid at cathode potential), noise continued to decrease with decreasing current. Above 0.3 A peak, the character of the noise output curves was similar for either accelerating anode or grid control, and the current for start-oscillation was the same. Figures 9, 10, and 11 show the great sensitivity of noise power output to sole voltage, with beam current set below start-oscillation. The arrows on the x-axis indicate the sole voltage setting for noise measurements as a function of beam current. No current to the circuit was observed in any of these measurements, nor when the beam current was raised to 1 A. The relatively low start-oscillation currents were attributed to RF reflections from the monitor-T's. These devices were omitted when the other tubes were measured.

The three other tubes which were tested were connected in the manner normally used in RW-620, with the output connected to a double-ridge waveguide. The only exception was that the input was terminated in a 50-ohm load. Beam current was varied by the accelerating anode. Power was measured by a bolometer load connected through a directional coupler. Figure 12 shows noise power as a function of current and Figure 13, 14, and 15 show noise power as a function of sole voltage for S/N 59505. Figure 16 shows noise power as a function of current and Figures 17, 18, and 19 show noise power as a function of sole voltage for S/N 59506. Figure 20 shows noise power as a function of current for S/N 59275. Oscillations were observed only above 0.6 A peak beam current, and generally in the vicinity of 6 GHz.

The curves of noise power as a function of sole voltage are difficult to analyze because there appear to be multiple periodicities. A segment of the curve for S/N 59506 at B = 2600 (Figure 19) was selected as an example because at the high end of the curve the periodicity appears simple. The voltage difference between peaks is about 310 V. Mean beam velocity v_e, is equal to E/B, or to $(V_L-V_S)/Bd$, where B is magnetic field, d is sole-line spacing, and V_L-V_S is sole-line voltage. Assuming V_L-V_S = 11860 and d = 0.002 m., $v_e = 2.28 \times 10^7$ m/second. Let us postulate a reflected wave model. The number of half wavelengths will be $v_e/\Delta v_e$, or 11860/310 $\approx$ 38. The quantity $\beta_e L$ is equal to 38 π, where L is the length of the reflected wave system, and $\beta_e = 2\pi f/v_e$ where f is a frequency. The length of the circuit is 0.0685 m. If we set this value equal to L, we find $f = 6.3 \times 10^9$, close to the frequency at which oscillations will start when current is increased. It is therefore a reasonable explanation that the peaks and voltages of noise are related to re-reflections on the circuit.

2.4 Magnetic Field

The magnetic field in the RW-620 is shown in the longitudinal direction by Figure 21, where the positions of the pole pieces and the cathode are indicated. Transverse measurements in three planes are shown. Figure 22 corresponds to the plane through the edge of the cathode nearest the interaction space, Figure 23 to a plane at the center of the interaction space, and Figure 24 to a plane through the collector. In the latter three sets of measurements the level was pre-set to 2400 Gauss at the center. A proportionality constant should be used corresponding to 2350 Gauss shown at the cathode in Figure 21. There is no significant pole piece saturation; proportionality constants are applicable to all locations.

2.5 Power Transfer Curves

Power output as a function of RF drive is shown in Figure 25 for S/N 59242, Figure 26 for S/N 59505, and Figure 27 for S/N 59506. The discontinuity in slope at 4 GHz for S/N 59242 is believed to be an actual phenomenon and not an error of measurement.

2.6 Cold Test Data

RF phase velocity v_{ph} is shown in Figure 28 for S/N 59242, Figure 29 for S/N 59505, and Figure 30 for S/N 59506. The plots show delay ratio, c/v_{ph}, as a function of wavelength, with frequency also indicated.

The interaction impedance of the RW-620 as a function of frequency is shown in Figure 31. The measurement method is that described by Arnaud,[1]

1 J. Arnaud, "General Properties of Periodic Structures", Crossed-Field Microwave Devices (E. Okress, ed.,) vol. 1, pp 17-33, Academic Press, New York, 1961.

which used dielectric perturbation. Several measurements were made at each of several frequencies across the band with different spacings between the dielectric perturber and the circuit, and for five different RW-620 delay line circuits. The differences of measured values at any one frequency for any one circuit were much greater than the differences between the different delay line circuits. The curves plotted represent statistical averaging of points observed, and the values of impedance with respect to frequency represent a curve which has been smoothed for best fit to the theoretical bar line model.[2] About 80 data points were used in this process. The statistical standard deviation of the measurements was more than 7 ohms. Because of the number of data points, the accuracy of the curves is believed to be much less than ± 7 ohms.

Circuit attenuation curves are shown in Figure 32 for S/N 59242, Figure 33 for S/N 59505, and Figure 34 for S/N 59506. The length of the circuit is 6.85 cm.

3 SYMBOLS

The following symbols were used in the graphs:

- B = Magnetic field
- I_b = Beam current
- V_L = Delay line voltage with respect to cathode
- V_S = Sole voltage with respect to cathode
- V_a = Accelerating anode voltage with respect to cathode

2 W. Sobotka, "Le TPOM en Regime Continu", Thesis, University of Paris, 25 June 1970.

V_g = Grid voltage with respect to cathode

c = Velocity of light

v_{ph} = Phase velocity of circuit

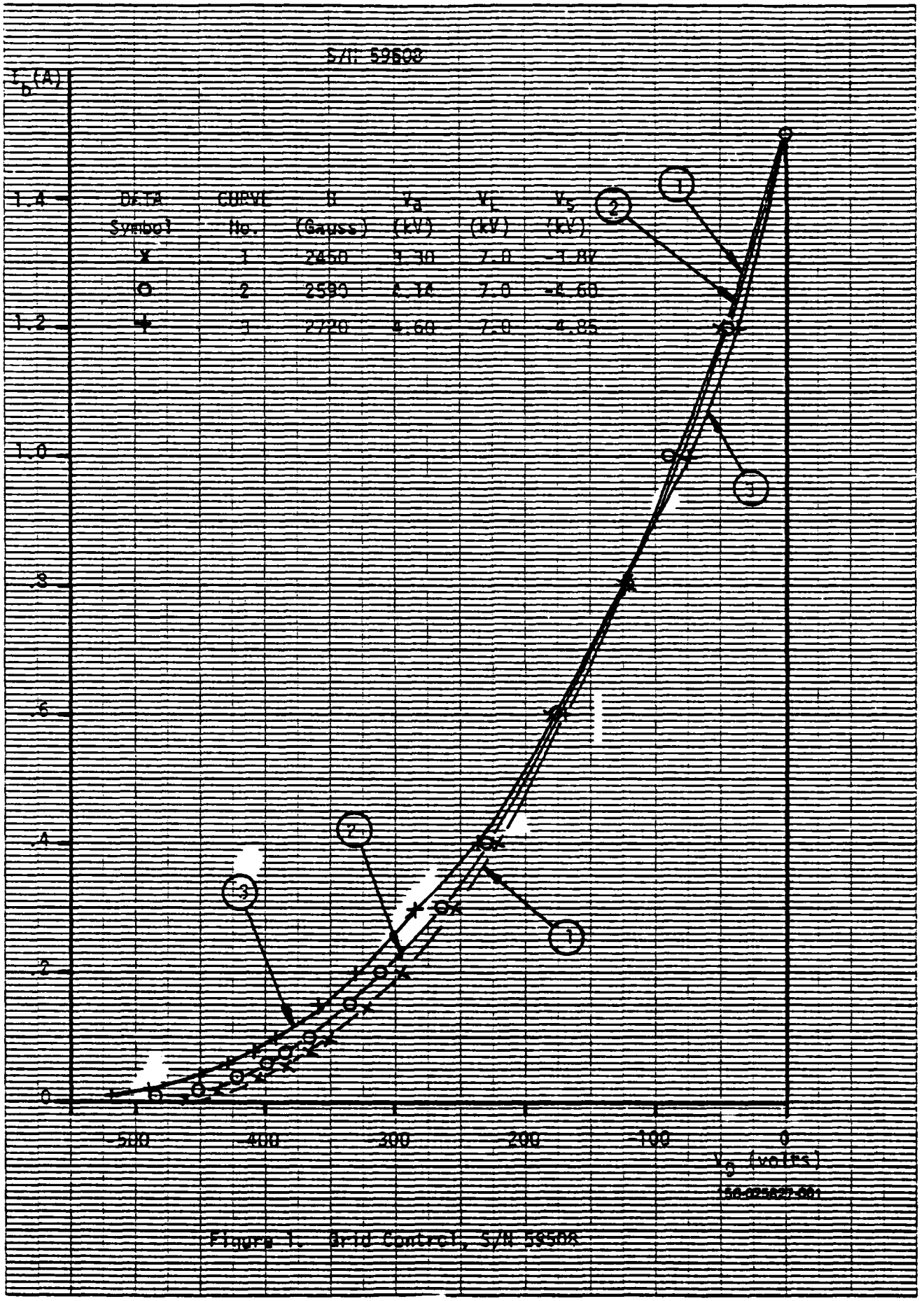

Figure 1. Grid Control, S/N 59608

S/N 59242

CURVE No.	G (Gauss)	V_s (kV)	V_t (kV)	V_a (kV)
1	2620	-4.20	7.0	4.0
2	2680	-4.84	7.0	4.47
3	2850	-5.10	7.0	4.5

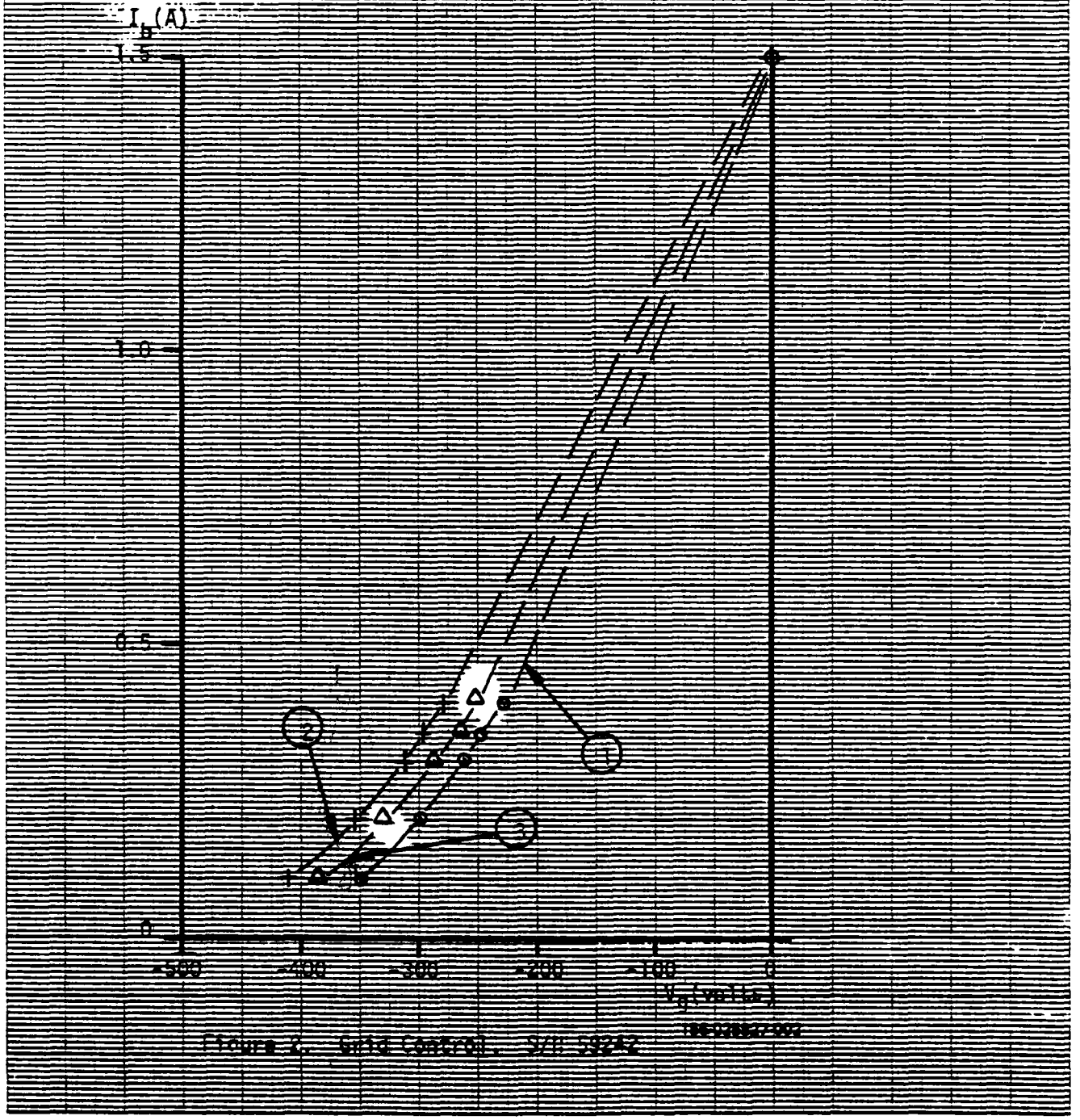

Figure 2. Grid Control, S/N 59242

S/N 59242

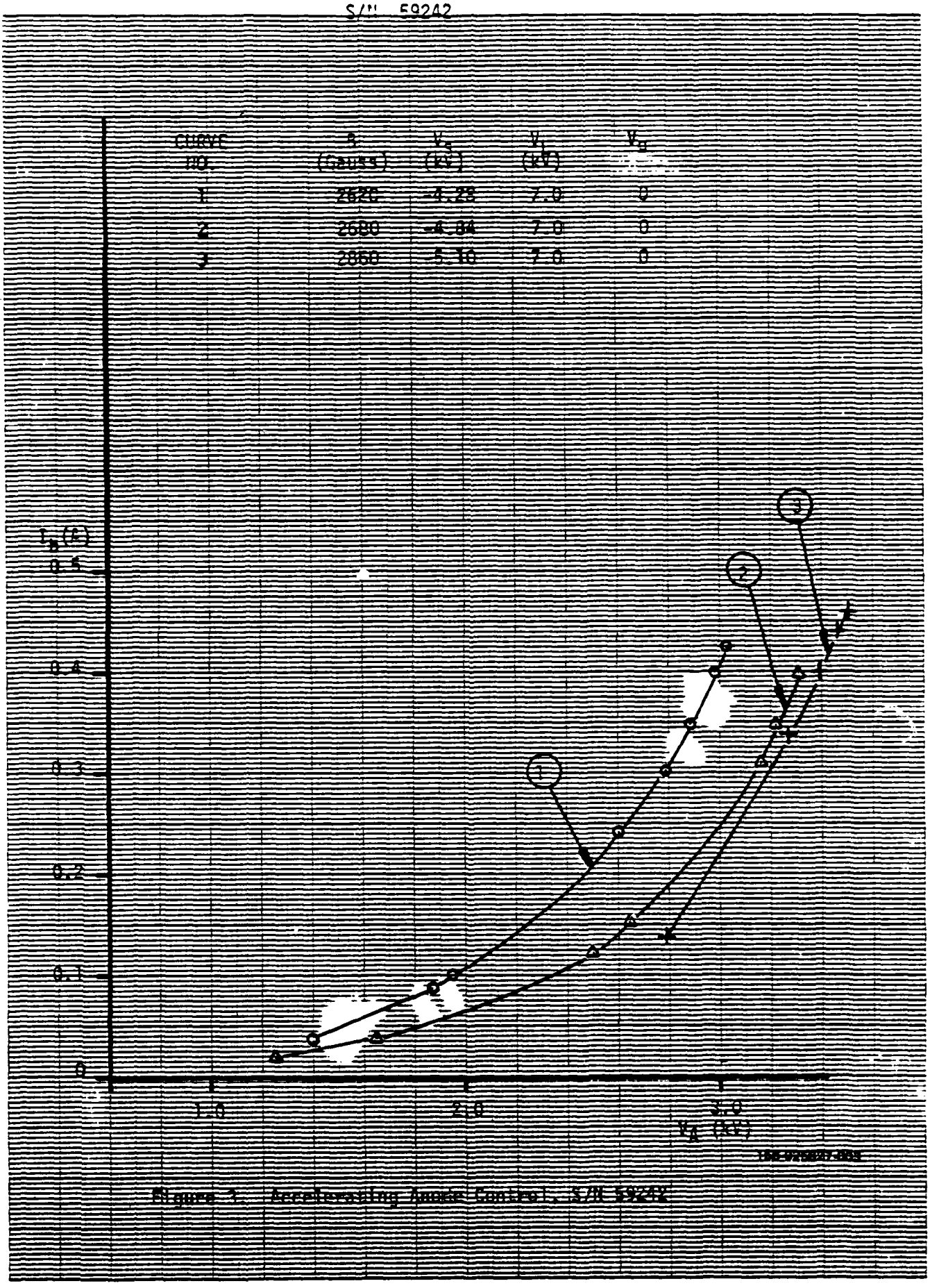

Figure 3. Accelerating Anode Control, S/N 59242

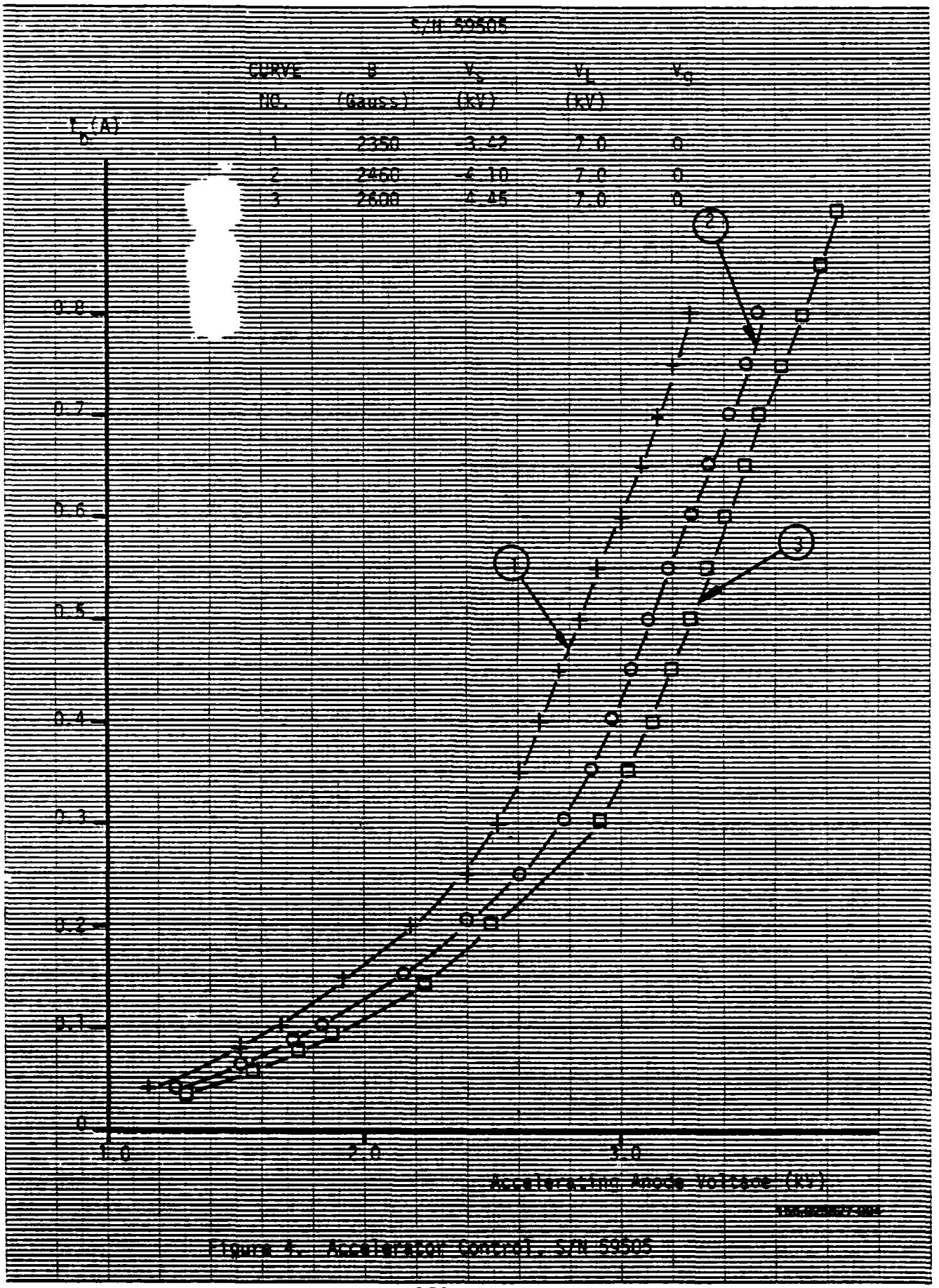

Figure 4. Accelerator Control, S/N 59505

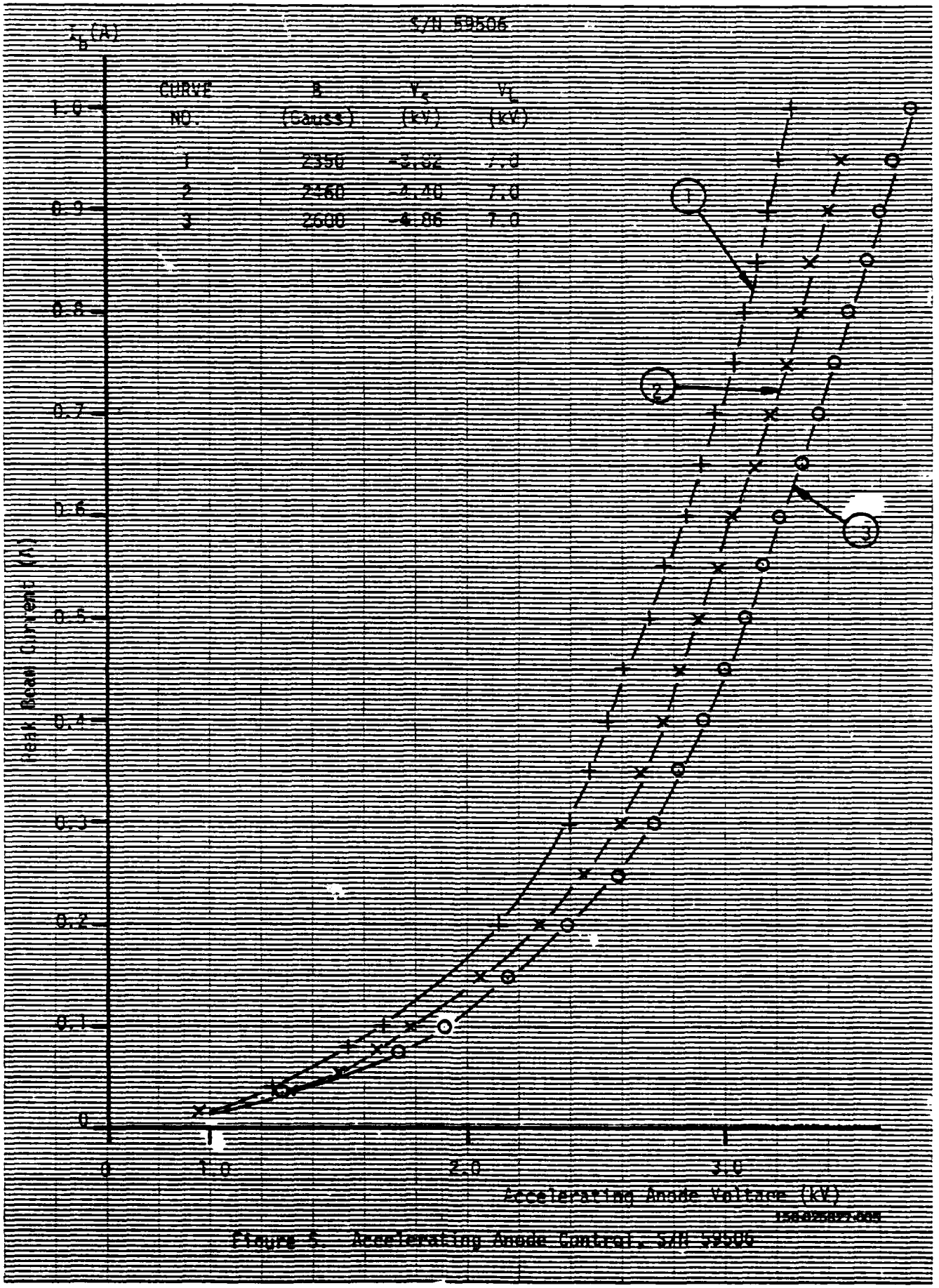

Figure 5. Accelerating Anode Control, S/N 59506

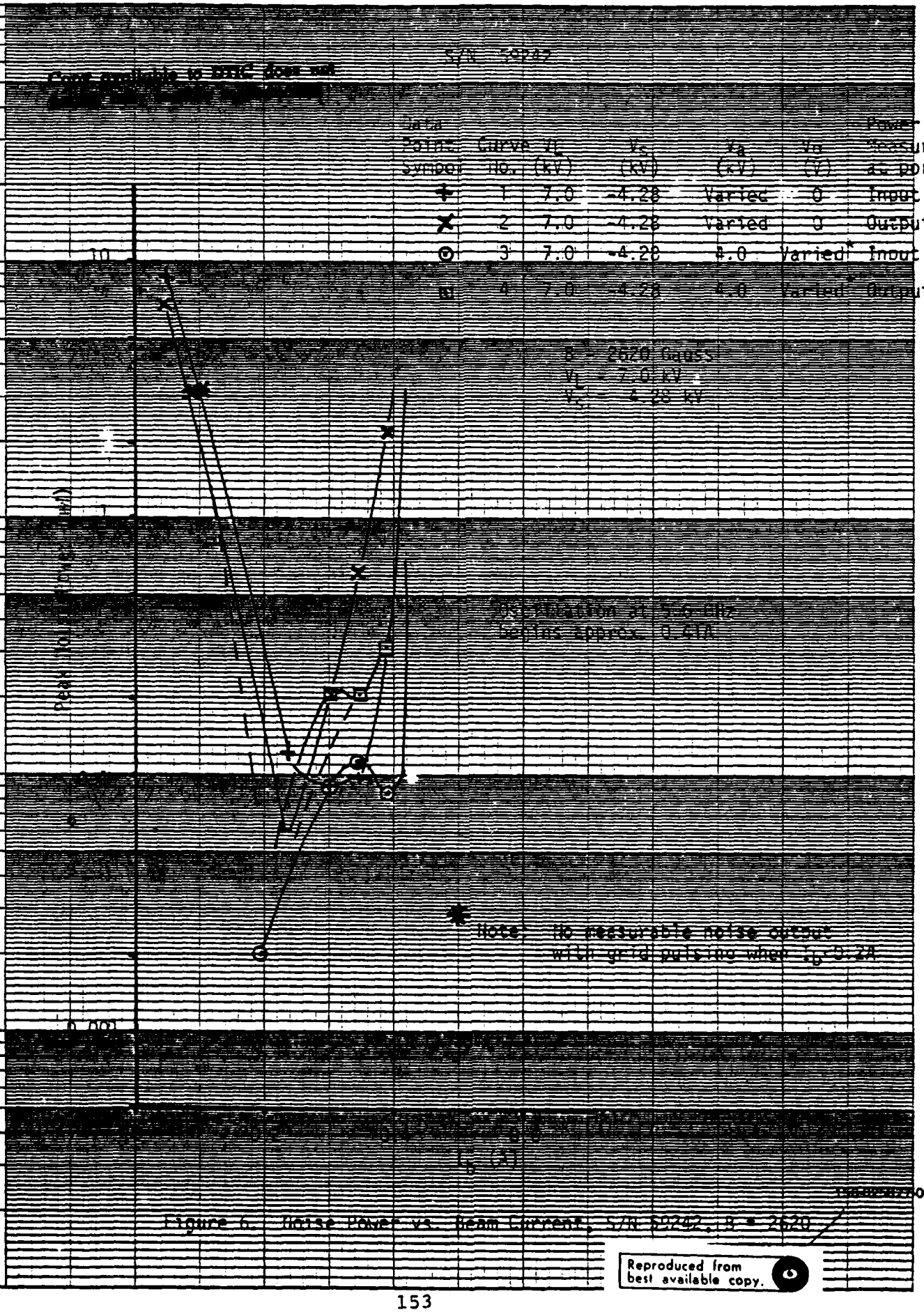

Figure 6. Noise Power vs. Beam Current, S/N 59242, B = 2620

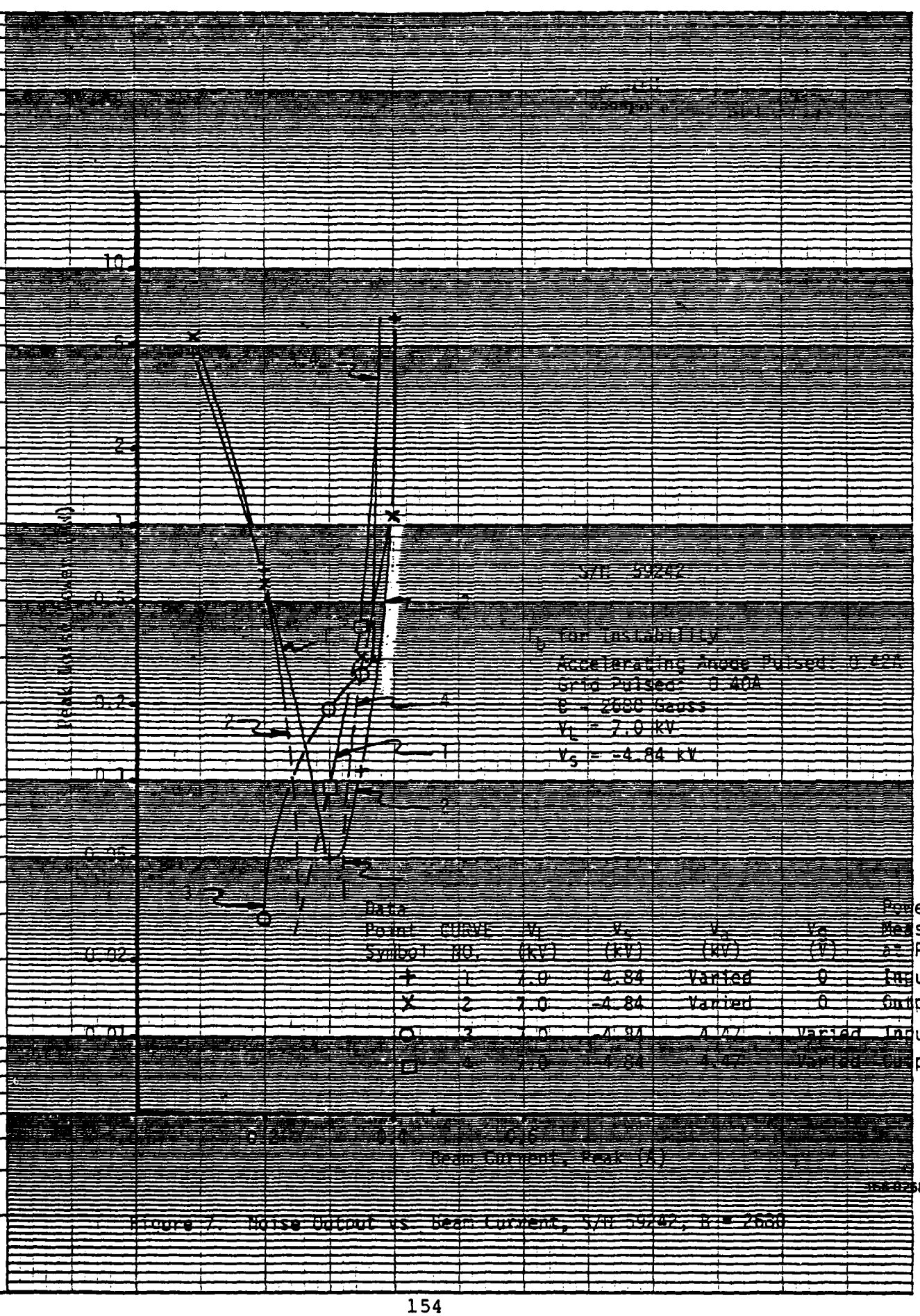

Figure 7. Noise Output vs. Beam Current, S/N 59242, B = 2600

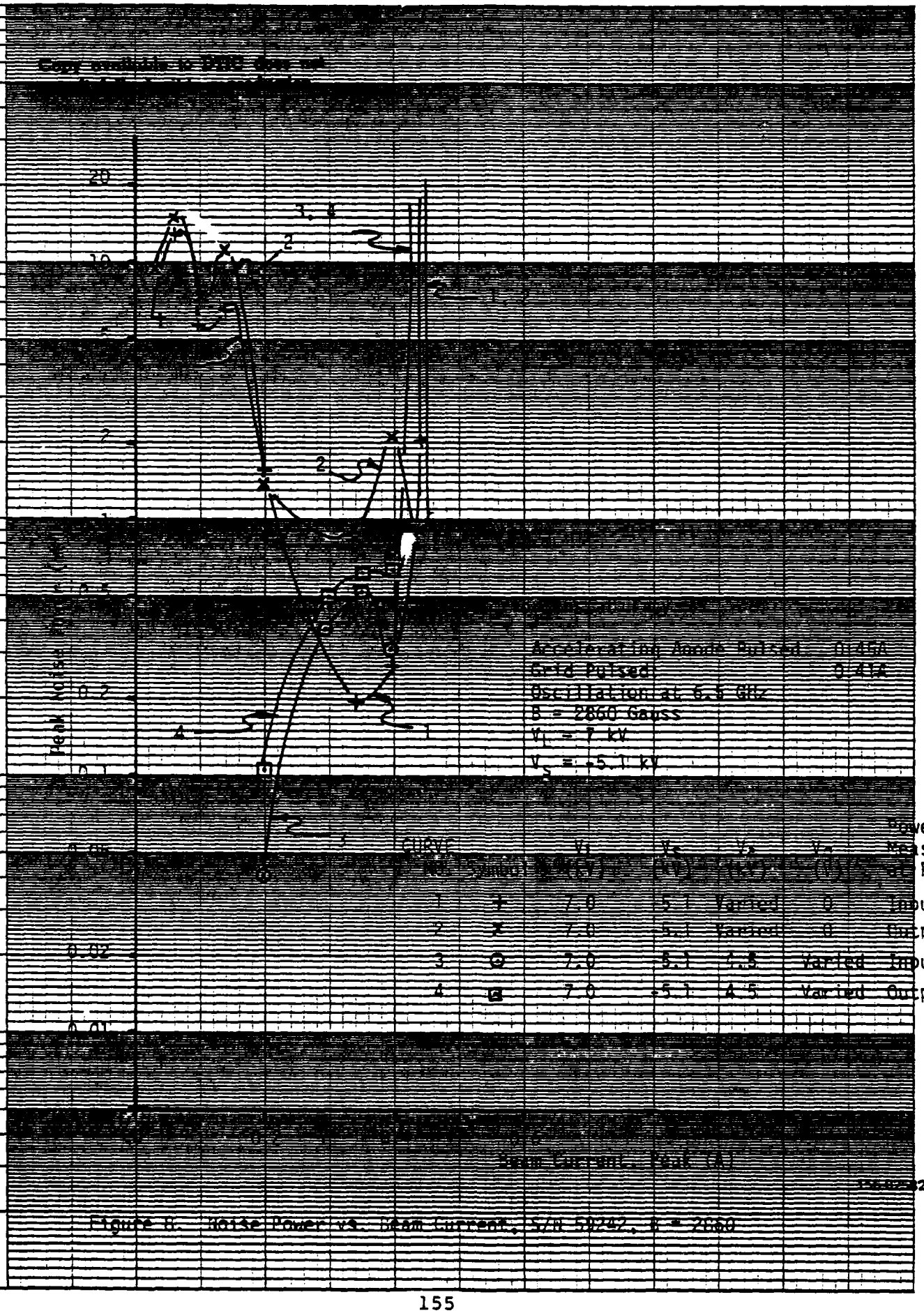

Figure 8. Noise Power vs. Beam Current, S/N 5042, B = 2860

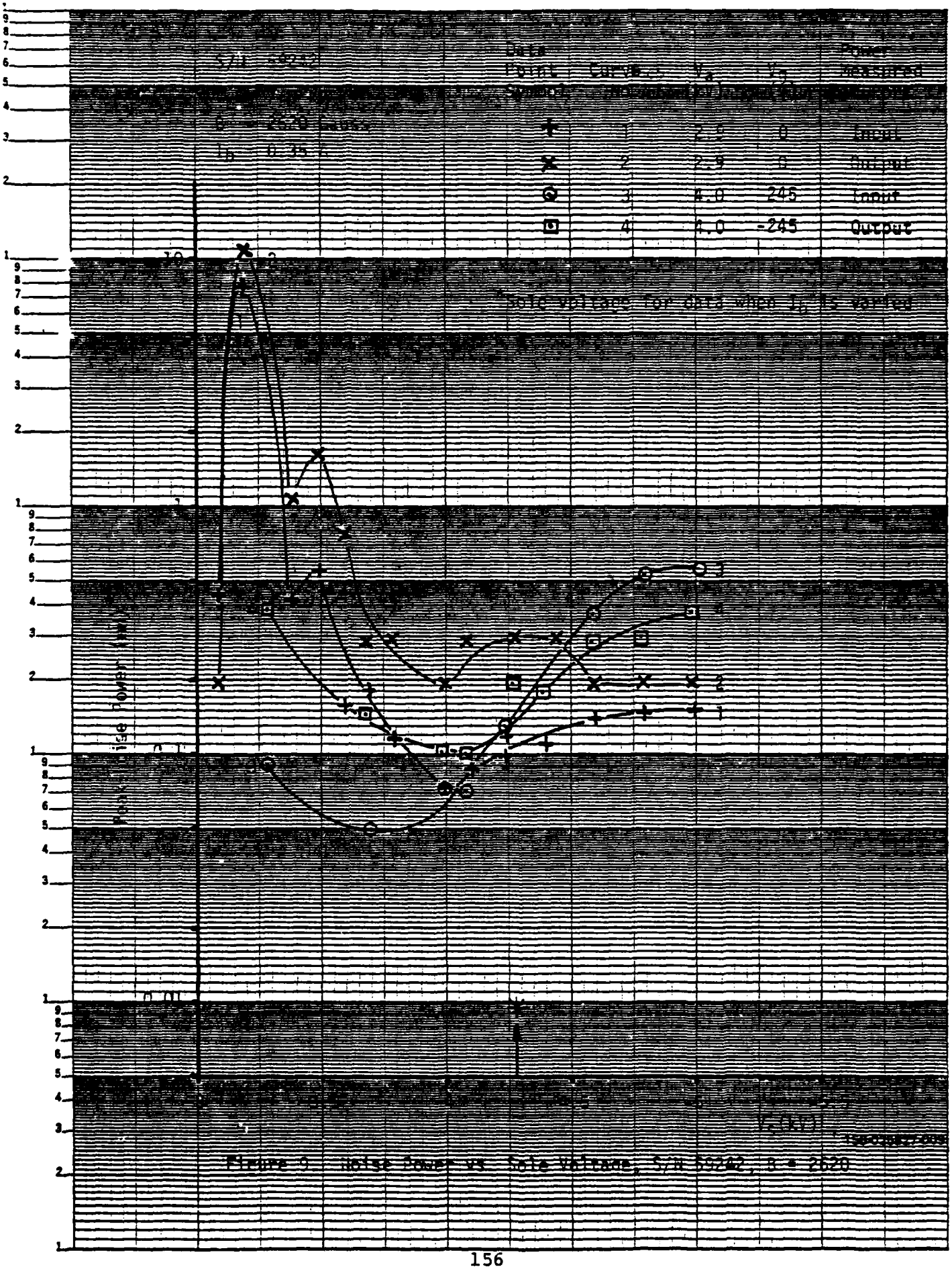

Figure 9. Noise Power vs Sole Voltage, S/N 9242, δ = 2620

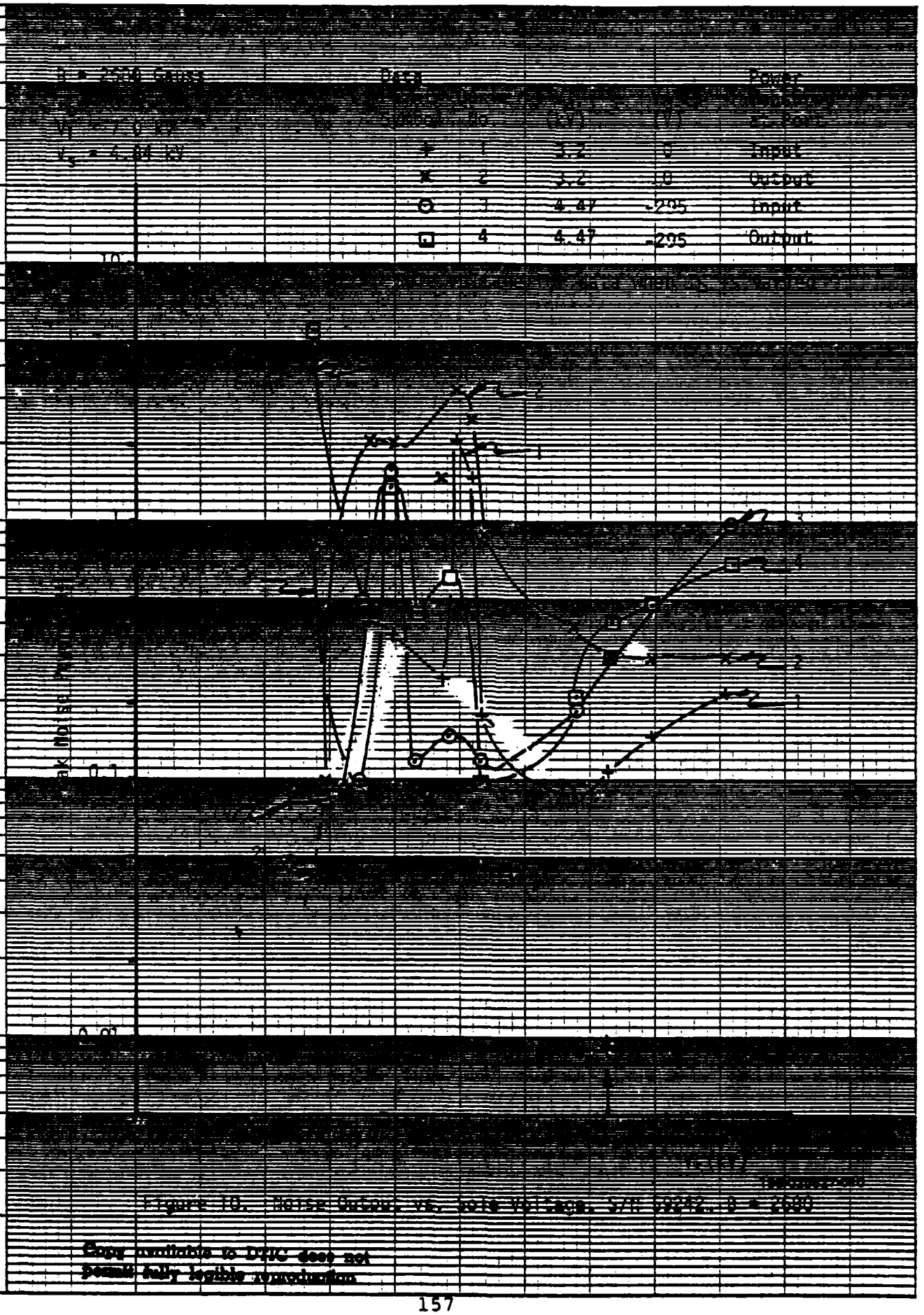

Figure 10. Noise Output vs. Gate Voltage, S/N 5924-10 B = 2530

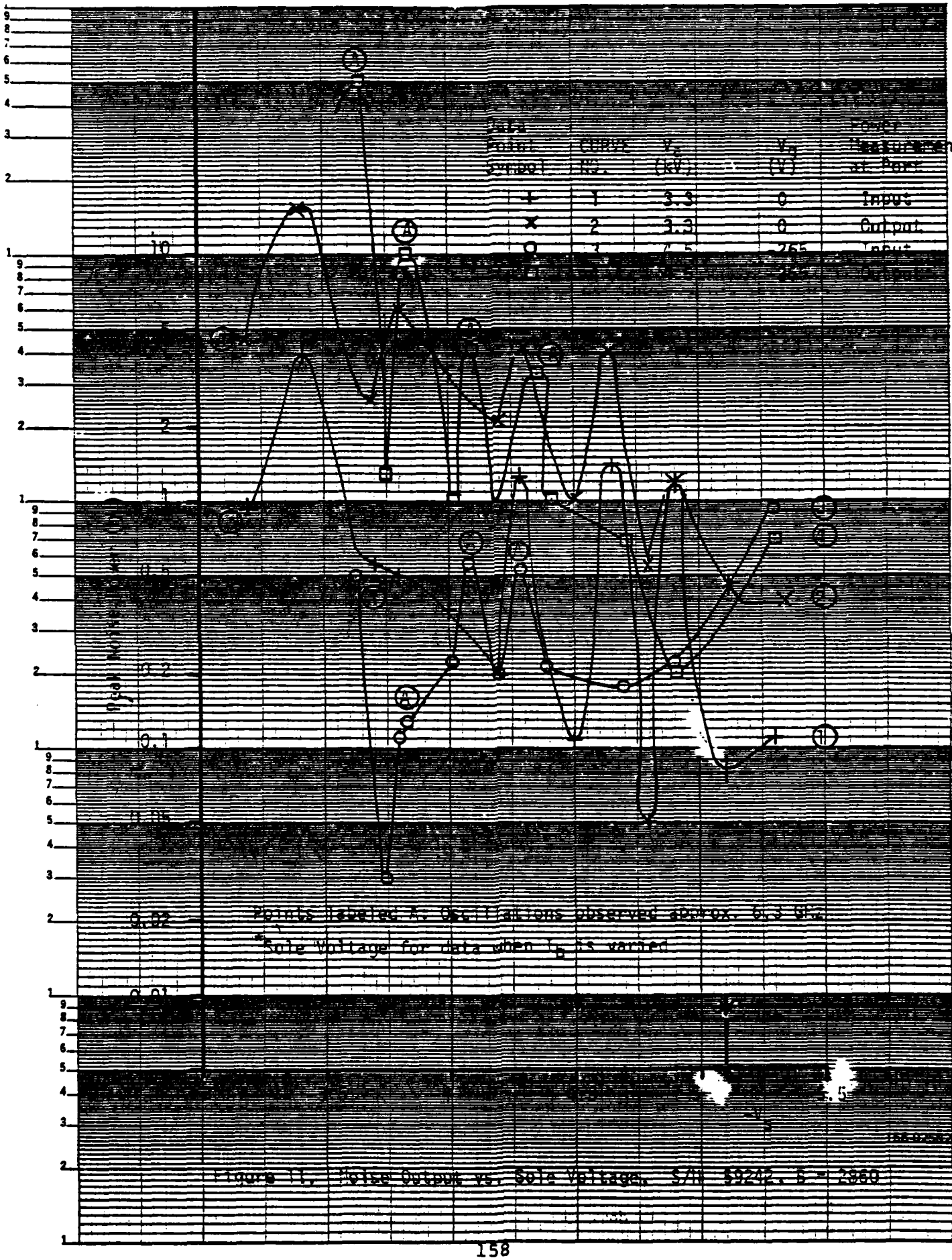

Figure 11. Noise Output vs. Sole Voltage. S/N 59242. I_b = 2860

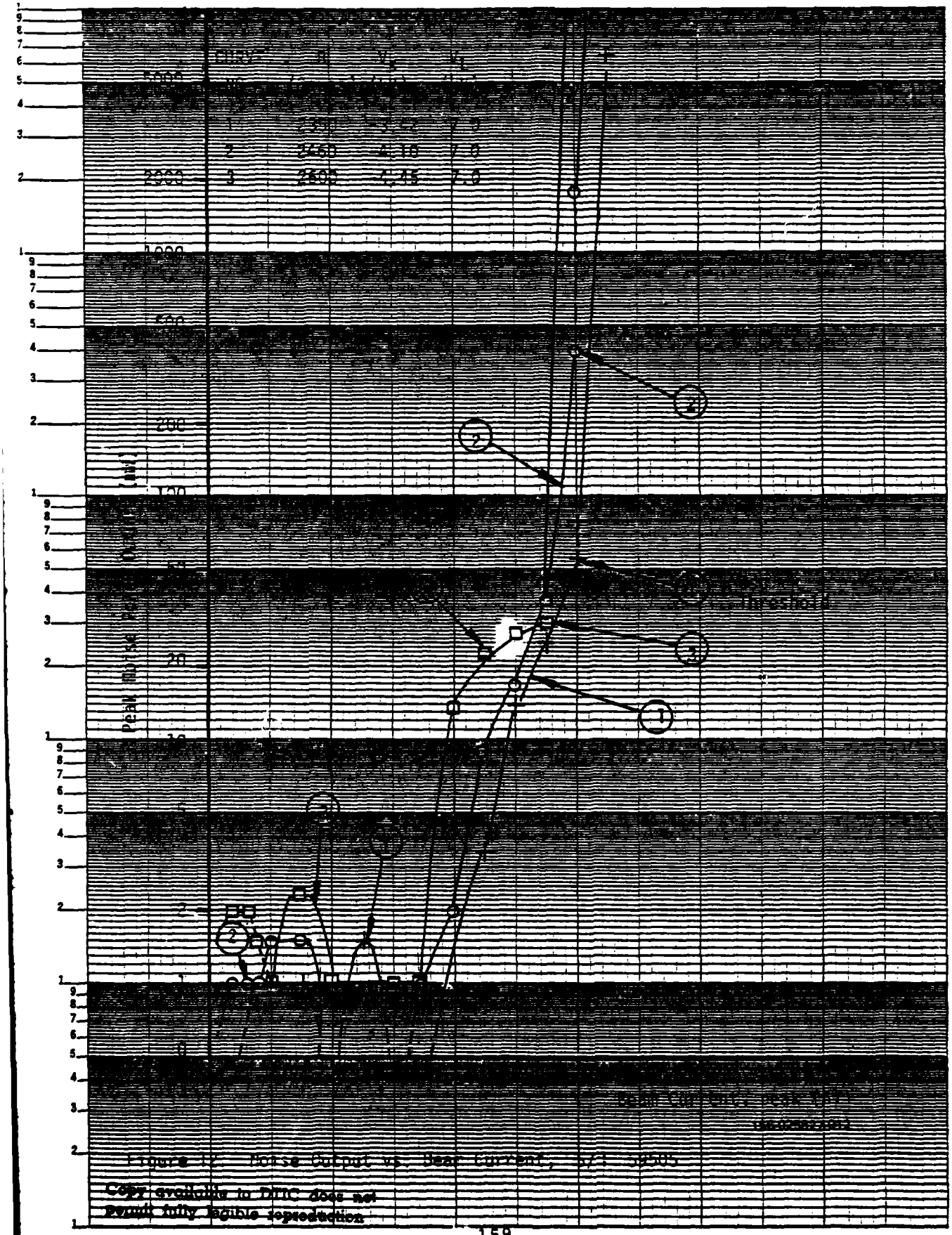

Figure 12. Noise Output vs. Beam Current, A/I 3505

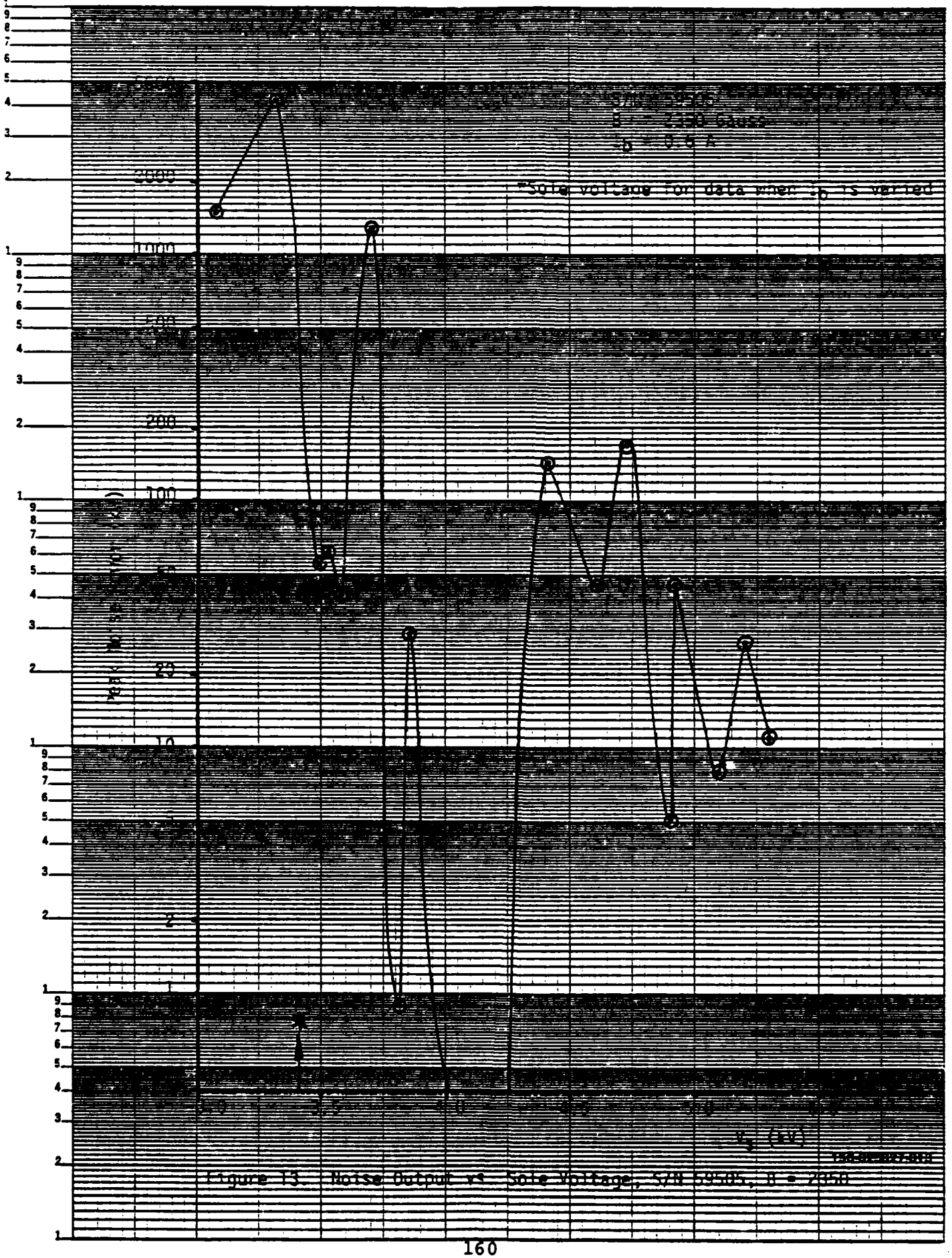

Figure 13. Noise Output vs. Sole Voltage, S/N 59505, B = 2350

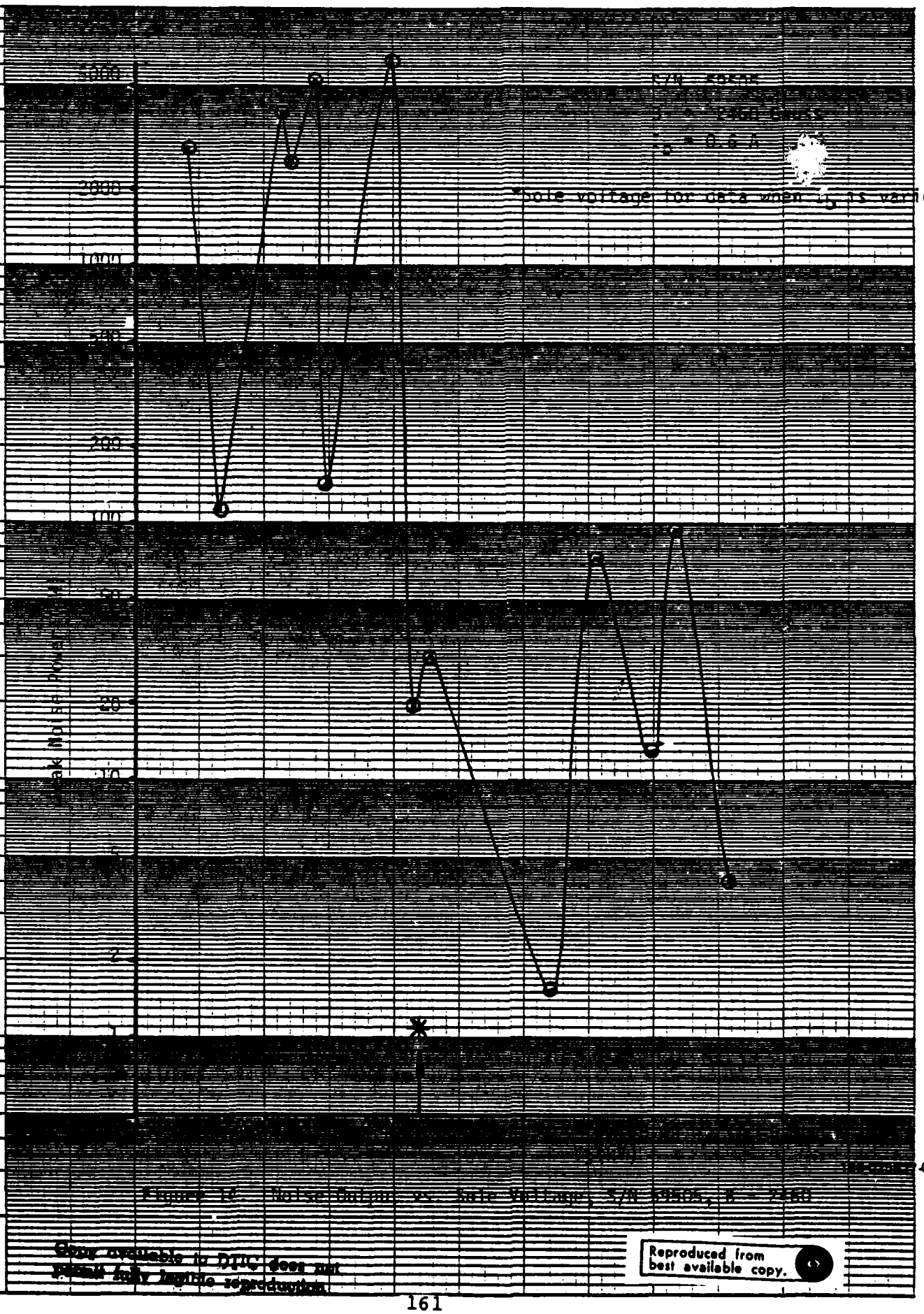

Figure 10. Noise Output vs. Safe Voltage, S/N 69505, I_5 = 2450

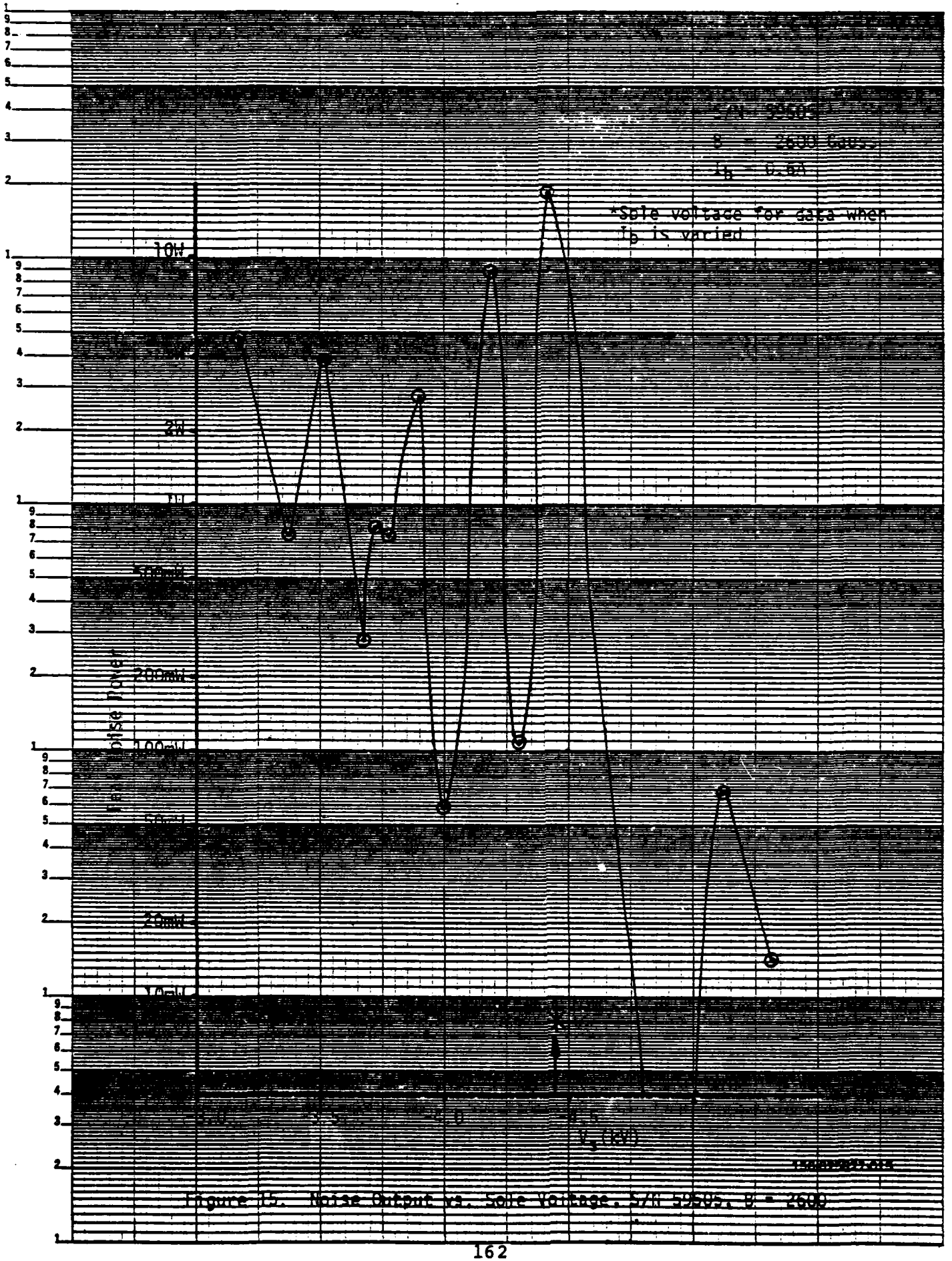

Figure 15. Noise Output vs. Sole Voltage. S/N 5050, B = 2600

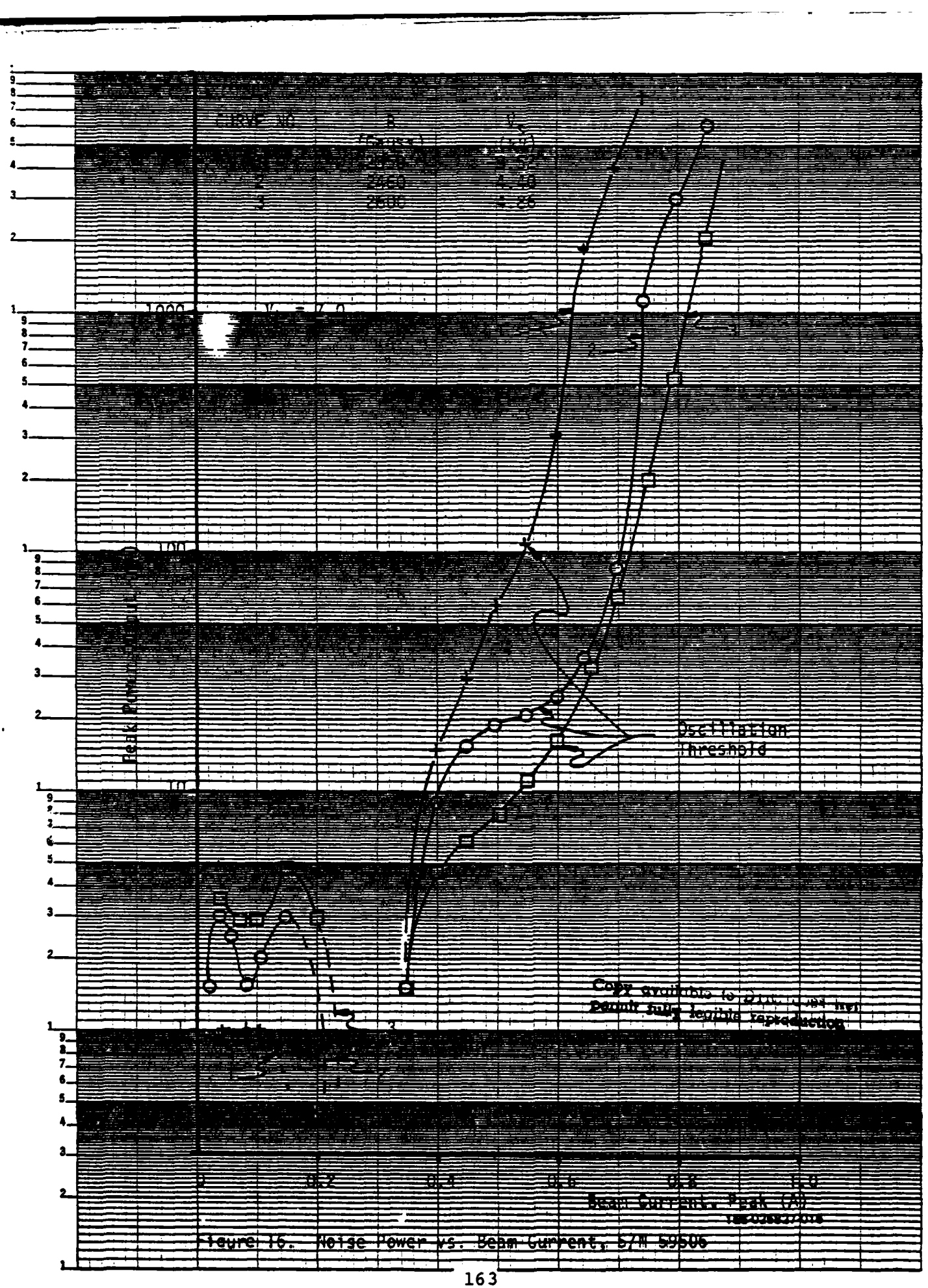

Figure 16. Noise Power vs. Beam Current, SFM 59506

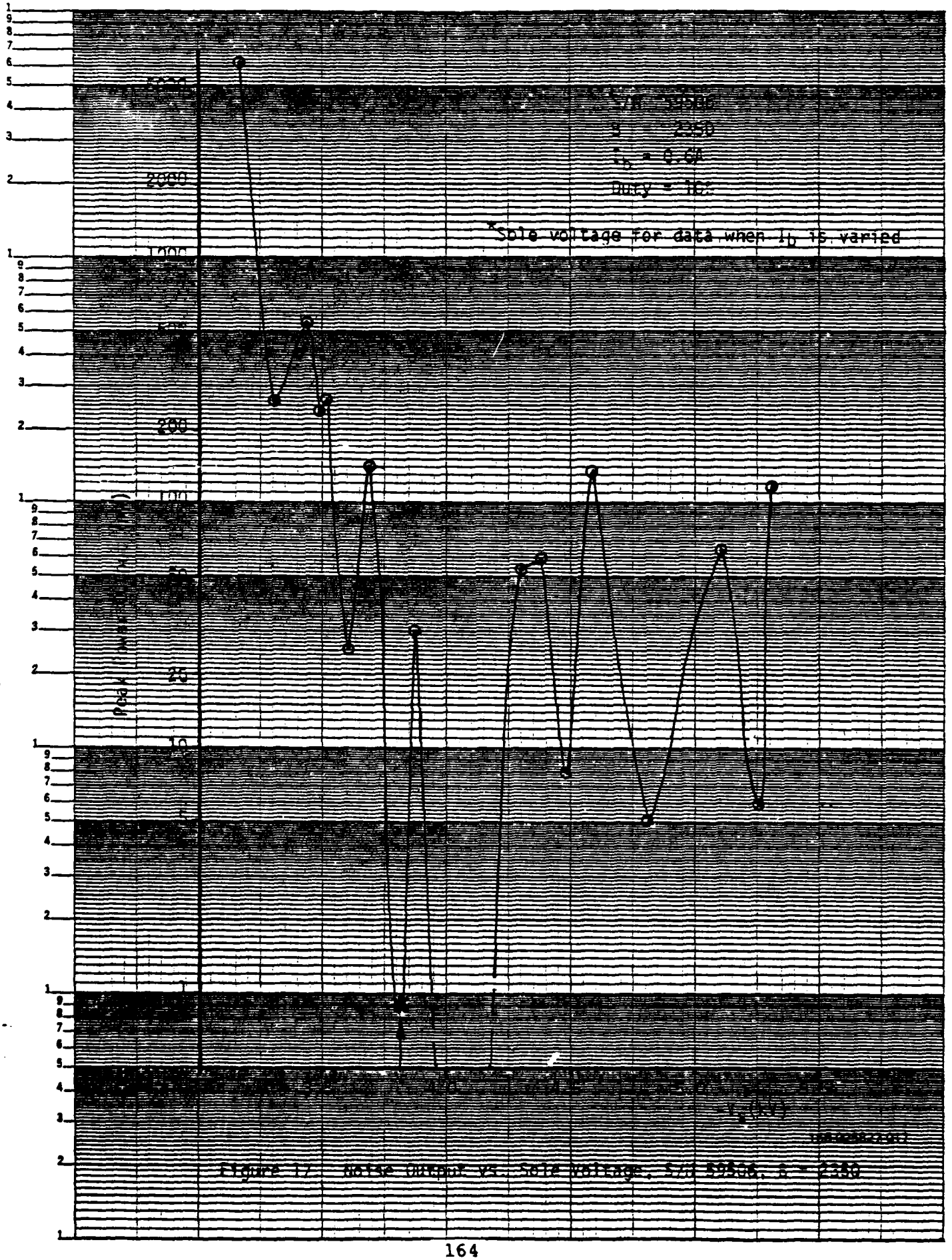

Figure 17. Noise output vs. Sole voltage, S/N 59506, S = 2350

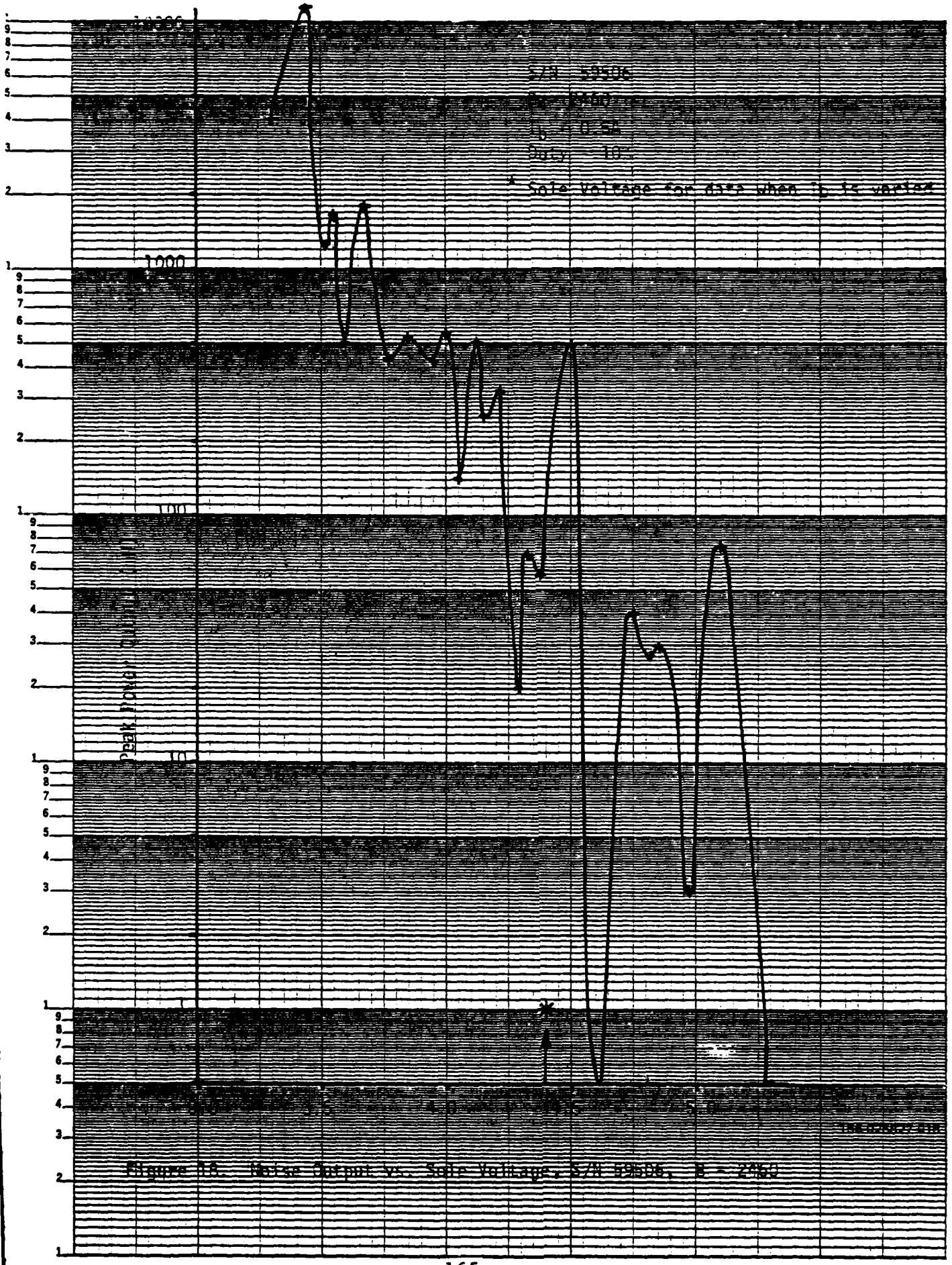

Figure 58. Noise Output vs. Sole Voltage, S/N 59506, T = 24°C

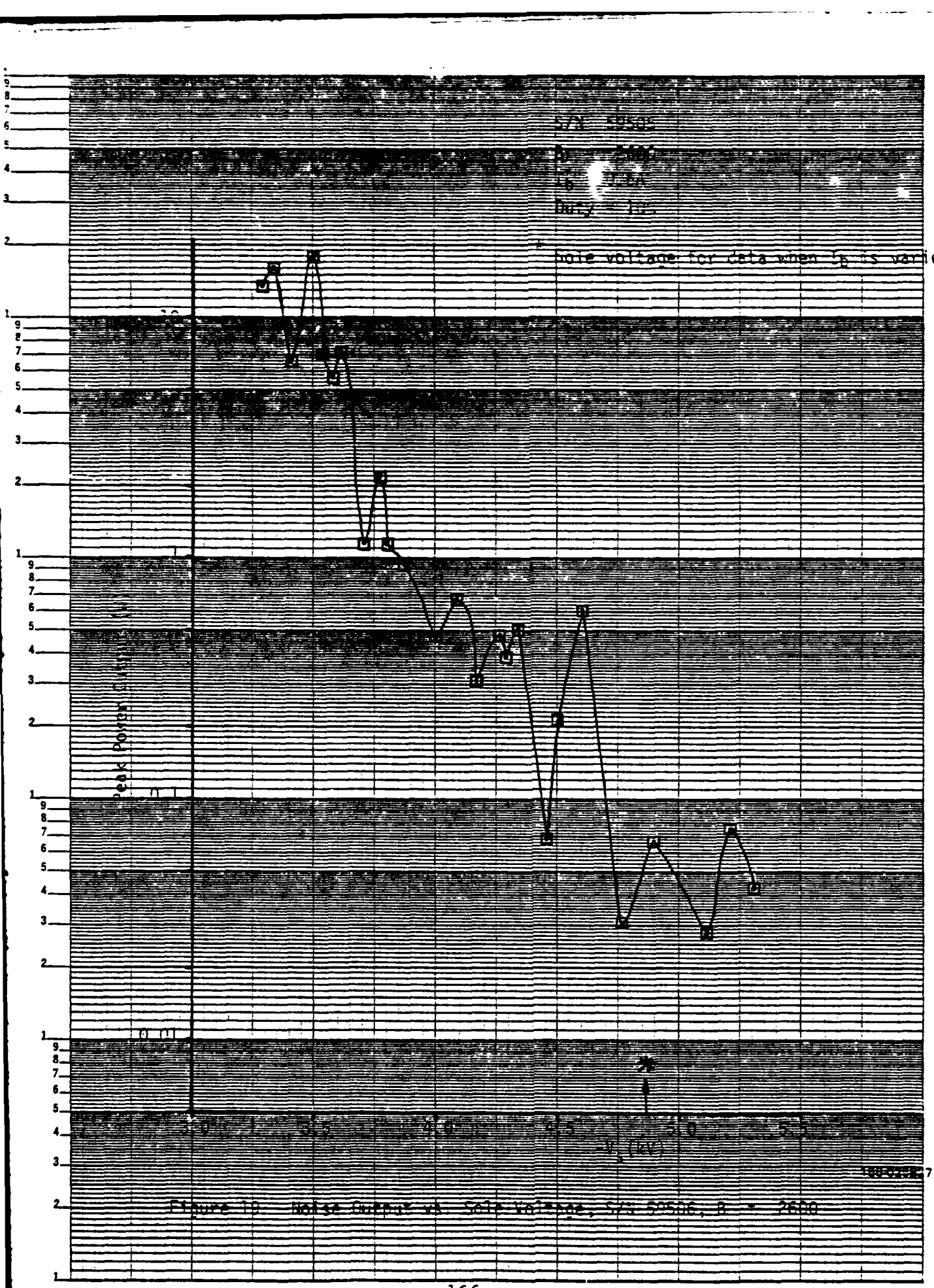

Figure 10 Noise Output vs Bias Voltage, S/N 5050E, R = 2600

Figure 20. Noise Output vs. Beam Current, S/N 5927.

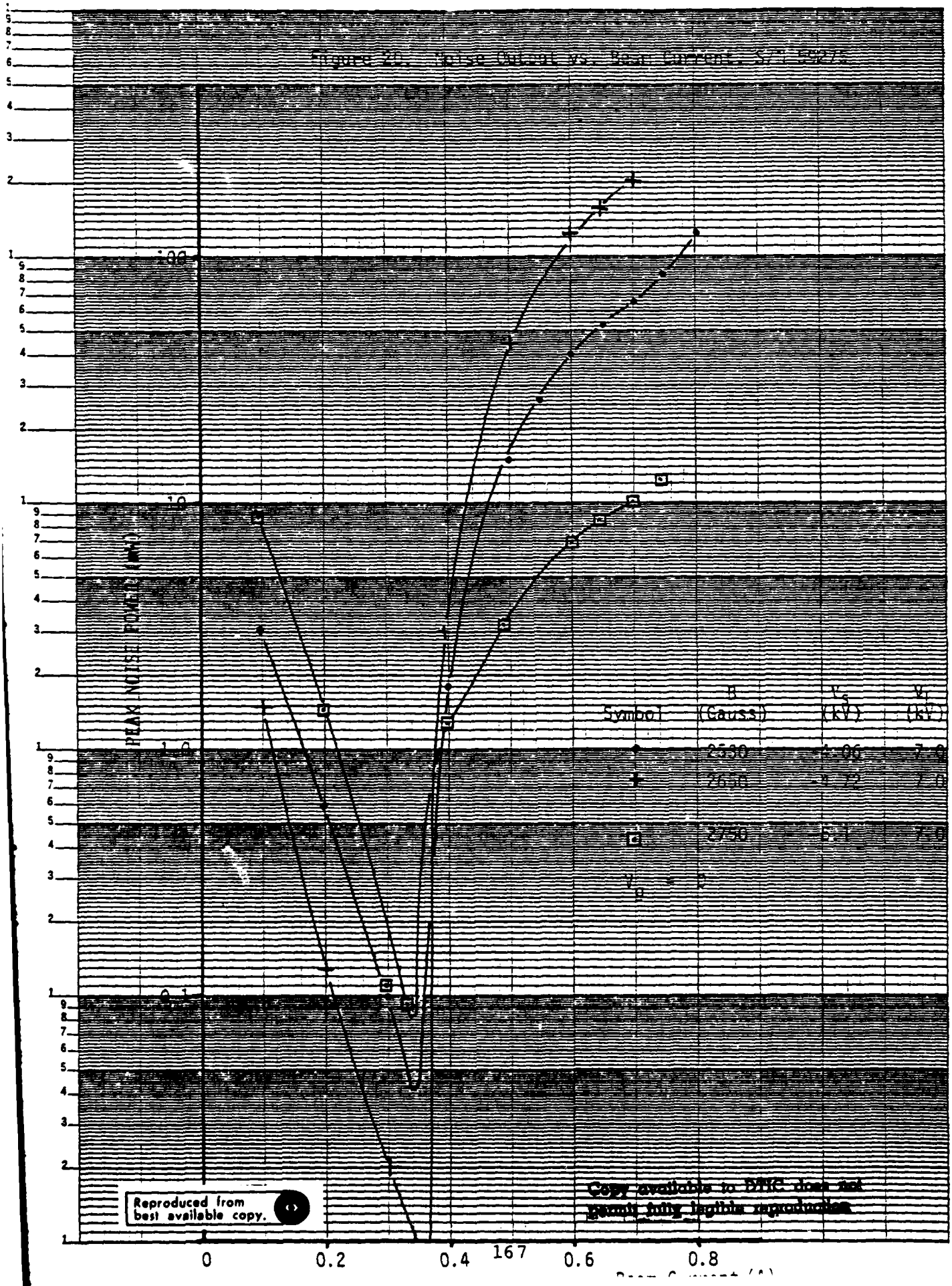

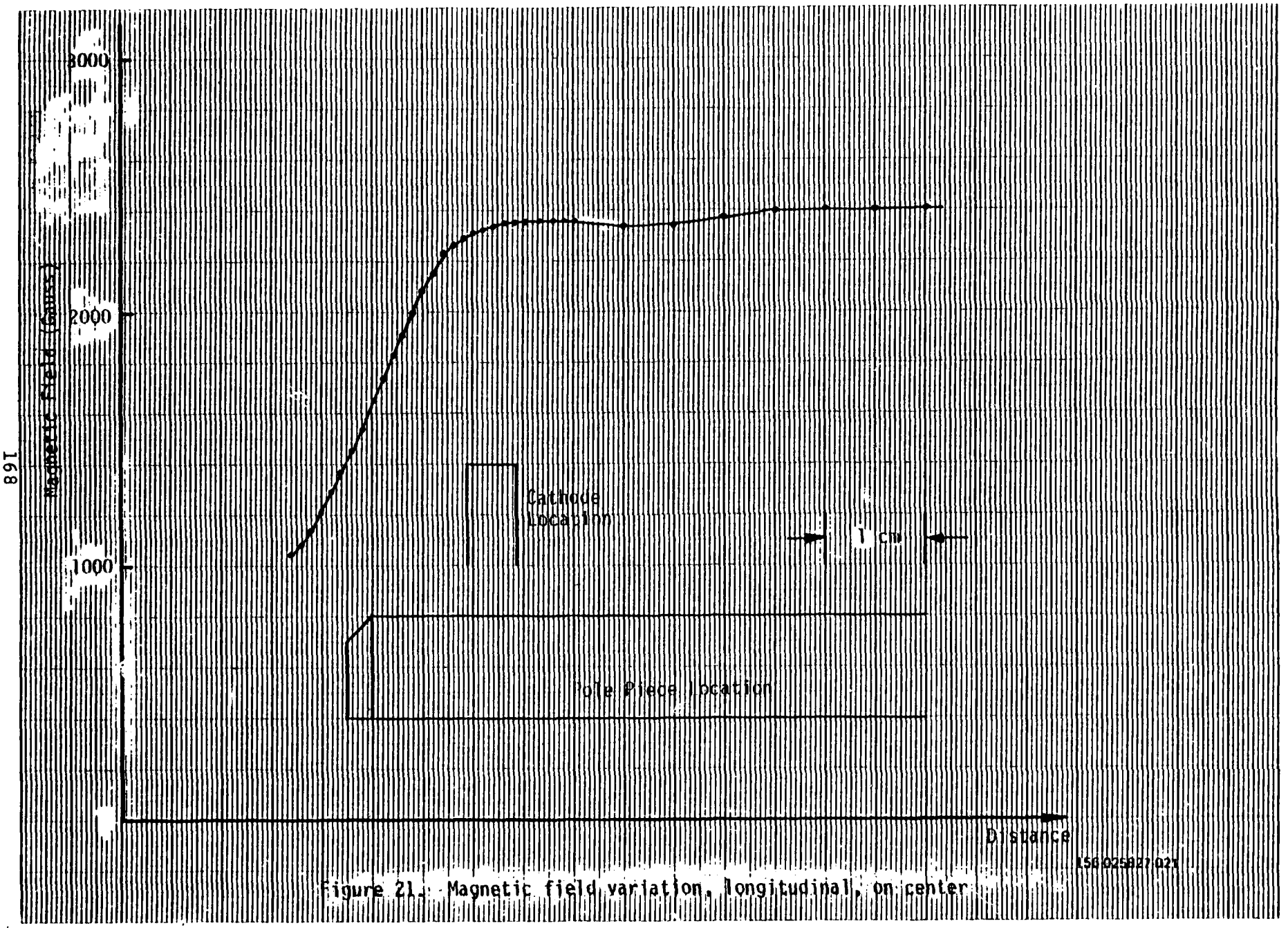

Figure 21. Magnetic field variation, longitudinal, on center

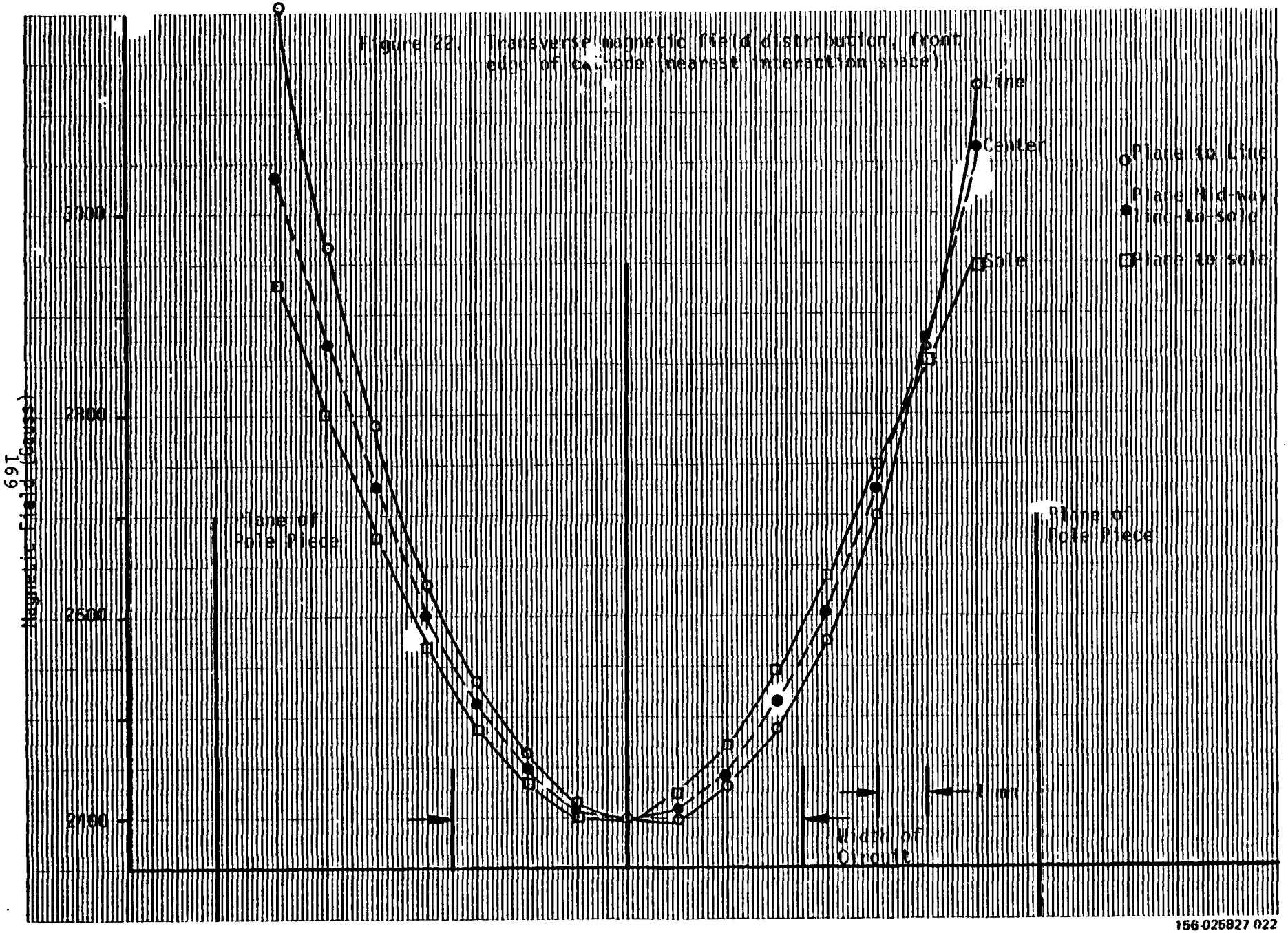
Figure 22. Transverse magnetic field distribution, front edge of cathode (nearest interaction space)
Magnetic Field (Gauss)
3000
2800
2600
2400
Plane of Pole Piece
Plane of Pole Piece
Line
Center
Sole
Plane to Line
Plane Mid-way Line-to-Sole
Plane to Sole
1 in.
Width of Circuit
169
156-025827 022

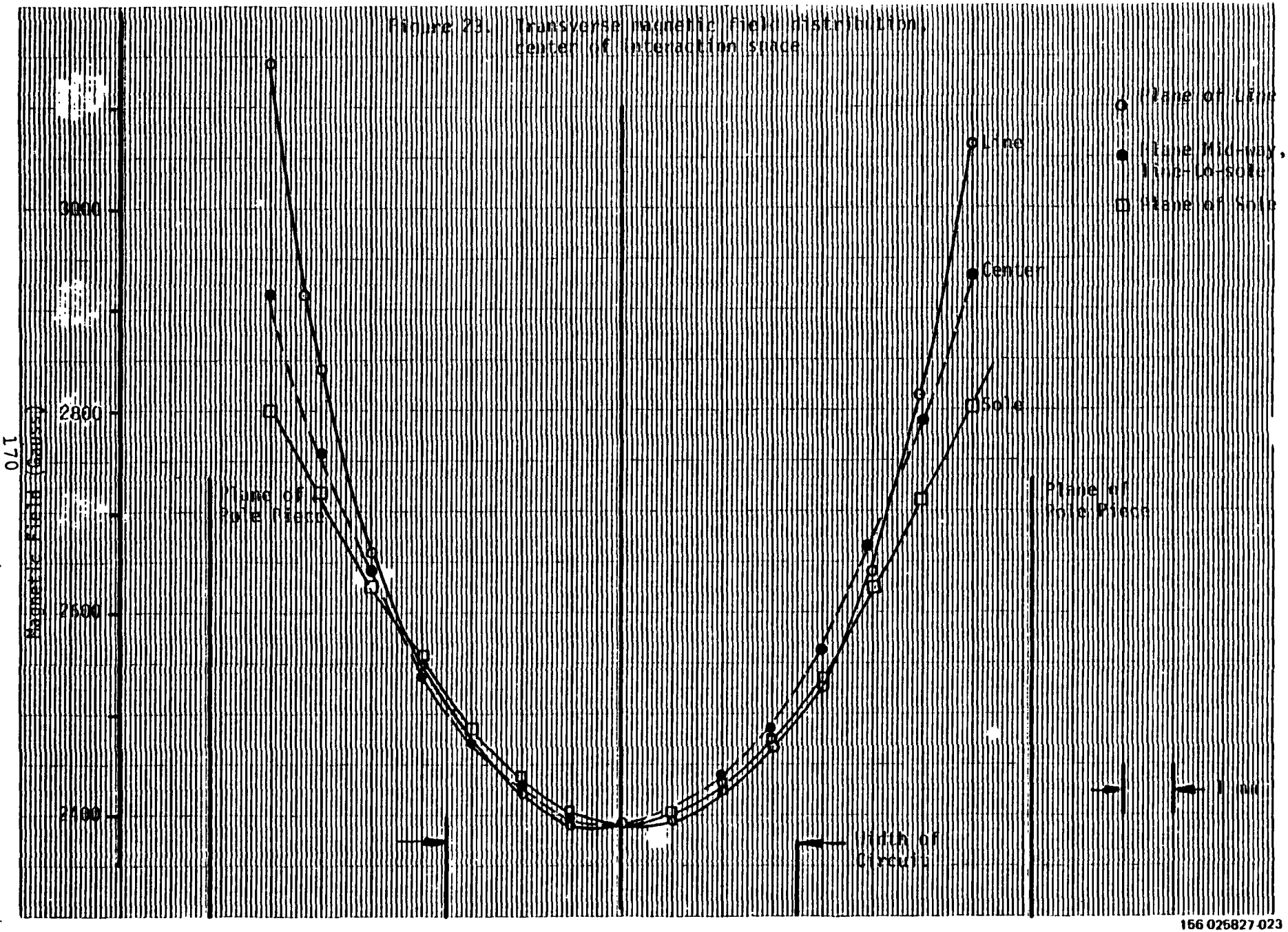
Figure 23. Transverse magnetic field distribution, center of interaction space
Magnetic Field (Gauss)
3000
2800
2500
2100
Plane of Pole Piece
Line
Center
Sole
Plane of Pole Piece
Width of Circuit
1 in
156 026827-023

Figure 24. Transverse magnetic field, collector area

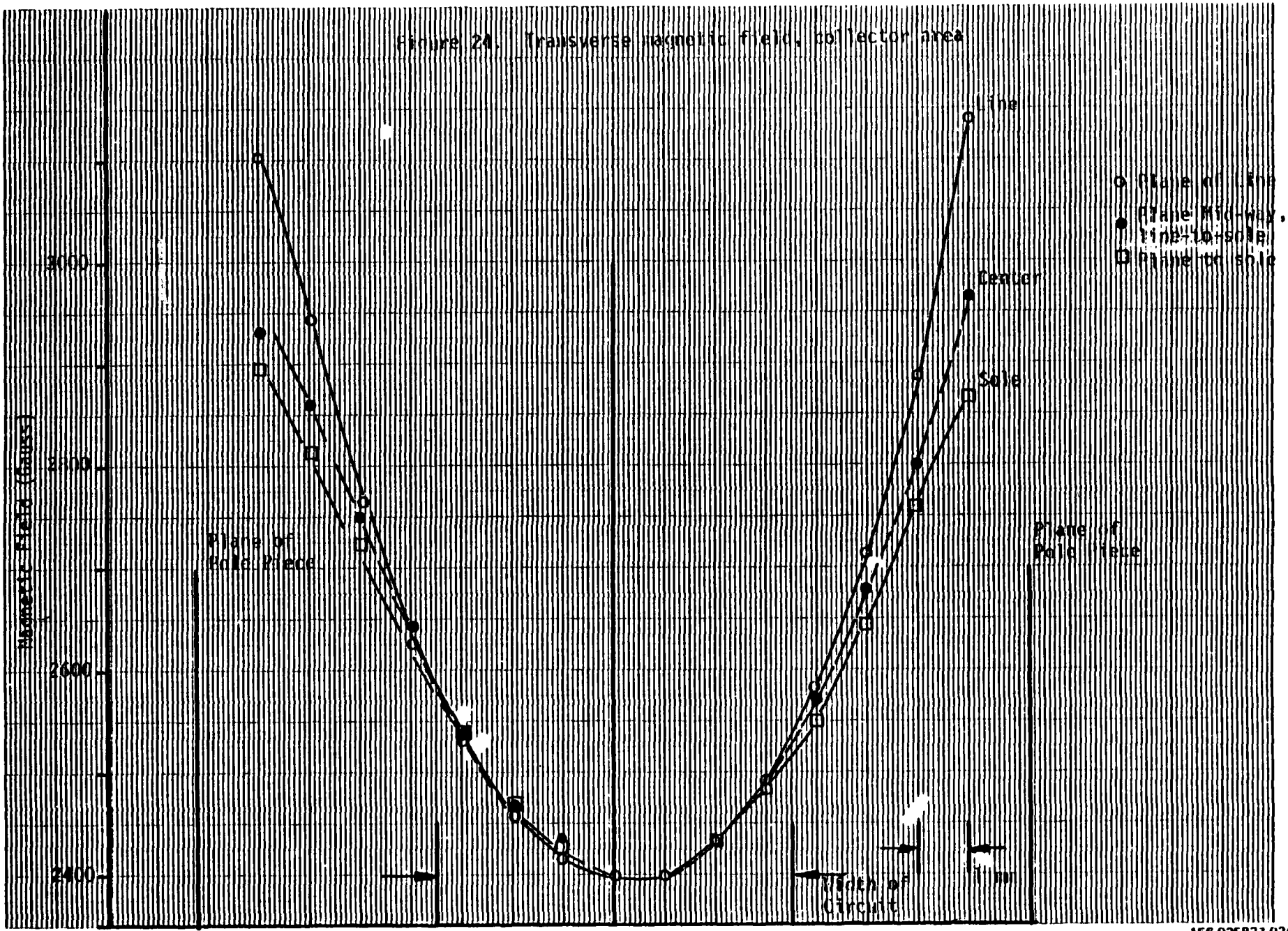

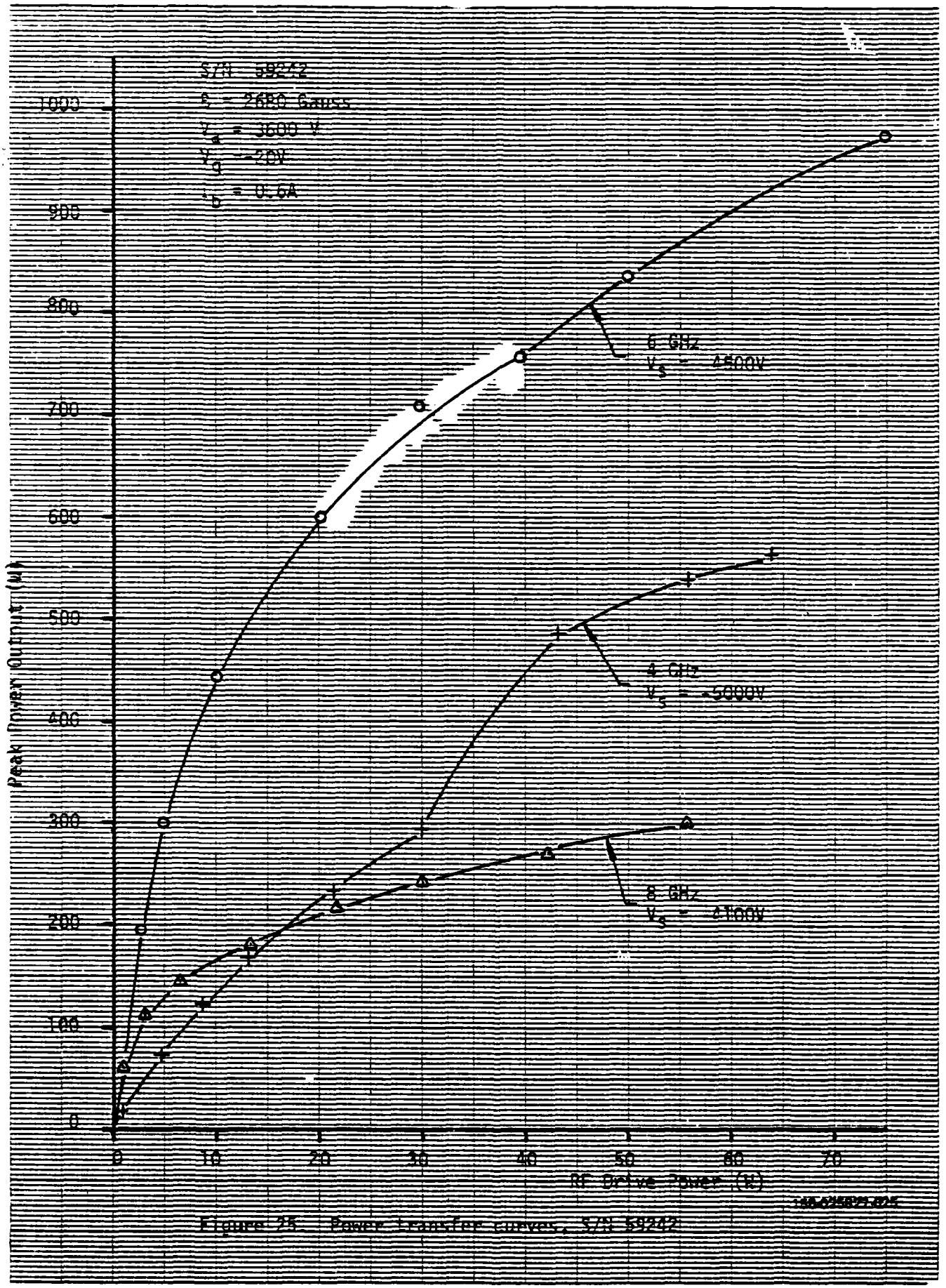

Figure 25. Power transfer curves, S/N 59242

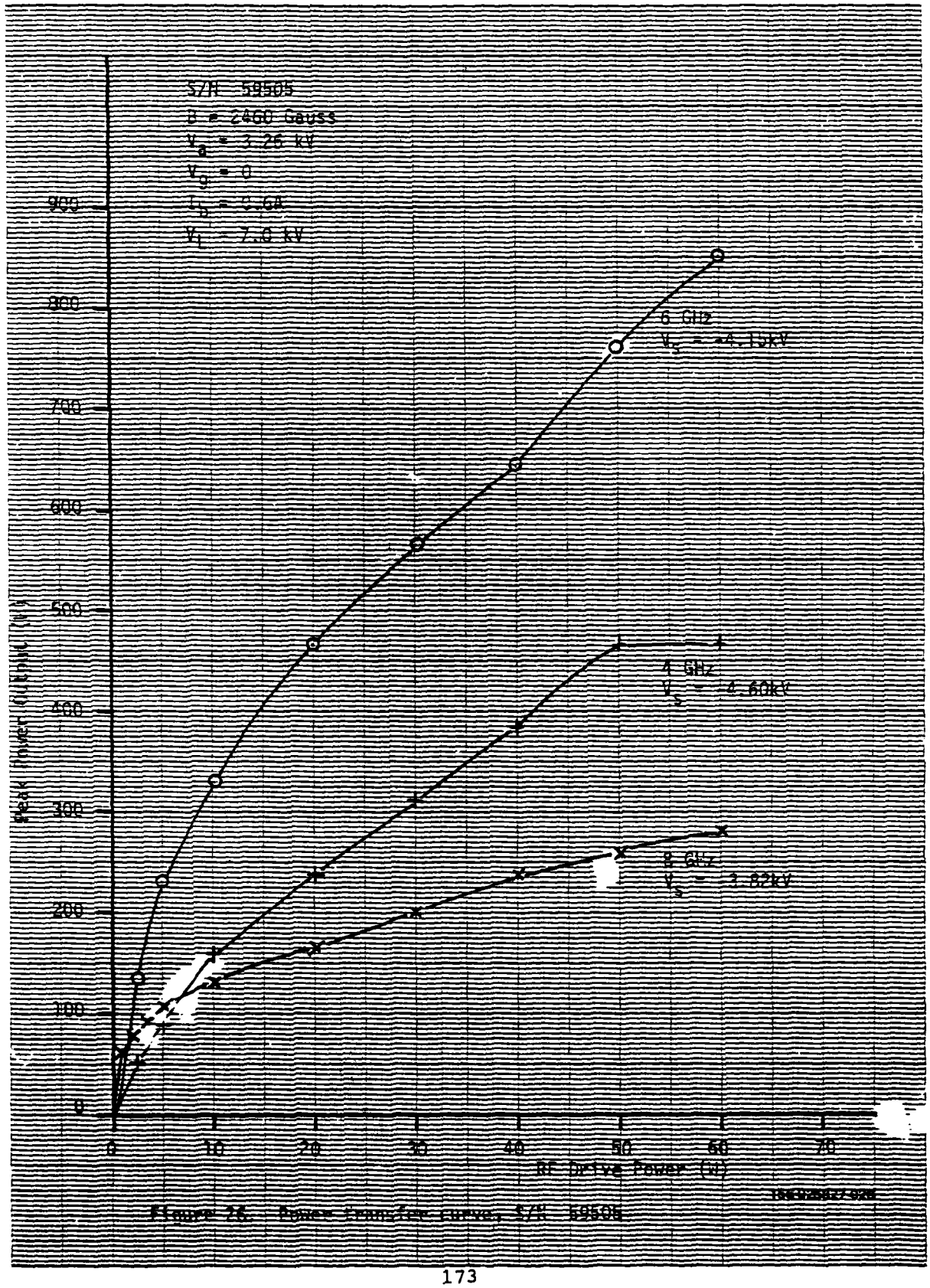

Figure 28. Power transfer curve, S/N 59505

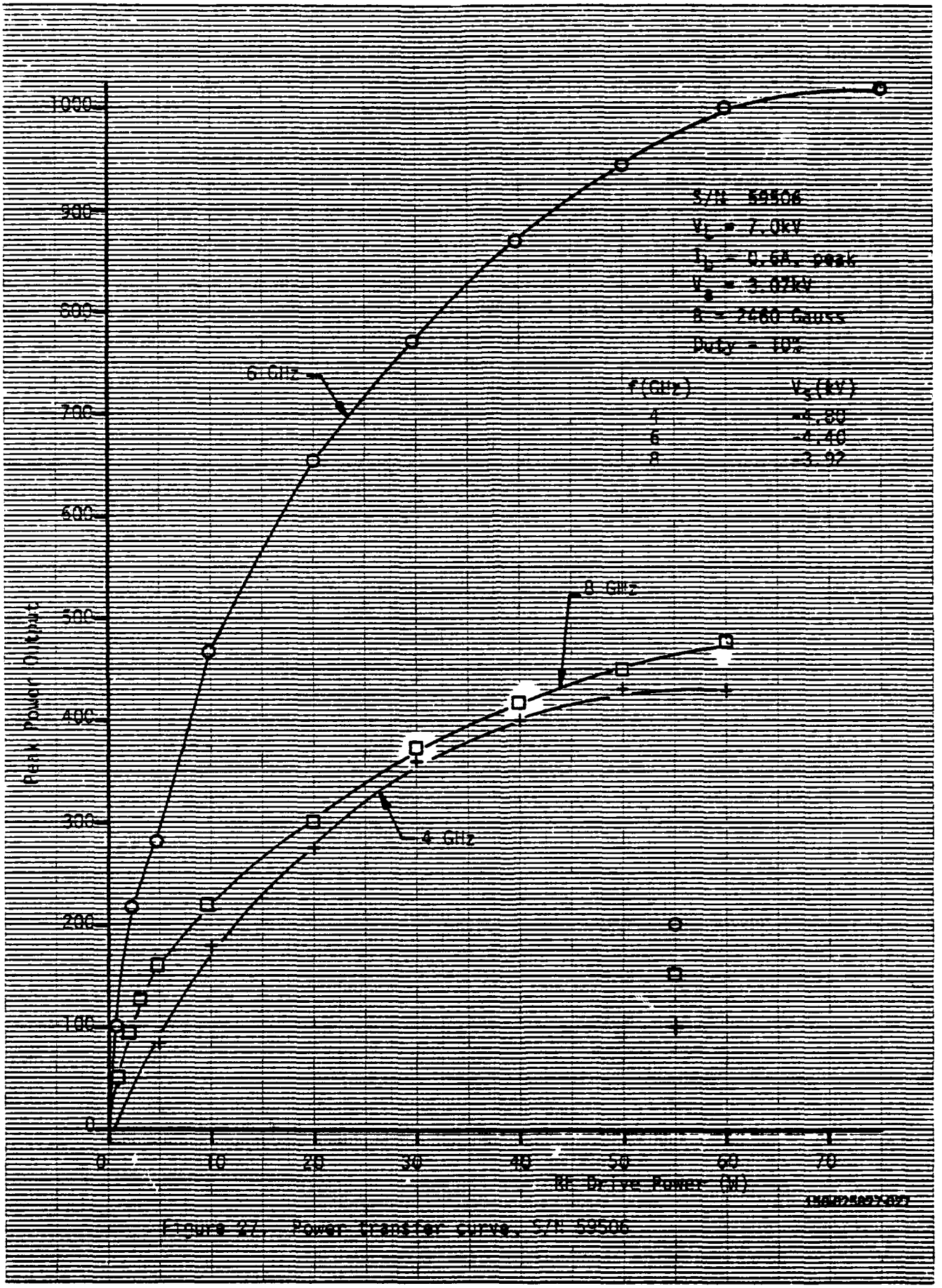

Figure 27. Power transfer curve, S/N 59506

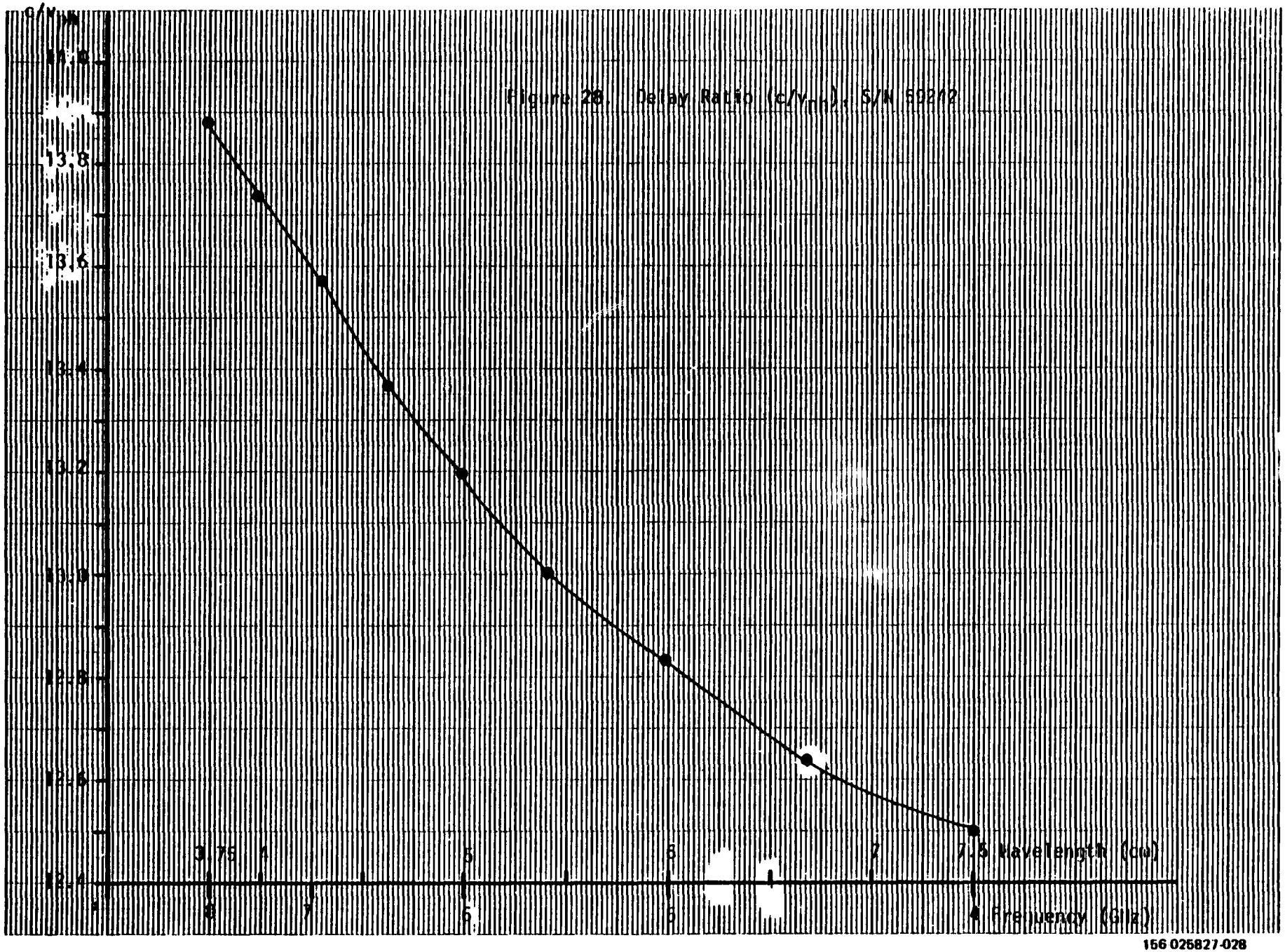

Figure 28. Delay Ratio ($c/v_{(nh)}$): S/N 502/2

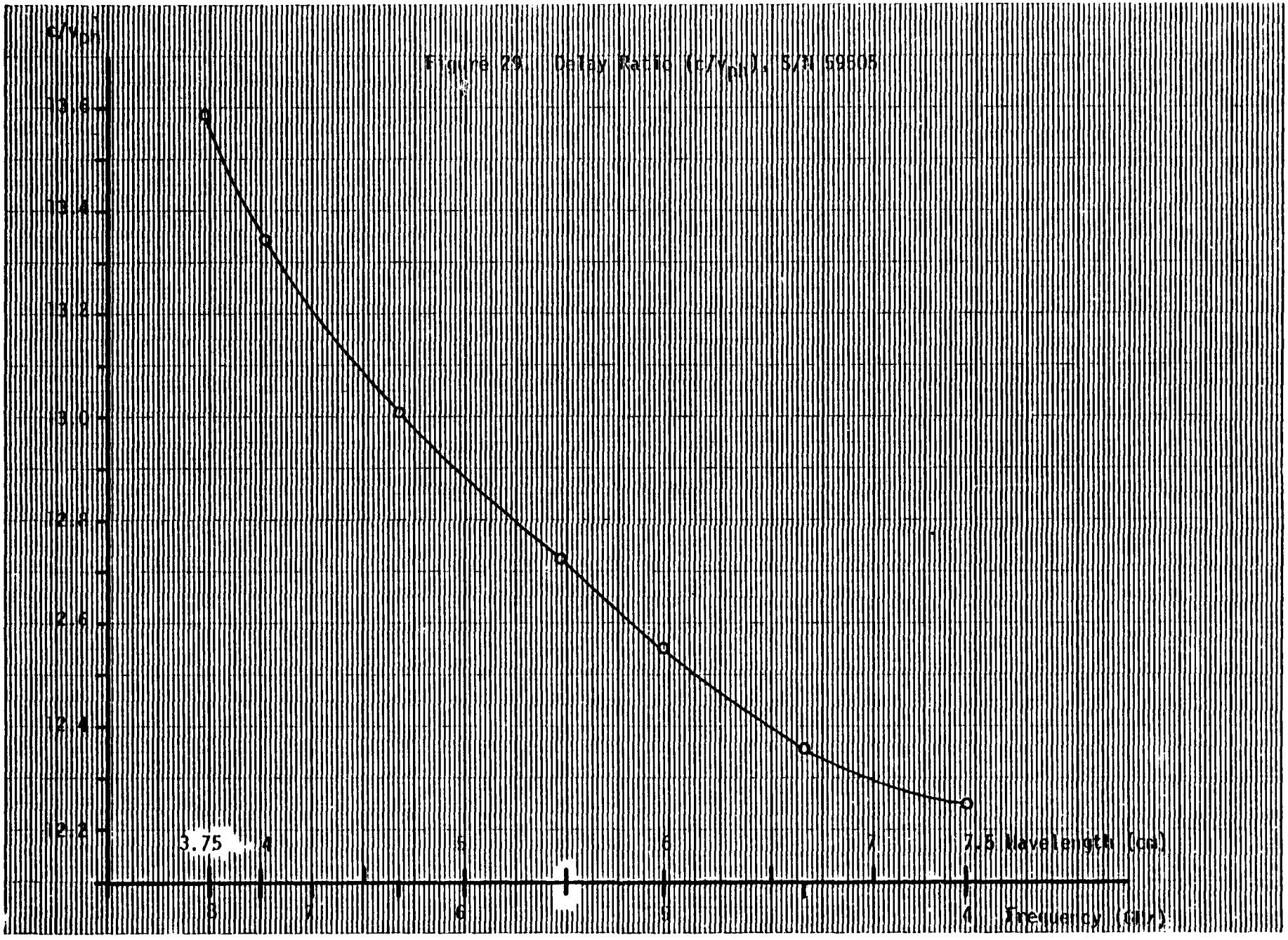

Figure 29. Delay Ratio (c/V_{ph}), S/N 59505

156-025827-029

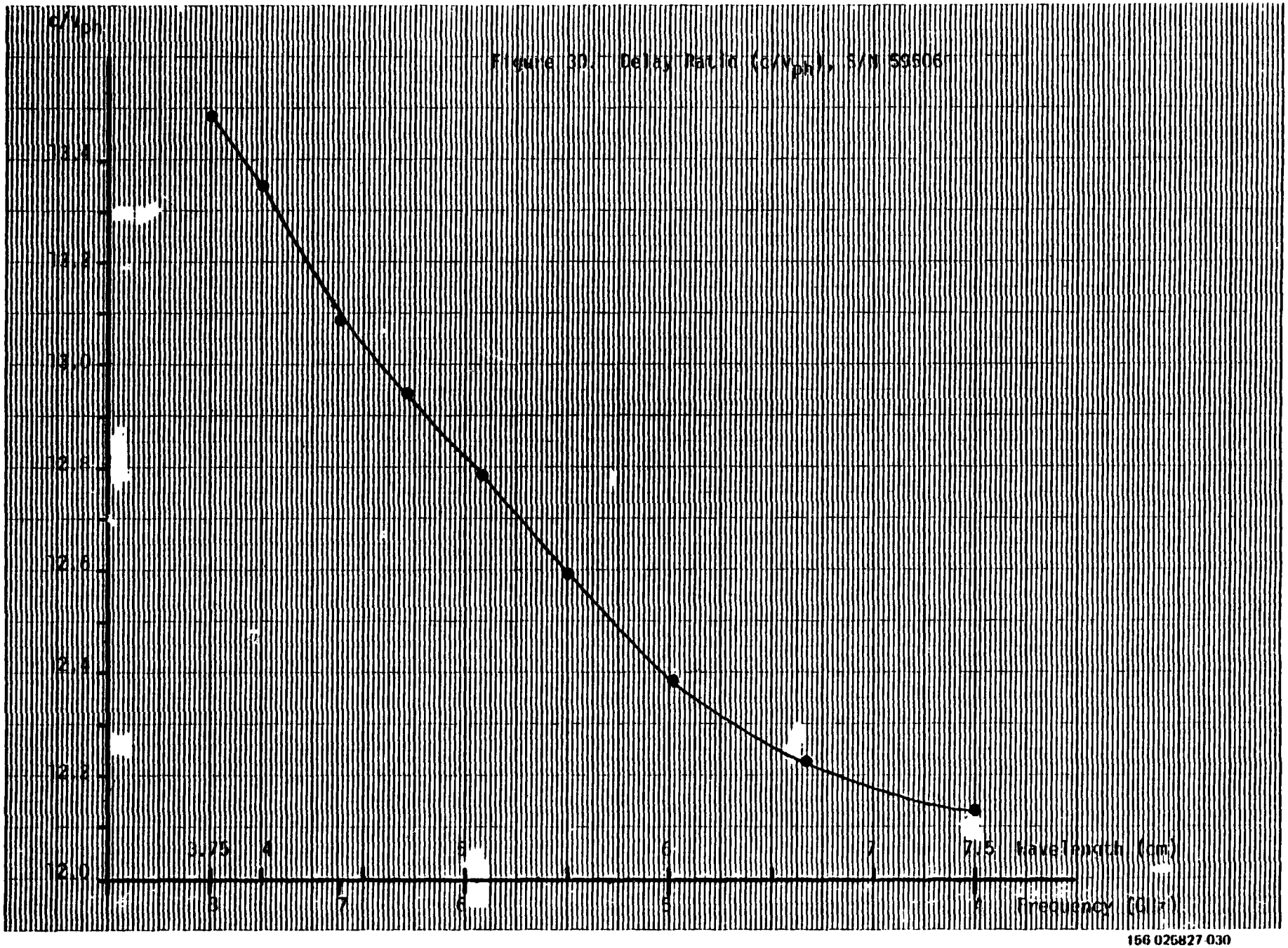

Figure 30. Delay Ratio (c/v_{ph}), S/N 93506

156 026827-030

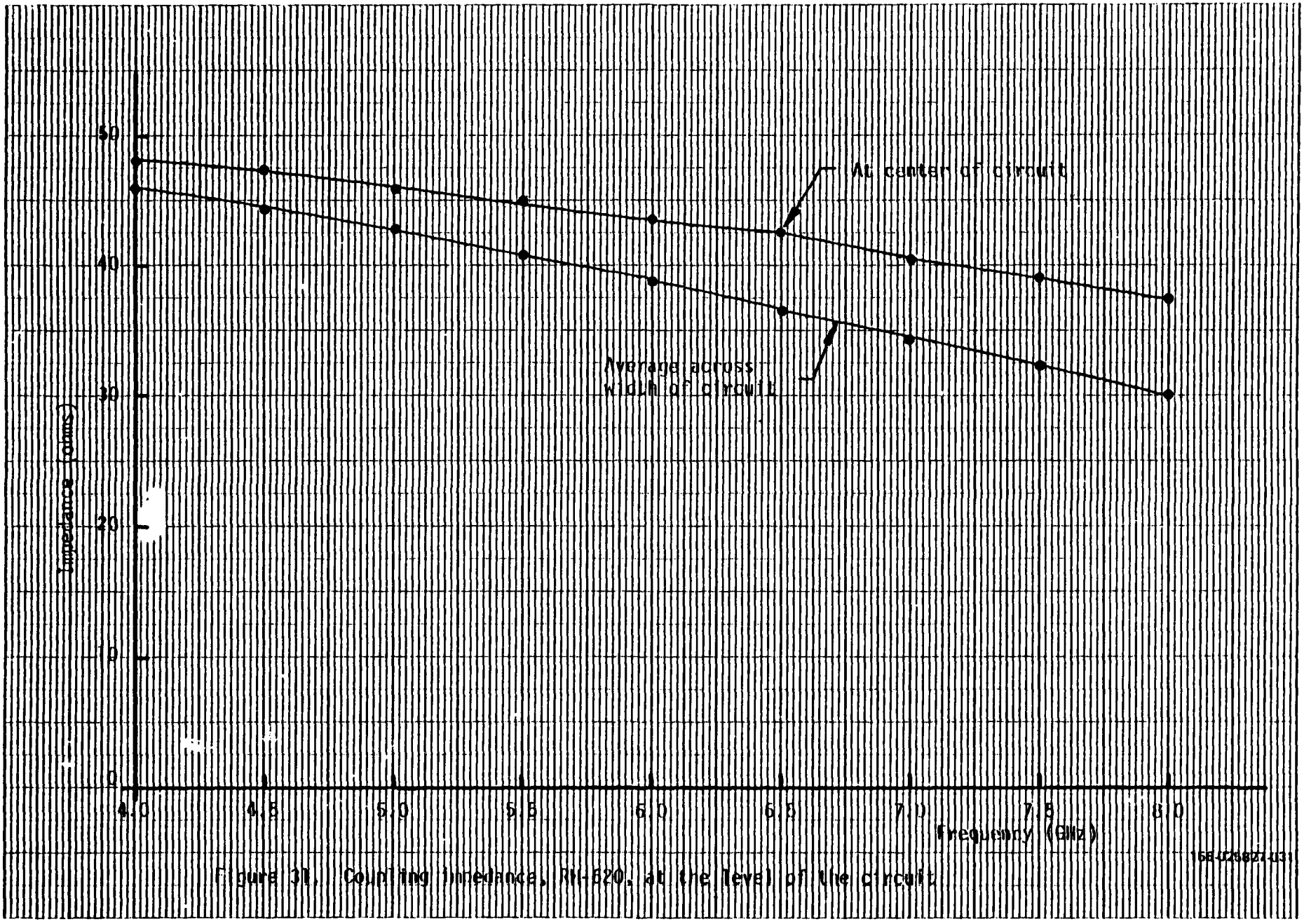

Figure 31. Counting impedance, RH-820, at the level of the circuit.

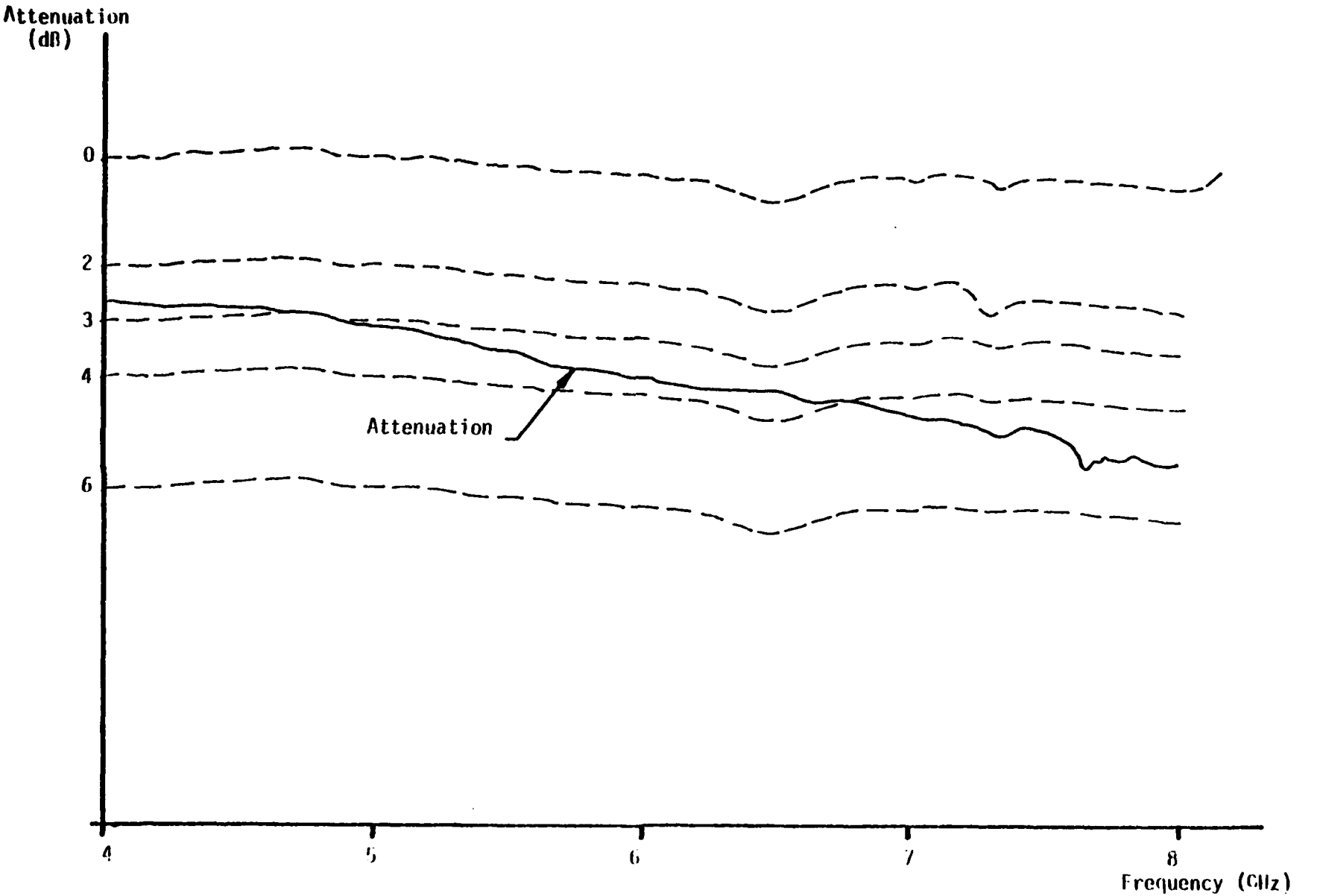

Figure 32. Attenuation of S/N 59242

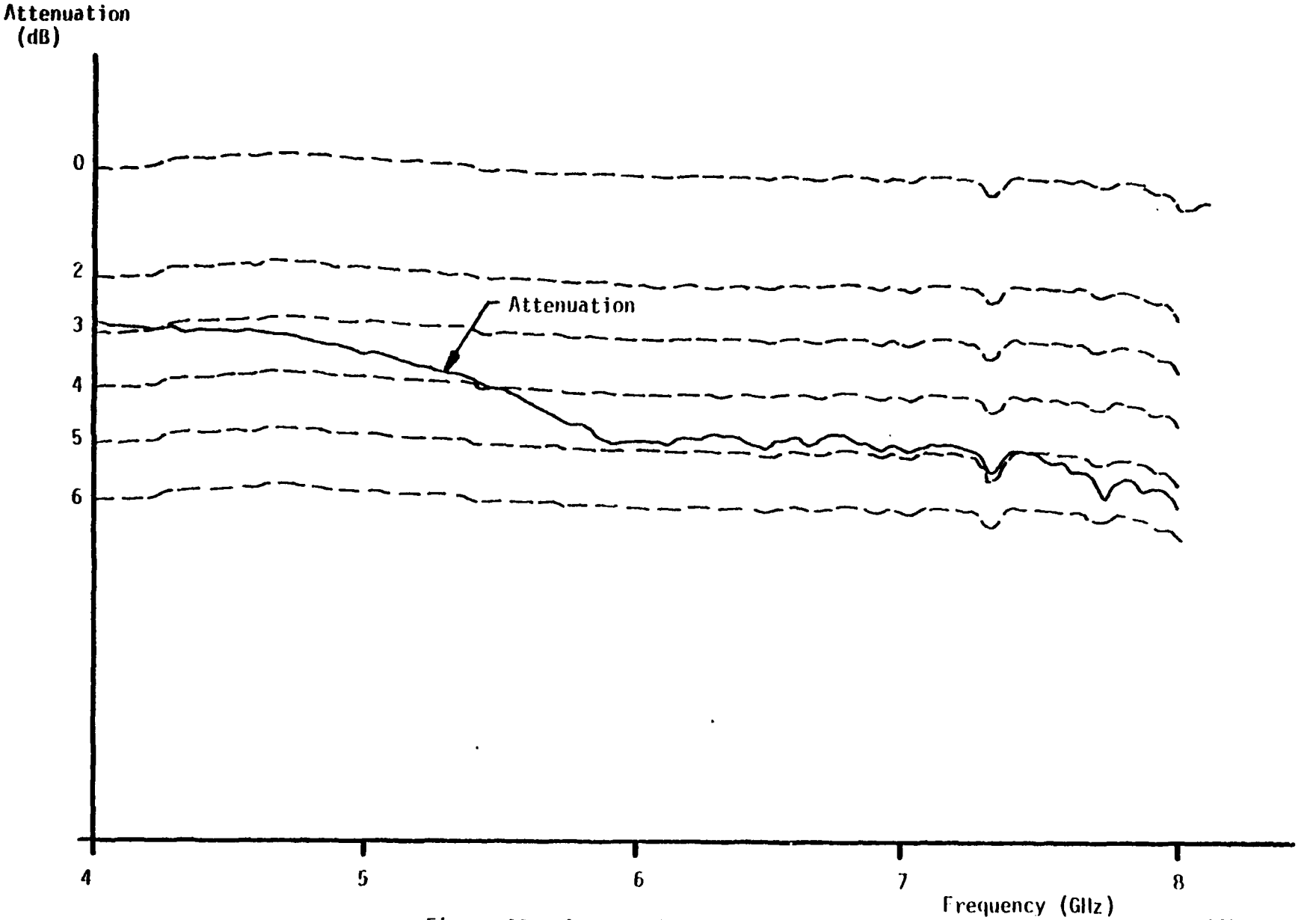

Figure 33. Attenuation of S/N 59505

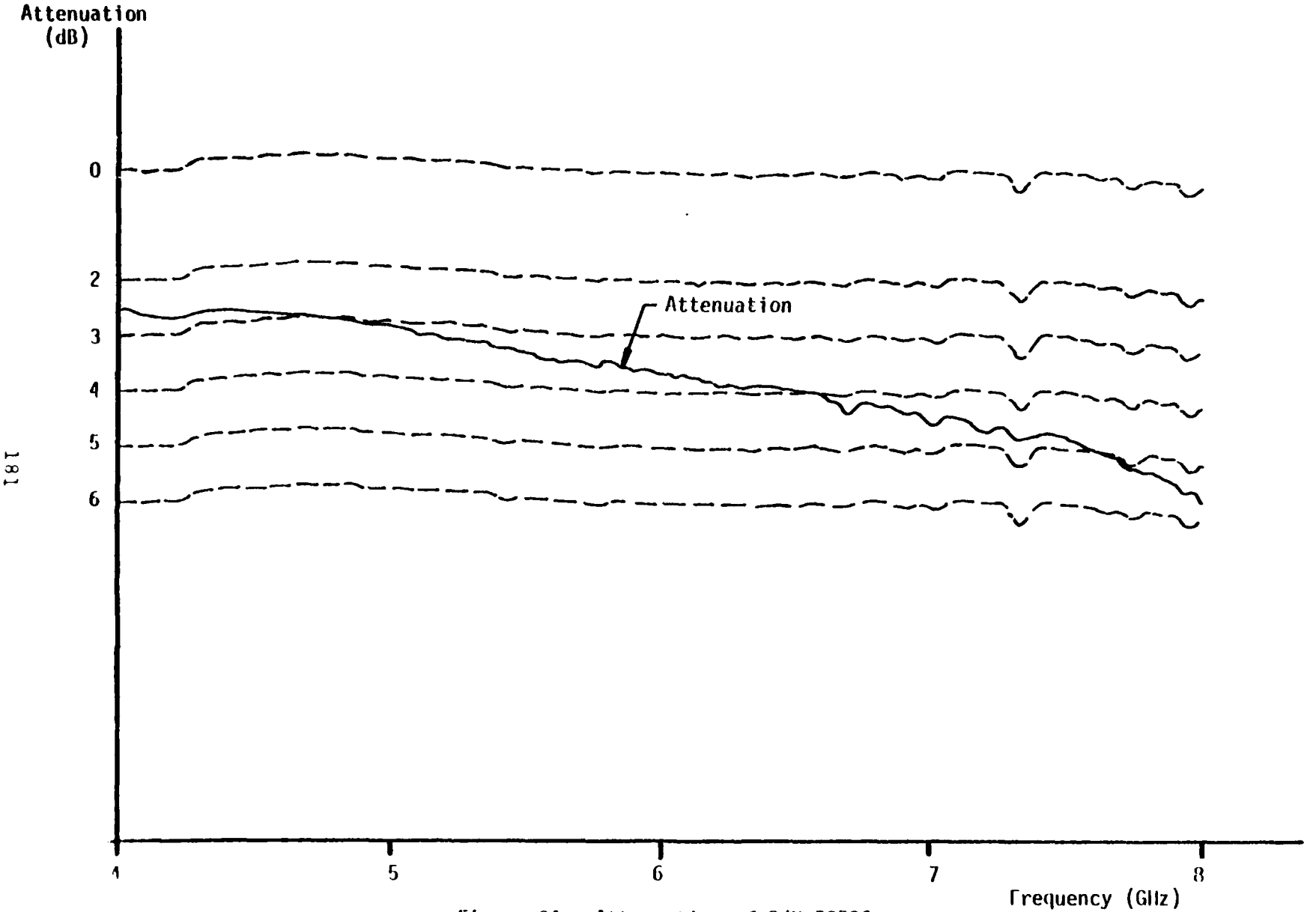

Figure 34. Attenuation of S/N 59506

AD-A125 341 SIMULATION OF DISTRIBUTED-EMISSION AND INJECTED-BEAM CROSSED-FIELD AMPLIF..(U) HARRIS SAI INC ANN ARBOR MI D N MACGREGOR ET AL. APR 80 AFOSR-TR-80-0553 3/3

UNCLASSIFIED F49620-77-C-0091 F/G 9/1 NL

END
DATE FILMED
1 83
DTIC

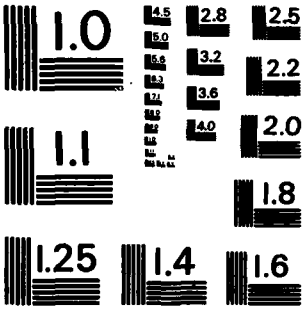

MICROCOPY RESOLUTION TEST CHART
NATIONAL BUREAU OF STANDARDS-1963-A

APPENDIX C

TUBE DATA AND OUTPUT INFORMATION FOR THE TIME-DEPENDENT IBCFA GUN ANALYSIS PROGRAM

A. Data

The following data are required for analysis of a gun.

- Drawings showing the gun shape, grids (if any), electrode positions and dimensions, including the boundary of the cathode emitting surface. Examples are given in Appendix A.
- Voltages of cathode, grids, accelerating anode (plate), line anode, sole, and other electrodes if any.
- Magnetic field.
- Cathode temperature (K).
- Maximum thermionic-emission current density on the cathode surface.

For program verification the measured beam current and the electrode interception currents should be supplied for various magnetic fields and specified electrode voltages, as in Appendix B.

B. Output

The present 20 model provides the following printed information, as in the example (Appendix C).

- Verification of data.
- Mesh plot.
- Important dimensions and beam parameters.

The remaining information is printed only at selected steps.

- The number of rods, total and active
- The number of charges emitted at the cathode, returned (BACK), and the net emitted number
- The number suppressed at the cathode as too small for emission (QSMALL)
- The number intercepted on the plate, line and sole
- The number crossing the exit plane
- The charge above each mesh point on the cathode, CGCAT C/m
- The local electric field EZCATH V/m
- The emitted charge DQEMIT C/m
- Normalized electric fields, charge densities and emitted current densities at the cathode
- Currents (A/m) averaged over several steps. The "EXIT" value printed is the mean beam current per meter width
- Mean cathode current density for each cathode point
- Plotted trajectory segments from a single time step

A separate program uses Tektronix PLOT10 subroutines to display the mesh, the equipotentials and the trajectory segments on a TEKTRONIX 4010 series graphics terminal.

APPENDIX D

SAMPLE OUTPUT FROM THE TWO-DIMENSIONAL TIME-DEPENDENT IBCFA GUN PROGRAM

1

HARRIS SAI, INC., ANN ARBOR, MICHIGAN

IRREGULAR MESH GUN ANALYSIS PROGRAM - RUN NO.62006

CONFIGURATION FOR NORTHROP RUGBO IBCFA
 22222 DATA FILE DATAR 22222 SMALL MESH DENSITY

ICNTRL	COOR	IMAX	JMAX	MAXPAR	ICVCMX	MAJCYC	MAC	MEPH	NSAM	NPRNT	IPRNT
3	VZ	28	36	3000	200	400	3	1	1	100	50

NPSAM	ISAVEP	IPLOTP
1	200	0

LPPLOT	NPCYCP	NDRILL	NCYCAU	IPRNTC
200	10	0	100	100

LIMSC	NOISFL	INBLM8	INBLM8
1	0	0	0

ITUA3	ALPHA1	EPS1	ALPHAU	EPSU	ZSCALE	CTEMPT	UCTHAN
0	1.700E+00	2.000E-02	1.700E+00	2.000E-02	8.540E-05	1.500E+03	4.500E+03

FBRILL	BC	FRT	VSOLE	ANGSOL	VAR	DCTHAN	CURR
3.000E+00	2.500E-01	3.700E+00	-4.000E+03	0.000E+00	7.000E+03	4.600E+01	2.000E+05

FRAC	EPSUEL
0.0000E+00	5.0000E-02

SOLE1	SOLE2	SOLE3	DUMIN4	DUMIN5
2.3600E+02	3.0000E+02	3.3000E+02	0.0000E+00	0.0000E+00

FBRILL	CONMIN	DUMIN8	DUMIN9	DUMI10
3.0000E+00	1.0000E-06	0.0000E+00	0.0000E+00	0.0000E+00

DIAGNOSTIC PRINT SWITCHES

DP(1)=N	DP(2)=N	DP(3)=N	DP(4)=N	DP(5)=N	DP(6)=N	DP(7)=N	DP(8)=N	DP(9)=N	DP(10)=N

PLOT SWITCH	HLFT	HRT	UBOT	UTOP	YLENTH
Y	-2.00000E+01	1.50000E+02	-3.00000E+01	3.00000E+02	7.00000E+00
Y	-2.00000E+01	1.50000E+02	-3.00000E+01	3.00000E+02	7.00000E+00
Y	-2.00000E+01	1.50000E+02	-3.00000E+01	3.00000E+02	7.00000E+00
N	-2.00000E+01	1.50000E+02	0.00000E+00	8.00000E+02	7.00000E+00
N	-2.00000E+01	1.50000E+02	0.00000E+00	8.00000E+02	7.00000E+00

10 EQUIPOTENTIALS TO BE PLOTTED

5.000E+02	1.000E+03	1.500E+03	2.000E+03	2.500E+03	3.000E+03	3.500E+03	4.000E+03	5.000E+03	6.000E+03

*** GEOMETRY DATA ***

NS	NTP
2	G

I	J	X	Y	U
4	25	0.00000E+00	2.02000E+02	0.00000E+00
11	25	1.30000E+01	2.02000E+02	0.00000E+00
11	6	1.30000E+01	1.00000E+01	0.00000E+00

NS	NTP
2	G

I	J	X	Y	U
4	24	0.00000E+00	1.94000E+02	0.00000E+00
9	24	8.00000E+00	1.94000E+02	0.00000E+00
9	6	8.00000E+00	1.00000E+01	0.00000E+00

NS	NTP
1	G

I	J	X	Y	U
24	29	7.00000E+01	2.37000E+02	7.00000E+03
22	24	6.59000E+01	2.00050E+02	4.50000E+03

NS	NTP
1	N

I	J	X	Y	U
20	3	5.72100E+01	-1.50000E+01	4.50000E+03
11	3	1.30000E+01	-1.50000E+01	0.00000E+00

NS	NTP
1	N

I	J	X	Y	U
2	36	-1.60000E+01	3.30000E+02	-4.80000E+03
23	36	6.30000E+01	3.30000E+02	7.00000E+03

NS	NTP
1	N

I	J	X	Y	U
22	23	1.20000E+02	1.81000E+02	7.00000E+03
22	23	6.69100E+01	1.81000E+02	4.50000E+03

NS	NTP
1	C

I	J	X	Y	U
4	5	0.00000E+00	0.00000E+00	0.00000E+00
4	23	0.00000E+00	1.81000E+02	0.00000E+00

NS	NTP
5	B

I	J	X	Y	U
11	3	1.30000E+01	-1.50000E+01	0.00000E+00

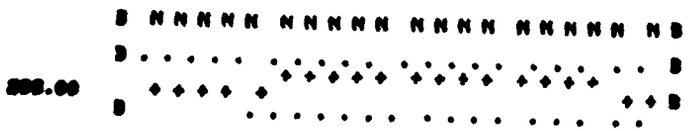

```
                   5   1.30000E+01     0.00000E+00     0.00000E+00
   11              6   1.30000E+01     1.00000E+01     0.00000E+00
    9              6   8.00000E+00     1.00000E+01     0.00000E+00
    9              5   8.00000E+00     0.00000E+00     0.00000E+00
    4              5   0.00000E+00     0.00000E+00     0.00000E+00
   NS            NTP
    4              B
    I              J             X               Y               U
    4             23   0.00000E+00     1.81000E+02     0.00000E+00
    4             24   0.00000E+00     1.94000E+02     0.00000E+00
    4             25   0.00000E+00     2.02000E+02     0.00000E+00
    2             29  -1.60000E+01     2.19000E+02    -4.80000E+03
    2             36  -1.60000E+01     3.30000E+02    -4.80000E+03
   NS            NTP
    4              B
    I              J             X               Y               U
   23             35   6.30000E+01     3.30000E+02     7.00000E+03
   23             31   6.30000E+01     2.60000E+02     7.00000E+03
   24             29   7.00000E+01     2.37000E+02     7.00000E+03
   26             25   1.20000E+02     2.02000E+02     7.00000E+03
   26             23   1.80000E+02     1.81000E+02     7.00000E+03
   NS            NTP
    6              B
    I              J             X               Y               U
   22             23   6.69100E+01     1.81000E+02     4.50000E+03
   22             24   6.59000E+01     2.00050E+02     4.50000E+03
   21             25   5.98400E+01     2.02700E+02     4.50000E+03
   20             25   5.28400E+01     2.02370E+02     4.50000E+03
   20             24   4.60000E+01     1.99000E+02     4.50000E+03
   20              5   5.63400E+01     0.00000E+00     4.50000E+03
   20              3   5.72100E+01    -1.50000E+01     4.50000E+03
   NS            NTP
   -2              U

1                                              *** END OF DATA ***
   RECTANGULAR MESH AT CATHODE CONTAINS   3 SEGMENTS NORMAL TO CATHODE
 MESH CONVERGED AFTER   31 ITERATIONS

      300.00                                          MESH FOR RUN 62005


            B N N N N N  N N N N N  N N N N  N N N N N  N B
            B . . . . .  . . . . .  . . . .  . . . .  . . B
      200.00  + + + + +  + + + + +  + + + +  + + + +    
            B          . . . . . .  . . . .  . . .  . . + + B
```

-2 U

1 *** END OF DATA ***

RECTANGULAR MESH AT CATHODE CONTAINS 3 SEGMENTS NORMAL TO CATHODE
MESH CONVERGED AFTER 31 ITERATIONS

MESH FOR RUN 82005

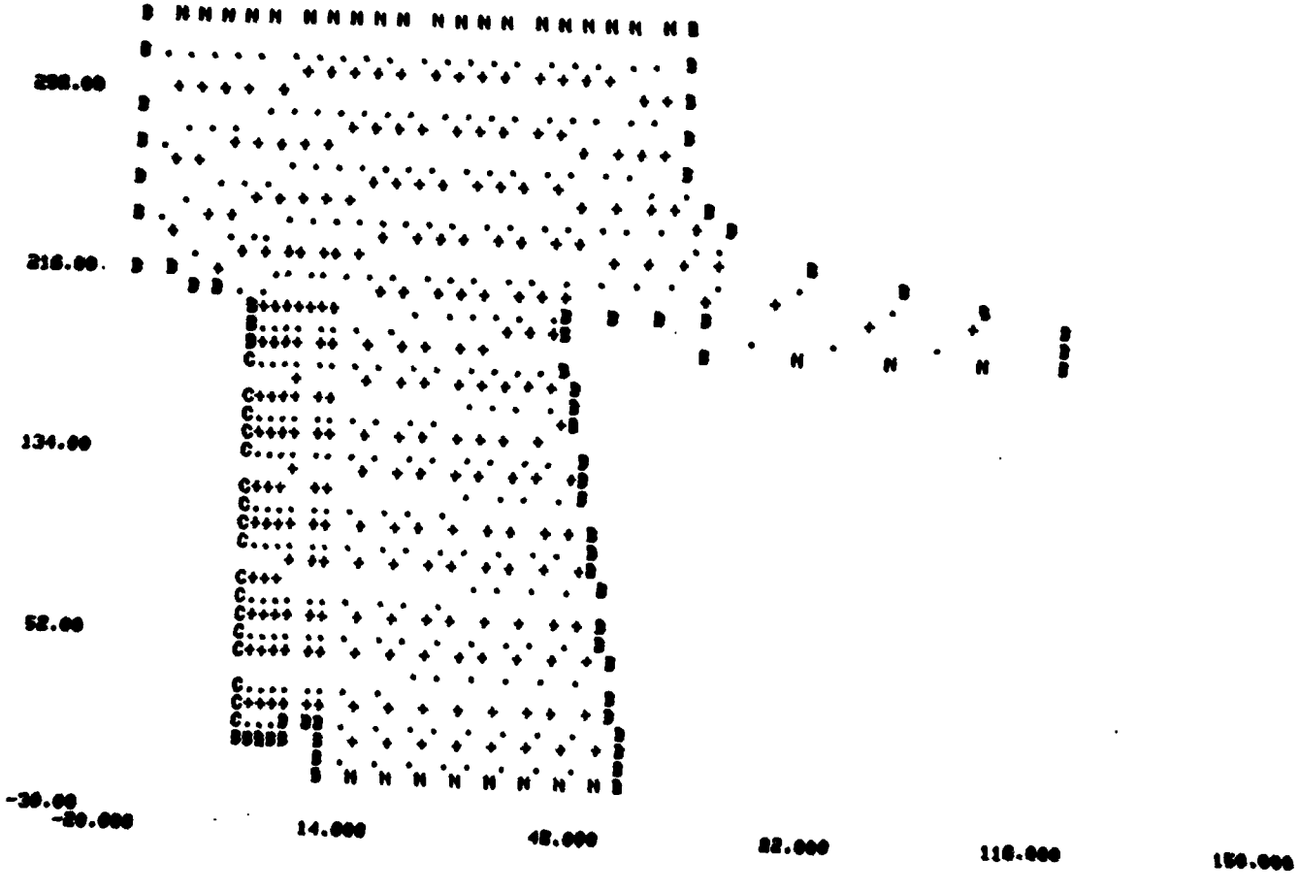

EMISSION CONTROLLED BY SPACE CHARGE

MESH INTERVALS NORMAL TO CATHODE :
4.602E-05 4.602E-05 4.602E-05 4.602E-05 4.602E-05 4.602E-05 4.602E-05 4.602E-05

MESH INTERVALS NORMAL TO CATHODE :
4.602E-05 4.602E-05 4.602E-05 4.602E-05 4.602E-05 4.602E-05 4.602E-05 4.602E-05

MESH INTERVALS NORMAL TO CATHODE :
4.602E-05

CATHODE LENGTH(M)	4.342E-03
PLATE HEIGHT(M)	1.168E-03
SOLE PLANE 1(M)	5.994E-03
SOLE PLANE 2(M)	7.620E-03
SOLE END(M)	8.382E-03
SOLE HEIGHT(M)	-4.064E-04
LINE HEIGHT(M)	1.600E-03
PARALLEL MESH INTERVAL(M)	8.554E-04
PERPENDICULAR INTERVAL(M)	4.602E-05
PARTICLES/INTERVAL	5.101E+00
THERMIONIC CURRENT DENSITY(A/M**2)	2.000E+05
CHARGE/ROD(C/M)	-1.430E-10
CATHODE TEMPERATURE(K)	1.500E+03
NORMAL VELOCITY(M/S)	1.820E+05
MAGNETIC FIELD(T)	2.500E-01
PLASMA FREQ/CYCLOTRON FREQ	4.211E+00
DEBYE LENGTH(M) AT CATHODE	1.109E-06
TIME STEP(S)	1.428E-11
STEPS/CYLOTRON PERIOD	1.001E+01

STEP	ITERS	# RODS	ACTIVE	EMITTED	BACK	NET IN	QSMALL	PLATE	LINE	SOLE	EXIT	DUMMY
50	11	1316	1273	46.36	16.89	29.46	0.00	0.00	0.00	0.00	26.76	0.00

**** AT CATHODE DURING STEP 100 OF RUN 62005 ****

CGCAT	-9.294E-11	-6.072E-10	-4.216E-10	-3.361E-10	-3.187E-10	-4.014E-10	-5.398E-10	-7.268E-10	
CGCAT	-9.548E-10	-1.147E-09	-8.958E-10	-1.387E-09	-1.024E-09	-1.515E-09	-1.077E-09	-1.432E-09	
CGCAT	-1.328E-09								
EZCATH	-7.017E+04	-8.539E+05	-1.391E+06	-1.628E+06	-1.548E+06	-1.472E+06	-1.098E+06	-9.982E+05	
EZCATH	-4.808E+05	-6.911E+06	-4.070E+05	-7.107E+05	-4.367E+06	-6.952E+05	-4.465E+05	-6.275E+05	
EZCATH	-2.441E+05								
DQEMIT	0.000E+00	-7.295E-10	-7.295E-10	-7.295E-10	-7.295E-10	-7.295E-10	-7.295E-10	-7.295E-10	
DQEMIT	-1.321E-10	-4.156E-10	-2.406E-11	-2.196E-10	0.000E+00	-5.689E-11	0.000E+00	0.000E+00	
DQEMIT	0.000E+00								

E/(E-MAX ; NO SPACE CHARGE) %					2	22	36	42	40	38	29	26	12	18	11	18	11	18	12	16	6
RHO/RHO-BRILLOUIN %					-15	-62	-36	-28	-27	-34	-46	-63	-82	-99	-77	-120	-89	-131	-93	-124	-231
J EMITTED/J THERMIONIC %					0	100	100	100	100	100	100	100	18	57	3	30	0	6	0	0	0
100	9	1347	1298	41.64	13.26	28.38	0.00	0.00	0.00	0.00	25.68	0.00									

CURRENTS(A/M) AVERAGED OVER 100 STEPS AFTER STEP 100

OVER CATH	SOLE IN	SOLE OUT	EMITTED	BACK	NET CATH	PLATE	LINE ANODE	SOLE	EXIT	DUMMY
0.00	0.00	0.00	559.92	229.36	330.56	0.00	0.10	0.00	211.18	0.00
MEAN J-CATH(A/M**2)	9.650E+02	2.000E+05	2.000E+05	2.000E+05	2.000E+05	2.000E+05	2.000E+05	2.000E+05	2.000E+05	2.000E+05
MEAN J-CATH(A/M**2)	8.710E+04	1.573E+05	8.437E+04	1.154E+05	6.219E+04	9.305E+04	6.065E+04	1.083E+05		
MEAN J-CATH(A/M**2)	6.870E+04									

STEP	ITERS	# RODS	ACTIVE	EMITTED	BACK	NET IN	QSMALL	PLATE	LINE	SOLE	EXIT	DUMMY
150	11	1383	1364	48.65	13.35	38.30	0.00	0.00	0.00	0.00	84.71	0.00

```
                                        ***** AT CATHODE DURING STEP  200 OF RUN 62005 *****
 CQCAT  -9.296E-11  -6.073E-10  -4.217E-10  -3.365E-10  -3.183E-10  -4.026E-10  -5.416E-10  -7.336E-10
 CQCAT  -8.029E-10  -1.142E-09  -9.059E-10  -1.284E-09  -7.809E-10  -1.069E-09  -7.902E-10  -9.721E-10
 CQCAT  -1.410E-09
EZCATH  -7.016E+04  -8.538E+05  -1.390E+06  -1.627E+06  -1.547E+06  -1.470E+06  -1.094E+06  -9.931E+05
EZCATH  -4.768E+05  -6.927E+05  -4.118E+05  -6.839E+05  -4.035E+05  -6.353E+05  -3.990E+05  -4.606E+05
EZCATH   1.945E+03
DQEMIT   0.000E+00  -7.295E-10  -7.295E-10  -7.295E-10  -7.295E-10  -7.295E-10  -7.295E-10  -7.295E-10
DQEMIT  -1.848E-10  -4.233E-10  -8.489E-11  -3.217E-10  -1.311E-10  -3.668E-10  -1.117E-10  -6.903E-11
DQEMIT   0.000E+00
 E/tE-MAX , NO SPACE CHARGE ) %          2  22  36  42  40  38  28  26  12  18  11  18  10  16  10  12   0
 RHO/RHO-BRILLOUIN %                  -15 -52 -36 -28 -27 -34 -46 -63 -77 -99 -78-106 -67 -93 -68 -84-246
 J EMITTED/J THERMIONIC %               0 100 100 100 100 100 100 100  25  58   3  44  18  50  15   9   0
  200       8    1419    1362   47.13   16.77   30.36    0.00    0.00    0.00    0.00   29.98    0.00

                                  CURRENTS(A/M) AVERAGED OVER  100 STEPS AFTER STEP  200
OVER CATH    SOLE IN   SOLE OUT   EMITTED      BACK   NET CATH     PLATE   LINE ANODE     SOLE      EXIT     DUMMY
    0.00       0.00       0.00     451.50    166.71    284.80      0.00       0.00       0.00    280.00      0.00
MEAN J-CATH(A/M**2)   0.000E+00  2.000E+05  2.000E+05  2.000E+05  2.000E+05  2.000E+05  2.000E+05  2.000E+05
MEAN J-CATH(A/M**2)   3.567E+04  1.134E+05  8.897E+03  7.698E+04  6.996E+03  8.706E+04  1.002E+04  2.789E+04
MEAN J-CATH(A/M**2)   0.000E+00
```

TRAJECTORY SEGMENTS FOR RUN 62005 STEP 200

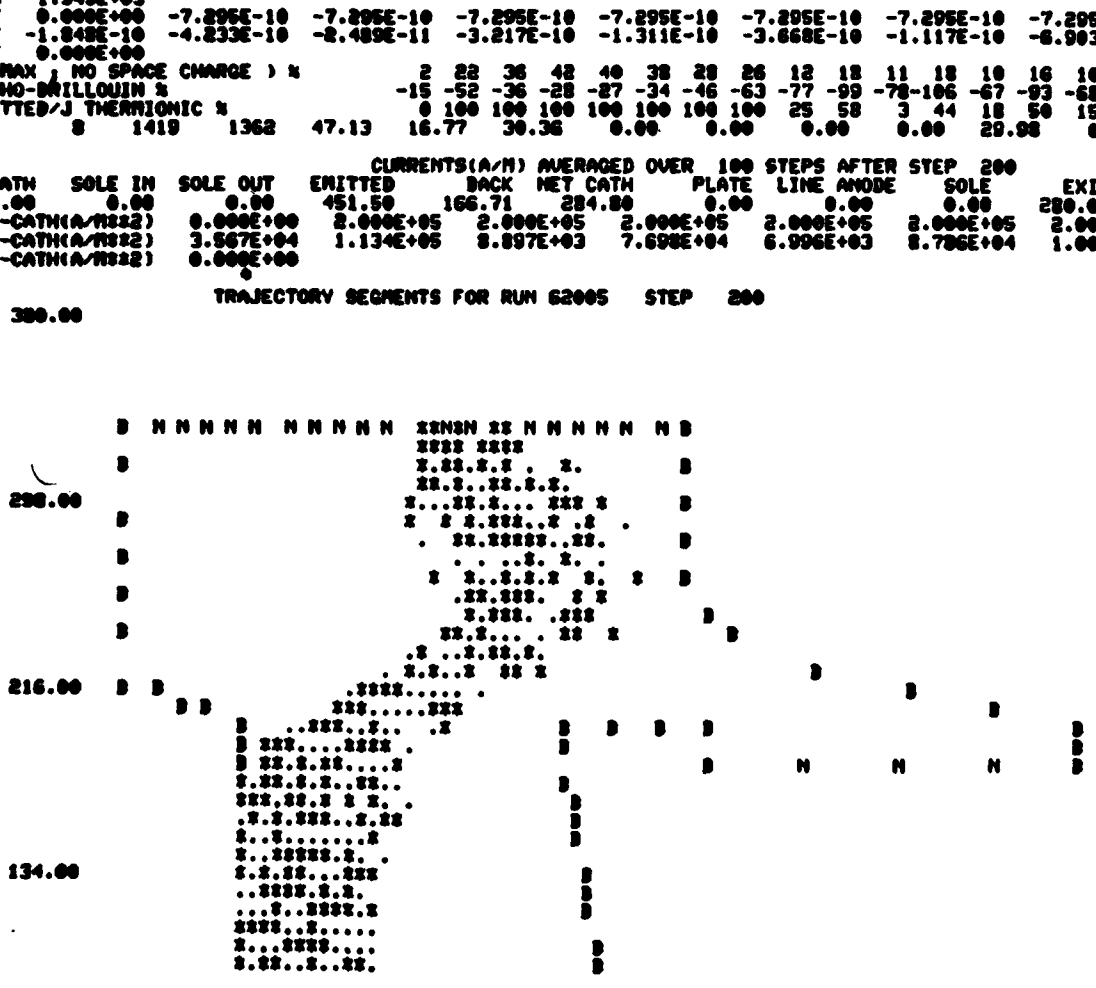

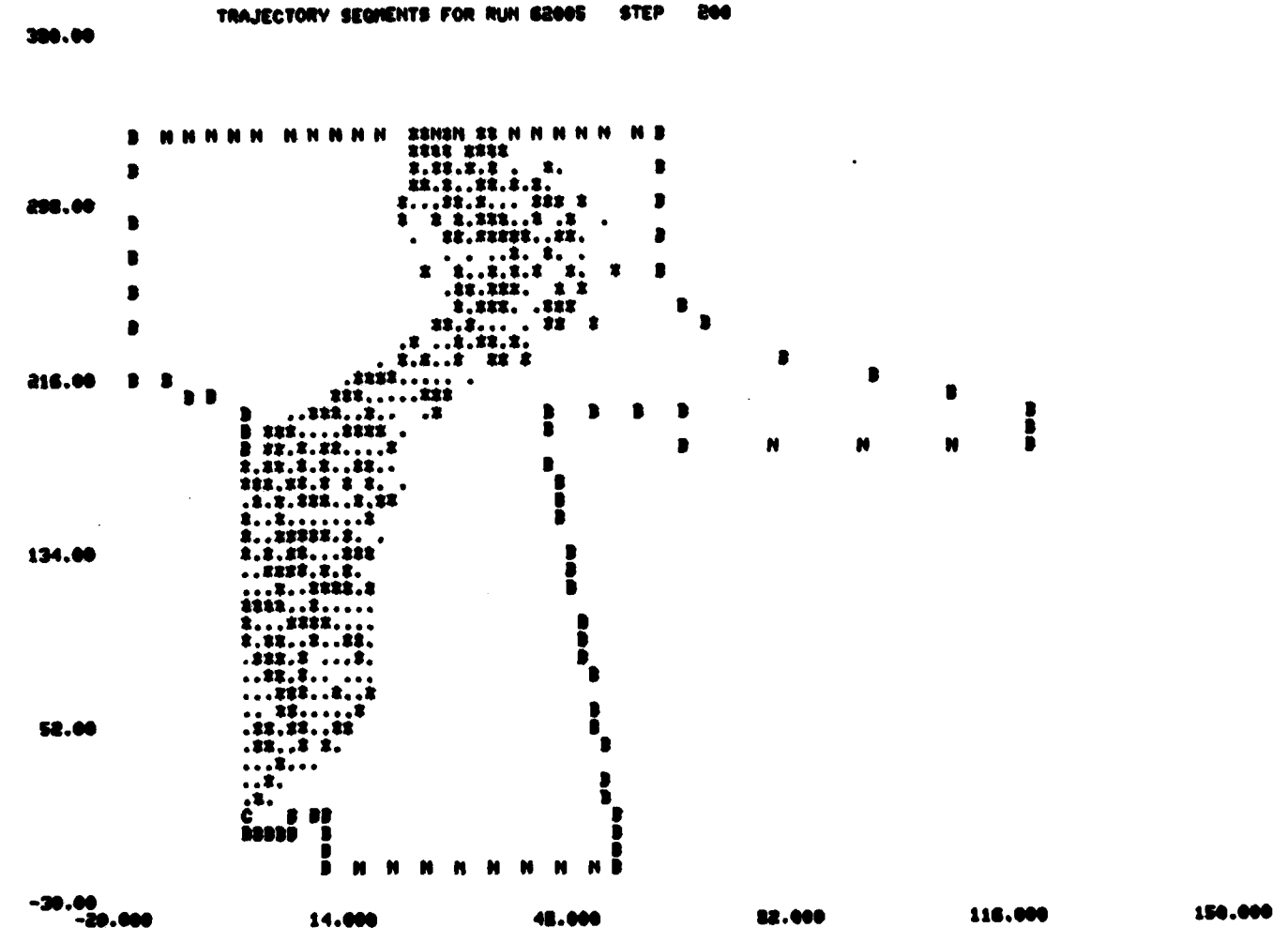

BEGIN SAVE AFTER TIME STEP 200
END SAVE AFTER TIME STEP 200

STEP	ITERS	# RODS	ACTIVE	EMITTED	BACK	NET IN	OSHALL	PLATE	LINE	SOLE	EXIT	DUMMY
250	0	1410	1367	45.78	14.34	31.45	0.00	0.00	0.00	0.00	27.54	0.00

AT CATHODE DURING STEP 300 OF RUN 62005

CCCAT	-9.895E-11	-6.973E-10	-4.817E-10	-3.364E-10	-3.198E-10	-4.824E-10	-5.414E-10	-7.351E-10

```
                    BBBBB  B                    B
                           B                    B
                           B  N  N  N  N  N  N  N  N B

      -30.00
          -20.000                14.000              48.000              82.000              116.000              150.000
     BEGIN SAVE AFTER TIME STEP  200
     END SAVE AFTER TIME STEP  200

  STEP   ITERS  # RODS  ACTIVE  EMITTED   BACK  NET IN  QSMALL   PLATE    LINE    SOLE    EXIT   DUMMY
   250      9    1419    1367   45.79   14.34   31.45    0.00    0.00    0.00    0.00   27.54    0.00

                                        #### AT CATHODE DURING STEP  300 OF RUN 62005 ####
  CGCAT  -9.295E-11  -6.073E-10  -4.217E-10  -3.364E-10  -3.192E-10  -4.024E-10  -5.414E-10  -7.351E-10
  CGCAT  -9.606E-10  -1.135E-08  -8.869E-10  -1.278E-09  -8.936E-10  -1.010E-09  -8.652E-10  -7.539E-10
  CGCAT  -3.191E-10
 EZCATH  -7.016E+04  -8.538E+05  -1.391E+06  -1.627E+06  -1.547E+06  -1.470E+06  -1.095E+06  -9.947E+05
 EZCATH  -4.816E+05  -6.983E+05  -4.195E+05  -6.848E+05  -3.819E+05  -5.958E+05  -3.616E+05  -3.194E+05
 EZCATH   7.101E+04
 DQEMIT   0.000E+00  -7.295E-10  -7.295E-10  -7.295E-10  -7.295E-10  -7.295E-10  -7.295E-10  -7.295E-10
 DQEMIT  -1.280E-10  -4.437E-10  -6.121E-11  -2.703E-10   0.000E+00  -3.364E-10   0.000E+00   0.000E+00
 DQEMIT   0.000E+00
  E/(E-MAX ; NO SPACE CHARGE ) %          2  22  36  42  40  38  28  26  13  18  11  18  10  15   9   8  -1
  RHO/RHO-BRILLOUIN %                  -15 -52 -36 -28 -27 -34 -46 -63 -83 -98 -77-111 -77 -87 -75 -65 -55
  J EMITTED/J THERMIONIC %               0 100 100 100 100 100 100 100  18  61   8  37   0  46   0   0   0
   300      11    1419    1357   44.38   12.63   31.75    0.00    0.00    0.00    0.00   32.11    0.00

                                        CURRENTS(A/M) AVERAGED OVER  100 STEPS AFTER STEP  300
 OVER CATH   SOLE IN   SOLE OUT   EMITTED      BACK  NET CATH     PLATE  LINE ANODE     SOLE      EXIT      DUMMY
      0.00      0.00       0.00    452.58    147.57    305.01      0.00       0.00      0.00    304.52       0.00
 MEAN J-CATH(A/M##2)   0.000E+00  2.000E+05  2.000E+05  2.000E+05  2.000E+05  2.000E+05  2.000E+05  2.000E+05
 MEAN J-CATH(A/M##2)   3.798E+04  1.131E+05  9.835E+03  7.797E+04  6.790E+03  9.069E+04  1.193E+04  2.452E+04
 MEAN J-CATH(A/M##2)   0.000E+00

  STEP   ITERS  # RODS  ACTIVE  EMITTED   BACK  NET IN  QSMALL   PLATE    LINE    SOLE    EXIT   DUMMY
   350     10    1420    1356   44.60   15.34   29.25    0.00    0.00    0.00    0.00   31.07    0.00

                                        #### AT CATHODE DURING STEP  400 OF RUN 62005 ####
  CGCAT  -9.295E-11  -6.073E-10  -4.217E-10  -3.364E-10  -3.192E-10  -4.023E-10  -5.409E-10  -7.272E-10
  CGCAT  -1.074E-09  -1.162E-09  -8.919E-10  -1.282E-09  -8.827E-10  -1.004E-09  -7.330E-10  -7.946E-10
  CGCAT  -4.133E-10
 EZCATH  -7.016E+04  -8.538E+05  -1.391E+06  -1.627E+06  -1.547E+06  -1.471E+06  -1.095E+06  -9.923E+05
 EZCATH  -4.751E+05  -6.936E+05  -4.119E+05  -6.908E+05  -3.988E+05  -5.914E+05  -3.458E+05  -3.549E+05
 EZCATH   5.732E+04
 DQEMIT   0.000E+00  -7.295E-10  -7.295E-10  -7.295E-10  -7.295E-10  -7.295E-10  -7.295E-10  -7.295E-10
 DQEMIT  -2.825E-13  -4.056E-10  -3.915E-11  -2.791E-10  -1.864E-11  -3.325E-10  -4.866E-11  -7.490E-12
 DQEMIT   0.000E+00
  E/(E-MAX ; NO SPACE CHARGE ) %          2  22  36  42  40  38  28  26  12  18  11  18  10  15   9   9   0
  RHO/RHO-BRILLOUIN %                  -15 -52 -36 -28 -27 -34 -46 -63 -93-101 -77-111 -78 -87 -63 -68 -71
  J EMITTED/J THERMIONIC %               0 100 100 100 100 100 100 100   0  56   6  38   3  46   7   1   0
   400      11    1420    1359   43.62   15.69   27.93    0.00    0.00    0.00    0.00   32.98    0.00

                                        CURRENTS(A/M) AVERAGED OVER  100 STEPS AFTER STEP  400
 OVER CATH   SOLE IN   SOLE OUT   EMITTED      BACK  NET CATH     PLATE  LINE ANODE     SOLE      EXIT      DUMMY
      0.00      0.00       0.00    452.97    149.03    303.93      0.00       0.00      0.00    304.64       0.00
 MEAN J-CATH(A/M##2)   0.000E+00  2.000E+05  2.000E+05  2.000E+05  2.000E+05  2.000E+05  2.000E+05  2.000E+05
 MEAN J-CATH(A/M##2)   3.810E+04  1.128E+05  8.989E+03  7.785E+04  6.529E+03  9.081E+04  1.136E+04  2.694E+04
 MEAN J-CATH(A/M##2)   0.000E+00

                    TRAJECTORY SEGMENTS FOR RUN 62005   STEP   400
```

APPENDIX E

COMPUTATION TIME AND STORAGE

Table E1 summarizes the parameters for a typical run of the 2D time-dependent program.

Approximate equivalent CPU times for other machines are as follows:

Computer	CPU time(sec)
Harris 550	1
IBM 360/67	1.16
IBM 370/148	0.51
CDC 6500	2.28
Amdahl 470V/6	0.124
Amdahl 470V/7	0.083

The three-dimensional analysis will require an estimated 10,000 particles (300 K 48-bit words of CPU storage) and 1 hour of CPU time per run for a single grid wire. It is expected to require about 32,000 particles (500 K words of storage) and 4 hours of CPU time per run for a full simulation including the end hats.

TABLE E1

COMPUTATION PARAMETERS FOR TWO-DIMENSIONAL SIMULATION OF RW-620 GUN

Mesh size:	28 x 36
Length of sole simulated:	2.9 mm
Number of time steps:	200 (20 cyclotron periods)
Number of interacting rods:	1350
CPU time on Harris 550 machine (sec):	508
CPU sec/rod/time step:	1.88×10^{-3}
CPU storage on Harris 550 machine (48-bit words):	160,000

APPENDIX F

PROFESSIONAL PERSONNEL AND INTERACTIONS

The principal investigators for this phase of the study of the injected-beam CFA are Dr. Joseph E. Rowe, Vice President for Technology of Harris Corporation, and Drs. Thomas P. Fontana, Donald M. MacGregor, and Richard Mains, Staff Engineers at Harris SAI, Inc.

The data for the RW-620 injected-beam CFA were supplied by Dr. Robert R. Moats of Northrop Corporation Defense Systems Division, Des Plaines, Illinois. A helpful discussion of the tube and the Northrop measurements took place between Dr. Moats and Drs. Fontana, MacGregor, and Mains of Harris SAI at Northrop on March 12, 1979.

Harris SAI is also grateful to Dr. Richard True of Litton Industries, Inc., who provided helpful information about the static gun calculation at the IEEE International Electron Devices Meeting in Washington, D.C. on December 4-6, 1978.

Some preliminary results of this contract are being presented at the Tri-Services Cathode Workshop, Rome Air Development Center, April 15-17, 1980, together with more detailed results from the distributed emission CFA study.

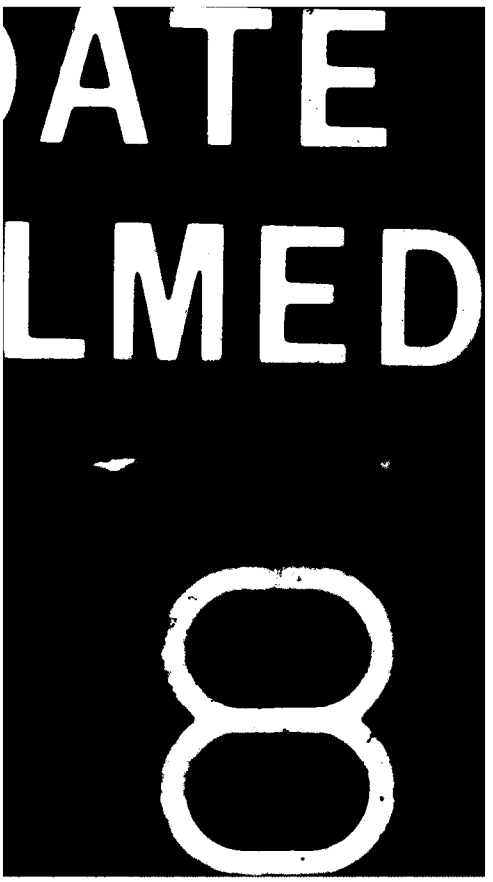
ATE
LMED
8